Quantum optics with 87Rb vapour in the hyperfine Paschen-Back regime

CLARE RACHEL HIGGINS

Quantum optics with ^{87}Rb vapour in the hyperfine Paschen-Back regime

Clare Rachel Higgins

A thesis presented for the degree of
Doctor of Philosophy

Quantum Light and Matter Group
Durham University
United Kingdom
9th February 2023

Quantum optics with ^{87}Rb vapour in the hyperfine Paschen-Back regime

Clare Rachel Higgins

Abstract

We present experimental studies of quantum optics with ^{87}Rb vapour in the hyperfine Paschen-Back (HFPB) regime. We use a 0.6 T magnet to enter the HFPB regime, where, for Rb, the atomic transitions are separated by more than their Doppler width. This allows us to create clean 3- or 4-levels systems, which we model simply and effectively by solving the Lindblad master equation. We study electromagnetically induced transparency in a V configuration in the HFPB, where we see large, clean absorption and corresponding transmission features. We model the system, and use the model to understand the role of coherence in the features seen. We carry out seeded four-wave mixing in a double ladder scheme ($5S_{1/2}$–$5P_{3/2}$–$5D_{5/2}$), both in and out of the HFPB regime, and compare the two regimes. The simplicity of the system in the HFPB regime allows us to model the system to understand the features we see in the experimental spectra. We convert our seeded FWM into spontaneous FWM, which we use to produce pairs of heralded single photons. We find the zero-field regime to be more efficient for the production of these pairs, and measure $g^{(2)}(0) = 0.25 \pm 0.02$, demonstrating that this is a single photon source. Throughout, we make use of lens cavity etalon filters, which we commission, characterise and compare to atomic line filters. We investigate fine structure changing collisions, which transfer atoms between 5P states, and can be a significant source of noise for quantum optics experiments in thermal vapours. We deduce that these are Rb-buffer gas collisions, measure the spectra of the fluorescence produced after a collision, and use the resolved spectra of the HFPB regime to determine that the nuclear spin magnetic quantum number, m_I, is preserved in these collisions.

Supervisors: Ifan Hughes and Kevin Weatherill

Acknowledgements

Thanks firstly, and most importantly, go to Ifan, who has been ever helpful, interested and encouraging, and generally an excellent supervisor. Thanks to Dani for being wonderful, for all the lab help and proofreading and running chats; your presence just made everything more enjoyable. To Renju, thanks for teaching me about the experiment; I really enjoyed our year working together.

Thanks to everyone in QLM (past and present) for making it such a friendly group to work in. Particularly to Tom and Lucy; our little chat made lockdown Zooms much more tolerable. Thanks to all the people at coffee, and Fatmol, and the people who came running, and the people who came to the pub (extra thanks to those of you who are featuring in many of these groups!).

Thanks too to all the people who made my summer project so fun that I decided to do another four years; James and Dan (I'm so grateful you suggested going climbing!), Will who showed me all the ropes in the lab, and Joschka and Steven for the politics chat.

Thanks to Matt and Viv for being a very encouraging review team, and for other, interesting non-work related discussions. Thanks to Kev for your help as a second supervisor, and your advice on marathons.

I would like to acknowledge the funding from EPSRC (Grant No. EP/R002061/1) and Durham University which made the work in this thesis possible.

Outside of QLM, thanks to Ellie and Alex and Matthew for being great friends to live with; to Adam and Kendra (and others) for all the lovely, and when-required stress-relieving, parkrun touring. To Christian for those things, and many more besides.

Thank you to my parents, whose support I know I can always rely on, and for the freedom and security which that brings. Living in Durham is wonderful, but

sometimes it is so nice to go back home, to see you and Peter and the peacefulness of Cherry Garth.

Contents

Declaration

The work in this thesis is based on research carried out at the Department of Physics, University of Durham, England. No part of this thesis has been submitted elsewhere for any other degree or qualification, and it is the sole work of the author unless referenced to the contrary in the text.

Some of the work presented in this thesis has been published in journals and conference proceedings - the relevant publications are listed below.

Publications

Chapter 4 is based on: Clare R. Higgins and Ifan G. Hughes, *Electromagnetically induced transparency in a V-system with ^{87}Rb vapour in the hyperfine Paschen-Back regime*, J. Phys. B: At. Mol. Opt. Phys. **54** 165403 (2021) [1]. `www.doi.org/10.1088/1361-6455/ac20be`

Chapter 5 is based on: Clare R. Higgins, Danielle Pizzey, Renju S. Mathew, and Ifan G. Hughes, *Atomic line versus lens cavity filters: a comparison of their merits*, OSA Continuum **3**, 961-970 (2020) [2] `https://doi.org/10.1364/OSAC.390604`

List of Figures

List of Tables

Chapter 1

Introduction

1.1 Alkali metal thermal vapours

In this thesis we will primarily investigate nonlinear optical effects in thermal rubidium (Rb) vapour. Rb is an alkali metal atom, meaning it lies in Group I in the periodic table, and has one electron it its outer shell: one valence electron. This means it has a simple electronic structure, similar to that of hydrogen [3], which makes it a good choice of atom to work with to develop our understanding of the fundamentals of atom-light interactions.

Alkali metals at room temperature are of metallic form, so can be easily stored in glass vacuum cells, which we heat to transfer some atoms to the vapour form. We work with Rb atoms in a thermal vapour, at around 100 °C. The number density of atoms in the vapour increases close to exponentially with increasing temperature, meaning we can achieve a number density change of three orders of magnitude with a temperature change of 100 °C [4], and high optical densities can be produced with ease. This makes working with thermal vapours relatively straightforward compared to working with cold atoms, which require a vacuum chamber setup with complex laser systems to cool and trap atoms.

Thermal vapours were the platform used to first demonstrate many staple experimental atomic physics techniques, such as coherent population trapping [5], electromagnetically induced transparency [6] and slow light [7]. Many important experimental breakthroughs were also demonstrated in thermal vapours, such as: a quantum memory for light [8, 9]; realising fluids of light [10, 11], orbital angular momentum transfer [12, 13], and coherent frequency up-conversion [14, 15]. Thermal vapours have also been used for a wide range of applications, including spectroscopy [16, 17], terahertz imaging [18], chip scale atomic clocks [19], brain sensors [20], and even for bovine magnetometry [21].

One disadvantage of using thermal vapours is the atomic motion. All the atoms in the vapour are constantly moving with a range of velocities given by the Maxwell-Boltzmann distribution. Due to the Doppler effect, the frequency of light in the laboratory frame which is resonant with a moving atom is shifted proportional to the atom's velocity [4]. This causes broadening of absorption features, which exceed the splitting of the transition frequencies. A solution to this is to work in a large magnetic field, as we will discuss later in this chapter, and demonstrate in the rest of this thesis. The motion also means that atoms spend only short times in the laser beam, leading to decoherence [22]. This effect can be reduced by using larger beams, and can be accounted for in modelling [1].

1.2 Nonlinear optics

Nonlinear optical effects occur in materials where the polarisation responds nonlinearly to the electric field of light incident upon it, causing the medium to gain frequency components which were not present in the incident light [23]. These components then act as sources of new light frequencies [24]. Thermal vapours have been used extensively to explore nonlinear optical effects, including electromagnetically induced transparency [25, 26, 27, 28, 29], which has in turn been applied to develop magnetometers [30, 31] and atomic clocks [32], and four-wave-mixing [33, 34, 12, 35]. Nonlinear atomic systems are promising areas for the development of fields such as quantum information, and have been shown to be suitable platforms for single photon generation [36, 37, 38] and quantum memories [39, 40].

1.3 Large magnetic field

We will briefly discuss the energy scales relevant to atom-light interactions of alkali atoms. Fig 1.1 shows the energy level structure of the ground (5S) and first excited (5P) states in ^{87}Rb. This gross structure, shown on the left, is the highest occupied electron orbital. Fine structure, due to the interaction between electron angular momentum and electron spin, is shown in the middle of the diagram. Hyperfine structure, shown on the right, is due to the interaction between the electron spin and angular momentum combination, and the nuclear spin. As shown in the diagram, they hyperfine splittings in the excited states are 100s MHz. This means that several of the transitions we excite have frequencies which are closer together than the Doppler width. Therefore we don't excite an individual transition but rather several at the same time, which this makes the system more difficult to understand

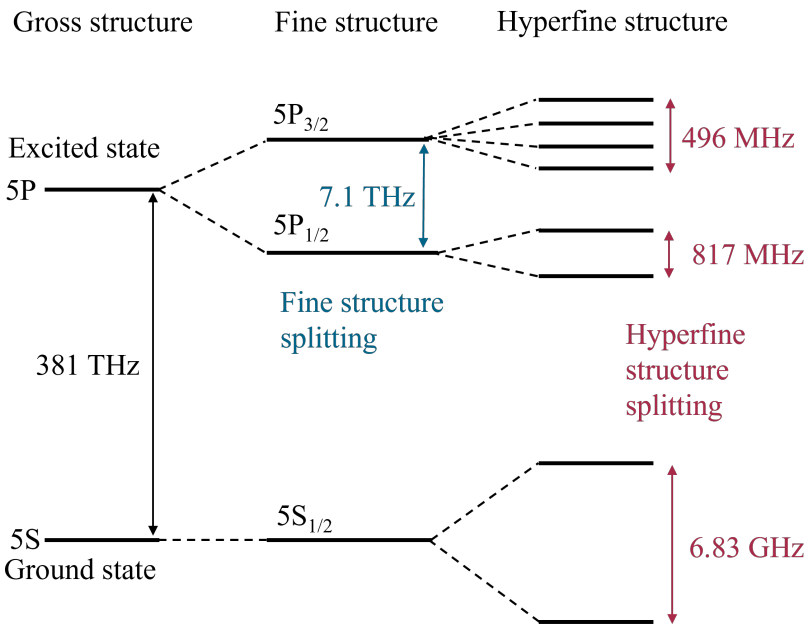

Figure 1.1: Diagram showing the energy level structure of the ground and first excited state of ^{87}Rb, showing fine and hyperfine structure splitting.

and model [41]. Each hyperfine energy level also contains many states which are degenerate (have the same energy) when there is no applied magnetic field.

Placing atoms in a magnetic field causes the energy of their states, and therefore the frequency of the light which excites transitions between those states, to shift [42]. This change in energy of a state due to the magnetic field is known as the 'Zeeman shift'. By appling a large magnetic field to our atoms we can use this effect to overcome the problem of exciting multiple close lying transitions at once. Many of the experiments described in this thesis are carried out in a 0.6 T magnetic field. This puts us in the hyperfine Paschen-Back regime [4], which is a regime where the Zeeman shifts exceed the hyperfine splitting. For Rb, it happens that in this regime all the transitions are separated by more than their Doppler width, so can be excited individually. This allows us so isolate clean energy level systems, such the 3- and 4-level systems we will use for V-EIT and four-wave mixing in Chapters 4 and 7, which can then be modelled relatively simply [25, 43, 1].

1.4 Motivation

The main aim of this investigation is to study nonlinear optical effects in Rb vapour, using the hyperfine Paschen-Back (HFPB) regime to simplify the atomic systems, and to allow us to model them effectively. We study the nonlinear process of EIT in

a V configuration, using the HFPB regime to model the system, and to understand the role of coherence in the features seen. We also carry out seeded four-wave mixing in a double ladder scheme ($5S_{1/2}$–$5P_{3/2}$–$5D_{5/2}$), both in and out of the HFPB regime and compare the effectiveness of the two schemes. The simplicity of the system in the HFPB regime allows us to model the system and understand the features we see in the spectra produced. Primarily, we study FWM with the aim of producing a single photon source, which we do by converting our seeded FWM setup to a spontaneous one, which produces pairs of heralded single photons. We find the zero-field regime to be more efficient for the production of these pairs, and measure $g^{(2)}(0) = 0.25 \pm 0.02$, demonstrating that this is a single photon source. We also investigate fine structure changing collisions, which transfer atoms between 5P states, and was previously found to be a significant source of noise in a FWM experiment in thermal Rb vapour [44]. We deduce that these are Rb-buffer gas collisions, measure the spectra of the fluorescence produced after a collision, and use the resolved spectra of the HFPB regime to determine that the nuclear spin magnetic quantum number, m_I is preserved in these collisions. To do this, we make use of a lens cavity etalon filter, which we commission and characterise.

1.5 Thesis structure

The remainder of this thesis is made up of a short chapter each on theory and experimental details, followed by four main results chapters, then a summary chapter. Each results chapter is self-contained, and includes its own, more specific, introduction and theory sections. A summary of the contents of each chapter is presented below.

Chapter 2: Theory. In this chapter we cover some of the theory relevant to the whole thesis. We cover the interaction of a hypothetical 2-level atom with light, and introduce the Lindblad master equation to model this system. We explain how the refractive index of a medium is calculated and how this leads to the absorption spectra that we measure. Finally we discuss how the atomic energy levels are affected by the presence of a magnetic field, and introduce the hyperfine Paschen-Back regime, which we reach by application of a large magnetic field.

Chapter 3: Experimental details. This short chapter covers some of the experimental details relevant to the whole thesis, including a description of the vapour cells and magnets used, and explains how the lasers are frequency stabilised.

Chapter 4: Electromagnetically induced transparency in a V-type system. This chapter contains an investigation into V-EIT in ^{87}Rb in the hyperfine

Paschen-Back regime. We demonstrate clean induced transmission and absorption features and present a model which shows good qualitative agreement with the experimental results.

Chapter 5: Narrowband spectral filtering techniques. We present an etalon lens cavity filter design, which we have built and characterised. We compare this to an atomic filter, discussing the advantages of each filter type.

Chapter 6: Collisional Transfer. We investigate fine structure changing collisions which we observe in our thermal ^{87}Rb vapour; we put in light on the D2 transition, and get light out on the D1 transition, and vice versa. We posit that this is due to collisions with buffer gas atoms. We analyse the spectral characteristics of the fluorescence produced, and find that the collisions conserve the nuclear spin quantum number.

Chapter 7: Four Wave Mixing. We implement a four-wave mixing setup in a double ladder scheme in ^{87}Rb. We investigate the effect of changing the intermediate level detuning, where we see a broad FWM feature when we detune out of the absorption feature. We then use our system as a heralded single photon source, and measure a dip in $g^2(\tau)$, showing that our source produces single photons.

Chapter 8: Summary and Outlook. This chapter summarises the thesis, and presents some thoughts on further related study.

Chapter 2

Theory

This chapter will cover some theory that is relevant to the whole thesis. More theory will be presented as necessary, and in greater detail, in individual chapters.

2.1 Atom light interactions

Most of the work in this thesis depends on the interaction between atoms and light. Here we will present a brief description of the semi-classical model we use to describe these interactions, and apply this model to a two-level atom. A more detailed description can be found elsewhere, e.g. [45, 46]. In Chapter 4 we will extend this model to a 3-level system, and in Chapter 7 to a 4-level system.

We begin by describing the interaction between a coherent light field and a hypothetical two level atom. The energy level diagram for this interaction is pictured in Fig 2.1. The atom has a ground state, ($|g\rangle$) with energy E_g, and an excited state ($|e\rangle$) with energy E_e, which have an energy gap $E_e - E_g = \hbar\omega_0$, where ω_0 is the angular resonance frequency of the transition. The driving field frequency, ω, can be detuned from the resonance frequency by Δ, where $\Delta = \omega - \omega_0$. Atoms in the excited state spontaneously decay to the ground state at rate $\Gamma = 1/\tau$, where τ is the lifetime of the excited state. The system can be describe by a density matrix [47], given by

$$\hat{\rho} = \begin{pmatrix} \rho_{gg} & \rho_{ge} \\ \rho_{eg} & \rho_{ee} \end{pmatrix}. \tag{2.1}$$

The diagonal terms, ρ_{aa}, represent the population of state a, and the off diagonal terms, ρ_{ab}, represent the coherences between states a and b. This matrix generalises such that an n-level system can be described by an n x n density matrix.

The incident optical field can be considered a plane wave of frequency ω and wavenumber $k = 2\pi/\lambda$, which propagates along z, and has electric field $\vec{E} =$

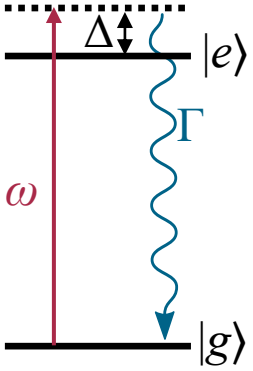

Figure 2.1: Basic diagram of a hypothetical 2-level atom interacting with a light field. The ground ($|g\rangle$) and excited ($|e\rangle$) states are coupled by an optical field with angular frequency ω which is detuned from the atomic resonance by Δ. Spontaneous decay from the excited state happens at rate Γ.

$\vec{\epsilon}E_0 \cos(kz - \omega t)$. $\vec{\epsilon}$ is the polarisation vector, E_0 the electric field amplitude and t is time. Under the dipole approximation [48], which is valid because the spatial extent of the atomic wavefunctions are much smaller than the wavelength of the light, this becomes

$$\vec{E} = \vec{\epsilon}E_0 \cos(\omega t) = \frac{\vec{\epsilon}E_0}{2}(e^{i\omega t} + e^{-i\omega t}). \tag{2.2}$$

The atom-field interaction can be described by the Hamiltonian

$$\hat{H}_{\text{int}} = -\hat{d} \cdot \vec{E}, \tag{2.3}$$

where

$$\hat{d} = \begin{pmatrix} 0 & \vec{d}_{ge} \\ \vec{d}_{ge} & 0 \end{pmatrix}, \tag{2.4}$$

and $\vec{d}_{ab} = -\langle a|e\vec{r}|b\rangle$ are the dipole matrix elements, e is the electron charge and $\vec{r}$ is the displacement vector.

The Hamiltonian evolves in time according to the von Neumann equation [46], as

$$\frac{d\hat{\rho}}{dt} = -\frac{i}{\hbar}[\hat{H}, \hat{\rho}]. \tag{2.5}$$

Here, the total Hamiltonian, $\hat{H} = \hat{H}_0 + \hat{H}_{\text{int}}$ is the sum of the interaction Hamiltonian from Eqn 2.3 and the unperturbed atomic Hamiltonian given by

$$\hat{H} = \begin{pmatrix} \vec{E}_g & 0 \\ 0 & \vec{E}_g \end{pmatrix}. \tag{2.6}$$

It is useful to now transform into a rotating frame, which oscillates at the driving field frequency, using the unitary operator

$$\hat{U} = \begin{pmatrix} e^{-iE_g/\hbar t} & 0 \\ 0 & e^{-iE_g/\hbar t}e^{-i\omega t} \end{pmatrix}. \tag{2.7}$$

This shifts the energy scale to make the ground state zero. We now have a transformed density matrix [49]

$$\tilde{\rho} = \hat{U}^{\dagger}\hat{\rho}\hat{U} = \begin{pmatrix} \rho_{gg} & \rho_{ge}e^{-\mathrm{i}\omega t} \\ \rho_{eg}e^{\mathrm{i}\omega t} & \rho_{ee} \end{pmatrix}, \tag{2.8}$$

where we are now using a tilde to show that we are in the transformed frame. The transformed Hamiltonian is

$$\tilde{H} = \hat{U}^{\dagger}\hat{H}\hat{U} - \mathrm{i}\hbar\hat{U}^{\dagger}\frac{\mathrm{d}\hat{U}}{\mathrm{d}t} = \frac{1}{2}\begin{pmatrix} 0 & \vec{d}_{ge}\cdot\vec{\epsilon}E_0[1+e^{-2\mathrm{i}\omega t}] \\ \vec{d}_{eg}\cdot\vec{\epsilon}E_0[1+e^{+2\mathrm{i}\omega t}] & 2[E_e - E_g - \hbar\omega] \end{pmatrix}. \tag{2.9}$$

We then use the rotating wave approximation to neglect the rapidly oscillating terms in the off-diagonal elements as their time dependence averages out on the much slower timescale of the atomic population evolution. We can use the definition of the Rabi frequency, $\Omega = \vec{d}_{ge}\cdot\vec{\epsilon}E_0/\hbar$, and the detuning, $\Delta = \omega - \omega_0$, to write a time-independent Hamiltonian

$$\tilde{H}_{\mathrm{RWA}} = \frac{\hbar}{2}\begin{pmatrix} 0 & \Omega \\ \Omega* & -2\Delta \end{pmatrix}. \tag{2.10}$$

The von Neumann equation, presented in Eqn 2.5 describes the closed system evolution between the two atomic states and the driving field. However, in reality the system also couples to the environment via spontaneous emission, which introduces decoherence. We add this process to our model by the introduction of a new term, $\hat{L}$, the Lindblad dissipator into our equation, to produce the Lindblad master equation [6]:

$$\frac{\mathrm{d}\hat{\rho}}{\mathrm{d}t} = -\frac{\mathrm{i}}{\hbar}[\hat{H},\hat{\rho}] + \hat{L}. \tag{2.11}$$

Here $\hat{L}$ is given by

$$\hat{L} = \sum_n \frac{1}{2}[2\hat{C}_n\hat{\rho}\hat{C}_n{}^{\dagger} - (\hat{\rho}\hat{C}_n{}^{\dagger}\hat{C}_n + \hat{C}_n\hat{C}_n{}^{\dagger}\hat{\rho})], \tag{2.12}$$

which is a sum over all decay modes, n, where $\hat{C}_n = \sqrt{\gamma_n}\hat{A}_n$ are collapse operators and $\hat{A}_n$ are operators which couple the environment to the system with rate γ_n. For the two level atom this means $\hat{C} = \sqrt{\Gamma}|g\rangle\langle e|$. Other processes which transfer atoms between states, such as collisions can be included in the model by including their rate in γ_n.

2.2 Absorption spectra

Much of the work in this thesis involves absorption spectroscopy: that is monitoring the transmission of a laser beam through an atomic medium as the optical frequency

is scanned. In order to model these spectra we must relate the coherences of our density matrix, ρ_{eg}, to the macroscopic properties of the medium made up of many atoms. We do this via the polarisation of the medium which can be written as [50]

$$\vec{P} = N\langle\hat{d}\rangle = \mathrm{Tr}[\hat{\rho}\hat{d}]N = N(\vec{d}_{ge}\rho_{eg}e^{-\mathrm{i}\omega t} + c.c.), \tag{2.13}$$

where N is the number density of dipoles, $\langle\hat{d}\rangle$ the average dipole moment and c.c. the complex conjugate. The polarisation can also be written as [24]

$$\vec{P} = \epsilon_0\chi(\omega)\vec{E} = \frac{1}{2}\epsilon_0\vec{E}(\chi e^{-\mathrm{i}\omega t} + c.c.), \tag{2.14}$$

where χ is the electric susceptibility of the medium, which is a frequency dependent complex number and ϵ_0 is the vacuum permittivity. Using Eqns 2.13 and 2.14 and the definition of Rabi frequency we can write χ in terms of ρ_{eg}

$$\chi(\omega) = -\frac{2Nd_{ge}^2}{\epsilon_0\hbar\Omega_{ge}}\rho_{eg}. \tag{2.15}$$

The complex refractive index of the medium, n, is given by $n = \sqrt{1+\chi}$. In the systems we use, $|\chi| << 1$, so $n \approx 1 + \chi/2$. The imaginary part of the refractive index n_I is required to calculate the absorption of a medium, via the Beer Lambert equation [4]

$$I = I_0 e^{-\alpha l}. \tag{2.16}$$

Here I is the intensity after the medium, I_0 is the incident intensity, l is the length of the medium and the absorption coefficient $\alpha = 2kn_\mathrm{I}$.

The equations allow us to calculate the absorption of the medium for a particular driving frequency. We calculate the absorption over a range of driving frequencies to build up a spectrum, as we would see in an experiment.

2.3 Lineshapes and Doppler broadening

In the weak probe limit, where the driving Rabi frequency $\Omega \to 0$, we find from solving Eqn 2.11 in the steady state that [45]

$$\lim_{\Omega\to 0}\frac{\rho_{eg}}{\Omega} = \frac{1}{2\Delta + \mathrm{i}\Gamma}. \tag{2.17}$$

This is the origin of the characteristic Lorentzian lineshape. For the ^{87}Rb 780 nm absorption lines, $\Gamma/2\pi = 6$ MHz [51] is the width of the Lorentzian component of the lineshape. However this is not what we see when we measure an absorption profile in the laboratory. That is because in this model so far, we have not included

the motion of atoms. Due to the Doppler effect, moving atoms have a resonance frequency which is shifted in the laboratory frame, by an amount proportional to their velocity. This must be included in the model.

Thermal atoms moving in 3D have a Maxwell-Boltzmann velocity distribution. However, their Doppler shift is determined by their velocity, v_z, along the excitation axis, which we usually chose to label as z. Along this axis the velocity distribution $f(v_z)$ is a Gaussian given by [52]

$$f(v_z) = \frac{e^{-v_z^2/u^2}}{u\sqrt{\pi}}, \tag{2.18}$$

where $u = \sqrt{2k_\mathrm{B}T/m}$ is the width of the distribution. T is the temperature, k_B the Boltzmann constant and m the atomic mass. We include this velocity distribution in the model by including the Doppler shifted frequencies as detunings (the Δ term in Eqn 2.10), using $\omega' = \omega - kv_z$ and setting $\Delta \to \Delta - kv_z$. The Lindblad master equation, Eqn 2.11, is then solved for each velocity class, and the resulting density matrices are weighted by the velocity distribution $f(v_z)$ and summed. In the two level system, including atomic velocities results in a Gaussian component to the absorption profile, which has Doppler width $\omega_\mathrm{D} = ku$, and a full-width-at-half-maximum at 75 °C of 580 MHz. This is approximately 100 times broader than the natural linewidth.

The total lineshape is a convolution of its Lorentzian and Gaussian components. The result of this convolution is known as a Voigt profile [4]. As a Lorentzian distribution has much slower decaying wings than a Gaussian distribution, a Voigt profile resembles a Gaussian at small detunings ($\Delta < \omega_\mathrm{D}$) and a Lorentzian at large detunings ($\Delta > 1.5\omega_\mathrm{D}$) [53].

The width of the Lorentzian part of the lineshape, Γ is the sum of the natural linewidth, Γ_0, and another term, γ_c, which is present because of collisional decays between states. γ_c increases linearly with atomic number density, N [54]. The dependence of N on temperature is discussed in the next section. At a temperature of ∼100 °C, $\gamma_\mathrm{c} \approx \Gamma_0$ and the Lorenztian linewidth becomes $2\Gamma_0$.

2.4 Number density and temperature

The number density of the atomic vapour, N, is the number of atoms per unit volume, and is required to calculate the electric susceptibility χ, as in Eqn 2.15. The number density of Rb increases close to exponentially with temperature, so a temperature change of a few degrees can lead to a doubling of number density [4].

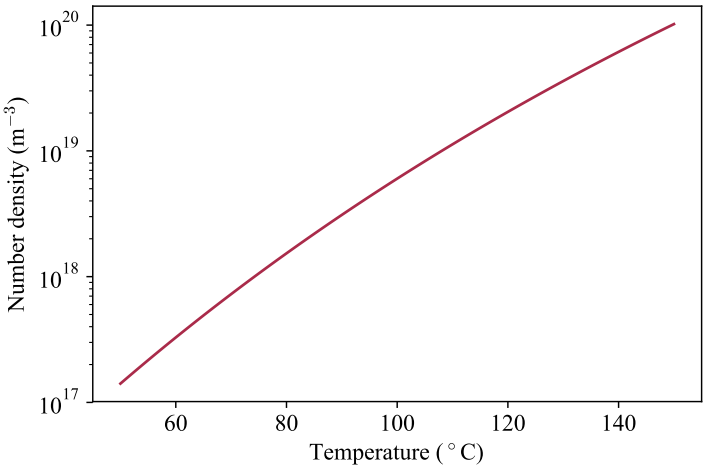

Figure 2.2: Relationship between temperature and Rb number density. Note that the y-axis is plotted on a log scale.

In order to calculate the number density from the temperature (in Kelvin), we first calculate the pressure p, (in atmospheres) using the empirical equation

$$\log_{10}(p[\text{atm}]) = A + \frac{B}{T[\text{K}]} + C\log_{10}(T[\text{K}]), \tag{2.19}$$

where $A = 8.316$, $B = -4275$, $C = -1.3102$ for liquid Rb [55]. Rb has a melting point of 39.5 °C [56], so for all our work Rb is in the liquid phase. The number density is then calculated from the ideal gas equation

$$N = \frac{p}{k_{\text{B}}T}. \tag{2.20}$$

Here p has units of Pa, and 1 atm = 101 325 Pa.

Fig 2.2 shows how the number density changes over a temperature range of 50–150 °C, and we see that there is an increase of three orders of magnitude over this range.

2.5 Atomic structure of Rb

We will now describe the energy level structure of ^{87}Rb atoms, to a level necessary for the subsequent chapters of this thesis. Natural abundance Rb is made up of 72.2% ^{85}Rb and 27.8% ^{87}Rb. However, all the work in this thesis is conducted on isotopically enriched ^{87}Rb vapour which is 98.2% ^{87}Rb [57], in order to have cleaner spectra with fewer transitions. Therefore the following theory will focus on ^{87}Rb.

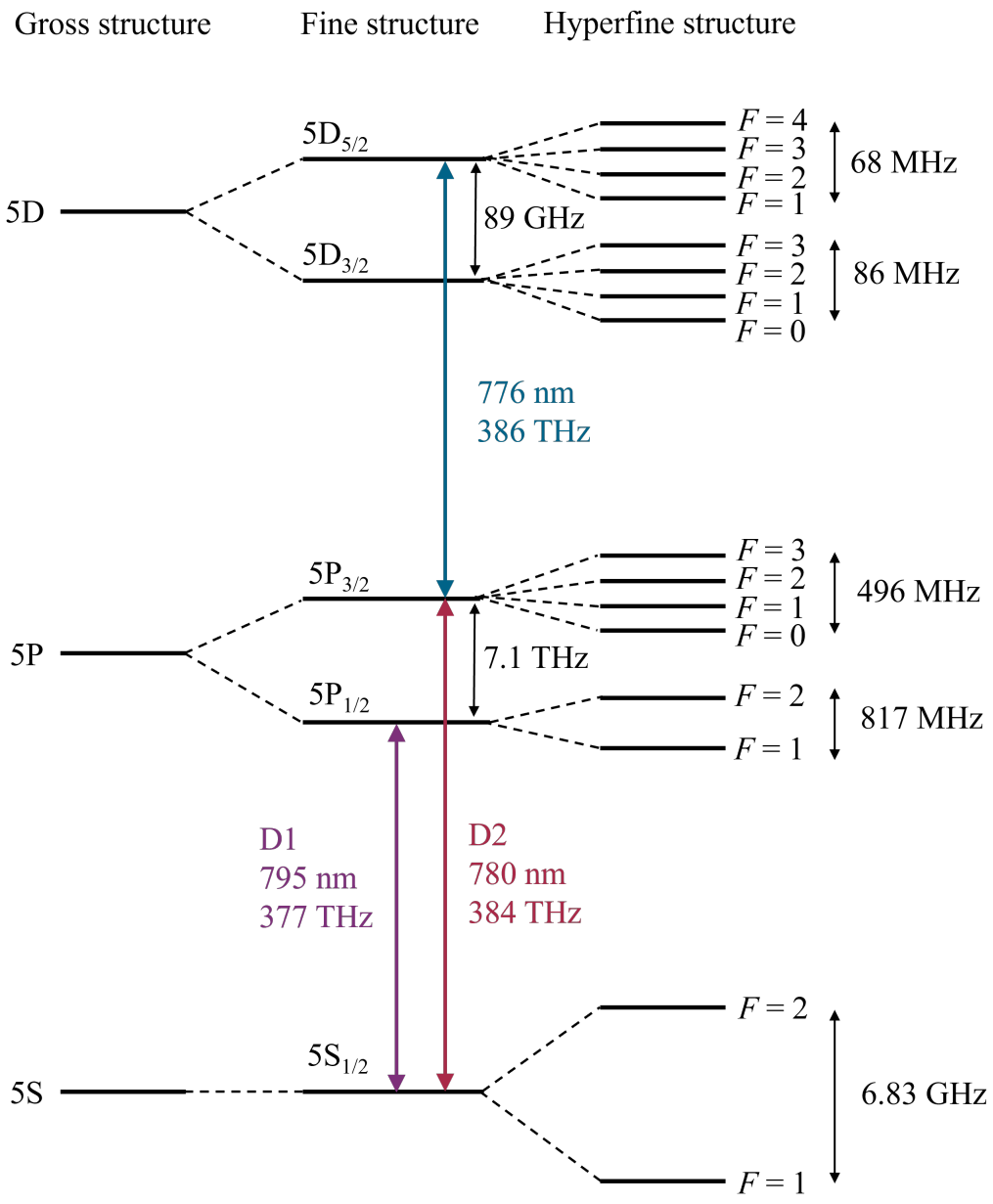

Figure 2.3: Energy level structure of ^{87}Rb, including gross, fine and hyperfine structure. The transitions at 780 nm, 795 nm and 776 nm which are predominantly used in this thesis are labelled. Data from [58] and [59].

^{87}Rb has nuclear spin $I = 3/2$. Fig 2.3 is a schematic diagram of its energy level structure. Rb has principal quantum number $n = 5$, so its gross structure, pictured on the left of the diagram starts at 5S, which has electron orbital angular momentum $\vec{L} = 0$. We use standard notation where $\vec{L}$ is denoted by a letter, with S,P,D,F... $= 0, 1, 2, 3....$ Moving to the centre of the diagram we see the fine structure splitting, which arises from spin-orbit coupling, that is the interaction between $\vec{L}$, and the electron spin, $\vec{S}$, which is always $1/2$ for atoms with one valence electron. These energy eigenstates have total angular momentum $\vec{J} = \vec{L} + \vec{S}$, and have quantum numbers $J = |\vec{L}+\vec{S}|$ and m_J, the projection of $\vec{J}$ onto a quantisation axis defined by the magnetic field. Therefore, without a magnetic field all the different m_J states are degenerate. For each J state, m_J takes all values from $-J$ to J which are separated by one (integer or half-integer, depending on J). In our notation states are labelled as nL_J. Frequency splittings between states are labelled in the figure; the 7 THz splitting between $5P_{1/2}$ and $5P_{3/2}$ will be of particular importance in chapter 6.

Hyperfine structure, shown on the right of Fig 2.3, arises from the interaction between the $\vec{J}$ and $\vec{I}$, the nuclear spin. The energy eigenstates have total angular momentum $\vec{F} = \vec{I} + \vec{J}$, and the good quantum numbers are now $F = |\vec{I} + \vec{J}|$ and m_F, where m_F is the projection of $\vec{F}$ onto a quantisation axis defined by a magnetic field. F and m_F remain good quantum numbers only when the applied magnetic field is small. In the presence of a large magnetic field, as will be described in the next section, we move into the hyperfine Paschen-Back regime where m_I and m_J become good quantum numbers.

2.5.1 The hyperfine Paschen-Back regime

When a magnetic field, $\vec{B}$ is applied, the atomic energy levels shift; this is known as the Zeeman effect. This effect is a result of the coupling of the magnetic field to the electron orbital motion, the electron spin and the nuclear spin. The interaction is described by the Hamiltonian [48]

$$\hat{H}_{\text{Zeeman}} = -\frac{\mu_{\text{B}}}{\hbar}\left(g_L\vec{L} + g_S\vec{S} + \frac{m_e}{m_p}g_I\vec{I}\right)\cdot\vec{B}. \tag{2.21}$$

Here μ_{B} is the Bohr magneton, g_L, g_S and g_I are the angluar momentum g-factors and m_e and m_p are the electron and proton masses, respectively. At small fields, this interaction is weaker than the hyperfine interaction, so each hyperfine level, of which there are $(2F+1)$ m_F levels are split symmetrically around E_0, the zero field energy. The energy level shift is proportional to B, and given by $\Delta E = g_F m_F \mu_{\text{B}} B$,

where g_F is the Lande g-factor for F [3]. This is the hyperfine linear regime, and $|F, m_F\rangle$ is a good basis.

As the magnetic field strength is increased, the coupling to the field becomes a similar strength to the hyperfine interaction; this happens in a field of approximately 0.24 T for the $5S_{1/2}$ state. In this regime there are no good quantum numbers. At larger fields, we reach a regime where the nuclear spin, $\vec{I}$, and spin-orbit angular momentum, $\vec{J}$, couple more strongly individually to the external field than to each other, and so decouple. This is the hyperfine Paschen-Back (HFPB) regime, where the Zeeman energy shift exceeds the hyperfine splitting. Now the energy levels again shift linearly with magnetic field, according to

$$\Delta E = g_J m_J \mu_B B, \tag{2.22}$$

where g_J is the Lande g-factor for J. In this regime F and m_F are no longer good quantum numbers, instead we now use m_J and m_I.

Figs 2.4 and 2.5 show theoretical absorption spectra on the D2 (780 nm) and D1 (795 nm) lines respectively, as B-field is increased. Panel a) is zero field, where F and m_F are good quantum numbers. The spectra look clean, however there are many unresolved close lying transitions within each absorption feature. Panel b) is at 0.1 T, the regime where there aren't good quantum numbers, and the spectra are messy. By panel c), at 0.3 T individual transitions are starting to resolve, but there is still some overlap. In panel d), at our working magnetic field of 0.6 T, we are very close to the hyperfine Paschen-Back regime where m_I and m_J are now good quantum numbers. When Rb is in this regime, the transitions happen to be separated by more than their Dopper width, so individual transitions are resolved.

Figs 2.6 and 2.7 again show these 0.6 T spectra, and now we plot the energy levels underneath to show which features arise from which transitions. In this regime the states are grouped in sets of 4 levels, with a common m_J, with each state in the set having a different m_I. The m_I and m_J states are labelled to the right. The excited states are pure $|m_J, m_I\rangle$ states, while the $5S_{1/2}$ states, labelled in dark blue, contain contributions from two different $|m_J, m_I\rangle$ states, split $\sim$ 98%:2%, so m_I and m_J are not yet perfect quantum numbers. This is because at 0.6 T we have not fully moved to the m_J, m_I basis for the ground states as there is still some residual hyperfine mixing. Increasing the magnetic field strength further would reduce and then remove this mixing. The strong absorption peaks in the top spectra are from transitions out of the 98% ground state components while the weak absorption peaks are transitions out of the 2% ground state components. The light blue arrows, and corresponding lines above, mark σ_+ transitions excited by left-hand circularly polarised light. The purple arrows, and corresponding lines

above, mark σ_- transitions excited by right-hand circularly polarised light, when $\vec{k} \parallel \vec{B}$ [61]. Linear light can be thought of as made up equally of left- and right-hand circularly polarised light, so in the case where $\vec{k} \parallel \vec{B}$, meaning there is no component of $\vec{E}$ along $\vec{B}$, σ_+ and σ_- transitions are excited equally.

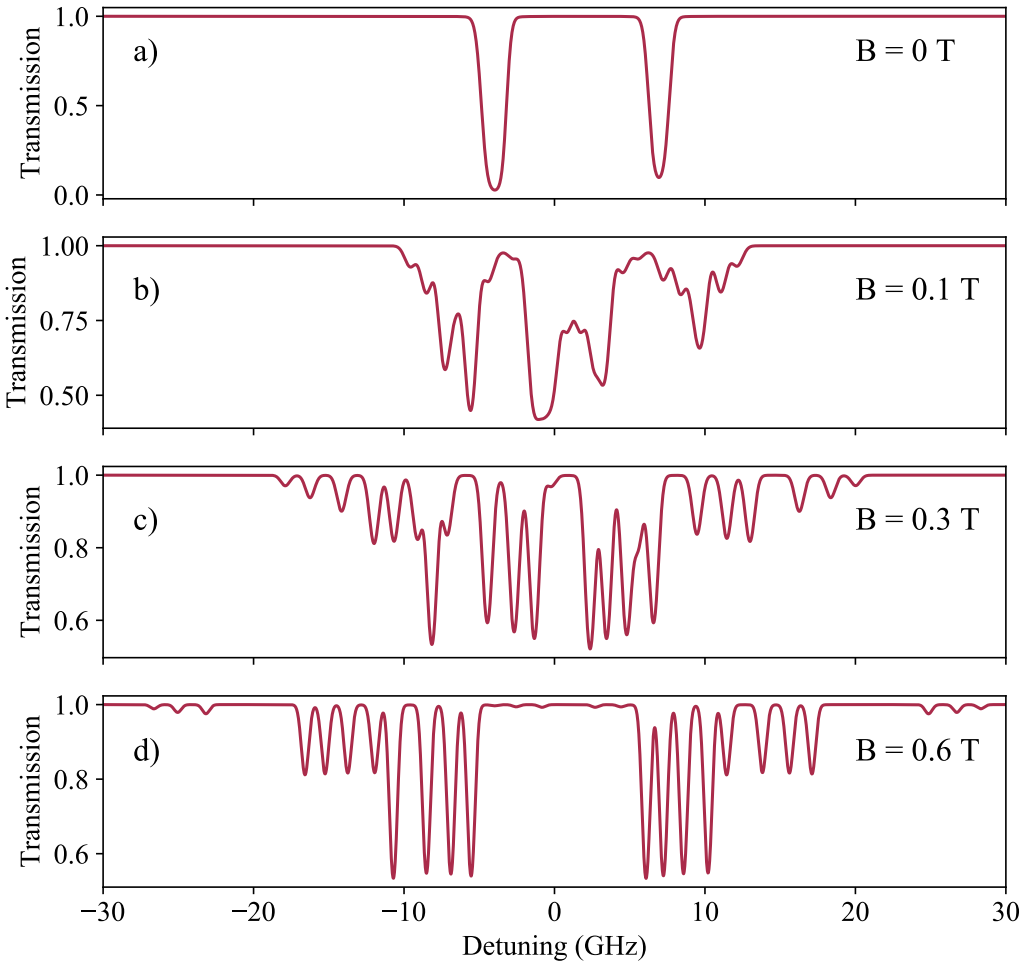

Figure 2.4: Theoretical D2 transmission spectra with changing B-field, calculated using Elecsus [60]. All spectra are in the weak probe regime at 75 °C. Note that the y-axis scale is not constant; as the B-field increases there are more, but weaker transitions. At 0.6 T the transitions are split by more than their Doppler width.

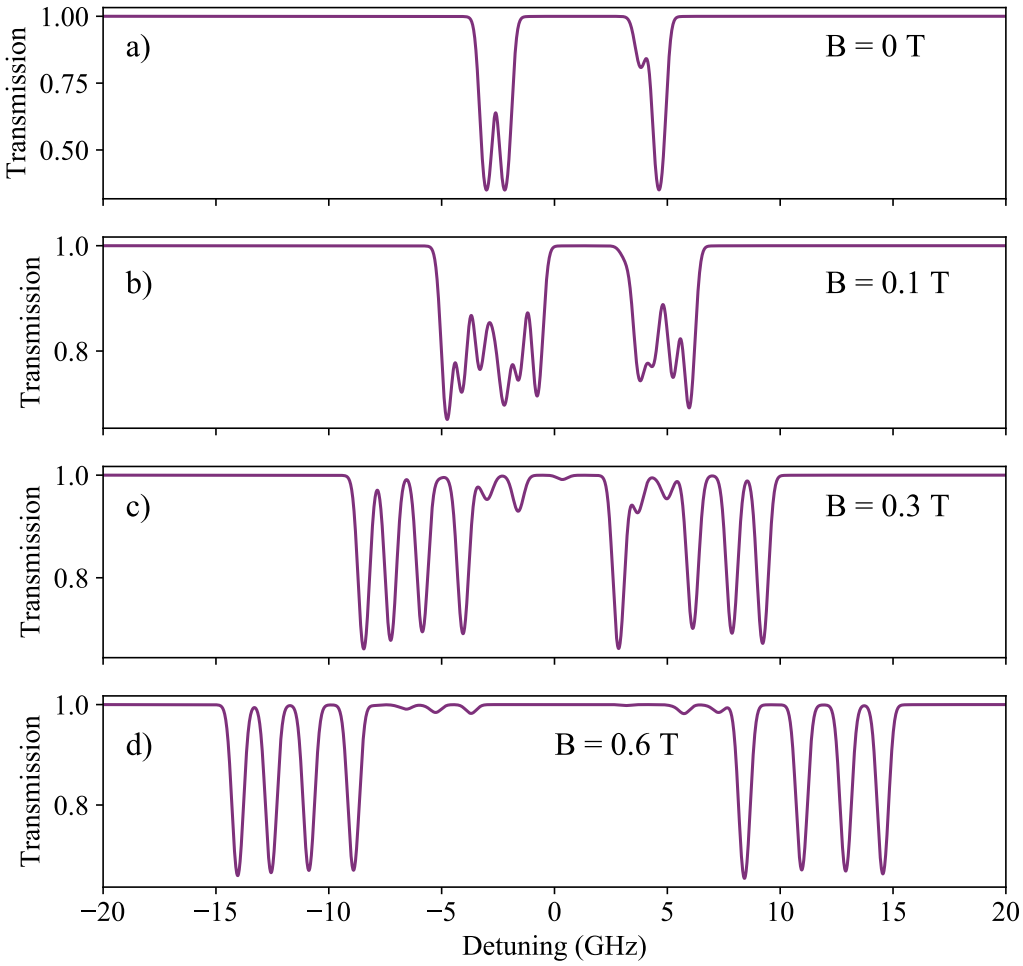

Figure 2.5: Theoretical D1 transmission spectra with changing B-field. Weak probe regime at 75 °C, calculated using Elecsus [60]. Note that the y-axis scale is not constant; as the B-field increases there are more, but weaker transitions. At 0.6 T the transitions are split by more than their Doppler width.

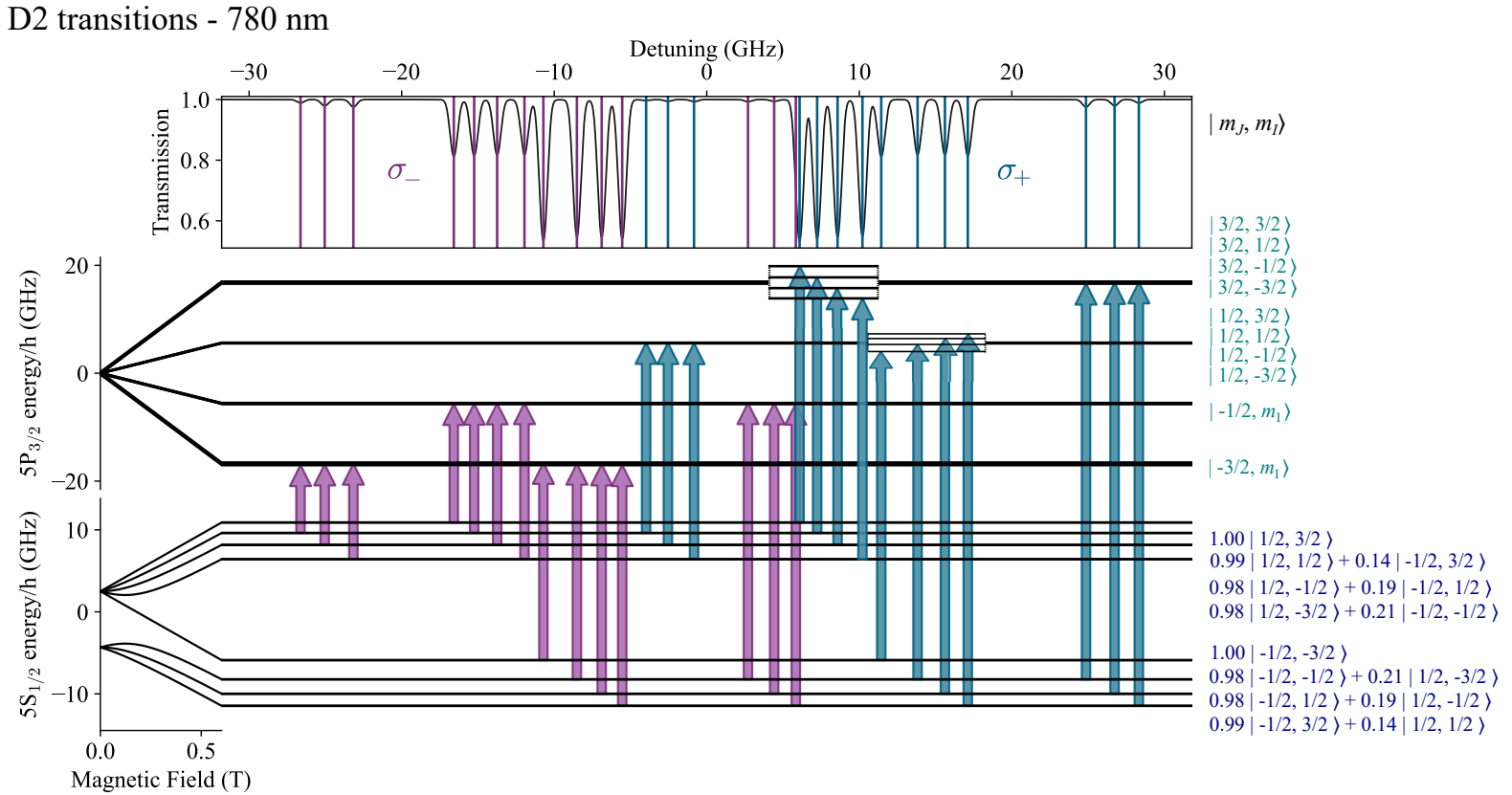

Figure 2.6: Diagram showing the energy levels involved in the D2 (780 nm) transitions at 0.6 T, which are between the $5S_{1/2}$ and $5P_{3/2}$ energy levels. The m_I and m_J states are labelled to the right. The absorption spectra of linearly polarised light resonant with the D2 transitions at 75 °C is shown in the top panel. The light blue arrows, and corresponding lines above, mark σ_+ transitions excited by left-hand circularly polarised light. The purple arrows, and corresponding lines above, mark σ_- transitions excited by right-hand circularly polarised light.

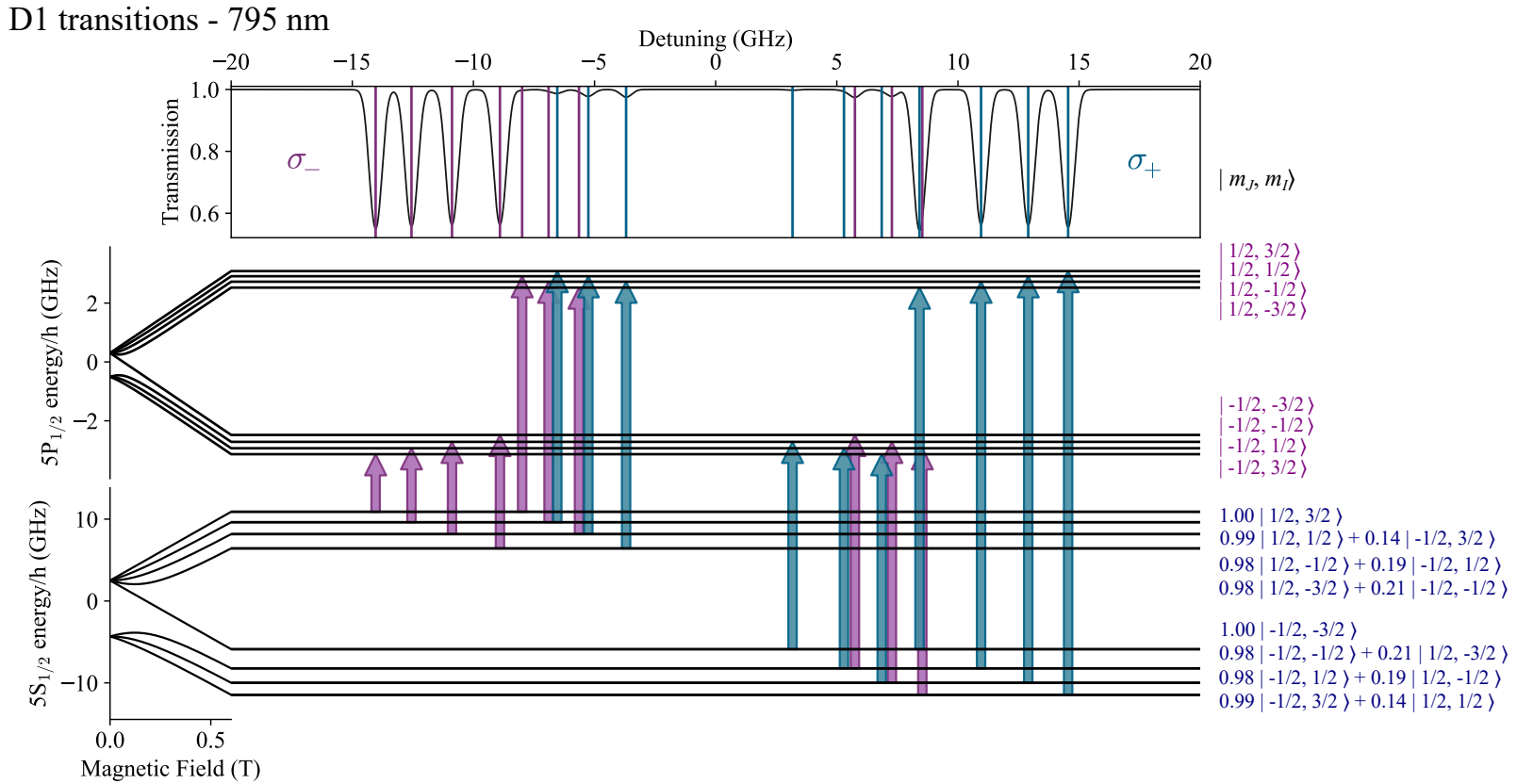

Figure 2.7: Diagram showing the energy levels involved in the D1 (795 nm) transitions at 0.6 T, which are between the $5S_{1/2}$ and $5P_{1/2}$ energy levels. The m_I and m_J states are labelled to the right. The absorption spectra of linearly polarised light resonant with the D2 transitions at 75 °C is shown in the top panel. The light blue arrows, and corresponding lines above, mark σ_+ transitions excited by left-hand circularly polarised light. The purple arrows, and corresponding lines above, mark σ_- transitions excited by right-hand circularly polarised light.

Chapter 3

Experimental details

This short chapter will briefly summarise some of the details of the experimental setup which are general to most of this work. In particular it will describe how the lasers are frequency stabilised (locked).

3.1 Vapour cells

We use several different vapour cells throughout this thesis. All are isotopically enriched ^{87}Rb, but they have different dimensions, and include different buffer gases.

(a) Side view of the 2 mm 'lollipop' vapour cell.

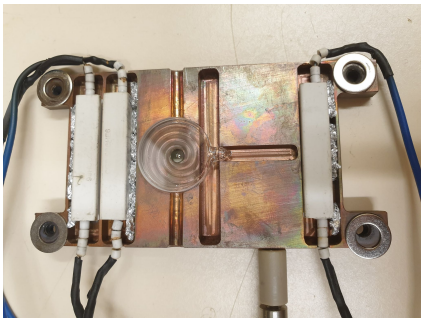

(b) 2 mm 'lollipop' vapour cell inside the copper cell heater.

Figure 3.1: Photos of the 2 mm 'lollipop' vapour cell

Our main experimental cell, which is used for most of this work is a 98% ^{87}Rb [57] 2 mm length cylindrical 'lollipop' cell, as pictured in Fig 3.1. The cell was purchased from Photonics Technologies, and has a diameter of 1 inch (2.54 mm), and a small stem, and is constructed from fused silica. We mount it in a copper cell heater (designed and produced in-house), also pictured, which can heat the cell to ∼200 °C and fits into our magnet setup. This cell nominally contains no buffer gas. The

cell heater has 4 mm diameter holes for light to pass through the centre of the cell, with $\vec{k} \parallel \vec{B}$, and 2 mm holes in the sides, to allow fluorescence out of the sides, perpendicular to $\vec{B}$. These holes are also used to insert a thermocouple to measure the cell temperature.

We use a second 'lollipop' cell as our second locking cell (locking setup discussed in Section 3.3). This cell has all the same specifications as the main cell, but is 1 mm in length. Both cells were purchased from Photonics Technologies.

In Chapter 6 we also make use of two 1 mm^3 cubic vapour cells, which have 99% ^{87}Rb [57]. These are also mounted in a copper heater, however this has optical access from along the laser axis, and from the top, but not from the sides. Both these cells contain hydrogen (H_2) and methane (CH_4) at low partial pressure from the fabrication process. The total pressure of these two gases has previously been measured to be ≈1 Torr [57]. The first of these cells, which we use primarily as our first locking cell contains only these buffer gases.

The second cubic cell also contains a large amount of helium (He). This was introduced when the cell was placed in a superconducting magnet, because glass is porous to helium. Initially (4 years ago) the additional broadening introduced by the He was ∼600 MHz. At the time of the experiments carried out in Chapter 6 it had reduced to ∼300 MHz.

3.2 Magnets

The magnet setup used is the same as that described in [50] Appendix A. Photographs of the mounted magnets are shown in Fig 3.2 b). The magnets are cylindrical top-hat shaped, made from N52 grade NdFeB alloy, and are separated by 15 mm. They have an axial hole through their centre with diameter 4.2 mm. The magnets are mounted in an aluminium block, which keeps them separated and axially aligned. They are mounted such that they can be screwed out of the block slightly, to increase their separation and decrease the magnetic field. The maximum field allowed by the mount is 0.6 T. The magnetic field over the length of the cell is uniform to 1% [57]. The measured magnetic field profile can be seen in Reference [50] Fig. A.1c), which is reproduced here as Fig 3.2.

3.3 Laser locking

For the experiments to follow in this thesis we require our lasers to be locked to atomic resonance features, and to have the ability to detune away from these

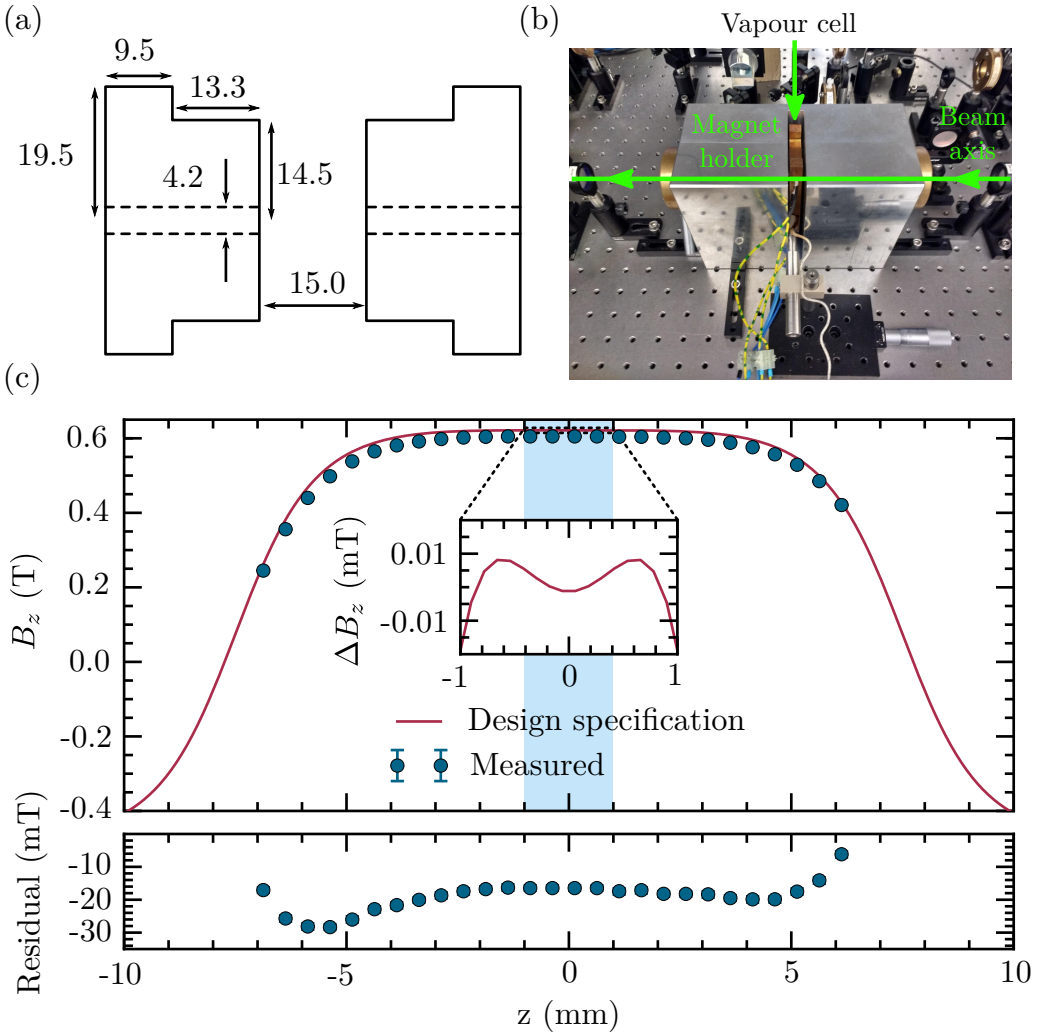

Figure 3.2: a) Dimensions and orientation of top hat magnets. b) Photograph of cylindrical magnets, mounted in an aluminium block. The magnets are mounted and screwed into the block, and the handles visible at the sides can be used to increase their separation and decrease the field strength. The cell heater is in place between the magnets. c) The axial magnetic field profile between the top hat magnets. Blue dots show the measured values with error bars too small to see. The solid red line shows the predicted magnetic field for the design specification. The difference of ∼20 mT seen in the residuals is likely due to a slight demagnetisation of the Neodymium since purchase. The inset shows the field variation over the space normally occupied by the vapour cell (blue shaded region) which has an RMS variation of 4 µT. Figure by Daniel Whiting and reproduced with permission from reference [50].

resonances by specified amounts, while remaining locked. We also require a two photon lock on the $5S_{1/2}$–$5P_{3/2}$–$5D_{3/2}$ ladder in which we can detune away from the intermediate state, but remain two photon resonant with the top state. The system is required to work at zero field and in the hyperfine Paschen-Back regime.

For the experiments described in this thesis, we have three different locking scenarios. They are:

1. The 795 nm laser is frequency stabilised to a D1 resonance feature. This is required to be tunable, and is used in Chapters 4 and 6.

2. The 780 nm laser is frequency stabilised to a D2 resonance feature. This is required to be tunable, and is used in Chapter 6.

3. The 780 nm laser is frequency stabilised to a D2 resonance feature, while the 776 nm laser is frequency stabilised to two-photon resonance. We require the detuning of the intermediate state to be tunable, but the sum of the two frequencies must remain two-photon resonant. This is used in Chapter 7.

We achieve this by using a modified version of the lock described in [62]. Our setup includes two locking vapour cells, each in a magnetic field, in addition to the experiment cell. The relevant parts of the experimental setup are shown in Fig. 3.3.

The locks for scenarios 1 and 2 are implemented in the same way, using only the 'Experimental cell' and 'Locking cell 1' panels of Fig. 3.3. As we only need either the 795 nm laser or the 780 nm laser locked at any one time we just switch the input laser beams and the interference filters to change between the two locks. The experimental cell transmission on a photodiode (PD) is used as a monitor for the frequency of the laser, and the signal on the photodiodes in the 'Locking cell 1' panel is used to lock the laser. These two photodiodes are set up with a polarising beam splitter cube (PBS) in a differencing configuration, meaning we subtract the signal of one from the signal of the other to obtain the Stokes parameter, S1. This parameter has zero crossings at the atomic resonance frequencies [63], so the laser frequency can be stabilised to the atomic resonance in locking cell 1 using the inbuilt PID locking module on the lasers (Toptica DL100 for 780 nm and 795 nm).

Fig 3.4 (reproduced with minor modifications from reference [62]) shows an example locking signal in the hyperfine Paschen-Back regime at 0.6 T. The top panel of part a) shows the 780 nm transmission through the experimental cell, in blue. The bottom panel shows the S1 locking signal in locking cell 1. Part b) shows a close up of the zero crossing feature used to lock. In this example the 780 nm beam is being locked to resonance so the magnetic fields in the experimental cell and first locking

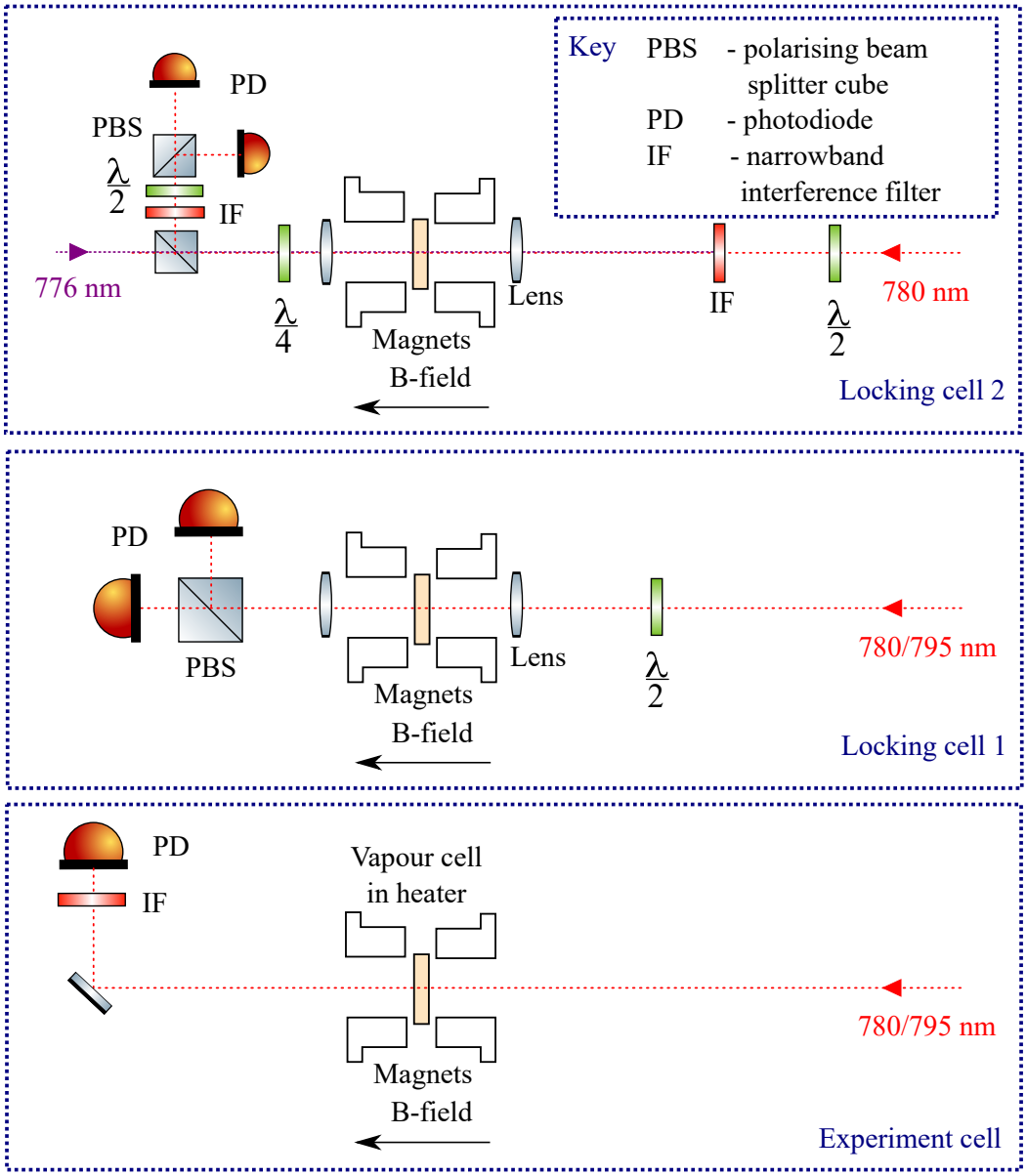

Figure 3.3: Schematic diagram of locking setup. In the experimental cell section the laser light passes through the heated vapour cell and transmission is monitored on a photodiode. In the locking cell setup the laser light passes through the heated cell which is in a large magnetic field, and is split by a PBS and directed to two photodiodes. The difference of these signals (S1) is calculated which is the locking signal. The magnetic field can be reduced by separating the magnets further to detune the locking signal relative to the experimental signal. The experimental cell and first locking cell are used to lock either the 795 nm laser or the 780 nm laser. The second locking cell is used to lock the 776 nm laser to be two photon resonant with the 780 nm laser. The locked 780 nm laser beam passes through the vapour cell and its transmission is monitored on a differencing photodiode setup. The 776 nm laser is scanned and counter-propagated through the cell which produces a two-photon absorption feature on the 780 nm transmission, to which the 776 nm laser is locked. The whole system can be used to lock to zero field transitions by removing the magnets from the experimental and second locking cells.

cell are the same. When locking away from resonance the magnetic field of the locking cell is lowered, by screwing the magnets out of the mount, as described in Section 3.2. This causes the purple locking spectra to shift towards zero detuning (according to Eqn 2.22) such that resonance in the locking cell is negatively detuned from resonance in the experimental cell. Parts c) and d) show example spectra from the second locking cell. By monitoring both signals simultaneously we can choose to move the lock point to our desired experimental detuning.

The lock we have just described also works when the experimental cell is in zero magnetic field, for the D2 lines. We only work in the HFPB regime on D1. The locking cell remains in a large magnetic field. The picture is slightly messier, as the transitions in the experimental and locking cell no longer line up, but because the spectrum at $\sim$0.6 T has so many resonances, we can adjust the field such that one appears at the detuning we wish to lock to. This can be seen by comparing panels a) and d) in Fig 2.4. Looking at Fig 2.5 we see that this would not be as simple on the D1 lines, as the B-field needs to be much lower to get atomic resonaces close to the zero field resonances.

For scenario 3, we introduce a second locking cell, with its own magnetic field. In this our method now differs from reference [62]. We require this extra cell to keep our laser pair two-photon resonant while the intermediate state is detuned. This criterion means that the experiment cell and the cell used to lock the upper step laser 776 nm must have the same field in order to have the same resonance frequencies. This second locking cell (third vapour cell) is shown in the top panel of Fig. 3.3. Here the already locked 780 nm laser passed through the heated vapour cell, after which it is directed onto a PBS which splits the light onto two photodiodes, in another differencing detection of S1. The scanning 776 nm laser beam is counter propagated through the cell. Lens are used on either side of the locking cell to increase the Rabi frequency of the beams and enhance the signal.

Scanning the 776 nm laser, whilst monitoring the absorption of the frequency stabilised 780 nm transmission (S0) spectrum produces a two photon absorption feature, as shown in Fig 3.4 d). We adjust the half waveplate before the differencing photodiode setup to balance the signal, to produce a steep slope to lock the 776 nm laser to, using the Toptical DLPro inbuilt lockbox.

This two-photon locking scheme also works in zero-field; in this case the magnets around the experimental cell and the second locking cell are removed, while the first locking cell field remains.

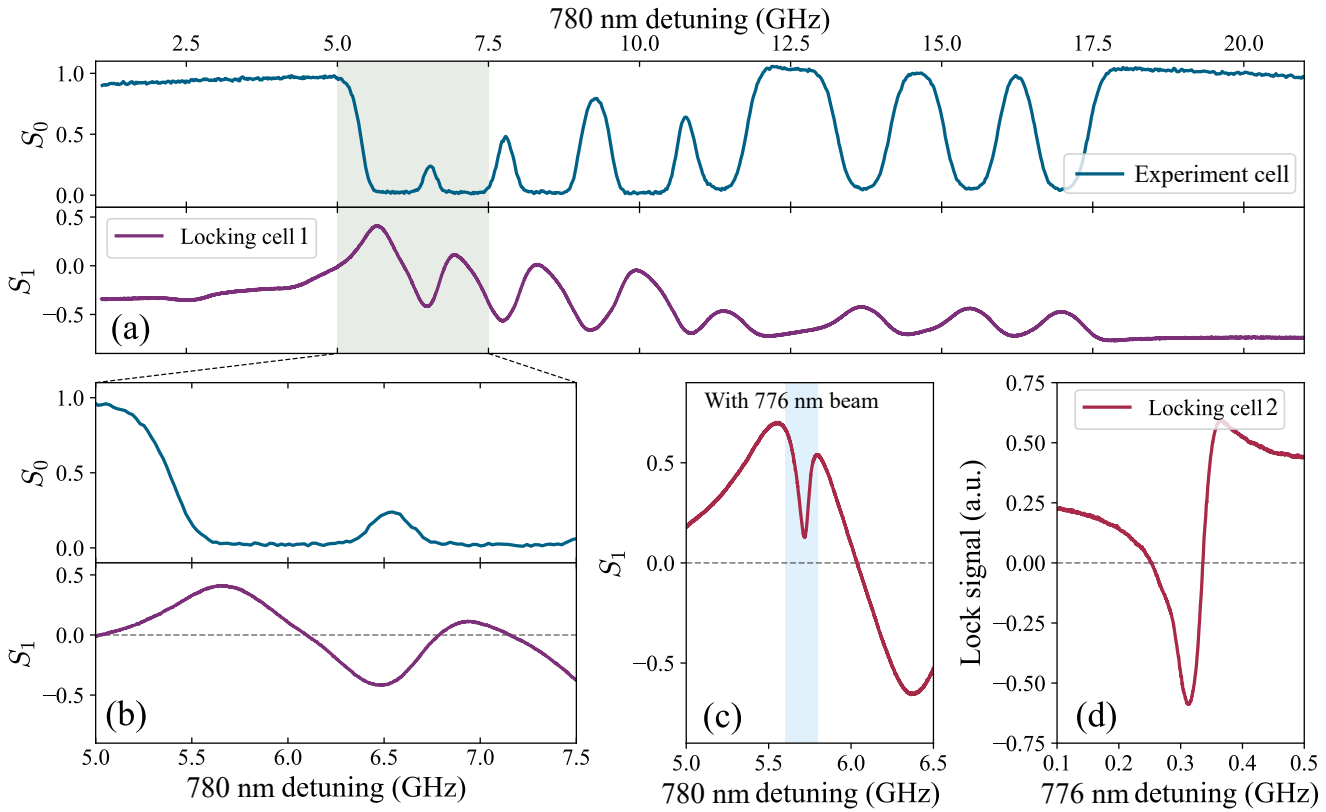

Figure 3.4: Example locking signals in the hyperfine Paschen-Back regime at 0.6 T. The top panel of part a) shows the 780 nm transmission through the experimental cell, in blue. The bottom panel shows the S1 locking signal in locking cell 1. Part b) shows a close up of the zero crossing feature used to lock. In this example the 780 nm beam is being locked to resonance. Parts c) and d) show example spectra from the second locking cell. In c) the 780 nm beam is scanned while the 776 nm is fixed (not locked), showing the two-photon resonance feature. In part d) the 780 nm beam is lock, and the 776 nm beam is scanned, producing a two-photon resonance feature to which the 776 nm beam is locked. This figure is reproduced, with minor modifications, from reference [62].

Chapter 4

V-EIT

This chapter is based on the following publication:

Clare R Higgins and Ifan G Hughes, *Electromagnetically induced transparency in a V-system with ^{87}Rb vapour in the hyperfine Paschen-Back regime*, J. Phys. B: At. Mol. Opt. Phys. **54** 165403 (2021) [1]. www.doi.org/10.1088/1361-6455/ac20be

4.1 Introduction

Electromagnetically induced transparency (EIT) is an optical phenomenon involving three quantum states coupled by two optical fields (laser beams). In an absorbing medium, a transparency window in the absorption feature of a weak probe beam on one transition is induced by the presence of a strong pump beam on another transition [5]. Throughout this chapter we refer to these beams as 'pump' and 'probe'. EIT has been widely studied and has potential applications in precision magnetometers [30, 31, 64], slow light generation [26, 29], quantum information [27, 28], and atomic clocks [32]. There are three possible configurations of EIT: V; lambda; and ladder [6]. V-EIT is the least studied of these because there is no stable dark state [65], as both of the singly coupled states are excited states and can decay to the ground state. Nevertheless, V-EIT has been extensively studied [66, 67, 29, 68, 69, 70, 71, 72, 73, 74, 75, 76, 77, 78, 79], and provides an interesting testing ground for ascertaining the relative importance of coherent and incoherent mechanisms in the generation of the transparency window [80, 81, 70].

One of the main obstacles to overcome in modelling and understanding V-EIT in thermal vapours is the complexity introduced by the overlapping spectral lines, as a consequence of the degeneracies of the magnetic sub-levels and the excited-state hyperfine splitting being less than the Doppler width of the probed transition. To

circumvent these difficulties, we use the hyperfine Pashen-Back regime [82, 59, 83, 84, 85, 86, 87, 88], where the energy levels are non-degenerate. This is discussed in greater detail in Section 2.5.1. A 0.6 T magnetic field used with ^{87}Rb vapour on the D1 and D2 lines leads to isolated transitions separated by more than their Doppler width. Previous work has shown that operating in this regime allows simplified energy-level schemes and theoretical models, leading to good agreement between theory and experiment [25, 43, 34, 36].

In a ideal lambda EIT system, the width of the transparency feature can theoretically be infinitely thin, and is proportional to the square of the pump Rabi frequency as in equation 27 of reference [6]. In practice though, this is not the case as the dark state is not infinitely long lived. In an atomic vapour collisions cause the rate of the forbidden transition between the ground states to be non-zero, which will widen the feature. In the V-system, as both states which would form a dark state are excited states and can decay, the linewidth of an EIT feature is limited by the natural lifetime of these states, to 6 MHz. In practice, there are other causes of decoherence, such as state changing collisions, which increase this linewidth.

4.2 Energy level scheme

Our V-EIT system, realised in the hyperfine Paschen-Back regime, is shown in Fig 4.1, part a). The levels we use, marked $|1\rangle$, $|2\rangle$ and $|3\rangle$, do not form a closed system. We use 'closed system' to mean the atoms do not decay to any states outside of the three EIT levels, and 'open system' when decay to other, non laser-coupled states, is possible. The pumped transition—from $|1\rangle$ to $|3\rangle$—is an open transition so $|3\rangle$ can decay to the other, uncoupled, ground state. This adds a fourth level into the system, which we label $|0\rangle$. The pump causes population transfer from $|1\rangle$ to $|0\rangle$, resulting in reduced absorption of the probe which couples $|1\rangle$ and $|2\rangle$. The driving Rabi frequencies are labelled Ω_{ab}, where a and b represent the initial and final states respectively. The decays between states have two contributions: the natural linewidth, Γ_{ab}, and a collisional decay to each ground state, γ_c. The second is present even where dipole-allowed transitions are forbidden, and the total collisional decay from an excited state has been experimentally determined in this vapour cell as $2\gamma_c/2\pi = 7$ MHz [25]. The natural linewidths (linear) of states $|2\rangle$ and $|3\rangle$ are 6.0 MHz and 5.7 MHz, respectively. These are split along the two decay paths according to the branching ratios calculated using Wigner 3-j symbols. Part b) shows the state configuration when the probe is instead tuned to the transition between $|0\rangle$ and $|2\rangle$. This is not an EIT setup, but allows us to see the enhanced absorption caused by the extra population in $|0\rangle$.

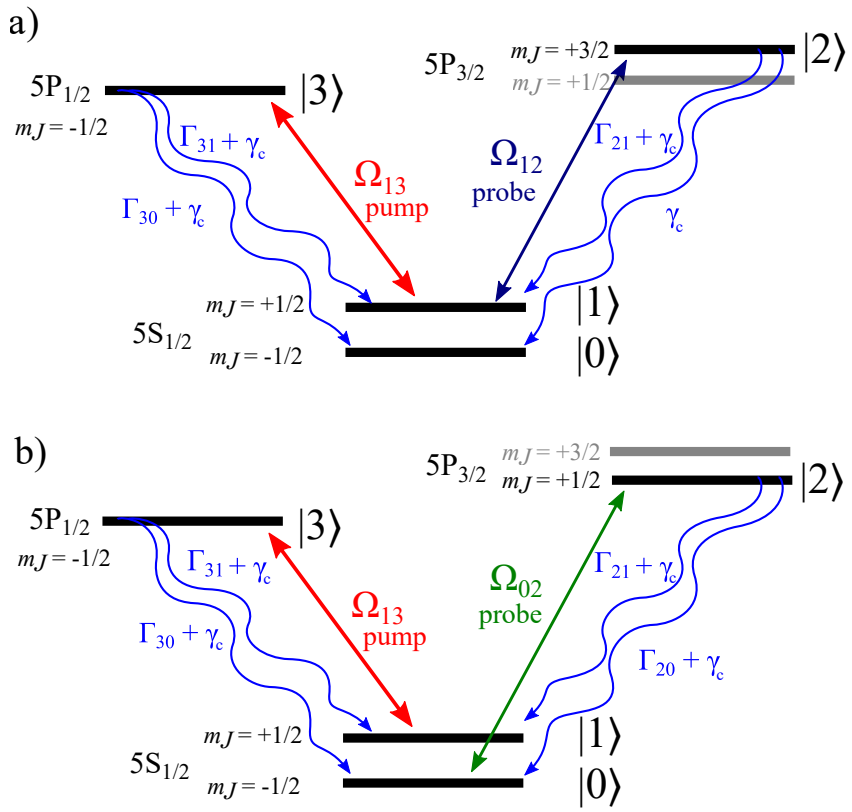

Figure 4.1: The energy levels involved in our system. a) shows the EIT configuration, in which the 780 nm probe beam is coupling $m_J = +1/2$ to $m_J = +3/2$. In b) the probe beam is instead tuned to couple the m_J = -1/2 to $m_J = +1/2$ transition, which excites out of $|0\rangle$, the non-pump-coupled ground state. This configuration does not produce EIT, but demonstrates that population moves from $|1\rangle$ to $|0\rangle$. These two probe positions produce the set 1 and set 2 of peaks in Fig 4.5, respectively. Ω_{ab} are the driving Rabi frequencies, between initial state a and final state b. The decays between states have two contributions: Γ_{ab}, the natural linewidth, and γ_c, the collisional decay to each ground state. The probe(pump) is left(right)-hand circularly polarised and couples $\sigma_+(\sigma_-)$ transitions [61].

4.3 Experimental Details

The experimental setup is shown in Fig 4.2. We use a 2 mm long 98% ^{87}Rb vapour cell in a magnetic field, parallel to the laser propagation direction, of 0.6 T, produced by two cylindrical 'top hat' magnets. The field is uniform across the length of the cell at the 1% level [57]. The cell and magnet setup is described in greater detail in chapter 3. The orthogonally linearly polarised 795 nm and 780 nm beams are combined on a polarising beam splitter cube. A quarter waveplate transforms the polarisation to left-hand circular and right-hand circular respectively. A lens of focal length 200 mm focusses the beams to waists of (100 ± 5) µm × (78 ± 5) µm (780 nm) and (65 ± 5) µm × (90 ± 5) µm (795 nm) inside the cell. We aim to overlap

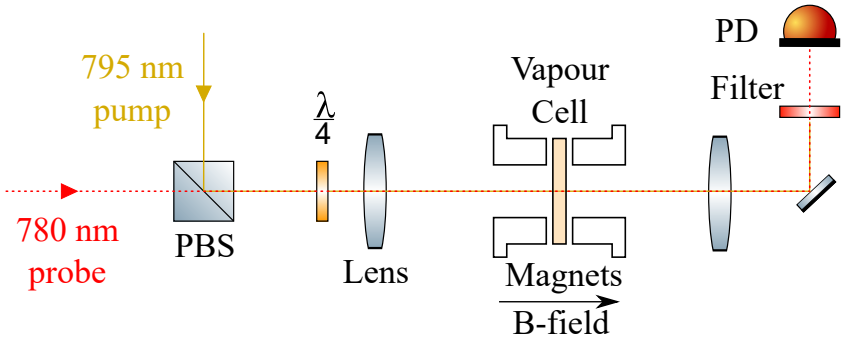

Figure 4.2: Experimental setup. Orthogonally linearly polarised 795 nm pump and 780 nm probe beams are combined on a polarising beam splitter (PBS) cube, and passed through a quarter waveplate converting them to right- and left-handed circularly polarised light, respectively. The beams are focused through a 2 mm vapour cell in a longitudinal 0.6 T magnetic field, to an average beam waist of (83 ± 5) µm.The light transmitted through the cell passes through an interference filter to remove pump light, and is recorded on a photodiode (PD).

the beams as completely as possible inside the cell by optimising the EIT feature, however due to the slight shape difference a perfect overlap is not possible. After the cell an interference filter removes pump light, and the probe transmission spectrum is measured on a photodiode. We have a strong, resonant 795 nm pump, and a weak 780 nm scanning probe. We use a vapour temperature of 80 °C; at lower temperatures the signals are smaller, and at higher temperatures the absorption saturates and the features are distorted.

4.4 Experimental Results

Fig 4.3 shows the advantage gained by using the hyperfine Paschen-Back regime. The top panels show theoretical D2 line spectra without a magnetic field (red) and with a 0.6 T field (blue). The two peaks used in the lower panels are shown highlighted. In the lower panels dotted lines are probe beam only; solid lines are when the pump beam is introduced. The probe only features have a Voigt profile with FWHM of $\sim$ 550 MHz at 80 °C. The profile is dominated by its Gaussian component, which is due to the Doppler effect; atoms at finite temperature travel at a range of velocities which each absorb at a frequency displaced from resonance, given by $\omega = \omega_0 + kv$. Here ω is angular frequency, ω_0 is resonance angular frequency, k is wavenumber and v is the velocity component along the direction of propagation of the laser beams. The left panel shows experimental EIT features with no magnetic field, which includes contributions from several transitions. The right shows the feature in a 0.6 T field, where one clean feature is visible. Both

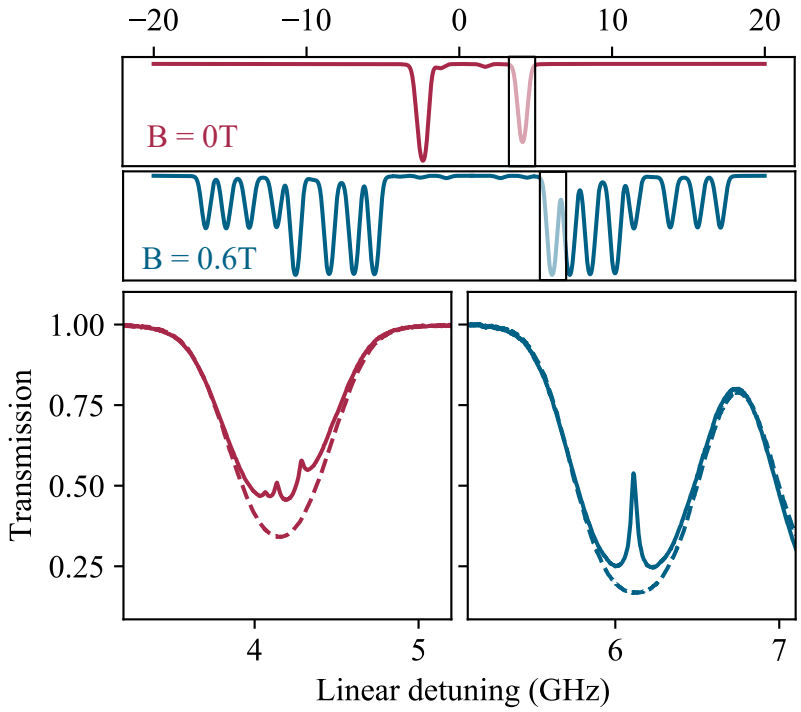

Figure 4.3: Upper panels: Theoretical scans over D2 features without magnetic field (top, red), and with 0.6 T magnetic field (second panel, blue). Shaded rectangles show where the experimental spectra in the lower panels fit in the spectra. In the lower panels dotted lines are probe beam only, solid lines are when the pump beam is introduced. Left: Experimental V-EIT feature with no magnetic field. Many hyperfine sublevels contribute producing a messy feature. Right: Experimental feature in 0.6 T magnetic field. Energy levels are separated by more than the Doppler width so a single clean feature is seen.

features are produced in the same cell, with the same laser powers.

Fig 4.4 shows a scan over the D2 σ_+ absorption lines in a 0.6 T magnetic field. The black trace is a probe only scan, and the red trace shows the effect of adding in a 20 µW pump beam. Here, and throughout the chapter, we use a probe power of 0.1 µW. All the optical power values reported throughout this chapter (and thesis) are measured before the vapour cell, and have an error of ±5%. We see that two different features appear; on the $m_J = -1/2 \rightarrow m_J = +1/2$ peak (left) we see a narrow transmission feature, characteristic of EIT. The states coupled at this point in the scan are shown in the left diagram above. Notably the probe is coupling out of $|1\rangle$, the upper ground state. On the $m_J = -1/2 \rightarrow m_J = +1/2$ peak (right) there is an enhanced absorption feature. In this case, as shown in the right diagram above, the probe couples out of $|0\rangle$, the lower ground state. This state is populated by spontaneous decay from $|3\rangle$, which is itself populated by the strong pump beam.

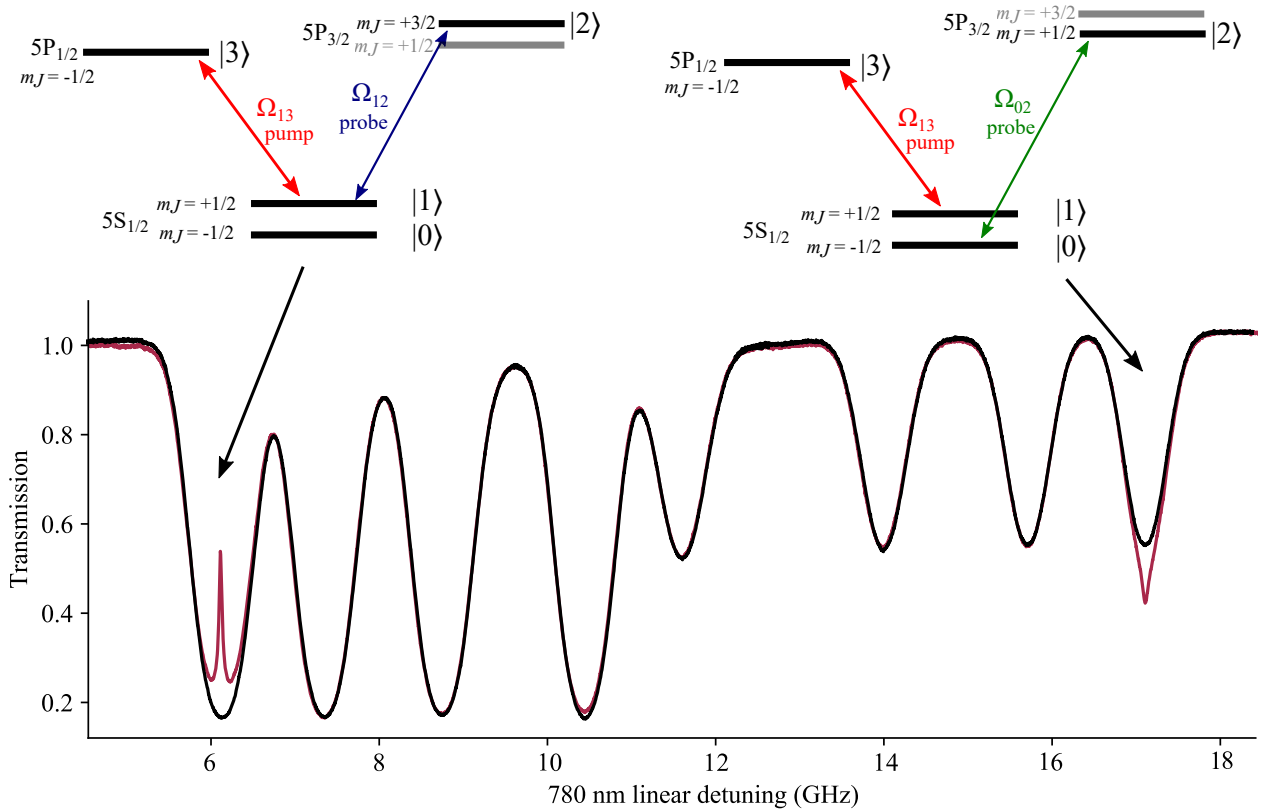

Figure 4.4: Figure shows a 0.1 µW, 780 nm probe beam scan over the σ_+ D2 transition lines at 0.6 T. The black trace is probe only, while the red traces shows the effect of introducing a 20 µW pump beam on the transition $|1\rangle \leftrightarrow |3\rangle$, as shown in the energy level diagrams. The two transitions which display features both couple between states with $m_I = 3/2$. The energy level diagrams show which m_J states the pump beam is coupling for the two features in the scan. Where the probe couples out of $|1\rangle$, there is a transparency feature, and where it couples out of $|0\rangle$ there is an enhanced absorption feature.

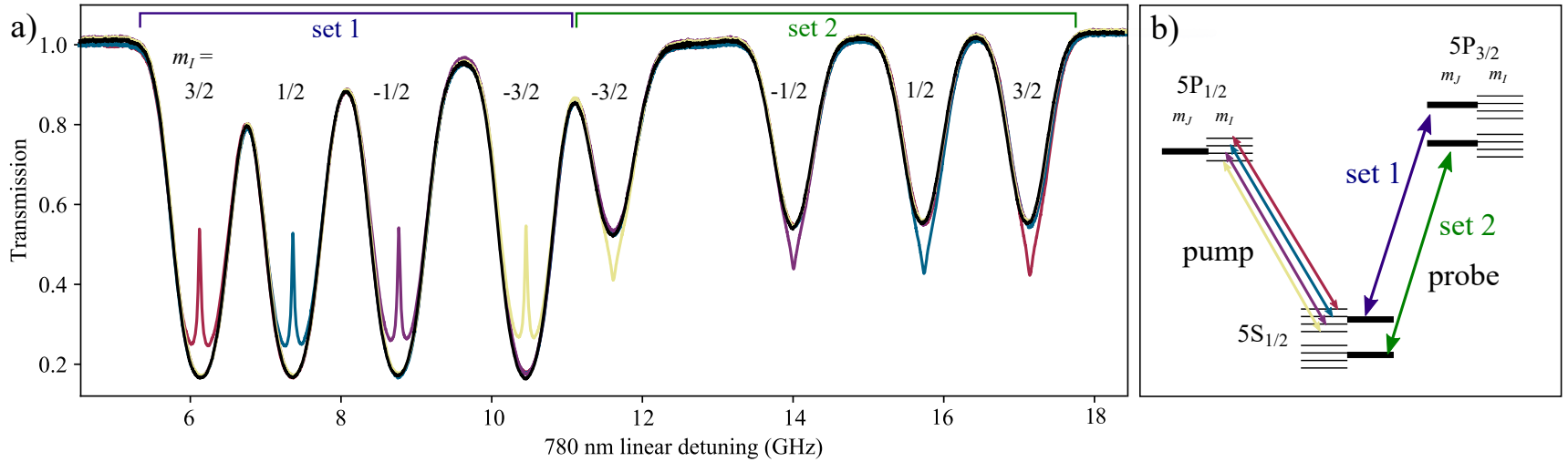

Figure 4.5: a) shows a 0.1 µW, 780 nm probe beam scan over the D2 transition lines at 0.6 T. The black trace is probe only, while the four coloured traces show the effect of introducing a 20 µW pump beam on the correspondingly coloured transition shown in b). Each of the four pump transitions has a different m_I value. Introducing a particular m_I pump transition induces a transparency in the peak in set 1, and an enhanced absorption feature in the corresponding peak in set 2, which have the same m_I.

Following on from Fig 4.4, Fig 4.5 shows the effect of tuning the pump beam to different m_I transitions. The black trace in a) shows a scan of the 780 nm probe over the D2 absorption lines at 0.6 T, with no pump. At 0.6 T, m_I and m_J are good quantum numbers. For ^{87}Rb, $I = 3/2$, therefore there are four possible values for m_I. The spectrum shows two sets of four transitions; in set 1(set 2) all four transitions are between states with initial $m_J = +1/2(-1/2)$ and final $m_J = +3/2(+1/2)$. Inside each set, each transition has a different m_I value, as labelled in the figure. The four coloured traces show the probe transmission when the pump is tuned to the correspondingly coloured transition in b). It is evident that when the pump is coupled to a particular m_I level in the upper ground state, $|1\rangle$, there is a transmission window in the probe absorption peak coupling out of that level (set 1 transitions). There is also a corresponding enhanced-absorption feature when the probe instead couples out of the lower ground state with the same m_I value, $|0\rangle$ (set 2 transitions). The transparency features shown in Fig 4.5 have a FWHM of (39 ± 3) MHz, which we describe as 'narrow' as they are substantially narrower than the Doppler width.

4.5 Model

Atomic systems can be modelled using the Lindblad master equation [6], as seen in Chapter 2,

$$\frac{\mathrm{d}\hat{\rho}}{\mathrm{d}t} = -\frac{\mathrm{i}}{\hbar}[\hat{H}, \hat{\rho}] + \hat{L}, \tag{4.1}$$

which describes the evolution of the density matrix. Here, we consider the 4-level density ρ,

$$\hat{\rho} = \begin{pmatrix} \rho_{00} & \rho_{10} & \rho_{20} & \rho_{30} \\ \rho_{01} & \rho_{11} & \rho_{21} & \rho_{31} \\ \rho_{02} & \rho_{12} & \rho_{22} & \rho_{32} \\ \rho_{03} & \rho_{13} & \rho_{23} & \rho_{33} \end{pmatrix}, \tag{4.2}$$

of the system. The diagonal elements, ρ_{aa}, are the population in each state, and the off-diagonal elements, ρ_{ab}, are the coherences between states. The system Hamiltonian, H, in the rotating wave approximation, has state detunings, Δ_{ab}, on the diagonals, and Rabi frequencies, Ω_{ab}, coupling the states on the off-diagonals. The Hamiltonian corresponding to the system in Fig 4.1 a) is

$$\hat{H} = \frac{\hbar}{2} \begin{pmatrix} 0 & 0 & 0 & 0 \\ 0 & 0 & \Omega_{12} & \Omega_{13} \\ 0 & \Omega_{12} & -2\Delta_{12} & 0 \\ 0 & \Omega_{13} & 0 & -2\Delta_{13} \end{pmatrix}, \tag{4.3}$$

while the Hamiltonian for Fig 4.1 b) is

$$\hat{H} = \frac{\hbar}{2}\begin{pmatrix} 0 & 0 & \Omega_{02} & 0 \\ 0 & 0 & 0 & \Omega_{13} \\ \Omega_{02} & 0 & -2\Delta_{02} & 0 \\ 0 & \Omega_{13} & 0 & -2\Delta_{13} \end{pmatrix}. \tag{4.4}$$

As we use a V system in a co-propagating geometry, we incorporate the Doppler effect into the model by setting $\Delta_{\text{pump}} \rightarrow \Delta_{\text{pump}} - k_{\text{pump}}v$ and $\Delta_{\text{probe}} \rightarrow \Delta_{\text{probe}} - k_{\text{probe}}v$. Prominent EIT features are observed with velocity groups where the residual two-photon doppler broadening $(k_{\text{pump}} - k_{\text{probe}})v < \Omega_{\text{pump}}$ [81]. This geometry makes the system Doppler insensitive, because the two photon resonance condition is maintained for atoms of non-zero velocity.

Decays between states are included in the Lindblad dissipator term, L, given by

$$\hat{L} = \sum_n \frac{1}{2}[2\hat{C}_n\hat{\rho}\hat{C}_n{}^\dagger - (\hat{\rho}\hat{C}_n{}^\dagger\hat{C}_n + \hat{C}_n\hat{C}_n{}^\dagger\hat{\rho})], \tag{4.5}$$

which is a sum over all decay modes, n, where $\hat{C}_n = \sqrt{\gamma_n}\hat{A}_n$ are collapse operators and A_n are operators which couple the environment to the system with rate γ_n. For our system this means $\hat{C}_{ab} = \sqrt{\Gamma_{ab} + \gamma_c}|b\rangle\langle a|$.

We solve the Lindblad master equation numerically for our four-level systems. In the model, on the $m_J = +1/2 \rightarrow m_J = +3/2$ transition, we use a probe beam Rabi frequency of 0.96 MHz (Hamiltonian in Eqn 4.3), and, due to the differing dipole matrix elements of the transitions, a probe Rabi frequency of 0.55 MHz on the $m_J = -1/2 \rightarrow m_J = +1/2$ transition (Hamiltonian in Eqn 4.4). This puts the probe beam in the weak-probe regime. In the weak-probe regime the presence of light does not cause significant population redistribution [4]. We use a range of pump Rabi frequencies to produce a range of features which span those seen experimentally. This range is 2–100 MHz. The pumping transition we use is open, as the excited state, $|3\rangle$, can decay to both m_J ground states, $|0\rangle$ and $|1\rangle$, as depicted in Fig 4.1a). The pump and probe only couple to $|1\rangle$ so in the steady-state solution all the population ends up in the uncoupled ground state, $|0\rangle$, resulting in no absorption. We therefore have to use the time-dependent solutions to Eqn 4.1, which requires that we know how long the atoms are spending in the beam.

We calculate this by following the method of [16]. We calculate the probability distribution, $F(l)$, of an atom having a path length l across a beam of radius a, which is given by

$$F(l) = \frac{l}{2a\sqrt{4a^2 - l^2}}. \tag{4.6}$$

The probability distribution function, $G(t, l)$, of having a transit time transverse to the beam, t, for a given l is calculated from the Maxwell Boltzmann velocity distribution at temperature T for a sample of atoms of mass m is

$$G(t,l) = \frac{ml^2}{k_B T t^3} \exp\left(-\frac{ml^2}{2k_B T t^2}\right). \tag{4.7}$$

From these two functions we calculate the probability distribution function of an atom being in the beam for time t, $H(t)$, which is given by

$$H(t) = \int_{l=0}^{2a} G(t,l)F(l)dl. \tag{4.8}$$

We have beams with an average $1/e^2$ radius of (83 ± 5) µm, from which we calculate the in-beam time-of-flight distribution shown in Fig 4.6. We see that the most common transit time is 0.5 µs and that very few atoms spend longer than 1.5 µs in the beam.

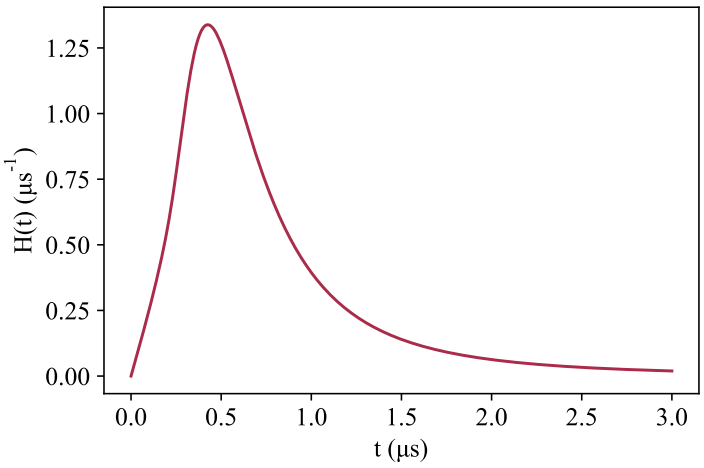

Figure 4.6: Time of flight distribution of atoms in a 83 µm laser beam. Most atoms spend about 0.5 µs in the beam.

We solve the Lindblad-Master equation (Eqn 4.1) time-dependently for 30 timesteps between $t = 0$ and $t = 3$ µs, initialising the system with population split equally between the two ground states. The greater the number of timesteps used, the more accurate the result, but more timesteps also increases the computation time. We find that the effect on the final result of increasing the number of steps past 30, and the maximum time past 3 µs, is negligible. For each probe detuning the solutions are summed over all longitudinal velocity contributions [89].

For each timestep we now have a density matrix solution, ρ_t. From the density matrix we calculate the absorption spectrum, which we can then compare to our experimental results. The term required for this calculation is the coherence between

the states coupled by the seed beam, which are ρ_{21} for Hamiltonian 4.3 modelling the energy system in Fig 4.1a), and ρ_{20} for Hamiltonian 4.4 modelling the energy system in Fig 4.1b). From this coherence we calculate the refractive index, n using

$$n = \sqrt{1 + \chi}, \tag{4.9}$$

where χ is the electric susceptibility given by

$$\chi = -\frac{2Nd_{ab}^2}{\epsilon_0 \hbar \Omega_{ab}} \rho_{ab}. \tag{4.10}$$

Here N is the number density, d_{ab} is the dipole matrix element of the transition between states a and b and ϵ_0 is the permittivity of free space. We then calculate the probe transmission, T, using Beer's Law [90]

$$T = e^{-2kn_{\mathrm{I}}l}, \tag{4.11}$$

where n_{I} is the imaginary part of the refractive index and l is the length of the medium, in our case 2 mm. Using the distribution of in-beam flight times shown in Fig 4.6 we calculate a weighted average of the transmission spectra for different timesteps, and this is the final presented result.

4.6 Comparison with experiment

Fig 4.7 shows the effect of changing pump power or Rabi frequency on the transmission and absorption features, with experimental results in the upper panels and model predictions in the lower panels. Optical power, P, is related to Rabi frequency, Ω, by the beam waist, ω_0, and the dipole matrix element of the transition, d, via the equations

$$\Omega = \sqrt{\frac{2I_0}{cn\epsilon_0}} \frac{d}{\hbar}, \tag{4.12}$$

and

$$I_0 = \frac{2P}{\pi \omega_0^2}. \tag{4.13}$$

I_0 is the on-axis beam intensity. Here, as we are not plotting theory and experiment on the same axis, we use optical power for experiment, and Rabi frequency for theory. We choose a range of values of optical power (experiment) and Rabi frequency (theory) such that the full range of EIT feature sizes are produced; we do not attempt to use equivalent powers and Rabi frequencies. We see good qualitative agreement, with both the narrow transmission and the extra absorption feature correctly predicted, though the features are slightly narrower in theory than in experiment. We attribute the small sub-features seen in the 0.5 and 1 mW spectra to

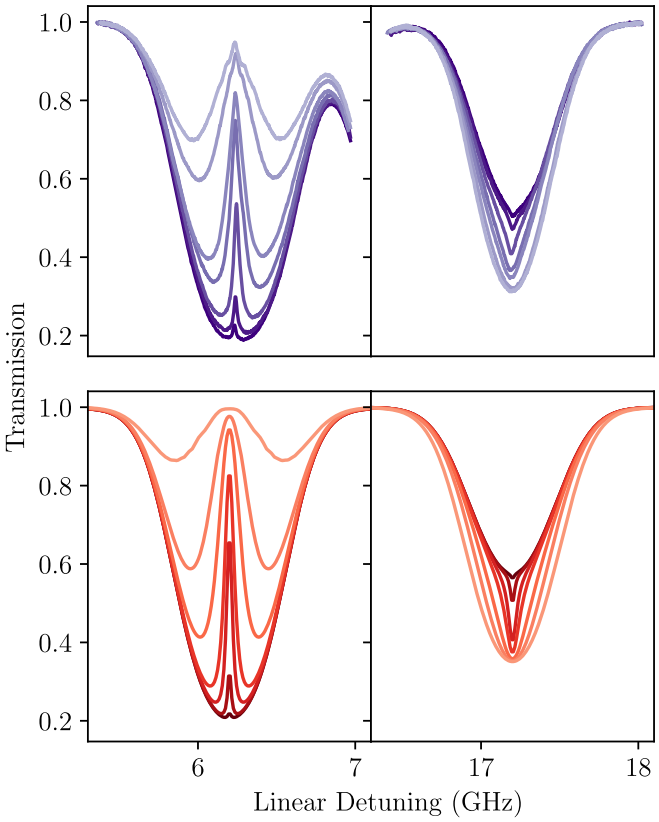

Figure 4.7: The effect of changing the 795 nm pump power on the induced transparency and enhanced absorption features on the $m_I = +3/2$ transitions of the D2 (780 nm, 0.1 µW) spectrum. Upper: Experimental transmission spectra with changing pump powers, with values of in µW of 1 (dark), 5, 10, 50, 100, 500, 1000 (light). These correspond to Rabi frequencies in the range 2–100 MHz. The EIT features shown in the top left panel have FWHM ranging from (21 ± 3) MHz (lowest pump power) to (247 ± 5) MHz (highest pump power). Lower: Modelled transmission spectra with pump Rabi frequencies in MHz of 1 (dark), 3, 10, 20, 50, 100, 300 (light). The range of Rabi frequencies was chosen to straddle the range of features seen in the experimental data; they are not calculated equivalents.

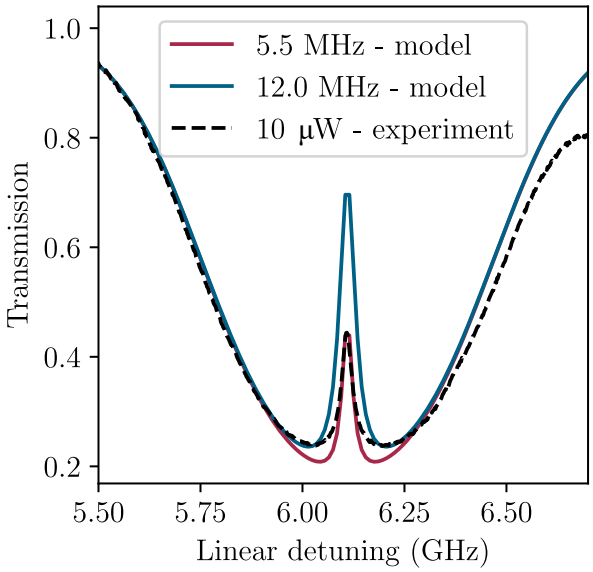

Figure 4.8: A comparison of experimental and modelled results. Black dashed line is experimental with 10 µW pump, which converts to an average linear Rabi frequency in the beam of 15 MHz. Two theory traces are plotted, chosen to fit the tip of the transparency feature (red) and the bottom of the absorption feature (blue). They have linear Rabi frequencies of 5.5 MHz and 12.0 MHz respectively, which are close to our experimental value. It is clear that for this model a pump Rabi-frequency cannot be chosen which fits well to all aspects of the feature; we must choose one or the other.

back reflections, which become more significant at higher powers. The discrepancy between theory and experiment in the left panel on the higher frequency side of the absorption profile is due to the presence of an adjacent higher frequency transition (as seen in Fig 4.4) which is not included in the model.

Fig 4.8 shows the experimental trace for 10 µW pump power (equivalent to 11 MHz peak Rabi frequency), plotted with 5.5 MHz and 12.0 MHz model predictions. We see that using this model, we can choose to fit the peak of the absorption window, or the depth of the feature, but not both at once. In our model we assume that the beams have uniform intensity, whereas in reality they have a Gaussian profile; consequently atoms will experience a varying pump intensity as they traverse the beam. The intensity they see is also correlated to the time they spend in the beam. These factors are likely to change the shape of the spectra. For a numerical comparison we use the average Rabi frequency of the beam within the $1/e^2$ waist, and an average power through the cell, taking into account absorption along its length and at cell windows. In this way, 10 µW input power converts to an average Rabi frequency in the cell of 15 MHz, which is close to the two model values. Both the issues mentioned above, and the fact that we don't fully take into account the

incomplete spatial overlap of the beams could explain this discrepancy. A more detailed numerical model beyond the scope of this work is required to fully account for the shape of the EIT features.

4.7 How significant is the coherent effect?

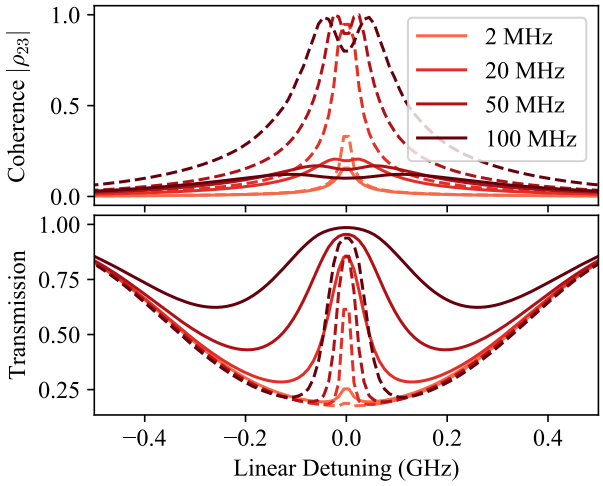

Figure 4.9: Plot showing the absolute value of the coherence between excited states $|\rho_{23}|$, as extracted from the model, and the corresponding probe transmission. On each plot we compare a closed system (dashed lines), and the open system of our experiment (solid lines), for linear pump Rabi frequencies as shown in the legend.

A relevant question in three-level-systems is whether the spectral features are caused by coherent or incoherent effects [65, 70, 80]. The presence of a prominent enhanced absorption feature on the transition out of the non-pump-coupled ground state, $|0\rangle$, is evidence that a significant part of the transmission feature does not arise from a coherent EIT effect, but instead from population transfer to a different (and uncoupled) ground state via velocity-selective optical pumping. However, the we suspect that coherent process is still present, and we can use the model to show this. The density matrix element ρ_{23} is the coherence between $|2\rangle$ and $|3\rangle$, the excited states of our system.

Fig 4.9 compares the transmission (lower panel) and corresponding coherence (upper) for a closed system – meaning no decays into $|0\rangle$ – (dotted lines) and our open system (solid lines). A range of pump Rabi frequencies are plotted and coloured according to the legend. We see that as pump Rabi frequency increases, the difference between the coherences in the closed and open systems increases, and that in our system, coherence increases as Rabi frequency increases up to a point (approx. 20 MHz), above which coherence at zero detuning decreases. We also note that for

a given pump Rabi frequency the closed system coherence is greater than the open system coherence, while the open system transmission is greater than the closed system transmission. This shows that in our open system the coherence is a small, but present, cause of the feature and that as the pump Rabi frequency increases, its proportional contribution decreases. This is in agreement with the finding in [80] that the coherence of a V-EIT system diminishes quickly as the system becomes open.

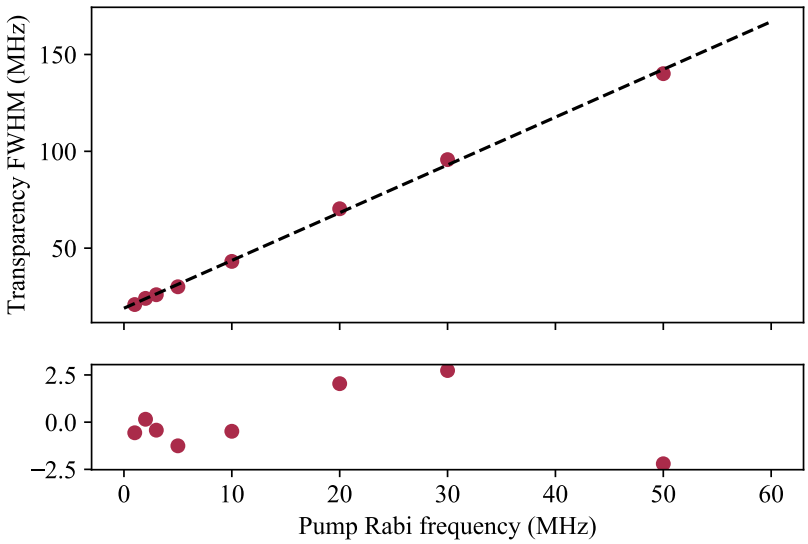

Figure 4.10: Linear dependence of modelled transparency feature linewidth on pump Rabi frequency. Widths are calculated by fitting Gaussians to the modelled transparency features shown in Fig 4.7. A linear fit is plotted (dashed line).

We also use the model to understand the linewidth of the transmission feature we see. The minimum linewidth of the feature in a V-system is set by the lifetime of the excited states, which have a natural linewidth of 6 MHz, however in practice in this vapour cell we measure a collisionally broadened linewidth of 13 MHz. The linewidth will also be broadened by the optical pumping process which occurs in our open system, and plays a significant role in the feature production. We calculate the widths of the modelled transparency features shown in Fig 4.7, by fitting a Gaussian to the section between the two minima of each trace. Fig 4.10 shows a plot of pump Rabi frequency against transparency feature FWHM, showing the width scales linearly with Rabi frequency. We use only Rabi frequencies up to 50 MHz for this fit, because above that the transparency feature saturates and is distorted. The fit has a y-intercept of (19.0 ± 0.9) MHz, giving us the minimum linewidth for our modelled system. This width includes the natural linewidth (6 MHz), the collisonal broadening of the linewidth (7 MHz), and transit time broadening (2 MHz from Fig 4.6). The gradient of the straight line fit is (2.47 ± 0.04). We postulate that

the linear dependence is due to our system being open, with optical pumping into the uncoupled ground state being the dominant cause of the transparency feature. This is in contrast to the quadratic dependence of the ideal lambda system where the transparency feature is due to a coherent effect.

4.8 Conclusions and Outlook

In conclusion, we have observed a clean, narrow transparency feature in a V-system and the concomitant enhanced absorption. We see that the transparency feature has contributions from a coherent process, and an incoherent optical pumping process. The incoherent contribution occurs because of the allowed decay from the excited states to both ground states, and is the cause of the enhanced absorption feature. Our theoretical model captures the main processes, and gives insight into the role of coherence in explaining the observed narrow spectral features. The theoretical treatment is greatly simplified because the experiment was conducted in the hyperfine Paschen–Back regime, leading to distinct non-overlapping resonances.

In the energy level scheme we have used, the Doppler mismatch between the two wavelengths used is small. However the clean system presented here would easily allow investigation of the effect of large mismatches, for example the 5S–5P 5S–6P V-system in rubidium [69, 79], and could be the subject of further study.

Chapter 5

Narrowband spectral filtering techniques

This chapter is based on the following publication:

Clare R. Higgins, Danielle Pizzey, Renju S. Mathew, and Ifan G. Hughes, *Atomic line versus lens cavity filters: a comparison of their merits*, OSA Continuum **3**, 961-970 (2020) [2] `https://doi.org/10.1364/OSAC.390604`

5.1 Introduction

Optical filters are used in a variety of applications for isolating a signal frequency from unwanted background noise. The best commercially available thin-film interference band-pass filters typically have transmission bandwidths of a few nanometres, where the transmission bandwidth is defined as the full-width-at-half-maximum (FWHM). In some research fields, in particular quantum optics where it is necessary to distinguish single photons from high background counts at similar wavelengths [91, 92, 93, 94], narrow-band optical filters are required: these filters can have sub-nm transmission bandwidths, while still retaining high on-peak transmission and off-peak extinction. Uses include the demonstration of quantum teleportation [95], quantum memory [96, 97] and quantum information processing [98], as well as in other fields of atomic physics such as atom trapping [99]. Examples of narrow-band filters include atomic line filters and cavity filters; these shall be the focus of this discussion.

Atomic line filters are often used in atmospheric LIDAR [100, 101, 102], optical communications [103], and laser frequency stabilisation [104, 105]. These filters consist of an atomic vapour cell placed between two crossed polarisers and subject

to a magnetic field which causes the polarisation of light to be rotated as it traverses the cell [106], leading to transmission through the second polariser. For an atomic medium, polarisation rotation only occurs near atomic resonances (which are intrinsically narrow), producing a narrow filter [107, 108]. Filters have been demonstrated in different atomic species, including Cs [109, 110, 111], Rb [112] and Na [113, 114]. The most commonly used atomic filter geometries have been the Faraday geometry, where the magnetic field, $\vec{B}$, and light propagation direction, $\vec{k}$, are parallel, and the Voigt geometry where $\vec{B}$ and $\vec{k}$ are perpendicular. However it is also possible to construct a filter with an arbitrary angle between $\vec{B}$ and $\vec{k}$, which is more computationally complex. The transmission spectrum behaves non-trivially as a function of temperature, magnetic field, and polariser angle for a given cell length. Therefore it is advantageous to use an accurate model of the filter spectrum to find optimum operating parameters; in this work we use a computational model, ElecSus [42, 60].

Cavity filters consist of two high-reflectivity (HR) dielectric coated surfaces, which are separated by a predetermined length [115]. Any light entering the cavity through the first surface will only exit at the second surface when it is resonant with the cavity and the standing wave condition is met [61], resulting in a periodic set of transmission peaks and high extinction elsewhere.

We have built and investigated two different types of narrow-band band-pass filter: monolithic cavity filters, both plano-convex [116] and planar-planar, and an atomic line filter in Rb vapour [60]. Each has advantages and disadvantages—in this chapter we present a study comparing the two.

5.2 Cavity filter

5.2.1 Plano-convex (Lens)

5.2.1.1 Design

We implement a monolithic cavity filter, as proposed in [116], where a spherical high-reflection ($R \sim 99\,\%$) coated plano-convex (PC) lens is used as the Fabry-Pérot cavity. This setup produces transmission peaks with widths of the order 70 MHz, where the central frequency is tunable with temperature. We chose to investigate this cavity design, over the well-known design that consists of two HR coated mirrors attached to a spacer of a given length, because it is intrinsically stable and requires no locking of mirror positions. The plano-convex geometry also provides spatial mode filtering, and allows a higher cavity finesse than a planar

etalon cavity [116]. The cavity quality is governed by finesse, and the ideal finesse of the cavity is given by $\mathcal{F} = \left(\pi\sqrt{R}\right)/(1-R)$. The achievable finesse is limited by surface defects and the mismatch between the wavefront and the surface. Due to diffraction, it is not possible to mode match wavefronts to two separated planar cavity mirrors. Choosing a larger beam diameter to compensate increases the effect of surface defects, limiting the finesse of a flat etalon to 100 [116]. The spherical mirrors of a Fabry-Pérot are much more forgiving, allowing a finesse up to 1×10^5 [117].

The required temperature stability of the cavity is determined by the desired frequency stability and the shift of resonant frequency, v, with temperature, T, given by

$$\frac{\mathrm{d}v}{\mathrm{d}T} \approx -\left(\alpha + \frac{1}{n}\frac{\delta n}{\delta T}\right) v, \tag{5.1}$$

where $\alpha = 7.1 \times 10^{-6}\,\mathrm{K}^{-1}$ and $n = 1.51$ are the thermal expansion coefficient and refractive index of Schott N-BK7 Glass and $\delta n/\delta T$ is calculated from the Sellmeier function [118]. The change in refractive index due to frequency is negligible in comparison to the other terms. The filter design parameters are: reflectivity, R; the radius of curvature of the convex face, r; and the thickness (or length), L. The transmission of a Fabry-Pérot cavity, $\mathcal{T}$, is given by [61]

$$\mathcal{T} = \left(\frac{S}{1-R}\right)^2 \left(1 + \frac{4R}{(1-R)^2}\sin^2\frac{\delta}{2}\right)^{-1}, \tag{5.2}$$

where δ is the frequency dependent phase shift per round trip, and S is the transmission at the mirror, which may not equal $1-R$ due to round trip losses. When R is close to 1, the extinction ratio is

$$\mathcal{T}_{\max}/\mathcal{T}_{\min} \approx \frac{4}{(1-R)^2} \approx \left(\frac{2\mathcal{F}}{\pi}\right)^2, \tag{5.3}$$

so a required extinction ratio sets the reflectivity. The bandwidth of the transmission peaks (Δv) is given by $\Delta v = \mathrm{FSR}/\mathcal{F}$, so a required bandwidth sets the free spectral range (FSR) of the cavity. The length is set via $\mathrm{FSR} = c/2nL$, where c is the speed of light. The spatial filtering requirements determine r; in the case that $L \ll r$, adjacent transverse modes are separated by

$$\Delta v_\perp = \frac{\mathrm{FSR}}{\pi}\sqrt{L/r}, \tag{5.4}$$

and r can be chosen to ensure that no significant subsidiary modes transmit at a frequency of interest.

The off-the-shelf lenses were purchased from, then coated by, Lambda Research Optics Inc, with $R = (99.0 \pm 0.5)\,\%$ for wavelengths in the range 740–860 nm. We

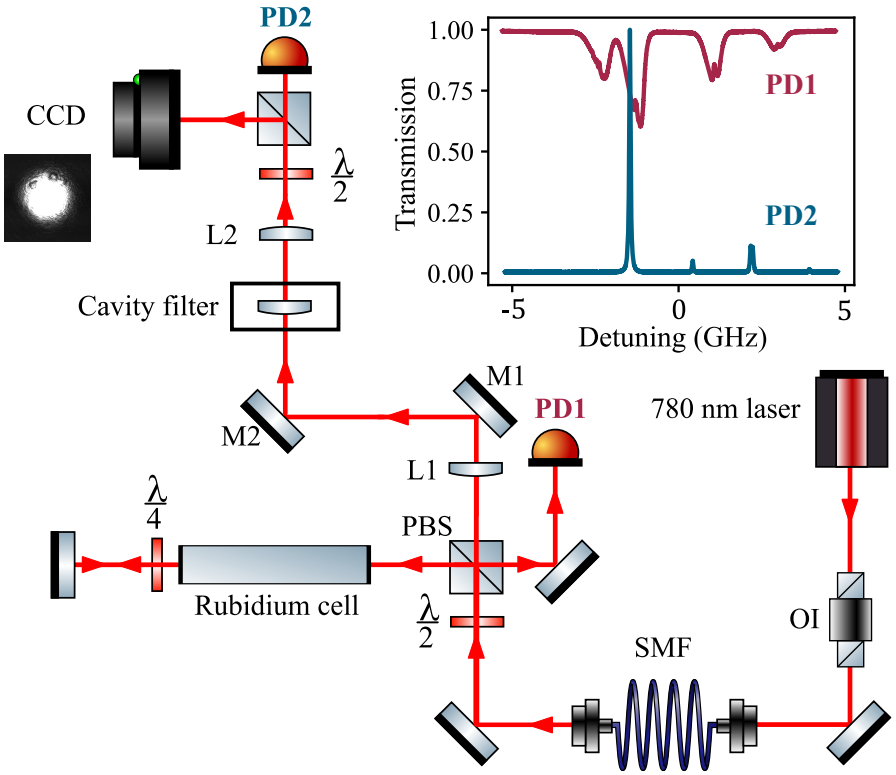

Figure 5.1: Experimental setup for cavity filter characterisation. 780 nm laser light is passed through an optical isolator (OI) and a single mode fibre (SMF), producing a beam with waist 0.5 mm and then split on a polarising beam splitter (PBS) cube. One arm double passes through a natural abundance rubidium vapour cell to provide an atomic frequency reference (red trace) on a photodiode (PD1). The other beam continues through a mode-matching lens (L1) and is steered by mirrors (M1 and M2) into the lens cavity filter. The beam is recollimated by lens (L2), and split with another PBS, allowing the transmission (blue trace) to be monitored on a photodiode (PD2) and the output mode to be imaged on a CCD camera.

chose five different cavity lengths, in the range 2.4–8.0 mm, resulting in cavity bandwidths ranging from 40–128 MHz. All have radius of curvature $r = 40.0\,\mathrm{mm}$.

Using Eqn 5.1, with $\alpha = 7.1 \times 10^{-6}\,\mathrm{K}^{-1}$, $n = 1.51$, $\delta n/\delta T = 2.54 \times 10^{-6}\,\mathrm{K}^{-1}$ and $v = \mathrm{c}/780\,\mathrm{nm}$ gives a frequency shift with temperature of $\mathrm{d}v/\mathrm{d}T = -3.4\,\mathrm{GHz\,K}^{-1}$, meaning a temperature stability of 3 mK is required for frequency stability of 10 MHz. This number is independent of the length of the cavity. We chose BK7 glass because a range of lenses matching our specification were commercially available, and the temperature stabilisation required is achievable. A glass with a lower thermal expansion coefficient or thermal refractive index change could be chosen if a higher frequency stability is required. To achieve this temperature stability, we mount the lens in a lens tube, which screws into a stainless steel block. This is

thermally contacted to a peltier and thermistor, and is further encased in a teflon cover. The cool side of the peltier is contacted to a large aluminium block mounted on the optical bench, providing a large heat sink. The temperature is controlled with a Koheron TEC100L temperature controller.

The experimental setup used to characterise the performance and stability of the cavity filter is shown in Fig 5.1. The cavity must be aligned to couple the correct mode (TEM_{00}). It is necessary to mode match into the fundamental mode of the cavity using a lens (L1), which is selected to match the curvature of the wavefronts with the spherical (front) surface of the cavity, focusing the beam at the planar surface. The beam waist of the fundamental cavity mode at wavelength λ is [119]

$$w_0 = \left(\frac{\lambda nL}{\pi}\left(\frac{r}{nL} - 1\right)^{1/2}\right)^{1/2}. \tag{5.5}$$

The focal length of the mode-matching lens required is given by $f = \frac{w_1 w_0 \pi}{\lambda}$ [61], where w_1 is the initial beam waist. For the 5 mm lens cavity at 780 nm, $\omega_0 = 62\,\mu m$. The incoming beam waist is measured to be $(550 \pm 20)\,\mu m$, so ideally a lens with focal length $f = 140\,mm$ should be used. In practice we use a 160 mm lens. Two steering mirrors (M1 and M2) after the mode-matching lens are used to optimise alignment into the cavity, giving full control of the x-y position and angle of the beam when it enters the cavity. The alignment is monitored mainly on the transmission spectrum, with the mode image used to identify the TEM_{00} mode, which we aim to maximise.

5.2.1.2 Results

Fig 5.2 shows a transmission spectrum across one FSR of the 5.0 mm and 6.5 mm lens cavities. The maximum transmission of both cavities was measured to be 50 %, with extinction of 20 dB over all frequencies away from the TEM_{00} mode. Maximum transmission is not 100 % largely due to imperfect mode-matching into the cavity. The spatial filtering properties of the filter are visible with subsidiary modes transmitting at different wavelengths, determined by Eqn 5.4. We fit the TEM_{00} mode of the 5.0 mm cavity to a Lorenztian (gold solid and black dashed lines in Fig 5.3), finding excellent agreement with residuals less than 1%. This is expected as in the high finesse limit the transmission peaks given by Eqn 5.2 become Lorenztian [61]. From this a width of (70 ± 1) MHz is extracted. This is close to the expected value of 64 MHz, and gives the actual reflectivity of the coating as (98.9 ± 0.1) %. A figure of merit often used to characterise the performance of optical filters is equivalent noise bandwidth, defined as ENBW $= \int T(\omega)\mathrm{d}\omega / T(\omega_s)$, where T is transmission, ω is angular optical fre-

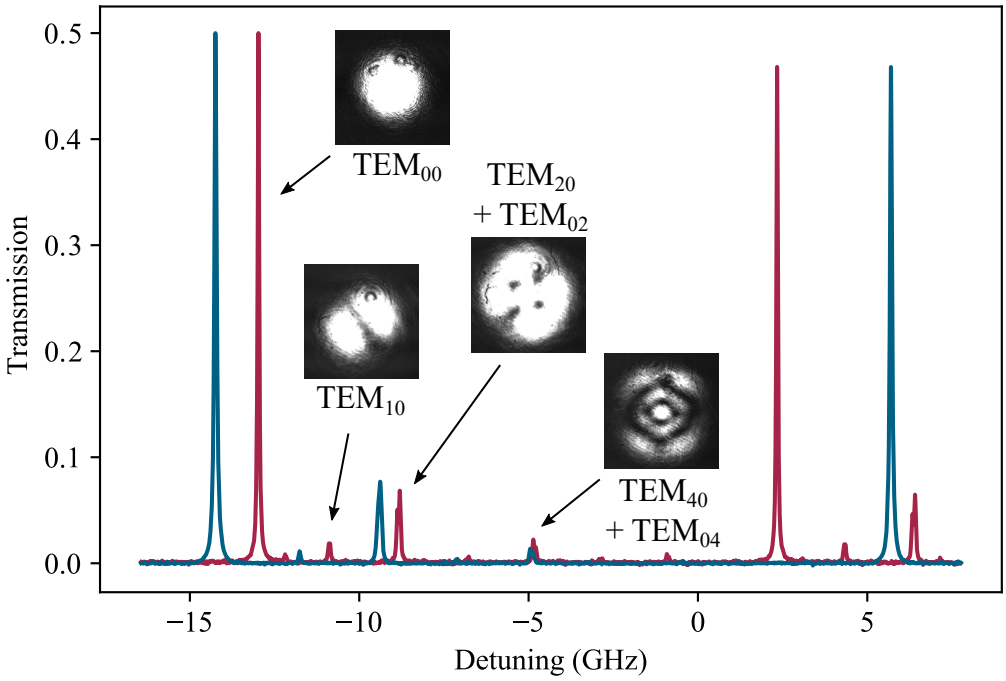

Figure 5.2: Normalised transmission spectra of cavities of length 5.0 mm (blue) and 6.5 mm (red), with CCD images of the transmitted modes. The TEM_{00} peaks are separated by (19.9 ± 0.1) GHz (5.0 mm) and (15.3 ± 0.1) GHz (6.5 mm). Higher order modes appear in between, with TEM_{10}, TEM_{20} + TEM_{02} and TEM_{40} + TEM_{04} (pictured) clearly visible. Spacing between the modes is 2.2 GHz (5.0 mm) and 1.9 GHz (6.5 mm) as expected.

quency and ω_s is the frequency of maximum transmission. However, for applications that require a high peak transmission and narrow bandwidth, a better figure of merit is FOM $= T(\omega_s)/\text{ENBW}$ [107]. FOM rewards filters with high maximum transmission and low overall transmission. As cavity peaks repeat every FSR the FOM for the lens cavity filter, if evaluated over all frequencies, is zero. However if we limit the calculation to one FSR, we obtain values of $(6.5 \pm 0.1)\,\text{GHz}^{-1}$ and $(7.3 \pm 0.1)\,\text{GHz}^{-1}$ for the 5.0 mm and 6.5 mm cavities respectively. Table 5.1 shows a summary of measure quantities for the 5 mm cavity, alongside expected values.

We determine the filter temperature stability by tracking the frequency of the TEM_{00} peak relative to a sub-Doppler rubidium spectral line. This allows us to passively monitor the cavity over many hours or days, sampling every second, and accounts for any laser frequency drift that may occur. Fig 5.3 shows the stability of the 5.0 mm cavity over a period of 24 hours, where there is a long term drift of $0.7\,\Delta v$ which we attribute to fluctuations in laboratory temperature. Also shown is the drift in a 2 hour window, during which the cavity peak is stable to $0.1\,\Delta v$.

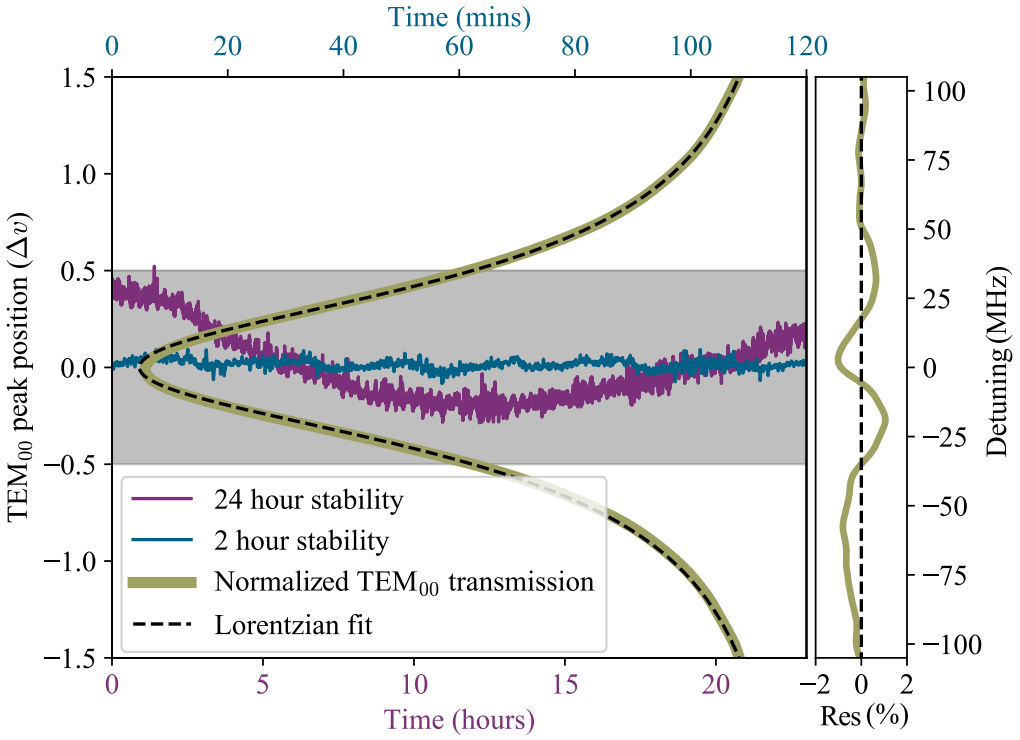

Figure 5.3: The stability of the 5.0 mm cavity over a 2 hour (blue) and 24 hour (purple) period. The TEM_{00} mode of the cavity is overlaid (gold), with a Lorentzian fit (black), and residuals. The grey shaded area shows one FWHM bandwidth (Δv). Over 2(24) hours the cavity is stable to 0.1(0.7) Δv.

Table 5.1: Comparison of expected and measured 5 mm cavity filter parameters

	Measured	Expected
Bandwidth	70 ± 1 MHz	64 MHz
FSR	19.94 ± 0.01 GHz	19.9 GHz
Finesse	285 ± 1	310
$\mathcal{T}_{max}$	50%	100%
dv/dT	(-3.36 ± 0.06) GHz K^{-1}	-3.4 GHz K^{-1}

We experimentally determine the resonant frequency change with temperature, $\mathrm{d}v/\mathrm{d}T$ (Eqn 5.1), to be $(-3.36 \pm 0.06)\,\mathrm{GHz\,K^{-1}}$ in agreement with the expected value of $-3.4\,\mathrm{GHz\,K^{-1}}$. As the transmission spectrum repeats every FSR, the maximum temperature change required is that to shift the modes by half the FSR: 9.9 GHz for the 5.0 mm cavity. We characterise the response time of the 5.0 mm cavity to a change in temperature set point, by measuring the movement of the peak after the set point is changed, as shown in Fig 5.4. We find that for smaller temperature changes (up to 2 K, 6.6 GHz) peak movement is well fitted to an exponential, with a 1/e time constant of 1.5 mins, as plotted. This is expected, and is a signature of the thermal capacity of the lens. Residuals are plotted and show very good agreement after about 30s. When the temperature change is larger than this the TEC board reaches the current output limit so peak movement is initially slower than exponential. For a 3.3 GHz shift (1.0 K), the time taken for the cavity to become stable to within Δv is 10 minutes; for an 11.1 GHz shift (3.4 K) this rises to 20 minutes.

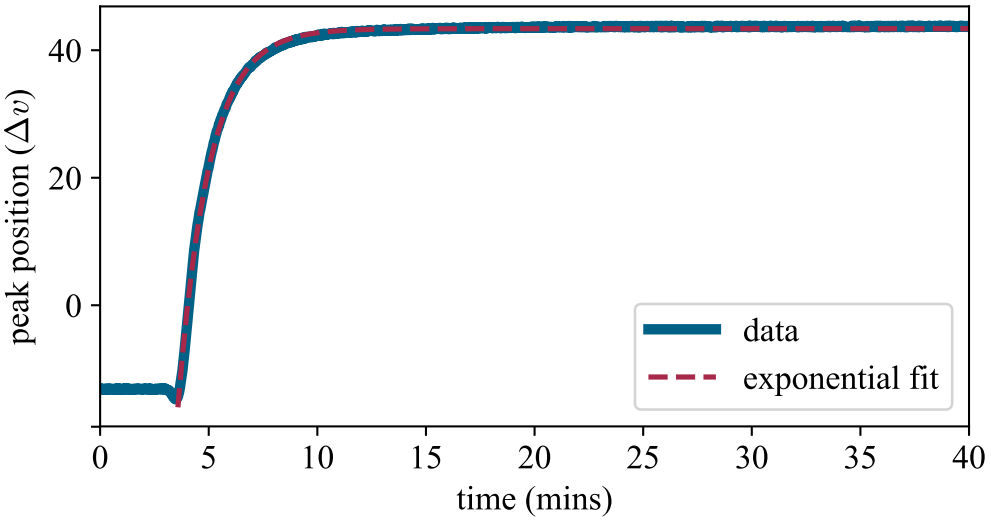

Figure 5.4: Response of the etalon transmission frequency to an increase in temperature set point of 1.2 °C. An exponential is fitted to the rise, which has a 1/e time constant of 1.5 mins.

Any birefringence in the glass of the cavity, caused by stress in the material, will induce a shift in the transmission frequency with changing polarisation, as noted in [116]. Our mounting method minimises stress across the lens and we measure a negligible frequency shift with rotation of incoming linear polarisation. Testing two lenses, we measure maximum shifts of 5 MHz and 10 MHz respectively, which is on the order of the fluctuations due to temperature instability, as seen in Fig 5.3.

There is also no significant change for circularly polarised input light.

5.2.2 Planar-planar cavity

We also implement a cavity filter consisting of a planar-planar (PP) circular glass piece of diameter 1 inch and length 1.7 mm, with reflectivity $R = 94\%$. As mentioned in Section 5.2.1.1, this design limits the possible finesse of the cavity, however for applications that do not require such a narrow linewidth, this is not a problem. The etalon is coated for 700–850 nm and was purchased from LightMachinery and has specification sheet which can be found here [120]. This etalon has a much wider transmission peak, due to the lower reflectivity coating, of ∼1.5 GHz (from the spec sheet, which states a FSR of 60 GHz and a Finesse ∼40). Linewidths of ∼0.33 GHz, and ∼0.75 GHz are also available from the same supplier [121].

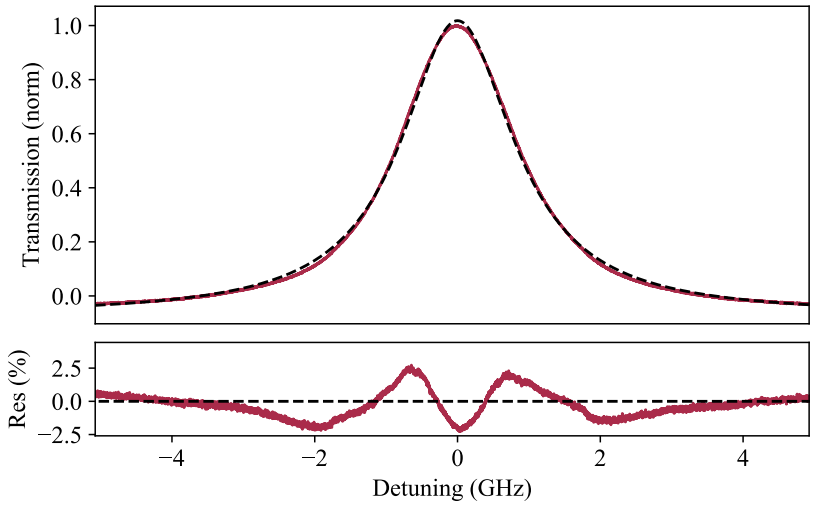

Figure 5.5: Transmission profile of the 1.7 mm planar-planar etalon (red) fitted to a Lorentzian (black dashed) with residuals plotted below. Fitted Lorentzian has a FWHM of (1.79 ± 0.02) GHz.

Fig 5.5 shows the transmission profile of the 1.7 mm thick planar-planar etalon (red) fitted to a Lorentzian (black dashed) with residuals plotted below. The residuals are about twice as large as those seen in the data and fit of Fig 5.3. These data were taken using a DFB laser, which has a less linear scan than the ECDL lasers. We are able to correct larger scale non-linearities using a comercial cavity, however it is likely that smaller scale non-linearities remain and result in greater residual structure. The fitted Lorentzian has a FWHM of (1.79 ± 0.02) GHz. This gives a finesse of 33.5 which is within the range stated by the manufacturer.

We temperature stabilise and frequency tune this etalon in exactly the same way

as the lens-cavity etalons, with similarly effective results. However, because the FWHM is a factor of ∼20 wider, this filter is, relative to its linewidth, a factor of 20 more stable. As this is a planar-planar cavity, different spatial modes are not split, and are all transmitted at the same frequency. Therefore, there are no subsidiary maxima, which is an advantage for applications where total extinction off resonance (until the next peak 1 FSR away) is required. Mode matching into the cavity is not required, and practically alignment is much easier, and we see transmission of up to 85%.

It is also possible to get thinner planar-planar cavities than plano-convex cavities, and so larger FSRs. This is because the PP cavity has the same thickness throughout while the PC cavity is thinner at its edges. The thinnest PC cavity we could use was 2.5 mm giving a FSR of 40 GHz. As the PP cavity we use has a length of 1.7 mm it has a FSR of 60 GHz.

5.3 Atomic line filter

The experimental setup for the atomic filter is shown in Fig 5.6. The beam passes through an input Glan Taylor polariser angled at θ_E to the horizontal, then through a 5 mm natural abundance Rb vapour cell, then an output polariser which is fixed at 90° to the first. For light at a frequency away from atomic resonance the crossed polarisers give very little transmission. Nearer resonance the atoms provide an optical rotation, giving in principle near perfect transmission. The input polarisation angle is a parameter which can be varied. The vapour cell must be short enough to ensure the magnetic field is homogeneous over its length. However decreasing cell length reduces optical depth, though this can be compensated for by increasing the atomic number density by raising temperature [42]. Zentile et al. [122] showed that filter performance degrades as cell length is reduced below a few millimetres because of the extra broadening associated with dipole-dipole interactions at higher densities. The vapour cell is mounted in a heater, and is placed in a magnetic field formed between two top-hat shaped permanent magnets. The magnetic field strength, $\vec{B}$, is adjusted by altering the separation of the magnets, and can produce a maximum field of 0.5 T. The magnets are mounted on a rotation stage so θ_B, the angle between the light propagation direction and the magnetic field direction, can be varied. An atomic filter spectrum with experimental data, ElecSus [42] fit, and residuals is displayed in Fig 5.7.

Atomic filters can be broadly classified as two types—line centre and wing—depending on where the transmission is relative to the atomic resonance. This filter uses a natural abundance Rb vapour cell (72.2% ^{85}Rb, 27.8% ^{87}Rb) which

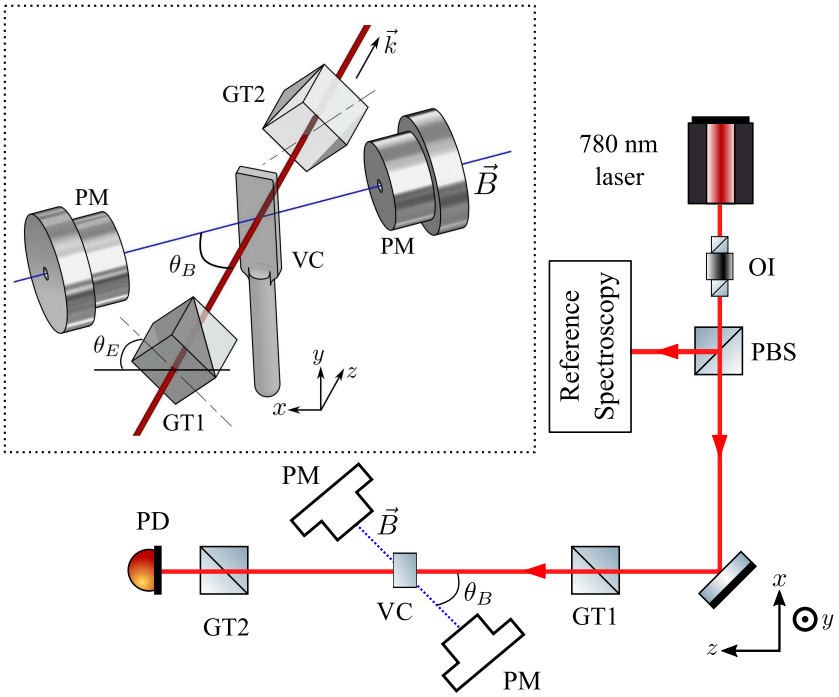

Figure 5.6: Experimental setup for the atomic filter. 780 nm laser light is split on a PBS and one beam is passed through a Rb vapour cell to provide a frequency reference, as in Fig 5.1. The second beam passes through an input Glan-Taylor polariser (GT1) angled at θ_E (a variable parameter) to the horizontal x-z plane, then through a 5 mm natural abundance Rb vapour cell (VC) and an output polariser (GT2) fixed at 90° to the first, to be detected on a photodiode (PD). The vapour cell is mounted in a heater, and is placed in a magnetic field formed between two top-hat shaped permanent magnets (PM). The magnetic field strength, $\vec{B}$, is adjusted by altering the separation of the magnets, and can be up to 0.5 T. The magnets are mounted on a rotation stage so θ_B, the angle between the light propagation direction and the magnetic field direction, can be varied. The inset figure is reproduced with permission from [107].

has narrow peaks at the line centres of the two isotopes, with the peak close to 0 GHz from the stronger ^{85}Rb transitions. The two outer peaks in the filter spectrum are residual wing-like features [42]. To determine the 100% transmission level, the second polariser is removed, allowing all of the far off-resonance, unrotated light to pass through the filter.

This spectrum has a FOM of $(0.66 \pm 0.01)\,\mathrm{GHz}^{-1}$, however optimising the parameters (temperature, magnetic field strength, magnetic field angle, input polariser angle) for FOM rather than maximum transmission leads to a filter with a FOM of $(1.04 \pm 0.01)\,\mathrm{GHz}^{-1}$. Changing the temperature, which in turn alters number density, from the value for maximum FOM lowers the FOM, with a steeper drop-off as temperature is increased. The FOM drops to half its maximum value when

T is increased by 7 K or decreased by 10 K. Once set, the angles and magnetic field are constant, however temperature will fluctuate. We model the effect of temperature change on the transmission spectrum, and find that while the central peak frequency shift is negligible (∼10 MHz over 20 K), the peak height and FWHM (Fig 5.7 insets), and subsidiary peak transmission vary significantly. However vapour cell temperature fluctuations on the scale expected in the laboratory (∼1 K) only cause small changes in the transmission spectra (FWHM ∼ 20 MHz, $\mathcal{T}_{\max} \sim 0.3\,\%$). The FWHM decreases with increasing temperature as the transmission peak is the gap between two absorption features, each of which gets wider as the temperature increases.

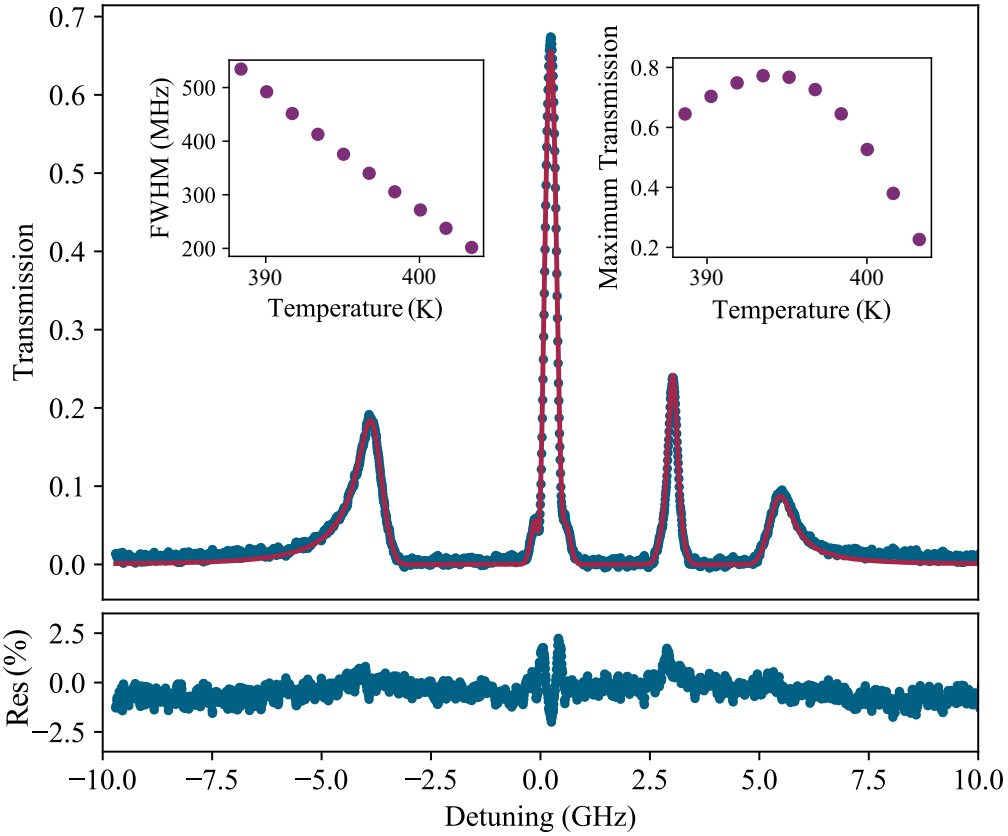

Figure 5.7: Experimental data (blue points) and theoretical fit (red line) for an atomic filter spectrum on Rb D2 line, with fit parameters $T = 399.0$ K, $|B| = 218$ G, $\theta_B = 80.2°$, $\theta_E = 1.6°$. Residuals are displayed and show excellent agreement between theory and experiment. This spectrum has a FWHM of (310 ± 1) MHz, a maximum transmission of $(66 \pm 1)\,\%$, and a FOM of $(0.66 \pm 0.01)\,\mathrm{GHz}^{-1}$. Insets show the effect of changing temperature on the FWHM and maximum transmission of the filter peak.

5.4 Comparison between filter types

The choice of filter type depends on the requirements of a particular experiment; here we outline how the tested filters compare over a range of criteria, summarised in Table 5.2.

The cavity filter can have a smaller bandwidth–tens rather than hundreds of MHz–however this is fixed at manufacture while the atomic filter bandwidth can be changed by adjusting experimental parameters. We find a higher maximum transmission for the atomic filter (75 %) than for the plano-convex cavity filter (50 %), though the planar-planar cavity can have an even higher transmission (85 %). However, the atomic filter has a worse extinction ratio due to having larger subsidiary peaks, and a lower FOM. The extinction ratio and bandwidth of the cavity filter are independent, unlike the atomic filter. When designing the cavity filter, a length can be chosen to produce high extinction at a given frequency from the transmission peak, whereas the frequencies of subsidiary transmission maxima of the atomic filter are fixed. Cavity peaks repeat every FSR, so while extinction of the atomic filter is poorer over 20 GHz around the main peak, it is much better elsewhere. It has been shown, however, that two cascaded monolithic cavity filters can produce a filter with an effective FSR of hundreds of GHz [123]. The FOM calculated across 1 FSR of this cascaded filter would be lower than that of the original, because the maximum transmission would approximately halve, though the exact numbers would depend on the specific implementation.

The atomic filter is stable to changes in temperature: a change of 1 K negligibly affects transmission frequency ($\sim$ 1 MHz) and does not alter bandwidth or maximum transmission significantly. In contrast, the cavity filter is very sensitive to temperature: a 1 K change shifts the peak by order 1 GHz. Conversely this means the cavity filter can be arbitrarily tuned with no change in bandwidth or transmission, while the atomic filter transmits at a fixed frequency determined by the resonances of the atom.

Imaging through the PC cavity filter is not possible because it filters spatially, transmitting different cavity modes at different frequencies (Fig 5.2). However, this is not the case for the PP cavity so imaging through it is possible. Imaging through the atomic filter is also possible; some basic imaging through our atomic filter is shown in Fig 5.8. Figs 5.8(a) and 5.8(c) show patterned laser beams imaged before the atomic filter, and 5.8(b) and 5.8(d) are the corresponding images after passing through the filter. Some distortion and extra noise has appeared, however the main features of both patterns are still clearly visible. This property is crucial to applications such as solar imaging [124].

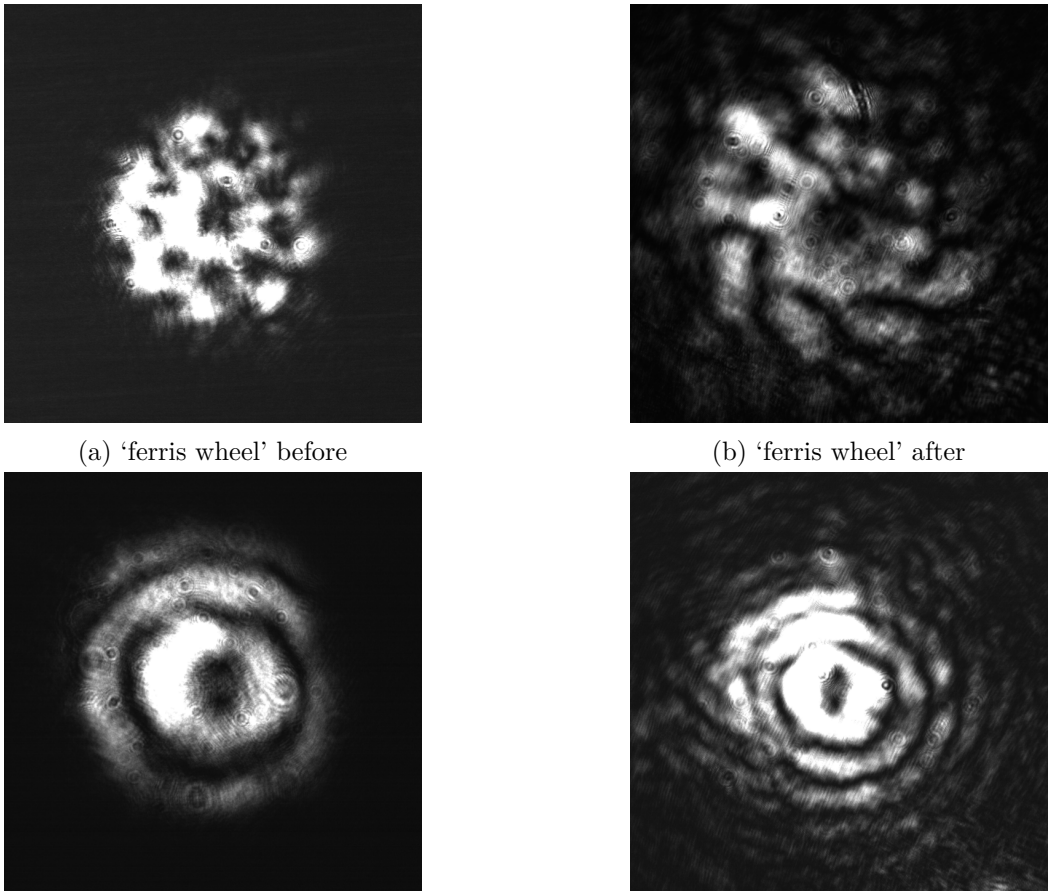

(a) 'ferris wheel' before

(b) 'ferris wheel' after

(c) LG_{21} before

(d) LG_{21} after

Figure 5.8: Light patterns imaged through an atomic filter.

The atomic filter is very sensitive to the polarisation of the input light, which should be linear, and set to match the angle of the first GT polariser. If this is not the case the transmission will be significantly reduced. Atomic filters can also be used as dichroic beam splitters [108]. The cavity filter is polarisation independent.

Table 5.2: Summary of relative merits of Lens Cavity and Atomic Line filters

	Lens Cavity	Atomic Line
Bandwidth	10s MHz	100s MHz
On-peak Transmission	50 %	75 %
Required Temp. Stability	1 mK	1 K
Bandwidth Tunability	Fixed on manufacture	Yes
Central Frequency	Arbitrary	Fixed
Imaging	No	Yes
Polarisation	Any	Highly sensitive
Footprint	$\sim$50 cm^2	$\sim$2500 cm^2
FOM (1 FSR)	$\sim$7 GHz^{-1}	$\sim$1 GHz^{-1}

The atomic filter setup used here has a bench footprint of at least $50\,\mathrm{cm} \times 50\,\mathrm{cm}$, which is dominated by the rotating stage for the magnets. This has not been optimised to be as small as possible and could be reduced if the field across the cell is allowed to be non-uniform. The magnet setup is custom made, as is the cell heater, and a 5 mm Rb (or other suitable atomic vapour) cell is required. Our vapour cell was filled in-house, however similar cells are commercially available. Glan-Taylor polarisers are also necessary for maximal extinction of light at undesired frequencies. The cavity filter is experimentally simple, requiring only the temperature stabilised high-reflection coated lens and mode-matching and collimation lenses, and is much smaller with a $7\,\mathrm{cm} \times 7\,\mathrm{cm}$ footprint. If required, the focal length of the mode-matching lens can be minimised by suitable choice of cavity radius of curvature. The temperature controller is not included in this footprint as it can be mounted away from the setup if long connecting wires are used.

We conclude that both designs have merits; the atomic filter is effective when signal light is close to an atomic resonance, while the cavity filter allows greater control over bandwidth and is arbitrarily tunable, but requires temperature stabilisation.

Chapter 6

Collisional Transfer

6.1 Introduction

In our laboratory, we have been exploring four-wave mixing (FWM) in isotopically enriched 98% ^{87}Rb in a 0.6 T magnetic field (in the hyperfine Pashen-Back regime, as discussed in Section 2.5.1) with the aim of creating a heralded single photon source. This scheme and its results are described thoroughly in the thesis of Renju Mathew [44]. The scheme used is a diamond, as shown in Fig 6.1. We excite up to the $5D_{3/2}$ state via $5P_{3/2}$ state using 780 nm and 776 nm lasers. The medium then emits pairs of correlated single photons back to the ground state via $5P_{1/2}$, and we observe these at 762 nm and 795 nm.

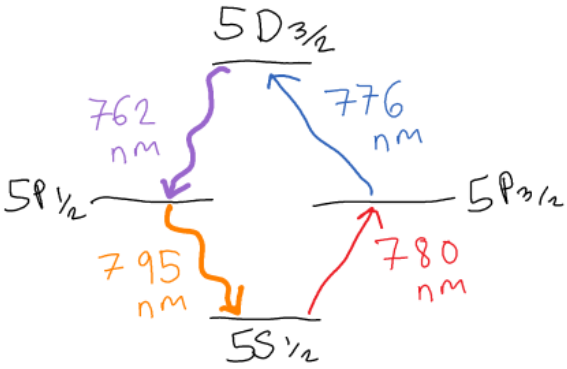

Figure 6.1: Energy level scheme for diamond four wave mixing. We excite up to $5D_{3/2}$ via $5P_{3/2}$ using 780 nm and 776 nm lasers. The medium then emits pairs of correlated single photons back to the ground state, and we observe these at 762 nm and 795 nm.

However, this is not the only decay process, and our experimental realisation of the scheme is dominated by noise. When only 780 nm (resonant with the D2 line) light is incident on the vapour, 795 nm (resonant with the D1 line) photons are emitted.

We hypothesise that this transfer is caused by collisions with buffer gas atoms, as illustrated in Fig 6.2. Even though our vapour cell is nominally 'buffer gas free', by fitting to Elecsus [42] we have found an additional 7 MHz broadening [50], which is attributed to buffer gas quenching.

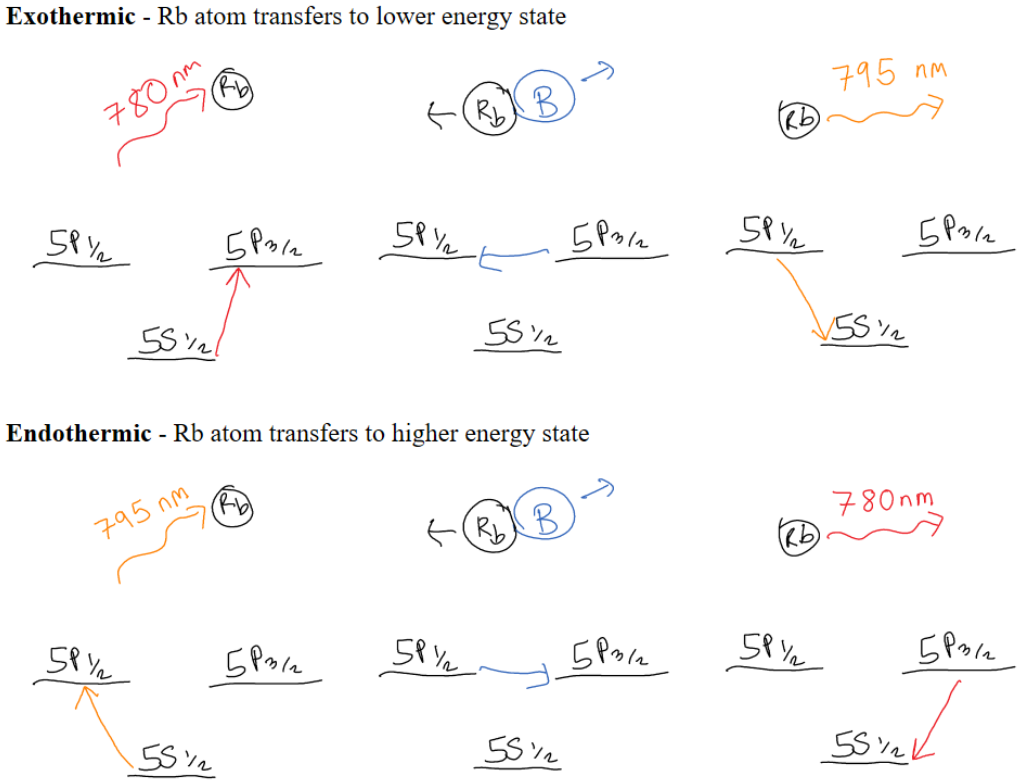

Figure 6.2: Diagram illustrating the process of the collision. In the exothermic process (upper row), the atom absorbs a resonant 780 nm photon and is excited to the $5P_{3/2}$ state. The atom then collides with a buffer gas atom, transferring it to the $5P_{1/2}$ state, which has a lower energy. From here the atom emits a 795 nm photon, which we observe. The lower row of diagrams illustrate the endothermic process, in which the atom absorbed a 795 nm photon to be excited to the $5P_{1/2}$ state (this is a higher energy state), collides with a buffer gas atom to transfer to the $5P_{3/2}$ state, and then emits a 780 nm photon to return to the ground state.

The buffer gas collisions can transfer the Rb atom from the $5P_{3/2}$ state to the $5P_{1/2}$ state (Fig 6.2 upper), but also in the reverse direction, from the $5P_{1/2}$ state to the $5P_{3/2}$ state (Fig 6.2 lower). The first of these transfers, $5P_{3/2} \rightarrow 5P_{1/2}$ is an exothermic process, meaning that energy is transferred from the internal state of the atom to the kinetic energy of the colliding atoms. The second, $5P_{1/2} \rightarrow 5P_{3/2}$, is an endothermic process, meaning kinetic energy from the colliding atoms is transferred to the internal energy of the Rb atom. This reverse process is therefore energetically unfavourable, and happens at a lower rate. Coincidentally, the energy

level structure of Rb is such that at 75 °C, a typical working temperature for our experiments, the thermal energy is approximately equal to the 5P fine structure splitting:

$$k_{\mathrm{B}}T \approx \Delta E. \tag{6.1}$$

There has previously been much interest in, and study into, the collisional transfer and quenching in alkali metal atomic gases. The Rb $+M$ (M represents a buffer gas atom or molecule) is an attractive system for theoretical study because of its relative simplicity: as an alkali atom Rb has only one outer shell electron, and the buffer gas can be an atom or molecule with no un-bonded valence electrons[125, 126]. There is also a more practical interest in the alkali metal collisional transfer process for use in Diode Pumped Alkali Lasers, which have been demonstrated to produce a 570 W Rb laser, and a 1.5 kW K laser [127].

Previous experimental studies have comprehensively measured the cross-sections of these state changing collisions for a range of atomic species with a wide range of molecular collision partners [128, 129, 130]. Here we do not attempt to reproduce these investigations, rather we use the 130 MHz etalon filter described in Chapter 5 to spectrally resolve the fluorescence photons, and in combination with non-degeneracy of energy levels provided by the large magnetic field, to investigate further what happens during the collisions.

Many proposals for quantum systems use thermal vapours. This collisional mixing process is not often considered; we show that it is a significant effect, and, when signal intensities are very low—quantum applications often require detection at the single photon level—a potentially problematic source of noise.

6.2 Energy levels

In order to understand the processes occurring in the collisions we need a clear picture of the energy levels of ^{87}Rb. This enables us to understand which transitions are available to us, and what wavelengths and polarisations of light will excite (or be produced by) these transitions.

Fig 6.3 shows the σ_+ and σ_- D2 transitions, which have a wavelength of 780 nm. The effect of the 0.6 T magnetic field on the $5S_{1/2}$ and $5P_{3/2}$ state energy levels are shown. In zero-field F and m_F are good quantum numbers, however, when we move into the hyperfine Paschen Back regime the states split and regroup such than the good quantum numbers are now m_I and m_J. More detail is given in Section 2.5.1. These states are grouped in sets of 4 levels, with a common m_J, with each state in the set having a different m_I. The m_I and m_J states are labelled to the right.

The excited states are pure $|m_J, m_I\rangle$ states, while the $5S_{1/2}$ states, labelled in dark blue, contain contributions from two different $|m_J, m_I\rangle$ states, split $\approx 98\%$:2%, as at 0.6 T we have not fully moved to the m_J, m_I basis.

The absorption spectra of linearly polarised light, with $\vec{k} \parallel \vec{B}$, resonant with the D2 line is shown in the top panel. The strong absorption peaks are from transitions out of the 98% ground state components while the weak absorption peaks are transitions out of the 2% ground state components. The light blue arrows, and corresponding lines above, mark σ_+ transitions excited by left-hand circularly polarised light. The purple arrows, and corresponding lines above, mark σ_- transitions excited by right-hand circularly polarised light.

Fig 6.4 shows instead the energy levels involved in D1 transitions at 795 nm, with the absorption spectrum above, and the transitions marked and colour coded in the same way.

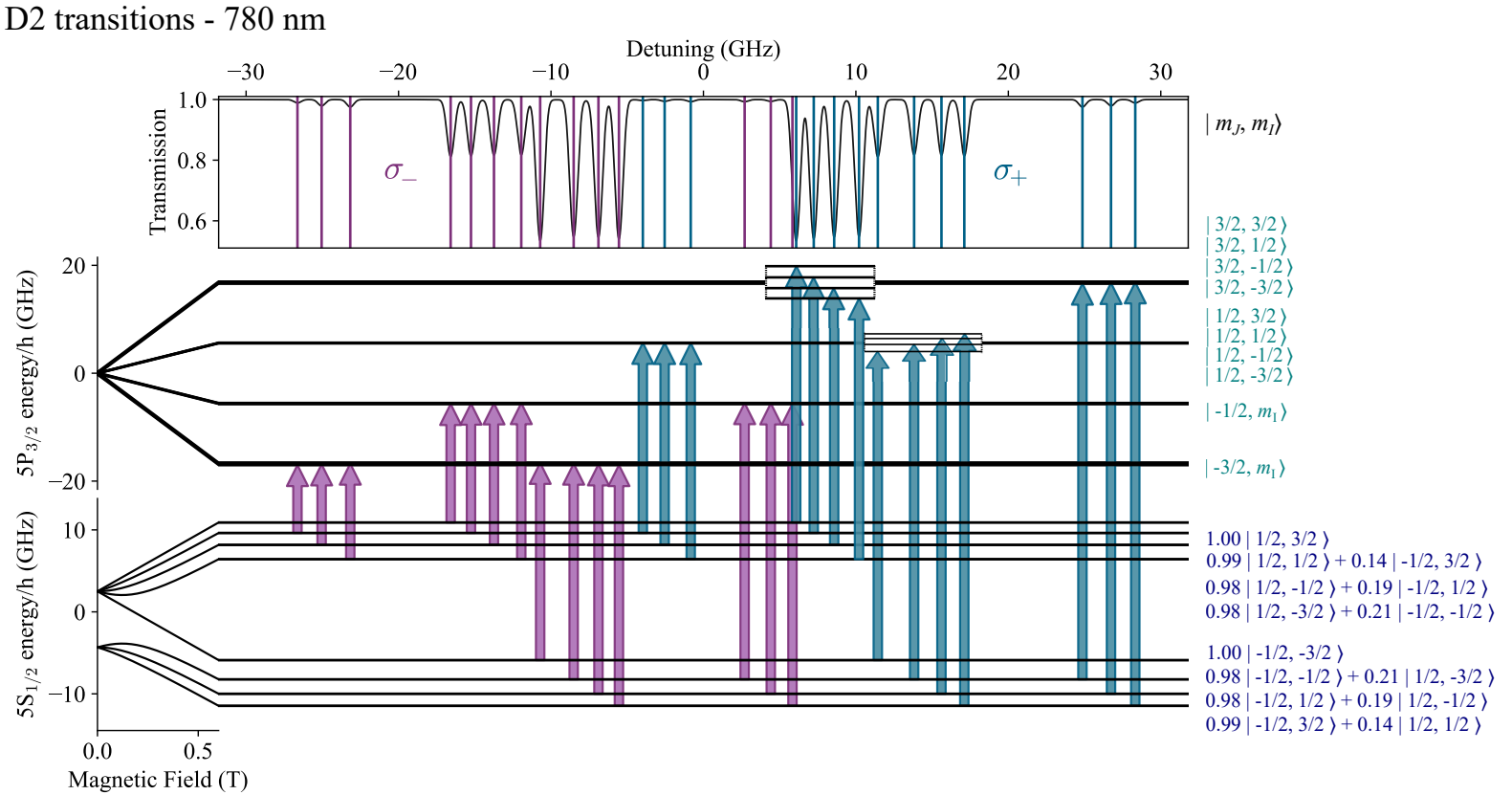

Figure 6.3: Diagram showing the energy levels involved in the D2 (780 nm) transitions at 0.6 T, which are between the $5S_{1/2}$ and $5P_{3/2}$ energy levels. The m_I and m_J states are labelled to the right. The absorption spectra of linearly polarised light resonant with the D2 transitions at 75 °C is shown in the top panel. The light blue arrows, and corresponding lines above, mark σ_+ transitions excited by left-hand circularly polarised light. The purple arrows, and corresponding lines above, mark σ_- transitions excited by right-hand circularly polarised light. This figure is a copy of Fig 2.6; we have reproduced it here for convenience.

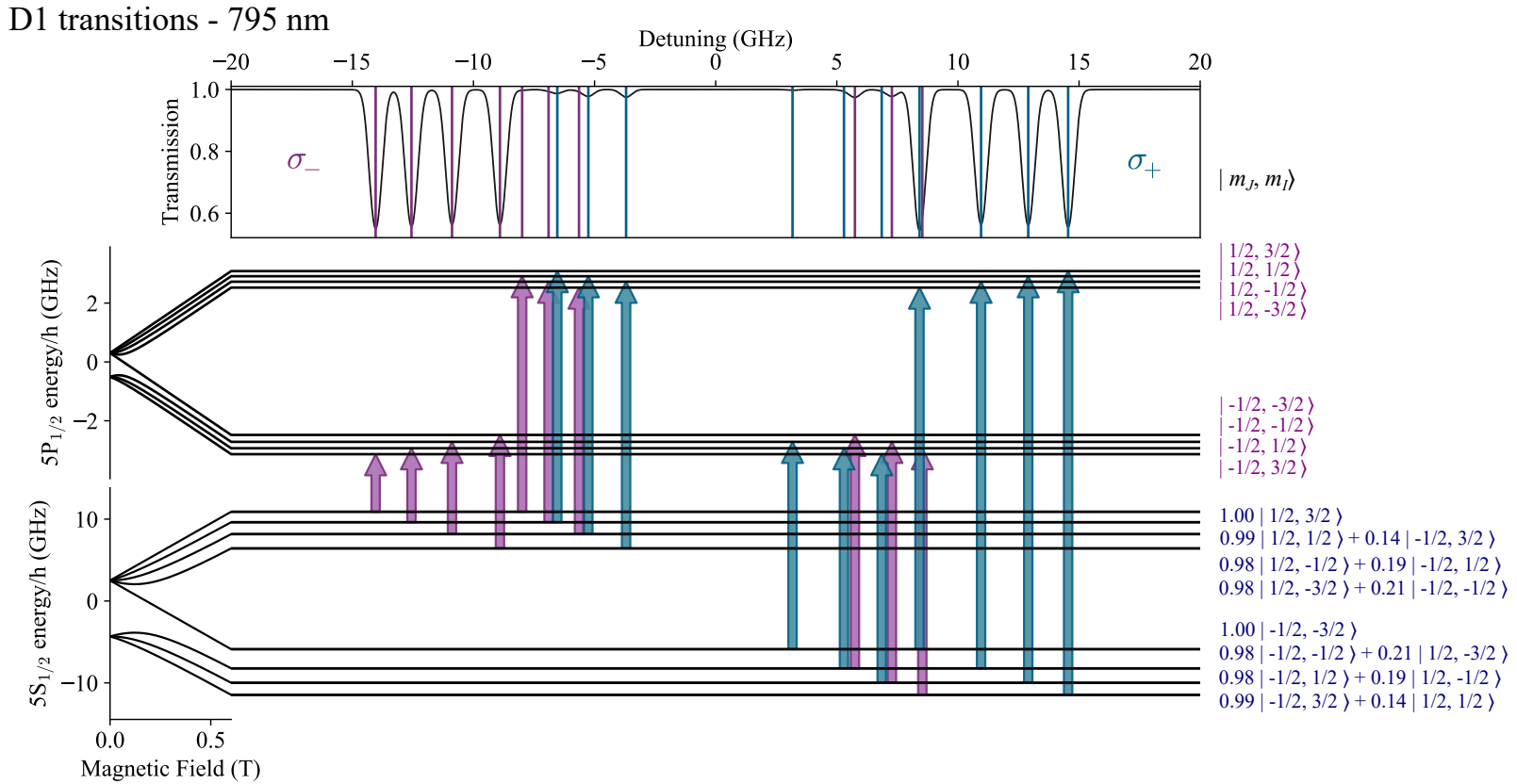

Figure 6.4: Diagram showing the energy levels involved in the D1 (795 nm) transitions at 0.6 T, which are between the $5S_{1/2}$ and $5P_{1/2}$ energy levels. The m_I and m_J states are labelled to the right. The absorption spectra of linearly polarised light resonant with the D2 transitions at 75 °C is shown in the top panel. The light blue arrows, and corresponding lines above, mark σ_+ transitions excited by left-hand circularly polarised light. The purple arrows, and corresponding lines above, mark σ_- transitions excited by right-hand circularly polarised light. This figure is a copy of Fig 2.7; we have reproduced it here for convenience.

6.3 Experimental setup

Fig 6.5 illustrates the experimental setup. We study state changing collisions of alkali atoms in the presence of a large (0.62 T) axial magnetic field [131]. Inclusion of the field lifts the degeneracy of the states and allows individual states to be probed. From the ground state of ^{87}Rb we can probe the D1 (795 nm) or D2 (780 nm) transitions to excite to the $5P_{1/2}$ and $5P_{3/2}$ states respectively. A polarising beam splitter cube (PBS) allows the interrogating light to be switched between 780 nm and 795 nm laser light. Before interrogating the atoms, the beams traverse a quarter waveplate ($\lambda/4$) to produce circularly polarised light, which is the most efficient way to drive the σ_+/σ_- transitions. The vapour cell is 2 mm long and contains isotopically enriched 98% ^{87}Rb vapour and nominally zero buffer gas. The cell is heated to 75 °C, which is required to increase the Rb number density in the cell to get appreciable absorption. When the temperature is too high the medium becomes optically thick and we see saturation effects. The cell heater has 2 pairs of entrance/exit holes for the laser beam; one pair is parallel to the magnetic field direction and k-vector of interrogating light, while the second pair is perpendicular to these. The cell and its heater are sandwiched between two NdFeB permanent magnets, which produce a 0.6 T axial magnetic field which is uniform across the length of the cell at the 1% level [57]. A pair of 20 mm focal length lenses are positioned either side of the vapour cell to focus the beam to a waist of (90 ± 10) µm, and recollimate the laser light. After the second lens the beam is split by a 50:50 beam splitter (BS) with light from the reflected port directed onto a photodiode to monitor absorption. The light that transmits through the BS is aligned into a single mode fibre. Fluorescence which passes out through the hole in the side of the heater mount, perpendicular to the magnetic field direction, is coupled into another optical fibre. We have the option here to include a half waveplate and PBS before the fibre to select a linear polarisation. Narrow bandpass filters are present on all three output optical paths; Semrock MaxLine LL01-780 [132] to transmit 780 nm light (T = 99.0%) or twisted Semrock MaxLine LL01-808 to transmit 795 nm light (T = 95.9%). The two fibre collection ports are connected with one split fibre, so light from both is out put in to the etalon section of the setup. In this section a non-polarising BS directs half the light directly into a multi-mode fibre and onto a photon counter, while the other half passes through the aligned etalon filter. The output of the etalon filter is split 90:10 between a multi-mode fibre to another photon counter, and a photodiode which is used for filter alignment.

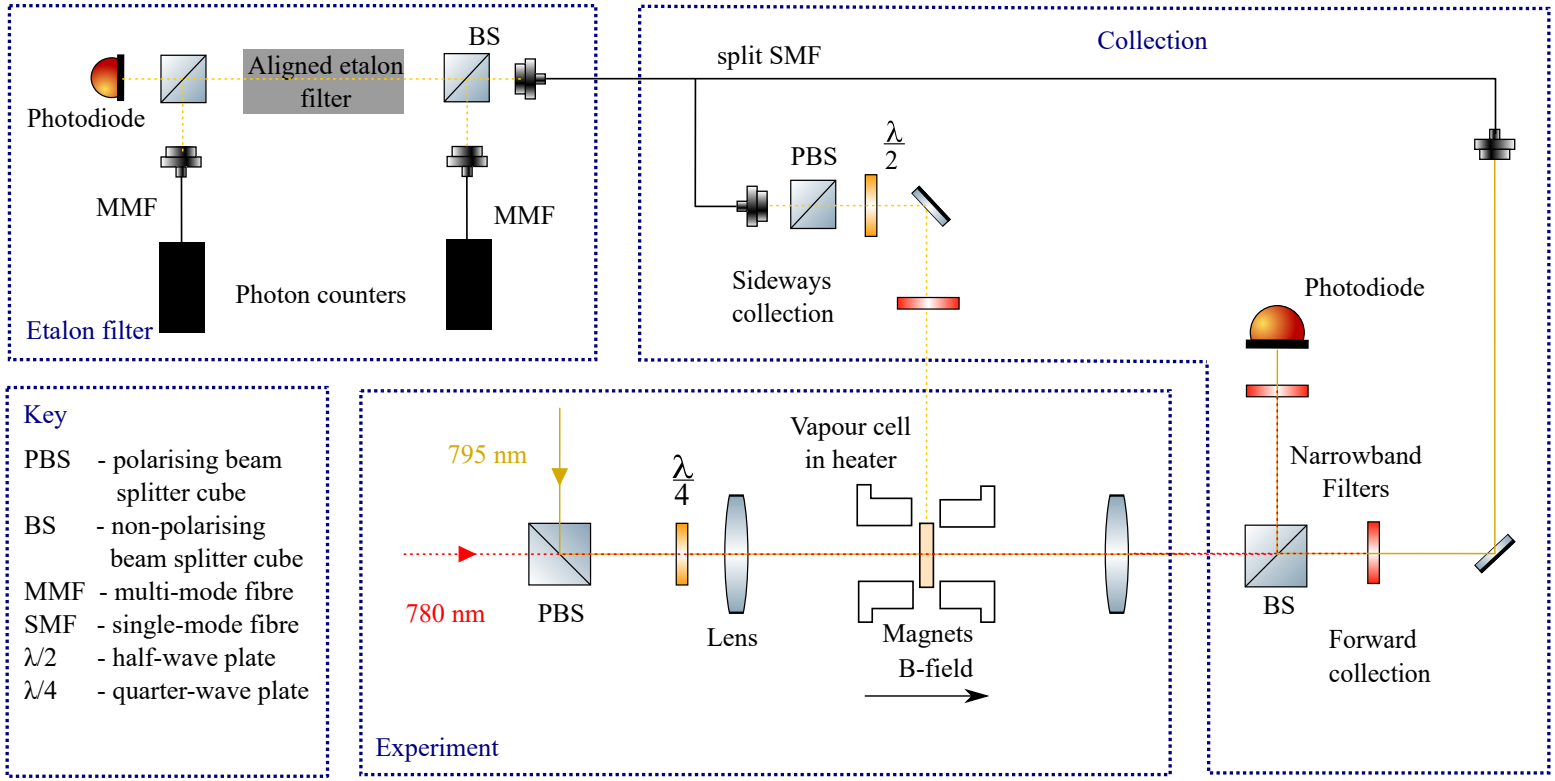

Figure 6.5: Diagram of the setup split into three sections; experiment, collection and etalon filter. A beam splitter cube allows the input laser light to be switched between 780 nm and 795 nm. The beams pass through a quarter waveplate ($\lambda/4$) to produce circularly polarised light, which is focused through the 2 mm long 98% ^{87}Rb vapour cell. The cell is mounted in a heater and surrounded by permanent magnets, which provide a 0.6 T axial magnetic field which is uniform across the cell at the 1% level [57]. The beam and any forward emitted fluorescence are incident on a 50:50 beam splitter (BS) with light from the reflected port directed onto a photodiode to monitor beam transmission. The through port is aligned into a single-mode fibre. Fluorescence emitted out of the side of the cell, perpendicular to the B-field direction, is collected into another fibre, before which a half waveplate and PBS can be used to select a linear polarisation. Narrow bandpass filters are present on all three output optical paths, and these can be rotated to transmit either 780 nm or 795 nm light. The two fibre collection ports are connected with one split fibre, which directs light from both into the etalon section of the setup. A BS then couples half the light into a multi-mode (MM) fibre to a photon counter, while the other half passes through the aligned etalon filter. The output of the filter is split 90:10 between a MM fibre to single photon counter, and a photodiode used for filter alignment.

6.4 Results without etalon filtering

Fig 6.6 shows the results of the transfer process when a scanning 780 nm laser beam is input and 795 nm fluorescence is collected. The top panel shows an absorption spectrum over the strong σ_+ D2 lines at 0.6 T, as we have seen in Fig 6.3. The bottom panel shows the corresponding 795 nm fluorescence collected, as the 780 nm laser is scanned. We observe that the collected 795 nm fluorescence count rate mirrors the transmitted 780 nm light through the Rb vapour. This is expected if we assume the collisional process illustrated in Fig 6.2; atoms must absorb a 780 nm photon in order to collide and change state, them re-emit at 795 nm.

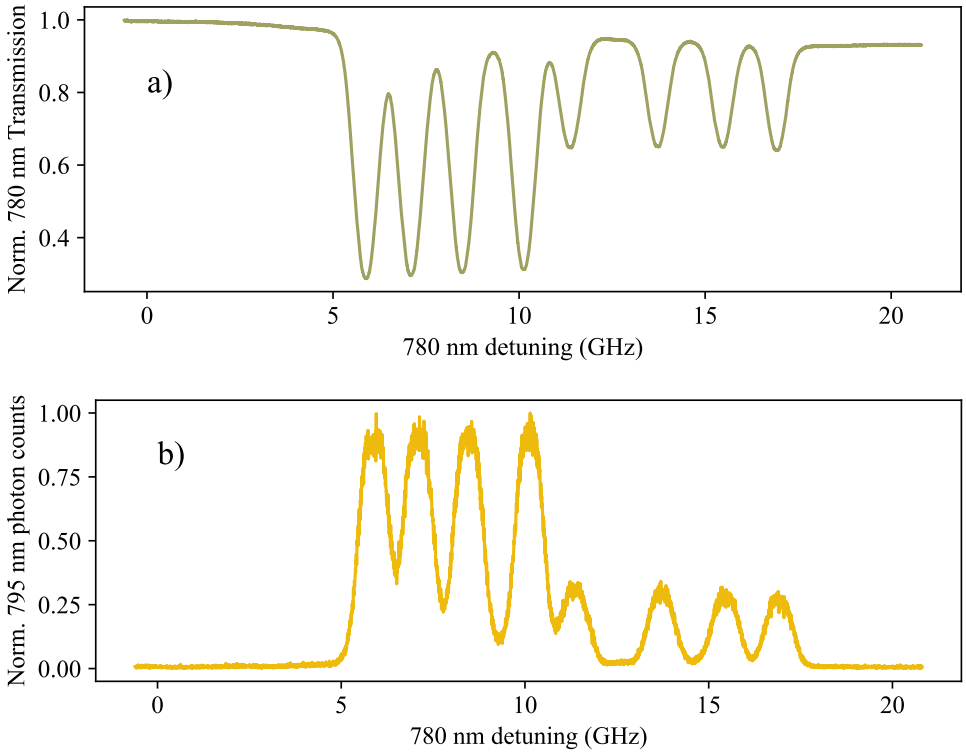

Figure 6.6: a) D2 σ_+ strong absorption lines. 75 °C, 1 µW. b) Corresponding 795 nm forward collected fluorescence as the 780 nm laser is scanned over the D2 σ_+ absorption lines.

By observing sideways out of the cell in order to minimise scattered laser light, we compare the rates of emitted fluorescence for both 780 nm and 795 nm input and output at 75 °C, which are visualised in Fig 6.7. We first input 780 nm (red trace) and record fluorescence count rate with no spectral filter, meaning we collect both 780 nm and 795 nm. This is the first $\approx 1/3$ of the time axis. A 780 nm bandpass filter is then inserted for the middle time section, and finally that filter is replaced with a 795 nm bandpass filter. This process is then repeated with 795 nm input

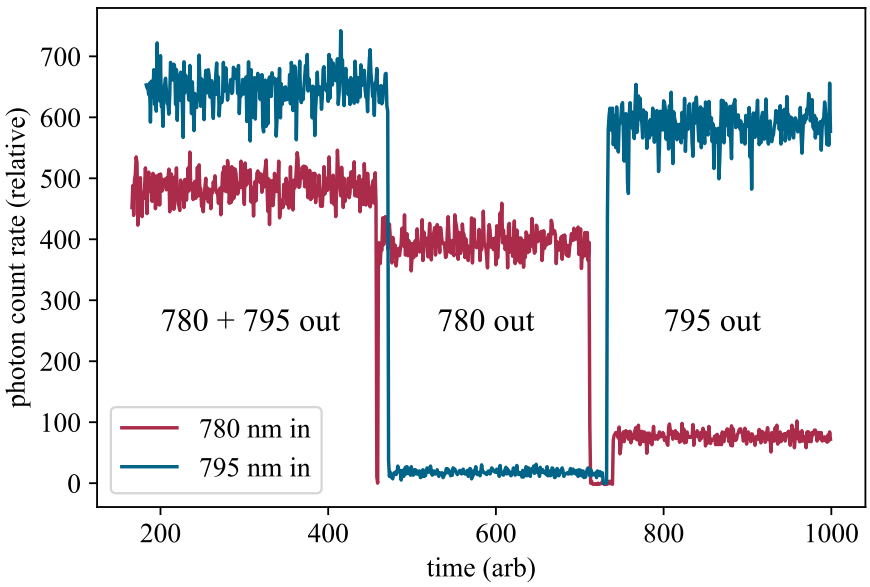

Figure 6.7: Red (blue) trace shows the relative fluorescence photon count rate collected out of the side port of the cell, when 780 nm (795 nm) light is input and different interference filters (IF) are place before the collection fibre. During the first third of the time axis there is no IF in place so both 780 nm and 795 nm fluorescence is collected. During the middle third of the graph a 780 nm IF is in place, so only 780 nm fluorescence is collected, and in the final third a 795 nm IF is in place so only 795 nm fluorescence is collected. The cell temperature is 75 °C.

light, shown by the blue trace. We find that for the exothermic process - 780 nm in, 795 nm out - the ratio of fluorescence 795 nm/780 nm = 0.20. For the reverse, endothermic process, the ratio 780 nm/795 nm = 0.032. These calculations take into account the differing transmissions through the narrowband filters. This means that fine structure change is 6 times more likely in the exothermic process than in the endothermic process.

These data tell us that the transfer process is significant; in the exothermic case when we input 780 nm light, 1/6 of the fluorescence we get out is at a different wavelength: 795 nm. This has the potential to be a serious problem for quantum optics experiments where the signal intensity is very low—photons are counted individually—and noise reduction is vital. It should also be noted though, that this fluorescence is emitted in all directions, while the signal photons produced in FWM are highly directional, so effective spatial filtering will be important.

6.4.1 Temperature dependence

The amount of fluorescence we see from the state that has not been excited by resonant laser light is dependent on the number of collisions that take place in the atomic medium. Since the number of collisions is dictated by the number of atoms in the vapour phase, we can control the ensemble collisional rate and process by changing the temperature of the vapour. The number density of atoms in the vapour phase has a close to exponential dependence on temperature [58], thus small changes in temperature (i.e. 5–10 °C) can lead to doubling of the Rb number density [4].

We measure the temperature dependence of the process by frequency stabilising the 780 nm laser to the $5S_{1/2}|1/2, 3/2\rangle \rightarrow 5P_{3/2}|3/2, 3/2\rangle$ transition (left most absorption peak in Fig 6.6), and recording the rate of 795 nm fluorescence as the temperature changes. From the temperature we calculate the Rb number density. Fig 6.8 is a log-log plot illustrating the dependence of 795 nm fluorescence on the number density of Rb atoms in the vapour. We plot log-log to make the relationship clearer. We see that for temperatures up to 86 °C the gradient is linear showing that in this regime the process is first order, so one Rb atom is involved. The other atom in the collision must therefore be a buffer gas atom. Between 86 °C and 110 °C the process becomes second order, suggesting that collisions now involve two Rb atoms. This is in agreement with the results reported in [54], showing that at this temperature lineshape broadening due to Rb-Rb collisions becomes comparable with the natural broadening. This crossover occurs when the Rb-Rb state changing collision rate exceeds the Rb-buffer gas state-changing collision rate. The number density at which this occurs depends on the pressure of buffer gas in the cell, and the relative cross-sections of the collisional processes. Above 110 °C the behaviour becomes more complicated as the medium starts to become optically thick. The following investigations are all carried out in the linear regime, at approximately 75 °C, with a number density of $1.1 \times 10^{18}\,\mathrm{m}^{-3}$. Coincidentally, in this regime the thermal energy is approximately equal to the fine structure splitting:

$$k_{\mathrm{B}}T \approx \Delta E. \tag{6.2}$$

This is not the case for all alkali metals, which will be discussed in Section 6.6.

6.4.2 Collisional Process equations

To describe the collisional processes that occur inside the atomic vapour cell, we need to consider when the Rb atoms are likely to collide with a buffer gas atom

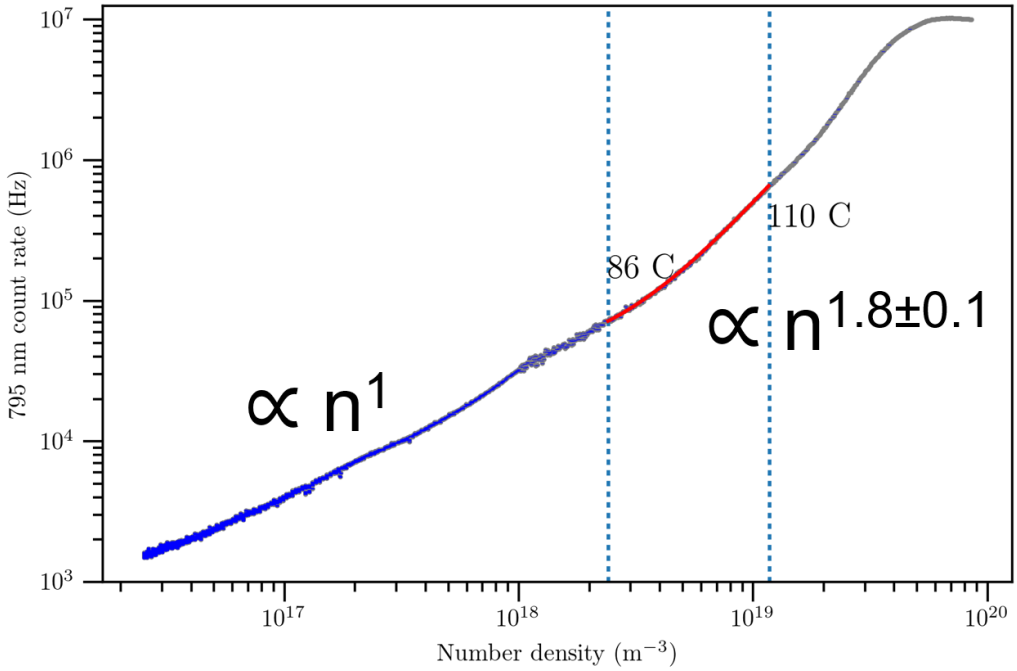

Figure 6.8: Number density dependence of 795 fluorescence rate. At low number densities (and therefore temperatures), up to around 86 °C 795 nm fluorescence count rate increases linearly with number density. In the next region, between 86 °C and 110 °C that relationship is close to quadratic ($\propto n^{1.8\pm0.1}$). Above 110 °C the increase begins to level off, and then decrease, as the medium becomes optically thick, and fewer of the produced photons escape the medium and are detected. Data and figure from Renju Mathew and reproduced here with permission [44].

(inter-species collisions) and when they might collide with another Rb atom (intra-species collisions). We discussed in Section 6.4.1 that at low temperatures (i.e. < 86 °C, as shown in Fig 6.8), the dominating collisions are between Rb and buffer gas atoms. Inter-species collisions can transfer the Rb atom to: the other 5P state (inter-manifold); to a different level within the same 5P state (intra-manifold); or back down to the ground state (quenching).

Each of these collisional transfer processes can be described mathematically using equations. We use M to represents a buffer gas atom (or molecule).

Inter-manifold collisions:

$$\mathrm{Rb}(5\mathrm{P}_{3/2}) + M \rightarrow \mathrm{Rb}(5\mathrm{P}_{1/2}) + M \tag{6.3}$$

$$\mathrm{Rb}(5\mathrm{P}_{1/2}) + M \rightarrow \mathrm{Rb}(5\mathrm{P}_{3/2}) + M. \tag{6.4}$$

Intra-manifold collisions:

$$\mathrm{Rb}(5\mathrm{P}_{3/2}) + M \rightarrow \mathrm{Rb}(5\mathrm{P}_{3/2}) + M \tag{6.5}$$

$$\mathrm{Rb}(5\mathrm{P}_{1/2}) + M \rightarrow \mathrm{Rb}(5\mathrm{P}_{1/2}) + M. \tag{6.6}$$

Collisional quenching:

$$\mathrm{Rb}(5\mathrm{P}_{3/2}) + M \rightarrow \mathrm{Rb}(5\mathrm{S}_{1/2}) + M \tag{6.7}$$

$$\mathrm{Rb}(5\mathrm{P}_{1/2}) + M \rightarrow \mathrm{Rb}(5\mathrm{S}_{1/2}) + M. \tag{6.8}$$

At higher temperatures (86–110 °C), we also see Rb–Rb collisions. These can cause all the same types of transfer processes given by Eqns 6.3–6.8 to occur, but the buffer gas, M is replaced by a Rb atom. These now dominate over the Rb–buffer gas collision, though the latter still occur. Below are equations for the fine structure changing collision processes which occur in this regime:

$$\mathrm{Rb}(5\mathrm{P}_{3/2}) + \mathrm{Rb} \rightarrow \mathrm{Rb}(5\mathrm{P}_{1/2}) + \mathrm{Rb} \tag{6.9}$$

$$\mathrm{Rb}(5\mathrm{P}_{1/2}) + \mathrm{Rb} \rightarrow \mathrm{Rb}(5\mathrm{P}_{3/2}) + \mathrm{Rb}. \tag{6.10}$$

6.5 Spectral filtering of the output fluorescence

To determine the states the atoms have transferred to after a collision, we require narrow-band spectral filtering. We use interference filters (IF) (Semrock MaxLine filters–LL01-780 and LL01-808) in the collection path, which have a typical full-width-at-half-maximum (FWHM) of 3 nm [132], to remove unwanted excitation light from the fluorescence detector. 795 nm light is filtered using a filter centred at 808 nm which is tilted to lower the transmission frequency. The bandwidth of the IF is much broader than the widths of the resonance features, thus we require a second narrow-band (typically narrower than the resonance features) filter for finer spectral resolution. We use an etalon filter, as described in Chapter 5. This filter consists of a high reflection (HR) coated plano-convex lens held in a temperature stabilised mount. It has a FWHM of 130 MHz and a central frequency which can be tuned by altering its temperature. The central frequency is stable to 10 MHz over a 2 hour period. We include a 50:50 beam splitter in the 795/780 nm detection arm of the experiment, with one output port passing through the etalon filter before being fibred into a SPAD (Single photon avalanche detector), and the other passing straight into a fibre and then detector. This allows the 'with etalon' and 'without etalon' paths to be monitored simultaneously and compared.

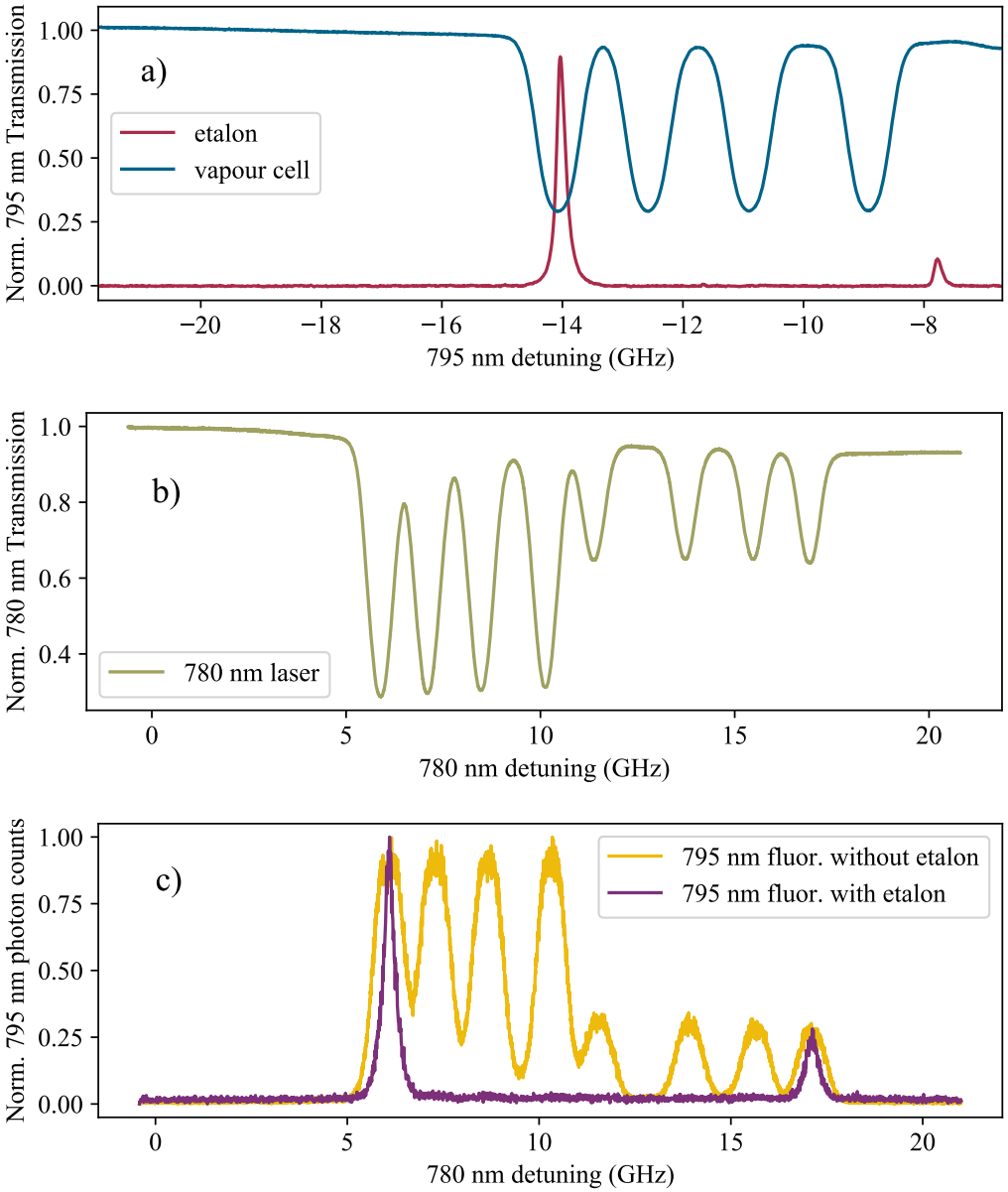

Figure 6.9: 780 nm input laser light, 795 nm fluorescence collected. At 75 °C, in the regime where collision rate is first order with respect to Rb concentration and Rb–buffer gas collisions dominate. Panel a) shows the etalon transmission profile on a 795 nm laser scan relative to the D1 absorption lines. Here the etalon is positioned on the left most transition ($m_J = 1/2, m_I = 3/2 \rightarrow m_I = -1/2, m_I = 3/2$). Panel b) shows a 780 nm laser scan over the D2 transition lines. Panel c) shows the fluorescence detected when the laser scan is that of panel b). Both yellow (without etalon) and purple (with etalon) traces show fluorescence that has passed through a narrow band interference filter with a central transmission frequency of 795 nm. Zero probe detuning for panel a) (panels b) and c)) is the weighted D1 (D2) line centre of naturally abundant Rb in zero magnetic field [133].

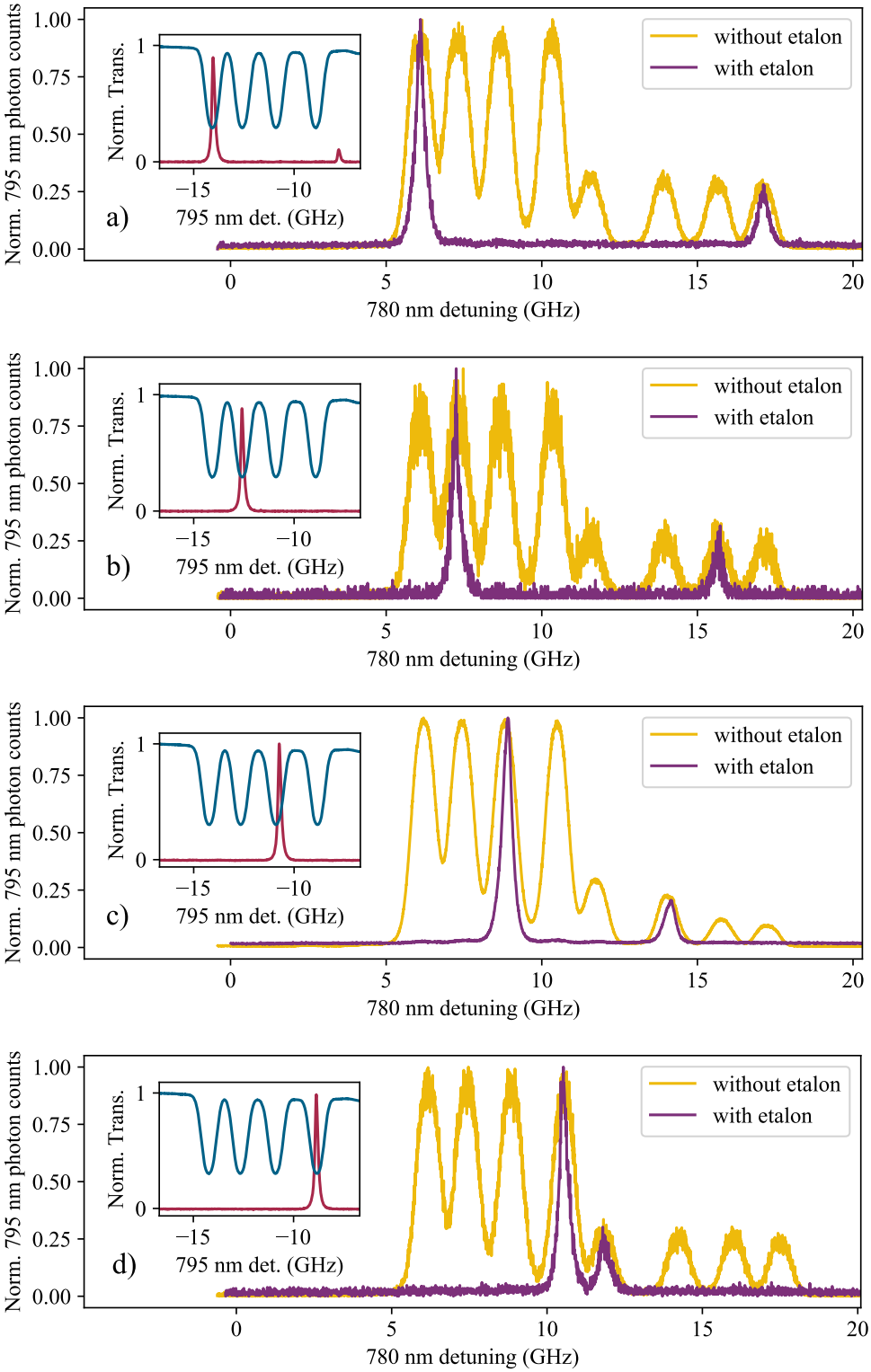

Figure 6.10: 780 nm scanning laser light in, 795 nm fluorescence out. Etalon transmitting on $|-1/2, 3/2\rangle \rightarrow |1/2, 3/2\rangle$ transition (top panel), $|-1/2, 1/2\rangle \rightarrow |1/2, 1/2\rangle$ (2nd panel), $|-1/2, -1/2\rangle \rightarrow |1/2, -1/2\rangle$ transition (3rd panel) and $|-1/2, -3/2\rangle \rightarrow |1/2, -3/2\rangle$ (bottom panel). Zero probe detuning is the weighted D2 line centre of naturally abundant Rb in zero magnetic field [133].

The transmission frequency of the etalon filter is set using the 795 nm laser relative to the D1 transition lines as shown in the top panel of Fig 6.9. This allows us to choose which hyperfine transmission frequency we allow through the filter.

6.5.1 Scanning input D2 frequency, while fixing etalon frequency window

Fig 6.9 builds on Fig 6.6, and shows the effect of introducing the etalon filter on one of the 795 nm transitions. The top panel show the transmission profile of the etalon relative to the D1 absorption features. Here the etalon is positioned on the left-most transition ($m_J = 1/2, m_I = 3/2$ to $m_J = -1/2, m_I = 3/2$). The middle panel shows the transmission spectrum of the 780 nm input laser, and the bottom panel shows the normalised detection rate of 795 nm photons, as the 780 laser frequency is scanned. In the bottom panel the yellow trace shows the 795 nm fluorescence collected without the narrowband etalon filtering. It contains no information on the frequency of the 795 nm photons other than they are in the range 793–797 nm (due to the interference filter in the collection path transmitting at (795 ± 2) nm); the x-axis is detuning of the 780 nm input light, not output photon frequency. It tells us that the rate of 795 nm photon production is higher when more 780 nm resonant laser light is absorbed by the medium. Adding the etalon (purple trace) however, gives us more information. Looking at the top and bottom panels together we learn that when the 780 nm input light is at the frequency of the left-most D2 hyperfine transition, the 795 nm photons produced by the medium, via collisional transfer, are at the frequency of the left-most D1 hyperfine transition, which is a decay from an excited state $5P_{1/2}$ with $m_J = 1/2$, $m_I = 3/2$. There are only two 780 nm input detunings which cause the production of these 795 photons: these detunings correspond to exciting the atoms into the $5P_{3/2}$ $m_J = 3/2$, $m_I = 3/2$ and $m_J = 1/2$, $m_I = 3/2$ excited states. We note that the width of the peaks in 780 nm frequency are narrower when passed through the etalon filter.

Translating the central frequency of the etalon transmission to a different D1 transition changes the fluorescence spectrum, which is evident in Figure 6.10. Viewing this in combination with the energy level diagrams in Figs 6.3 and 6.4, we summarise the transitions involved in Table 6.1. We deduce that during the collisional transfer process, which transfers an atom from the $5P_{3/2}$ state to the $5P_{1/2}$ state, the m_J quantum number of the atom can change, but the nuclear spin projection quantum number, m_I, is preserved.

Many studies have previously covered alkali metal-buffer gas spin transfer, such as [134, 125, 126], though not in the HFPB regime. [126] suggests that m_I is

Table 6.1: State change during collisions

780 nm excitation transition $(\|m_J, m_I\rangle \rightarrow \|m'_J, m'_I\rangle)$	795 nm fluorescence transition $(\|m'_J, m'_I\rangle \rightarrow \|m_J, m_I\rangle)$
$\|1/2, 3/2\rangle \rightarrow \|3/2, 3/2\rangle$ $\|-1/2, 3/2\rangle \rightarrow \|1/2, 3/2\rangle$	$\|-1/2, 3/2\rangle \rightarrow \|1/2, 3/2\rangle$
$\|1/2, 1/2\rangle \rightarrow \|3/2, 1/2\rangle$ $\|-1/2, 1/2\rangle \rightarrow \|1/2, 1/2\rangle$	$\|-1/2, 1/2\rangle \rightarrow \|1/2, 1/2\rangle$
$\|1/2, -1/2\rangle \rightarrow \|3/2, -1/2\rangle$ $\|-1/2, -1/2\rangle \rightarrow \|1/2, -1/2\rangle$	$\|-1/2, -1/2\rangle \rightarrow \|1/2, -1/2\rangle$
$\|1/2, -3/2\rangle \rightarrow \|3/2, -3/2\rangle$ $\|-1/2, -3/2\rangle \rightarrow \|1/2, -3/2\rangle$	$\|-1/2, -3/2\rangle \rightarrow \|1/2, -3/2\rangle$

conserved during these collisions. This is because the direct collisional interaction is several orders of magnitude stronger on the electronic spin than the nuclear spin, nuclear reorientation occurs mainly through the hyperfine interaction of the nucleus with the reoriented electron. We are in the HFPB regime so the electronic and nuclear spins are decoupled, so this interaction should not occur. Even without the field, though, in the case of alkali-metal atoms, the hyperfine interaction time is far longer than the duration of a typical binary collision, so little nuclear reorientation occurs during the collision itself [126].

6.5.2 Spectral profile of emitted fluorescence

So far we have used the etalon filter to learn between which states the collisional transfer process can move Rb atoms. We can also use it do determine the spectral characteristics of the emitted fluorescence, namely the lineshape and linewidth. When working with thermal vapours there are normally two characteristic widths; the natural linewidth (5.7 MHz for the D1 line [58]) of a transition, which is a result of the finite lifetime of the excited state and has a Lorentzian lineshape, and the Gaussian width (≈ 600 MHz at 75 °C) which results from Doppler broadening. We use the etalon filter to determine what effect the collisions have on these spectral characteristics.

We investigate the spectral distribution of the produced 795 nm fluorescence by fixing the 780 nm laser frequency and moving the transmission frequency of the etalon. We measure a profile by moving the etalon transmission window through the emitted fluorescence, and recording the photon count rate for each central

Etalon FWHM (MHz)	Measured FWHM (MHz)	Calculated fluorescence FWHM (MHz)
130±2	400±10	270±10
70±1	330±10	260±10
41±1	260±10	220±10

Table 6.2: Table showing the measured spectral width of the 795 nm fluorescence, for different etalon widths used to take the measurement.

frequency of the etalon. An example of a set of etalon positions is shown in Fig 6.11. The profile we measure must be a convolution of the etalon profile, and the profile of the emitted fluorescence. Fig 6.11 shows the profile measured with the 130 MHz etalon filter. We fit to a Lorentzian profile, given by

$$L(\nu) = \frac{A\Gamma}{(\nu - \nu_0)^2 + (\Gamma/2)^2} + c, \tag{6.11}$$

where ν is the frequency, ν_0 is the central frequency, Γ is the full-width-at-half-maximum (FWHM), A is a scaling constant and c is a y-axis offset constant. The measured profile fits well to a Lorentzian (residuals <5%), and has a FWHM of 400 MHz. On the whole deconvolutions are very difficult to calculate, however in this case we know that both the final measured profile and the profile of the etalon are very close to Lorentzian, and that the convolution of two Lorentzians produces a third Lorentzian with a FWHM of $\Gamma_f = \Gamma_1 + \Gamma_2$ [135]. From this we determine that the actual fluorescence is also close to Lorentzian, and that its width is the difference between the measured width, and the width of the filter used to take the measurement. Therefore, we conclude that the fluorescence is approximately Lorentzian with a FWHM of approximately 270 MHz.

We repeat this process with three different etalon filters of varying widths, as described in Table 6.2 and arrive at a value for the FWHM of the produced fluorescence of 250 ± 20 MHz.

6.5.3 Model for fluorescence profile

To better understand what we see in our system, we create a basic model of the collisions in the medium. We use a simple Monte-Carlo model to simulate the collisions, and to explain the FWHM and lineshape of the emitted fluorescence. We carry out these operations array-wise, and model 10 million collisions, which runs in approx 30 seconds on an i5 processor. The model results shown in this section use a buffer gas of molecular nitrogen, N_2. Other likely candidates for

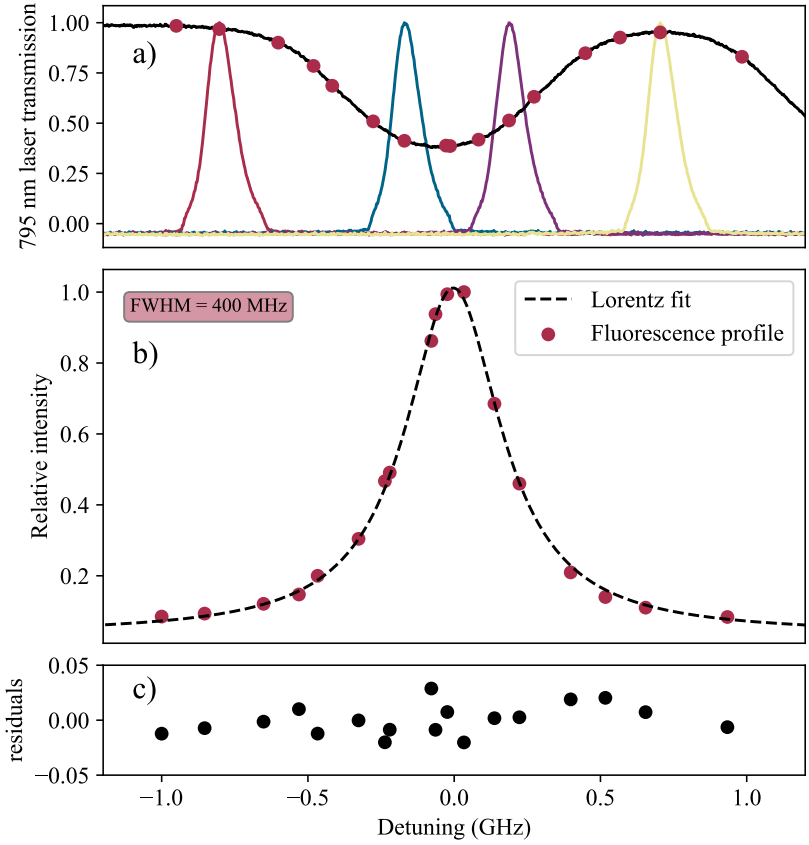

Figure 6.11: Panel a) illustrates how data points are frequency calibrated. Shown are the locations of the etalon transmission peaks (red dots) relative to the $m_I = 3/2$ σ_- D1 absorption line (black line). Four etalon trace positions are shown as examples. These don't look Lorentzian because of the high scan rate. b) shows the relative intensity of 795 nm fluorescence (red dots) as the etalon transmission frequency is altered, with a Lorentzian fit to the measured fluorescence rate profile (black dashed line). This is the convolution of the etalon transmission profile (130 MHz Lorentzian) and the fluorescence profile emitted by the atoms. Zero detuning is the central resonance frequency of the $m_I = 3/2$ σ_- D1 absorption line. Residuals are shown in c).

residual buffer gas in a cell, such as CH_4, He, Ne, Ar, are all considerably lighter than Rb, so choosing a different buffer gas has a negligible effect on the final results.

For each collision we initialise the x, y and z velocities of both (Rb and buffer gas) atoms. In the experiment we excite with a resonant 780 nm beam directed along the z-axis, so only interact with atoms which have $v_z < \Gamma/k_z$, where Γ is the natural linewidth of the excitation transition, and k_z the z-component of the light wavevector (though in this case $k = k_z$). In the model, v_z of all Rb atoms is set to be 0 m/s, and all other velocity components are randomly chosen from a Gaussian distribution at $T = 75\,°\mathrm{C}$. We use a simple spheres colliding picture (like that illustrated in Fig 6.2), based on [136], to calculate the velocities of both particles after the collision. To do this we also randomly select an impact angle for each collision, and from this calculate the contact normal vector, $\vec{n}$. We then calculate the relative velocity along the contact vector

$$v_{\mathrm{rel}} = (\vec{v}_{\mathrm{Rb}} - \vec{v}_{\mathrm{Buff}}) \cdot \vec{n}. \tag{6.12}$$

The velocities after the collision, with i denoting the 'intermediate' state of our calculation, are given by

$$\vec{v}_{\mathrm{Rb,\,i}} = \vec{v}_{\mathrm{Rb}} - v_{\mathrm{rel}} \frac{2m_{\mathrm{Buff}}}{m_{\mathrm{Buff}} + m_{\mathrm{Rb}}} \vec{n}, \tag{6.13}$$

and

$$\vec{v}_{\mathrm{Buff,\,i}} = \vec{v}_{\mathrm{Buff}} + v_{\mathrm{rel}} \frac{2m_{\mathrm{Rb}}}{m_{\mathrm{Buff}} + m_{\mathrm{Rb}}} \vec{n}. \tag{6.14}$$

These solutions are the velocities of both particles after a perfectly elastic collision, and do not take into account the energy change from the state change which occurs during the collision.

We have tried several methods for adding in the extra energy released from the state change induced by the collision. The most reasonable looking results are produced by treating extra energy as an $e > 1$ coefficient of restitution in the collision. This calculation is carried out in the centre-of-mass (cm) frame

$$\vec{v}_{cm} = \frac{m_{\mathrm{Rb}}\vec{v}_{\mathrm{Rb,i}} + m_{\mathrm{Buff}}\vec{v}_{\mathrm{Buff,i}}}{m_{\mathrm{Rb}} + m_{\mathrm{Buff}}}, \tag{6.15}$$

and final velocities are given by

$$\vec{v}_{\mathrm{Rb,f}} = (\vec{v}_{\mathrm{Rb,i}} - \vec{v}_{cm}) \cdot e + \vec{v}_{cm}, \tag{6.16}$$

and

$$\vec{v}_{\mathrm{Buff,f}} = (\vec{v}_{\mathrm{Buff,i}} - \vec{v}_{cm}) \cdot e + \vec{v}_{cm}. \tag{6.17}$$

Again, i denotes the previously calculated intermediate velocities, f the final velocities, and e is the coefficient of restitution.

The extra energy we are adding in the collision is ΔE, the energy difference between the $5S_{3/2}$ and $5S_{1/2}$ states. At our operating temperature, 75 °C, this energy is very similar to the thermal energy of the atoms, $k_B T \approx \Delta E$. The coefficient of restitution, e, is numerically calculated to conserve the total energy over a large number of collisions, n, such that

$$\sum_n \left[\frac{1}{2} m_{\mathrm{Rb}} v_{\mathrm{Rb,i}}^2 + \frac{1}{2} m_{\mathrm{Buff}} v_{\mathrm{Buff,i}}^2 + \Delta E\right] = \sum_n \left[\frac{1}{2} m_{\mathrm{Rb}} v_{\mathrm{Rb,f}}^2 + \frac{1}{2} m_{\mathrm{Buff}} v_{\mathrm{Buff,f}}^2\right]. \quad (6.18)$$

This results in a value of $e = 1.3$. This method does not, however, conserve energy for each individual collision. We have tried other methods, which conserve energy within each collision by distributing the extra energy between the two collision partners, however these produced odd, unphysical looking lineshapes.

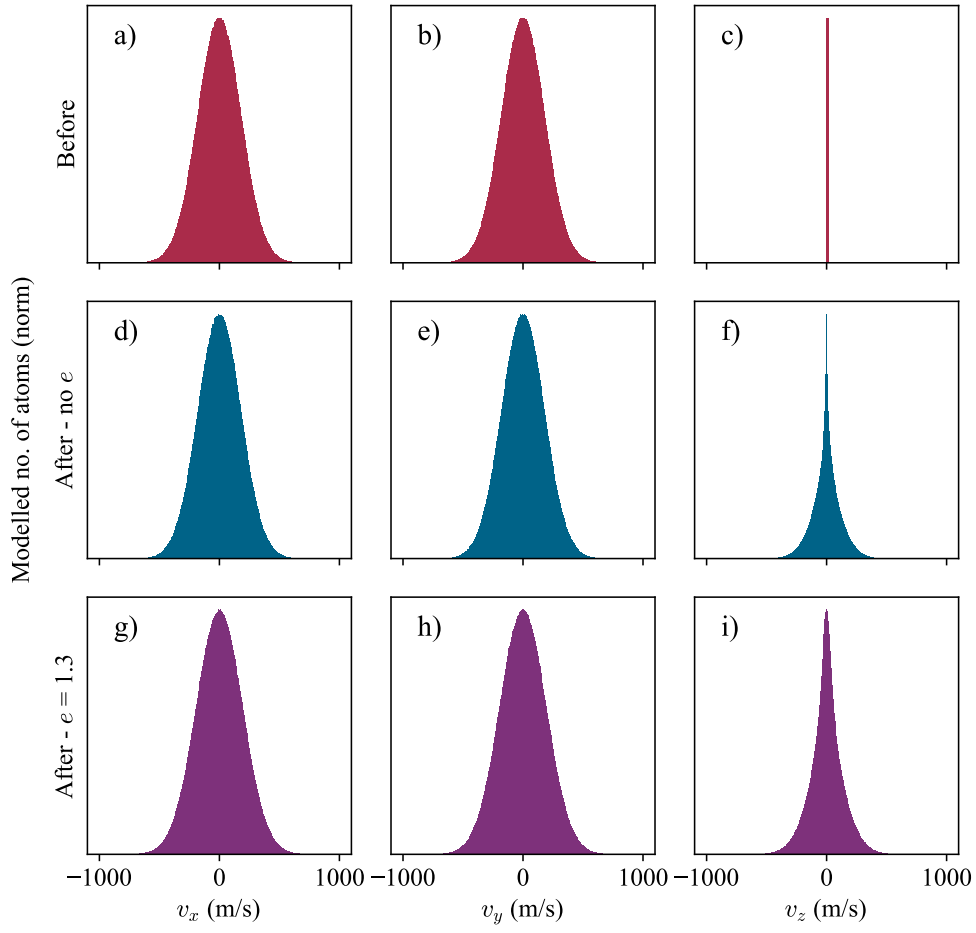

Figure 6.12: Simulated 795 nm atomic velocity distributions along x (left column), y (middle column) and z (right column) before the collision (red, top row), and after the collision, without (blue, middle row) and with (purple, bottom row) including the extra energy from the state change via a coefficient of restitution of 1.3.

We obtain a fluorescence lineshape from the calculated velocities by histogramming the final Rb velocities along the observation axis (initially v_z), and converting velocity to detuning, via $\Delta\nu = v_z/\lambda$. Fig 6.12 is a grid of modelled velocity distributions along x (left column), y (middle column) and z (right column). Distributions are plotted for before the collision (red), and after the collision, without (blue) and with (purple) including the extra energy from the state change via a coefficient of restitution of 1.3. It can be seen that the distributions in x and y, which start Gaussian, are changed very little by the collision, though they are broadened slightly when the extra energy is included (g) and h)). The distribution in z, on the other hand, changes significantly. Initially all atoms have v_z=0, (panel c)). After the collision, when the extra energy is not included (panel f)), the distribution still has a high narrow peak at $v = 0$, and is very cusped. Including the extra energy via the coefficient of restitution $e = 1.3$ gives the distribution in i), which is broader, less cusped, and closer to Lorentzian. This lineshape is in agreement with previous studies where velocity changing collisions have been observed to have cusped lineshapes [137, 138] and a cusped lineshape collision kernel has been described [139].

The velocity distribution in panel i) is converted to a frequency profile and fitted to a Lorentzian. This fit is shown in Fig 6.13, and has a FWHM of 230 MHz. The fit is not very good; the modelled fluorescence has a much sharper and higher peak at zero detuning. However, convolving with the known etalon filter profile allows us to compare our model to the lineshape that we measure, where we see much better agreement.

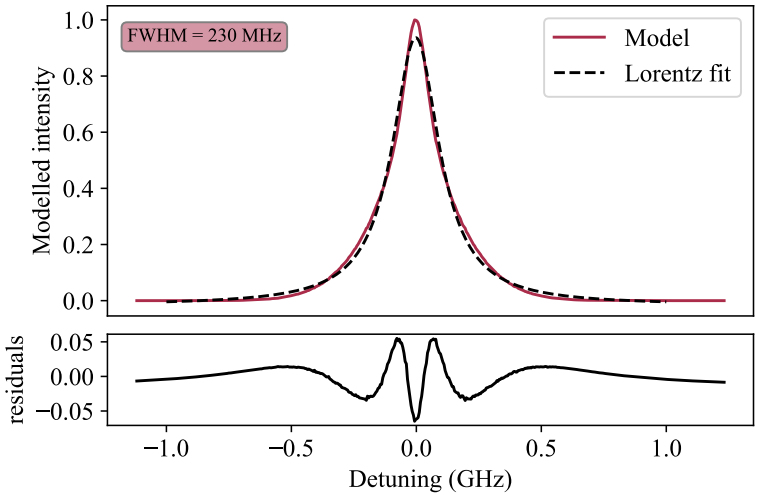

Figure 6.13: Simulated rate of 795 nm photon rate detected forward out of the cell (red solid), including the extra energy modification, fitted to a Lorentzian (black dashed).

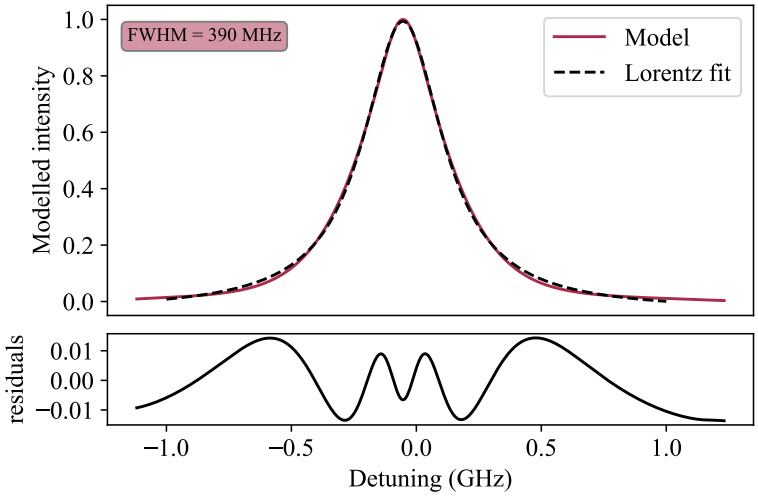

Figure 6.14: Fit of the model to a Lorentzian, after convolution with the 130 MHz Lorentzian etalon filter profile. The width of this profile is 390 MHz, and is a very good fit to the Lorentzian.

Fig 6.14 shows a fit of the model to a Lorentzian, after convolution with the 130 MHz Lorentzian filter profile. The width of this profile is now 390 MHz, which matches very closely the 400 MHz measured profile. The fit is excellent, with residuals of <1%.

The method used in this model assumes that only the internal energy of the Rb atom changes during the collision, so the internal energy of the buffer gas atom remains the same. The very good fit seen between model and experiment suggests that this assumption is likely to be correct in our case. This could be an indication that our buffer gas particles are atoms, which don't have internal ro-vibrational degrees of freedom, rather than molecules, which do.

6.5.4 Exciting off resonance

From the theoretical model discussed in Section 6.5.3, we infer that when the excitation light is detuned away from the centre of the absorption feature, the lineshape of the emitted fluorescence becomes asymmetric. This is because the beam now selects a non-zero velocity class, so we initialise all Rb atoms with a constant $v_z \neq 0$, related to the detuning by $v_z = \Delta\nu\lambda$. We have observed this asymmetry, as shown in Fig 6.15. This data set was collected using a 40 MHz filter. Residuals are plotted and we see that the skewed Lorentzian (purple) is a better fit with an RMS error of 0.022, than the standard Lorentzian fit (black) with and RMS error of 0.046. We define a skewed Lorentzian as an adapted Lorentzian,

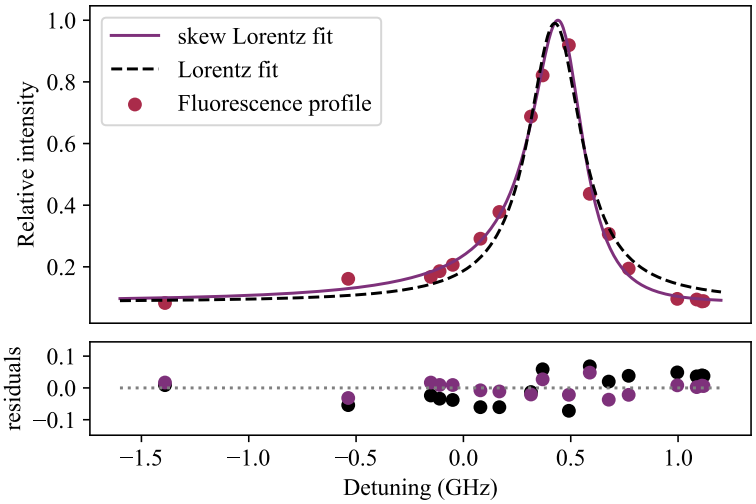

Figure 6.15: Red dots show measured points of a 795 nm fluorescence profile measured using 780 nm excitation laser detuned by approx 0.5 GHz from the central resonance frequency of the $m_I = 3/2$ σ_+ D2 absorption line, and by varying the transmission frequency of the 40 MHz etalon filter. Zero detuning is the central resonance frequency of the $m_I = 3/2$ σ_- D1 absorption line. The fluorescence profile is fitted to a Lorentzian with (purple), and without (black dashed), a skew parameter. The skewed fit has a FWHM of (300 ± 10) MHz and a skew factor of 3. The RMS errors of the standard/skewed Lorentzian fits are 0.046 and 0.022 respectively.

replacing Γ, the FWHM, with $\Gamma(\nu)$, such that the width varies with frequency. Our previously defined Lorentzian (Eqn 6.11) becomes [140]

$$L_{\text{skew}}(\nu) = \frac{A\Gamma(\nu)}{(\nu - \nu_0)^2 + (\Gamma(\nu)/2)^2} + c, \tag{6.19}$$

where $\Gamma(\nu)$ is given by

$$\Gamma(\nu) = \frac{2\Gamma}{1 + e^{k(\nu - \nu_0)}}, \tag{6.20}$$

with skew factor k.

6.5.5 Reverse endothermic process

When we instead input light on the D1 line, at 795 nm and observe decays on the D2 line (780 nm) we again see that a transfer process is occurring. The process in the low temperature regime ($T <$ 86 °C, from Fig 6.8) can be expressed as

$$\text{Rb}(5\text{P}_{1/2}) + M \rightarrow \text{Rb}(5\text{P}_{3/2}) + M, \tag{6.21}$$

where M represents the buffer gas atom, and in the high temperature regime (86 °C< T< 110 °C) as

$$\mathrm{Rb}(5\mathrm{P}_{1/2}) + \mathrm{Rb} \rightarrow \mathrm{Rb}(5\mathrm{P}_{3/2}) + \mathrm{Rb}. \tag{6.22}$$

Again, we operate in the low temperature regime at 75 °C.

This collision process moves atoms to a higher energy state, and is therefore suppressed compared to the energy favourable (exothermic) process. We operate in a temperature regime where the thermal energy is approximately equal to the fine structure splitting:

$$k_{\mathrm{B}}T \approx \Delta E. \tag{6.23}$$

This means that most collisions (≈ 85% according to our model as shown in Fig 6.16) have more kinetic energy than the energy gap, and a collision could cause the atom to transfer to the higher energy state, and lower its velocity.

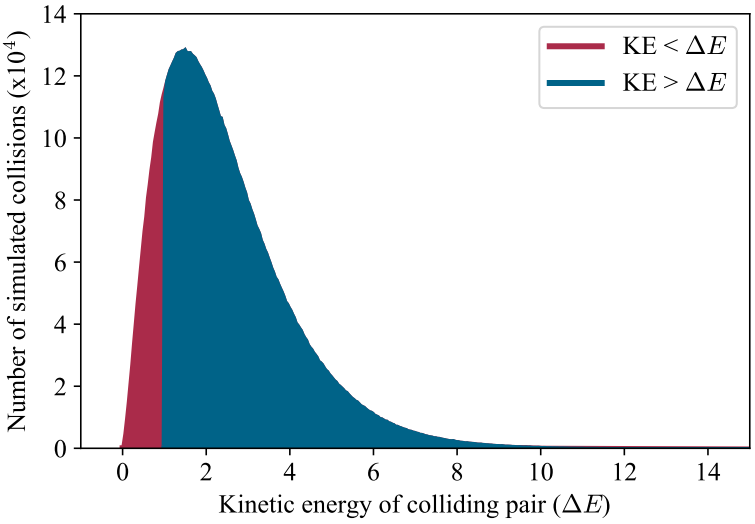

Figure 6.16: Simulation of distribution of total kinetic energy of colliding pairs of atoms at 75 °C. Individually both atoms has a Maxwell Boltzmann velocity distribution. In red are the collision pairs without enough energy to change to the higher energy state; in blue are the atom pairs which do. 85% of the collisions are in the blue region.

6.5.5.1 Scanning 795 nm laser

We repeat the earlier experiments, but with the wavelengths exchanged: scanning the 795 nm laser and fixing the etalon on a 780 nm transition. The results are shown in Fig 6.17. The insets show the eight D2 σ_+ absorption lines, with the

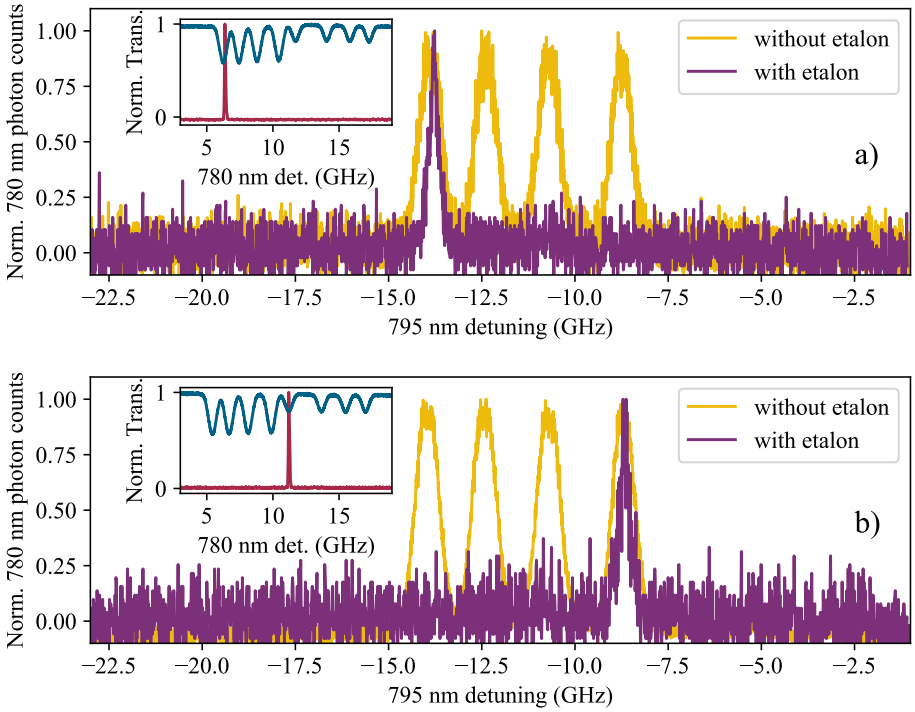

Figure 6.17: Scanning the input D1 795 nm light, with etalon transmission window fixed on the D2 transitions as shown in the insets. Zero probe detuning is the weighted D1 line centre of naturally abundant rubidium in zero magnetic field [133].

etalon transmitting on one of them; here we choose one stronger line and one weaker line. It is immediately obvious that these endothermic fluorescence spectra are much noisier than their exothermic equivalents (Fig 6.10), because we see less collisional transfer fluorescence in the energy unfavourable direction. In the main plots we see the four characteristic lines of the 795 nm spectrum without the etalon, in yellow. With the etalon, in purple, we see that fluorescence only gets through the filter if it was excited by one particular D1 transition, and again that m_I must be conserved.

6.5.5.2 780 nm fluorescence lineshape

We also measure the lineshape of the forward emitted 780 nm fluorescence with 795 nm excitation. We see the fluorescence is again Lorentzian, and slightly narrower, see Fig 6.18. In the exothermic case, with the 130 MHz filter we measured a FWHM of (400 ± 10) MHz. Here, in the endothermic case, we measure a FWHM of (350 ± 10) MHz. These uncertainties are calculated from the covariance of the fit, and do not take into account any error from the determination of the filter frequency, so will be an underestimate. To illustrate how this data set was collected,

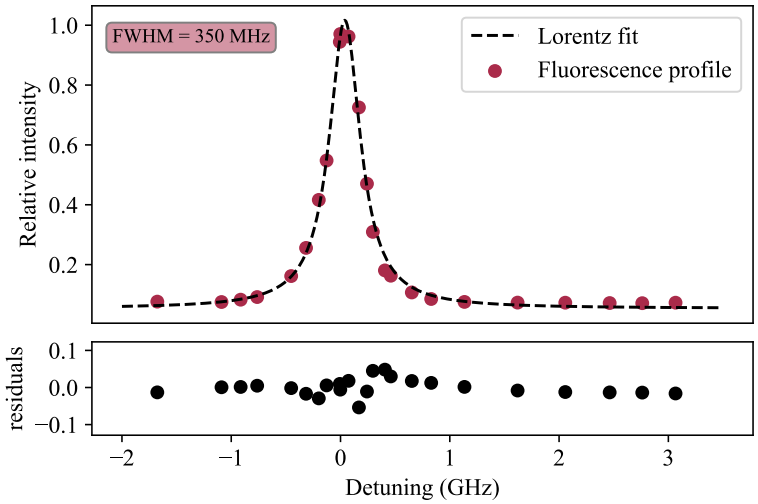

Figure 6.18: A Lorentzian fit to the 780 nm fluorescence profile when 795 nm light laser light, on resonance with the $m_I = 3/2$ σ_- D1 absorption line is input. The filter is used is 130 MHz. Zero detuning is the central resonance frequency of the $m_I = 3/2$ σ_+ D2 absorption line. The FWHM $= (350 \pm 10)$ MHz. This is lower than the FWHM seen in the exothermic process.

Fig 6.11 shows many etalon filter frequency locations, relative to the 795 nm absorption feature. For each frequency the position of the etalon relative to the position of the minimum of the absorption feature was calculated, and used as the detuning. There will also be an uncertainty contribution from the (in)accuracy of the frequency calibration of the absorption spectrum, which uses the spacing between the absorption features, the measurement of which has an error (0 ± 20) MHz. As this range is over 10 times the width of our profile, the added uncertainty from this is negligible. Any jitter in accurately identifying the peak locations would appear in the residuals, rather than shifting all points uniformly.

We apply our model to this reverse endothermic process, using the same method as for the exothermic process except for two changes:

- the coefficient of restitution is < 1, to remove the kinetic energy required for the state change. We set this to 0.6, which we calculated numerically to conserve overall energy. This causes a narrowing of the lineshape.
- Only atom pairs which have the required energy are allowed to collide. These are the blue section of Fig 6.16. This removes relatively more of the slow moving Rb atoms from play, and has the effect of removing the cusp shape and therefore widening the lineshape, as shown in the upper panel of Fig 6.19.

We fit the modelled endothermic lineshape to a Lorentzian (Fig 6.19, lower panel),

extracting a width of 310 MHz. This value is lower than the measured experimental value of (350 ± 10) MHz, but importantly both are lower than in the exothermic case. Residuals are calculated and are up to 2% of the maximum intensity, so the fit is not as good as in the exothermic case.

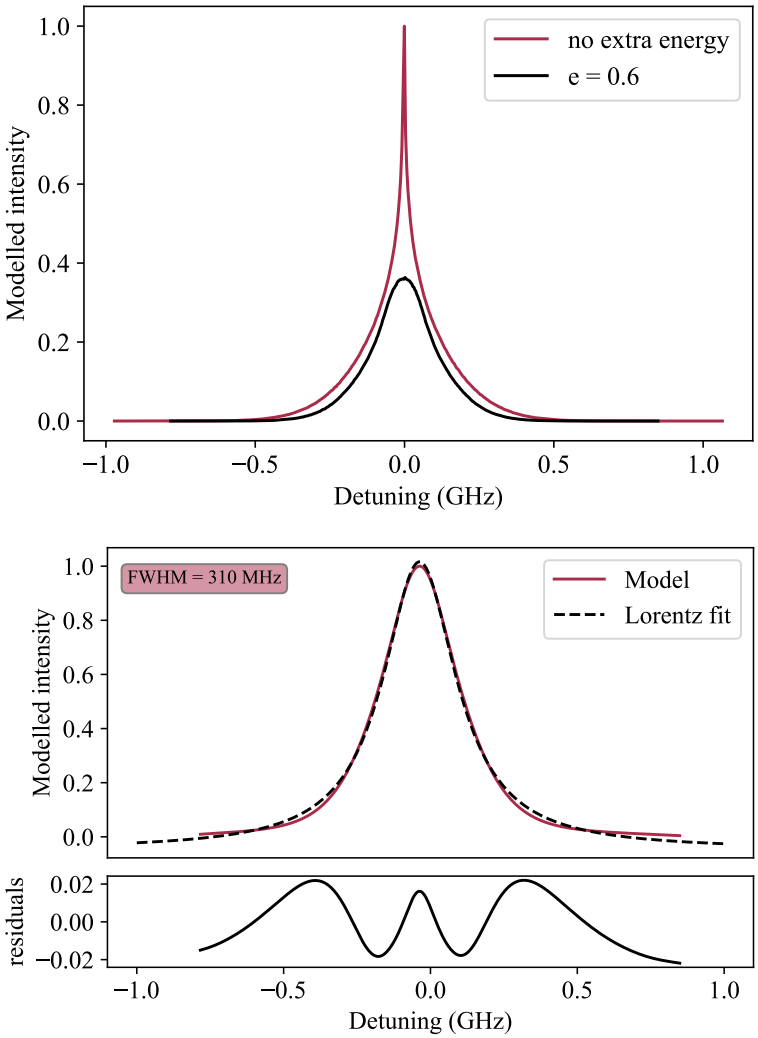

Figure 6.19: Upper: Modelled 780 nm fluorescence profile before (black) and after (red) removing energy from collision. Lower: when profile is convolved with the 130 MHz Lorentzian filter, and fitted to a Lorentzian, giving a FWHM of 0.31 GHz. Residuals are plotted and are up to 2% of the maximum intensity, so the fit is very good, but not as good as in the exothermic case.

6.5.6 Sideways observation

The geometry of our vapour cell heater enables the radial fluorescence to be monitored from the 2 mm long cylindrical vapour cell (see Section 3.1 for more details);

this allows us to investigate intra-manifold transitions (i.e. exciting axially with 780 nm and observing radially at 780 nm). Although the radial fluorescence must propagate further to exit the confines of the vapour cell heater, hence a weaker fluorescence signal, we are able to separate the fluorescence from the excitation light and also collect fluorescence from π transitions. Neither of these studies possible in the axial geometry.

6.5.6.1 Intra-manifold transitions

We investigate intra-manifold transitions (780 nm in, 780 nm out) by scanning over the D2 transitions, and observing perpendicular to the B-field through a 780 nm narrowband interference filter. These transitions cannot be observed in the forward direction as it is not possible to separate the 780 nm fluorescence from the 780 nm laser light. We input linearly polarised light, which can be thought of as being made up equally of LH and RH circularly polarised light [61], and therefore excite both σ_+ and σ_- transitions. We scan over the whole D2 spectrum (σ_+ and σ_-), as shown in Fig 6.20, at 75 °C. The top panel shows the absorption spectrum (blue), the etalon transmission spectrum (red). As we are now scanning over all the transitions, a full 40 GHz FSR and two transition peaks are now visible on our etalon filter spectrum. It is important to make sure the second does not happen to line up with another transition. The lower panel shows the fluorescence without the etalon filter (yellow), and the fluorescence through the etalon filter (purple). This time we see four clear peaks in the purple spectrum (five if you look closely). The etalon was positioned on the left-most of these peaks, and we see that this is the largest, by a factor of 2; these decays are most likely from atoms which were excited directly and have not been transferred by a collision. However, as the collisional transfer rate is high it is possible multiple transfers will have occurred. We see that the m_I conservation rule still applies.

6.5.6.2 π transitions

Observing from the side allows fluorescence from π transitions to be collected. Using polarisation filtering we demonstrate that we observe π transitions and that they follow the m_I conservation rule. Fig 6.21 shows the polarisations produced by σ_+, σ_- and π transitions along the axes relative to the direction of the magnetic field. In a magnetic field only σ_+/σ_- transitions can be excited, or fluoresce, axially, and the light required, or produced, is correspondingly left-hand or right-hand circularly polarised [61]. π transitions can only be excited perpendicular to

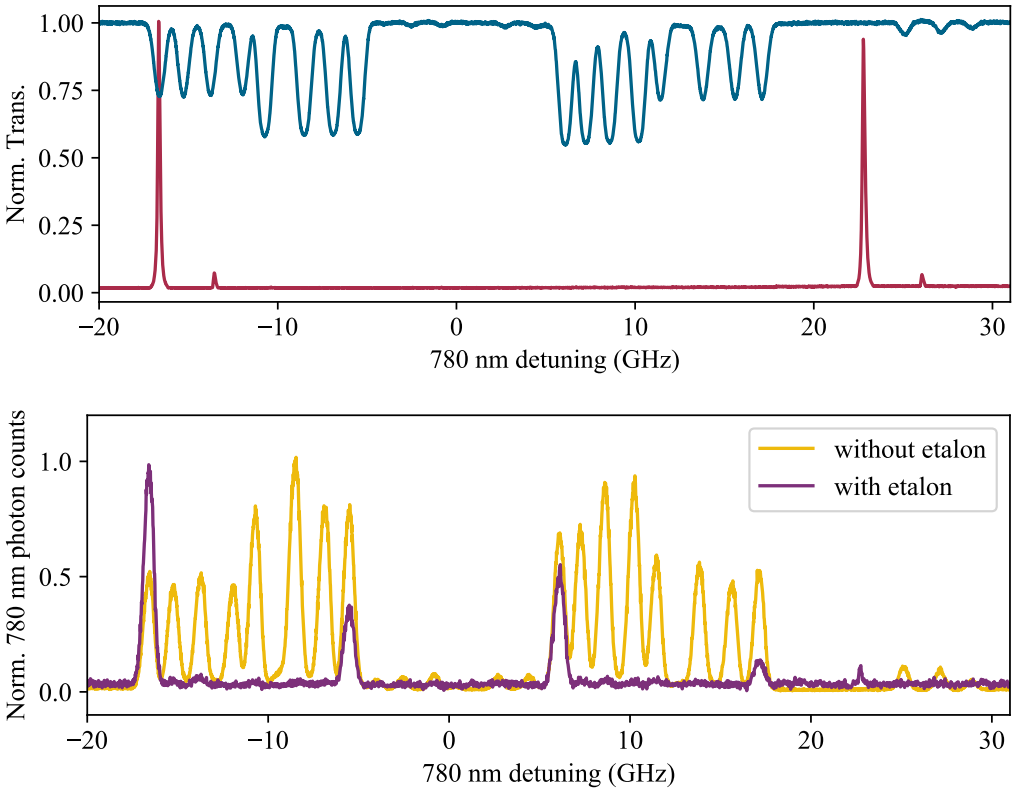

Figure 6.20: Figure showing $5P_{3/2}$ intra-manifold transitions. Upper panel shows a scan over all D2 σ_+ and σ_- transitions (blue), along with the etalon peak positions. The etalon filter used here has a FSR of 40 GHz so the TEM_{00} mode appears twice on this scan. Lower panel shows the fluorescence without the etalon filter (yellow), and the fluorescence through the etalon filter (purple). m_I is again preserved during the collision. Zero probe detuning is the weighted D2 line centre of naturally abundant rubidium in zero magnetic field [133].

the magnetic field direction, and here the light is linearly polarised, and orthogonal to the light emitted on σ_+/σ_- transitions.

We position the etalon filter at a frequency resonant with both a σ transition and a π transition at 780 nm, as shown by the red rectangle in Fig 6.22. These transitions have different m_I values, so we see two sets of fluorescence peaks as the 780 nm laser is scanned, on transitions with $m_I = 1/2$ (from the π transition) and $m_I = 3/2$ (from the σ_+ transition). We can use polarisation (see Fig 6.21 to confirm that this is the case, by inserting a half waveplate followed by a PBS before the collection fibre. The waveplate can be rotated so that either light that was originally horizontally polarised (from a π transition) or vertically polarised (from a σ transition) is is transmitted through the PBS. Fig 6.23 panel 2 shows the fluorescence intensity with 780 nm scan. As before, the yellow trace is fluorescence without the etalon filter, and purple is fluorescence after passing through the etalon

filter. In the third panel, both with and without etalon traces are now polarisation filtered to only transmit the horizontally linearly polarised light from π transitions. In the fourth panel the polarisation filtering is switched to only transmit vertically polarised light from σ transitions. We see that the four peaks in panel two are now clearly split into the two different m_I sets.

We also note that without the etalon filter, the relative height of the fluorescence peaks change significantly with changing observation polarisation, meaning changing whether the light was produced by a σ or π transition. This is because the different initial excited states have different likelihoods of being transferred to a state that will decay via a σ transition as opposed to a π transition.

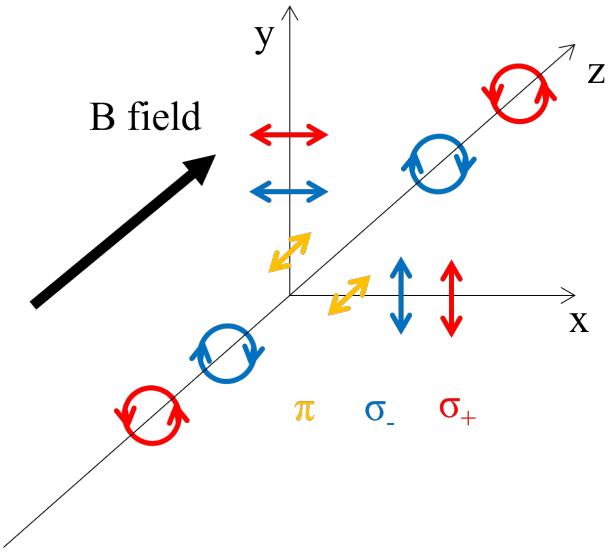

Figure 6.21: Diagram showing the polarisation of light (left- or right-handed circularly polarised or linearly polarised which can excite or be fluoresced during σ_+, σ_- or π transitions in the presence of a magnetic field.

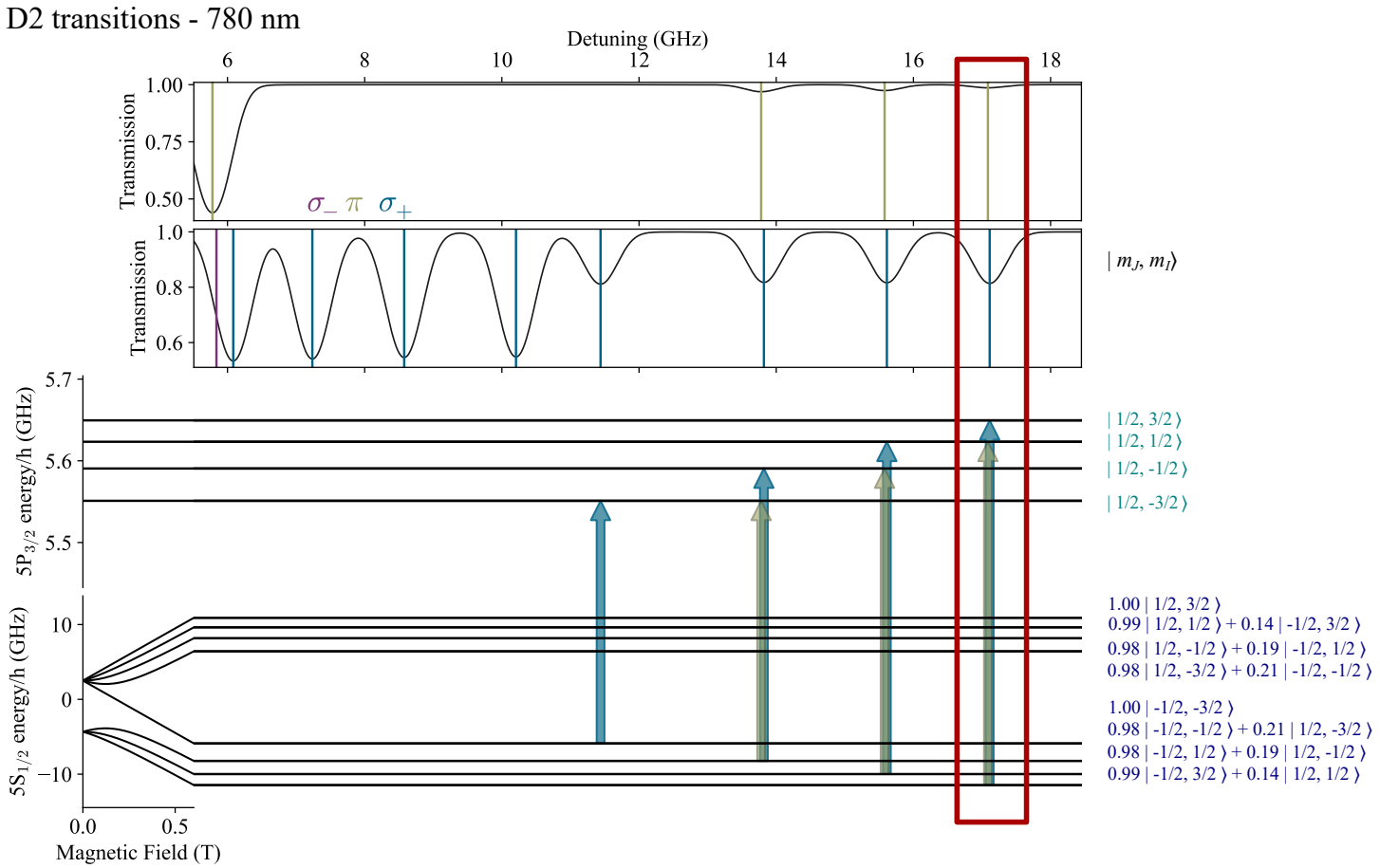

Figure 6.22: Transmission spectra (π transitions top panel and σ_+/σ_- transitions second panel) and energy level diagram (bottom) showing the transitions used when observing π and σ transitions out of the side of the cell, highlighted by the red rectangle. σ_+ transitions are shown by blue lines/arrows and π transitions by yellow lines/arrows. The m_J and m_I numbers of the states are shown to the right, showing that the two transitions in question couple states with different m_I values.

6.5.6.3 Sideways Lineshape

When we observe in the direction orthogonal to the axis of laser propagation ('sideways'), we expect to see a different fluorescence lineshape compared to the forward observation case. This is because the excitation laser only velocity selects atoms along the z-axis—its direction of propagation—so there is no velocity selection along the x- or y-axis, and the pre-collision x- and y-velocities of the atoms we excite have a Gaussian distribution. We are now observing the velocities of Rb atoms post-collision along the x-axis. We would not expect their x-axis velocity distribution to be affected significantly by the collision, as the colliding buffer gas atoms will have Gaussian velocity distributions along all three axes. This thought process is in agreement with our model, of which the result for the endothermic without-filter convolution is shown in Fig 6.24. The lineshape produced has a FWHM of (490 ± 10) MHz and is an excellent fit to a Gaussian. The starting Gaussian width of the model was 430 MHz, so the extra energy released in the collision has broadened the lineshapes in the x and y directions by 60 MHz, according to our model.

Experimentally, we find the lineshape of the fluorescence emitted orthogonal to the laser propagation axis to be asymmetric, which is not expected. The width is approx 700 MHz, which is close to what we expect for a Doppler broadened profile convolved with the 130 MHz Lorentzian filter, and much wider than the forwards lineshapes (approx 250 MHz unconvolved). The asymmetry is more significant for the energy changing (inter-manifold) collision than for the intra-manifold transition. Fig 6.25 shows the measured 795 nm lineshape, with axial 780 nm excitation, and orthogonal (sideways) observation. The 130 MHz filter was used. A fit to a Gaussian is shown, and gives a FWHM of (690 ± 10) MHz, and residuals are plotted beneath. It can be seen that the fit is not good; the residuals are very structured and an asymmetry can clearly be seen. It should also be noted that the collection count rates out of the side of the cell are lower than in the forward case. This is because the fluorescence has to travel further to escape the cell heater, and the exit hole in the side is smaller than the forward hole, so a much lower proportion of fluorescence escapes. The edge of the glass cell is also curved, which has the effect of defocussing the light that passes out of the cell this way. These factors result in much noisier profiles, as seen by the background level of 0.2, when the spectrum is normalised to 1. In the forward case the background in negligible.

We do not have a convincing explanation for the asymmetry we observe in the experiment; the excitation laser is on resonance, and a detuning along z should not produce a skew along x, so the mechanism is not the same as the detuning-induced skew seen in Section 6.5.4. As the asymmetry is more significant for inter-

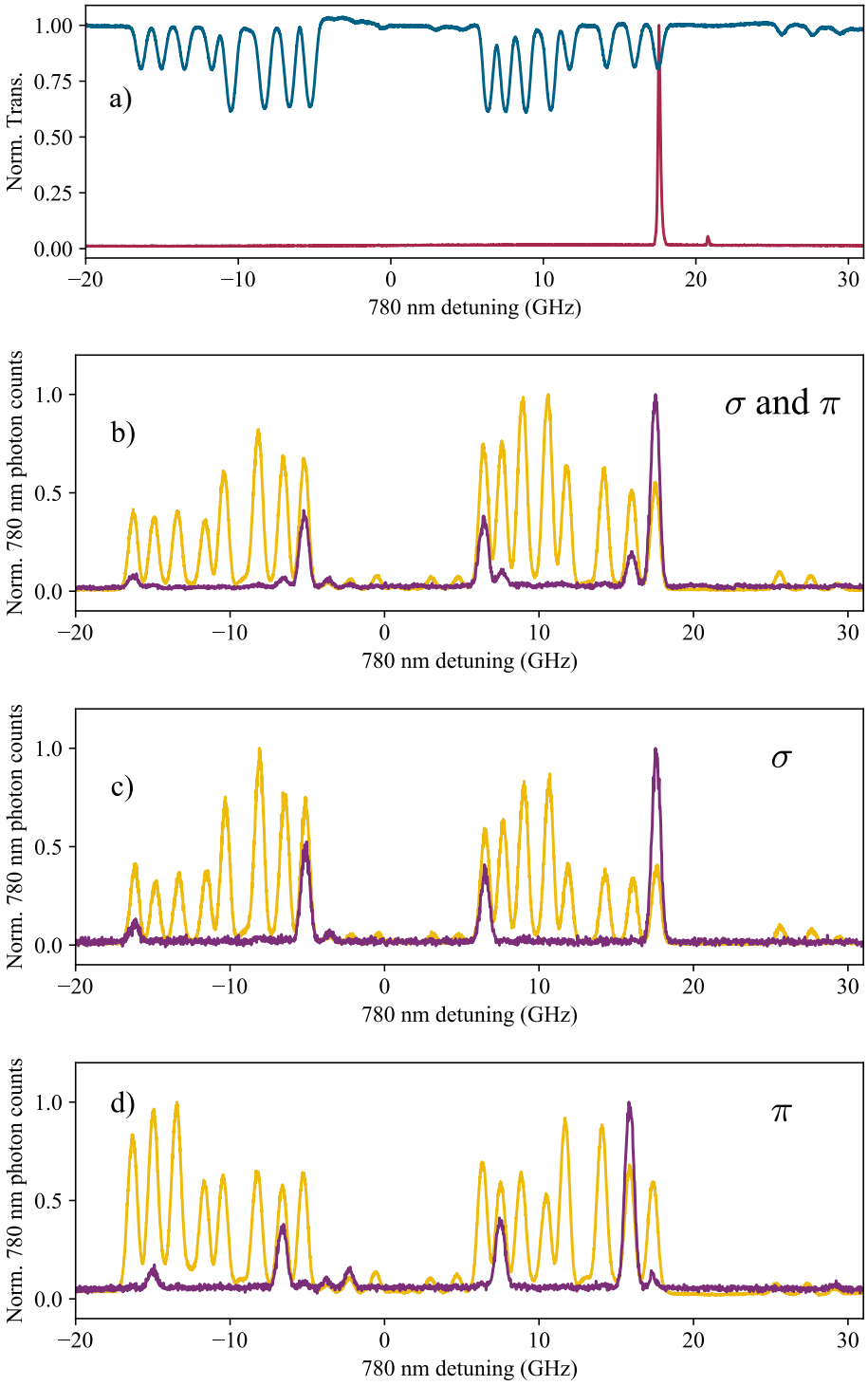

Figure 6.23: Excitation and fluorescence detection both D2(780 nm). Detection is sideways. a) show the absorption spectrum, and the etalon transmission window. b) shows the 780 fluorescence emission spectrum with no polarisation filtering with (purple) and without (yellow) etalon filtering. c) (d)) is the same b), but with polarisation filtering to only transmit σ (π) light. Zero probe detuning is the weighted D2 line centre of naturally abundant Rb in zero magnetic field [133].

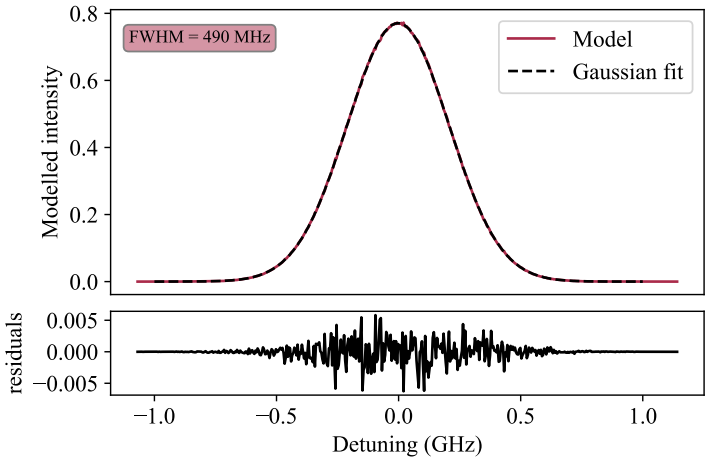

Figure 6.24: Modelled fluorescence lineshape orthogonal to excitation axis (sideways). The profile is Gaussian (a fit is shown) with a FWHM of 490 MHz.

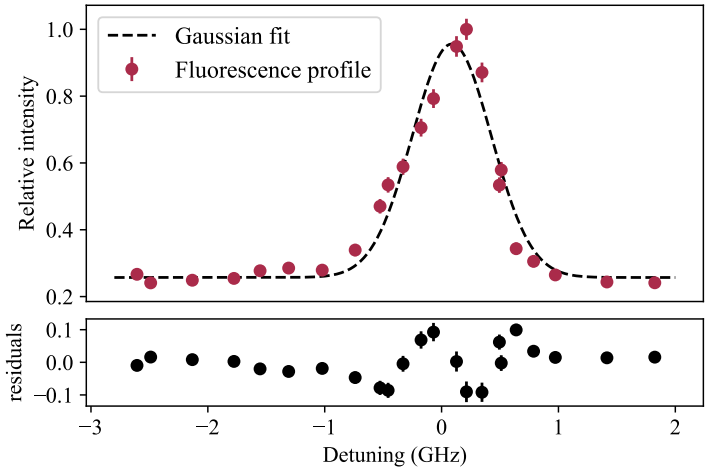

Figure 6.25: Measured 795 nm lineshape, with axial 780 nm excitation, and orthogonal (sideways) observation. Zero detuning is the central resonance frequency of the $m_I = 3/2$ σ_- D1 absorption line. A fit to a Gaussian is shown, and gives a FWHM of (690 ± 20) MHz, and residuals are plotted beneath. Error bars are $\sqrt{N}$. The residuals are large and show clear structure.

compared to intra-manifold transitions it is likely that the cause is something in the redistribution of the extra energy released by the state change. However it is odd that this effect did not appear in the forwards observation case.

6.5.7 Different vapour cells

The vapour cell used in the studies discussed so far in this chapter was commissioned to contain no gases other than the atomic species of interest, which is ^{87}Rb

in this work. However, we have shown in this chapter that there is some additional gas present due to collisional transfer. Since the additional gas, or gases, in our vapour cell is unknown, we have repeated the studies earlier in the chapter with vapour cells with known buffer gases and concentrations. These cells are cubes with side lengths of 1 mm and contain methane and molecular hydrogen, which is known to produce a combined additional broadening of 24 MHz [57]. One of these cells also contains a large amount of helium, which provides another 300 MHz additional broadening [141].

The fluorescence spectra for the He-broadened cell are shown in Fig 6.26. This data set was taken in the forward observation geometry; exciting with 780 nm input light scanning of over the σ_+ D2 absorption lines (transmission spectrum shown in the top panel of Fig 6.26) and observing forward using a 795 nm interference filter only (yellow trace), or interference filter and 130 MHz etalon filter (purple) with the etalon transmission window aligned with a particular D1 absorption feature, as shown in the insets. As previously, data was taken in the low temperature regime, at 75 °C. We observed the same m_I conservation pattern in both cells, despite the additional 300 MHz broadening meaning the transition peaks are no longer well distinguished. We would expect the temperature–collision rate graph, equivalent to Fig 6.8 for the main vapour cell, to switch from the linear to the quadratic regime at a different temperature, because the buffer gas number density is higher, and the different buffer gas will have a different collisional cross-section. Therefore the crossover point, where Rb–Rb state changing collisions happen at a higher rate than Rb–buffer state changing gas collisions will occur at a higher different temperature.

6.6 Summary and Outlook

In this chapter we have investigated the state-changing collisional process in Rb vapour. By investigating the temperature dependence of the process we have determined that in the low temperature regime when T<86 °C the process is dominated by Rb-buffer gas collisions and have carried out subsequent experiments in this temperature regime. We have used an narrow linewidth (∼100 MHz) etalon filter to investigate the collisions further, and conclude that during the collision the m_I quantum number is conserved. We have also used the filter to measure the spectral profile of the emitted fluorescence, and have implemented a basic model which agrees very well with the experiment in most cases.

We have learnt from these investigations that the buffer gas collisional mixing is a significant process, even in vapour cells where no buffer gas has been intentionally

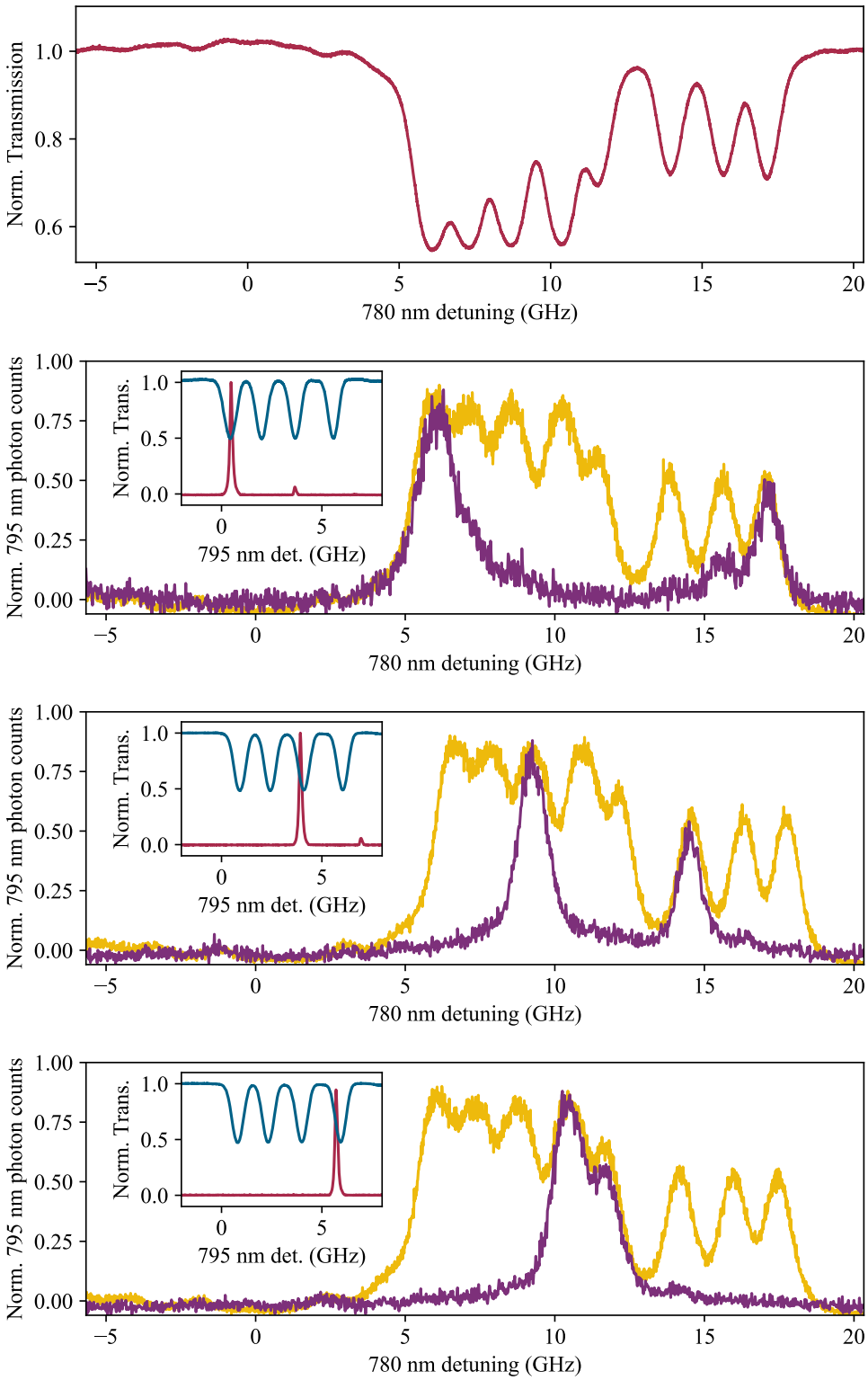

Figure 6.26: In 300 MHz He broadened cell. 780 nm in, 795 nm out. 780 nm transmission spectrum (top panel). Fluorescence without etalon (yellow) and with etalon (blue) transmitting on $|-1/2, 3/2\rangle \rightarrow |1/2, 3/2\rangle$ transition (2nd panel), $|-1/2, -1/2\rangle \rightarrow |1/2, -1/2\rangle$ transition (3rd panel) and $|-1/2, -3/2\rangle \rightarrow |1/2, -3/2\rangle$ (bottom panel).

Atom	$k_B T/\Delta E$ at 100 °C	$k_B T/\Delta E$ at $N = 6 \times 10^{18}\,\mathrm{m}^{-3}$
K	4.5	4.9
Rb	1.1	1.1
Cs	0.48	0.46

Table 6.3: Table of ratios of thermal energy to P-state fine-structure splitting in alkali atoms, at 100 °C (second column) and at a number density of $6 \times 10^{18}\,\mathrm{m}^{-3}$ (third column).

included. This effect is detrimental in our experiment which uses a four-wave mixing system as a source of single photons, and could be similarly problematic for other thermal vapour technologies where low noise is important. As the buffer gas is not intentionally introduced during the cell production process, it is likely that the amount of buffer gas in each cell could vary significantly, and that better or worse cells could be found. This collisional transfer measurement could be used to test cells to determine how close to zero buffer gas they actually are.

We also link this work to the investigation into V-EIT carried out in Chapter 4. As that work was carried out in the cell of unknown buffer gas investigated in this chapter, we know that the collisional transfer effect will be present. In response to this we included collisional transfer in our model, as decays between the two excited states of the system via the Lindblad dissipator. However we found the effect on the final spectra to be negligible.

Rb happens to have a fine structure splitting approximately equal to $k_B T$ at 75 °C. Table 6.3 shows how this splitting varies in alkali metal atoms, both for a constant temperature and a constant number density. In our laboratory, we have also observed this effect in other alkali metal vapours: Cs and K, and seen that in K where the energy splitting is much smaller, as shown in Table 6.3, the transfer effect seems to be more significant. This has been observed in experiments where K vapour is used as a solar filter [124] and a more detailed investigation is ongoing.

It is possible that performing the same diamond four wave mixing experiment in Cs, rather than Rb, would be more successful, as the collisional transfer process would be less significant. This is a possible future direction for the project. Other options, involving different energy level schemes, are also possible, and will be discussed in the next chapter.

A possible future application of the collisional process measurements described in this chapter could be as a measure of the buffer gas pressure in a vapour cell. Currently this can be done by fitting absorption spectra to a theoretical model using ElecSus, however this method is very sensitive to small errors in background fitting and laser frequency calibration. The collisional process could potentially be used

by measuring the relationship between temperature/alkali metal number density and fluorescence count rate (as in Fig 6.8) and determining the point at which the relationship changes from a linear dependence to squared dependence. Measurements would be carried out on cells of known buffer gas makeup and pressure to confirm whether the regime change occurs when Rb and buffer gas pressures are equal, or are at some other specific ratio, and how this depends on the type of buffer gas. These calibrations, if successful, would allow for determining the pressure of buffer gas in unknown cell.

Chapter 7

Four-Wave Mixing

7.1 Introduction

Four-wave mixing (FWM) is a nonlinear optical process in which three (or two) optical fields are combined coherently to create a fourth (third and fourth), in the presence of a nonlinear medium. It has many applications, including as a source of correlated single photon pairs [37] (as we will discuss further in the next chapter), for making collective spin excitations [91] and quantum beats [36].

Four-wave mixing processes can be split into degenerate and non-degenerate FWM. Degenerate FWM is a process in which all the fields have the same optical frequency, but at least three of the have distinct propagation directions, meaning distinct wavevectors [142]. Degenerate FWM has uses in image aberration correction [143, 144], and has potential for generating low-noise, portable squeezed light source [142]. In contrast, in non-degenerate FWM the generated fields have both optical frequencies and directions different to those of the pump fields. We will be investigating non-degenerate systems.

Non-degenerate FWM can be carried out in different 'geometries' meaning different configurations of energy levels. Common energy level schemes are 'double ladder' [37, 38, 35, 145], 'double lambda' [146, 147, 148, 149] and 'diamond' [150, 151, 152, 34, 50, 44]. These three schemes are illustrated in Fig 7.1, and have different advantages and disadvantages. All the schemes involve four fields, or beams, and there may be multiple beams on a single transition. As indicated in the figure, the double ladder scheme uses three atomic levels, each spaced by an optical transition. The same transitions are used moving up and down the 'ladder'. An example of this in Rb uses the $5S_{1/2}$–$5P_{3/2}$–$5D_{5/2}$ states. The diamond differs in that it uses four separate states, and four separate transitions. This has the advantage that all the frequencies involved are easily distinguishable so spectral filtering is compar-

atively easy. However, unlike the double ladder, it is not possible for all the states used to be stretched states, so weaker transitions have to be used. The double lambda system again has only 3 states and two transitions, however now there are two ground states which cannot decay and have similar energies, and one excited state. This makes two of the frequencies identical (bar any excitation detunings), while the two pairs of transitions have frequencies which cannot be resolved using an interference filter. For example, if the two ground states chosen are the $F = 1$ and $F = 2$ $5S_{1/2}$ states in ^{87}Rb the splitting is only 6 GHz.

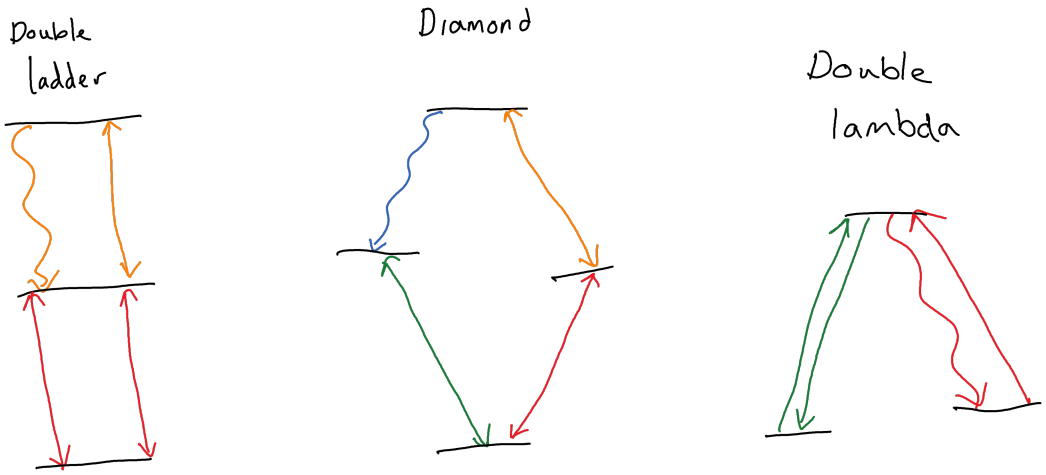

Figure 7.1: An illustration of three common four wave mixing geometries: double ladder, diamond and double lambda.

The diamond configuration has been well studied, both in zero field [150, 151, 152], and in the Hyperfine-Paschen Back regime [34, 50, 44]. In the latter case, the scheme was used to experimentally determine an excited state dipole matrix element in Rb, and as a heralded single photon source, as mentioned in the previous chapter. The characterisation of this source is fully detailed in [44], and we will mention the main findings here. The source worked; heralded single photons were produced with a $g^2(\tau = 0) = 0.35 \pm 0.02$, however the production rate was very slow at $\sim$1 Hz. This compares very unfavourably to other reported sources, particularly that of Lee et al. [37], who used a zero field double ladder scheme on the $5S_{1/2}$–$5P_{3/2}$–$5D_{5/2}$ transitions of ^{87}Rb resulting in a minimum $g^2(\tau = 0) = 0.037 \pm 0.003$, and pair rates of MHz. This setup has also been successfully repeated elsewhere [38], so we have chosen to implement it, and compare with our previous diamond scheme. We have investigated the seeded and spontaneous cases, and compared the system with and without the magnetic field. These experiments and their results are detailed in this chapter.

We chose to use a counter-propagating geometry, meaning the two excitation lasers, the pump beam at 780 nm and the probe beam at 776 nm, propagate in exactly

opposite directions. This is termed the 'Doppler free' geometry when in a ladder excitation scheme as nearly all atomic velocity classes will be resonant with the two-photon transition. This results in a larger signal than when using the 'Doppler selective' geometry, as many more atoms contribute.

7.2 Seeded four-wave mixing

The first step along the way to using FWM as a single photon source, is seeded FWM. In this case three beams are input into the nonlinear medium, which produces a fourth in the phase-matched direction. The phase matching requirement is given by:

$$\vec{k}_{\text{pump}} + \vec{k}_{\text{coupling}} = \vec{k}_{\text{seed}} + \vec{k}_{\text{signal}}. \tag{7.1}$$

Seeded FWM is of interest in its own right, and has been used in electromechanical cantilever displacement measurements [153]; in demonstrating localised entanglement [147]; and in photon storage [154]. Here we primarily make use of seeded FWM as an alignment tool, but in doing so we learn more about our FWM system, including valuable information about the frequency of the emitted photons. This information allows us filter more efficiently when we come to using spontaneous FWM to generate single photons.

7.2.1 Theory

7.2.1.1 Nonlinear optics

Nonlinear effects, of which FWM is one, arise when the polarisation, $\tilde{P}(t)$, of a medium (the dipole moment per unit volume) responds nonlinearly to the electric field, $\tilde{E}(t)$, of light incident upon it. The polarisation of a material can be expressed as:

$$\tilde{P}(t) = \epsilon_0[\chi^{(1)}\tilde{E}(t) + \chi^{(2)}\tilde{E}^2(t) + \chi^{(3)}\tilde{E}^3(t) + ...], \tag{7.2}$$

where ϵ_0 the vacuum permittivity and $\chi^{(n)}$ are the n-th order nonlinear optical susceptibilities. Following the notation of Boyd [24], a tilde, ˜, is used to denote a quantity that varies rapidly in time. In linear optics, when the intensity of light is low, only the $\chi^{(1)}$ term is significant and the polarisation scales linearly with electric field so there are no nonlinear effects. When the light intensity is sufficiently high most materials exhibit optical nonlinearities, meaning $\chi^{(n>1)}$ terms become significant. In this regime the polarisation of the medium develops frequency components not present in the incident field, which act as sources of new optical field frequency components.

In thermal vapours $\chi^{(3)}$ is the component of interest; $\chi^{(2)}$ is only non-zero for crystals which do not display inversion symmetry [24]. In the case of seeded FWM, where three fields, $\tilde{E}_1(t)$, $\tilde{E}_2(t)$ and $\tilde{E}_3(t)$, are coherently combined to produce a fourth, the relevant term is $\chi^{(3)}\tilde{E}^3_{\text{total}}(t)$, with $\tilde{E}_{\text{total}}(t) = \tilde{E}_1(t)+\tilde{E}_2(t)+\tilde{E}_3(t)$. The four interacting waves of index i are represented as

$$\tilde{E}_i(\vec{r},t) = E_i(\vec{r})e^{-i\omega t} + c.c = A_i(\vec{r})e^{i(\vec{k}_i\cdot\vec{r}-\omega t)} + c.c., \tag{7.3}$$

where $A_i(\vec{r})$ are slowly varying amplitudes and c.c. is complex conjugate. The full expansion of the $\chi^{(3)}\tilde{E}^3_{\text{total}}(t)$ term has many terms, but only one which will produce a signal which is amplified through the medium, which is of the form [24]

$$P^{NL} \propto \chi^{(3)}E_1E_2E_3^* = \chi^{(3)}A_1A_2A_3^*e^{i(\vec{k}_1+\vec{k}_2-\vec{k}_3)\cdot\vec{r}}. \tag{7.4}$$

This exponential term is the origin of the phase matching condition given in Eqn. 7.1, as the fourth field wavevector is required to satisfy

$$\vec{k}_1 + \vec{k}_2 - \vec{k}_3 = \vec{k}_4. \tag{7.5}$$

7.2.1.2 Level scheme

In this work we use a 'double ladder' energy level scheme in ^{87}Rb vapour, as illustrated in Fig 7.2, using the $5S_{1/2}$-$5P_{3/2}$-$5D_{5/2}$ ladder, which has transitions at 780 nm and 776 nm, and stronger transitions than if we were to use $5D_{3/2}$. These wavelengths are very similar, which makes satisfying the phase matching criterion less sensitive to the angles of our beams. We directly counter-propagate pump (on resonance 780 nm) and coupling (on resonance 776 nm) beams. The seed (scanning 780 nm) beam is input at a small angle. The optimal angle for phase-matching would be 0°, however a finite angle has to be chosen to allow the FWM beam to be separated from the laser beam. The FWM beam is produced by the medium at 776 nm in a direction dictated by the phase-matching condition. Fig 7.2 part a) shows the level structure in zero-field, where F and m_F are good quantum numbers, and states are split by much less than the Doppler width. This means that a laser beam resonant with one transition will also couple to other close lying transitions. Part b) shows the level scheme in the presence of the 0.6 T magnetic field. Here the good quantum numbers are m_J and m_I and the states have been Zeeman-shifted such that they are separated by more than their Doppler width, so individual transitions can be isolated.

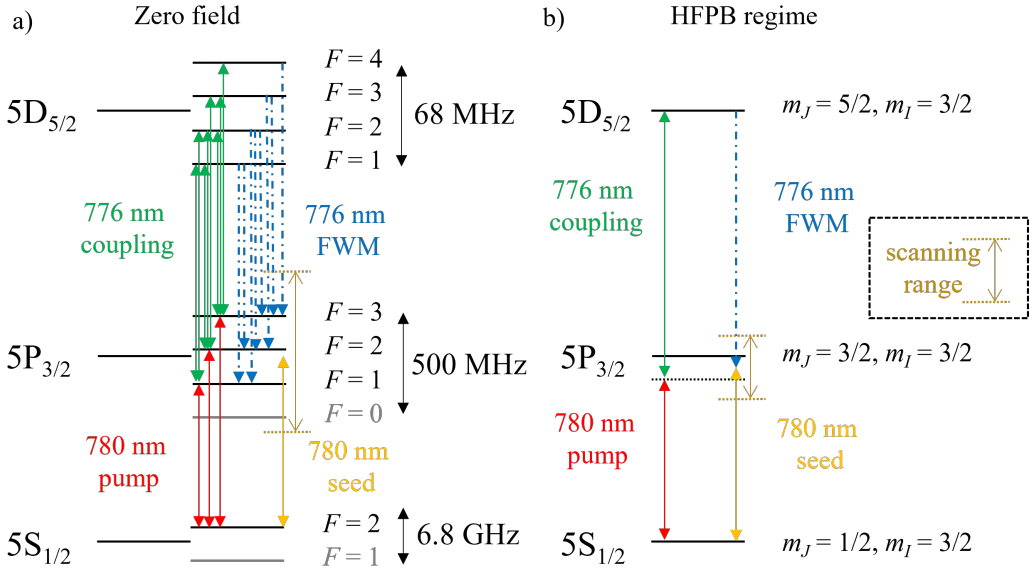

Figure 7.2: Diagram showing the energy levels and optical transitions involved in the seeded four-wave mixing process in a) zero field and b) the HFPB regime. In zero field the transitions to the $5P_{3/2}$ manifold are separated by less than the Dopper width so are not fully resolved and the excitation laser excites multiple transitions at once. In the HFPB regime the transitions are resolved and we are able to isolate a 3-level system and excite just one transition with each laser. The pump and coupling laser frequencies are fixed, and can be detuned from the resonance frequency, while the seed laser is scanned over resonance.

7.3 Experimental setup

Fig 7.3 shows the experimental setup used to measure the seeded FWM signal. The 2 mm isotopically enriched ^{87}Rb vapour cell is mounted in a copper heater and is heated to ≈125 °C. The temperature chosen is a balance between increasing the number density of Rb atoms to increase the absorption strength, while keeping below the temperature at which the medium becomes optically thick, when light produced no longer escapes the medium. We have the option to place the vapour cell in a 0.6 T magnetic field, which is produced by two cylindrical NdFeB magnets which are placed either side of the cell. The magnets have a top-hat profile [131] and produce a field which is uniform across the cell to the 1% level. The magnets can be easily removed by sliding their mounting block out sideways, without having to move the vapour cell in its heater mount.

We measure the temperature of the vapour cell using a thermocouple, which is placed inside the heater and in contact with the glass vapour cell. We then correct this temperature by fitting absorption spectra with ElecSus [42], and find the thermocouple reads 5–10 °C too high. These corrected temperatures are presented

throughout the chapter.

Three lasers are used in the setup; a 780 nm ECDL Toptica DL100 (pump), a 776 nm ECDL Toptica DLPro amplified by a Toptica BoosTA (coupling), and a 780 nm DFB (seed). The pump and coupling beams are frequency stabilised and are directly counter-propagated through the vapour cell. Both the pump and coupling beams are coupled through optical fibres before reaching the cell to provide a clean Gaussian mode, and have $1/e^2$ beam waists of (1.0 ± 0.1) mm. The seed beam does not pass through an optical fibre so has a shape which is not circularly symmetric, and a beam FWHM of (1.5 ± 0.1) mm in the x direction and (0.8 ± 0.1) mm in the y direction. All beam waists were measured by fitting a Gaussian intensity profile to a CCD image of the beam.

The 780 nm pump laser can be stabilised to an arbitrary frequency, which we chose to be on, or close to, the atomic resonance. This is achieved using the locking setup described in Section 3.3. The 776 nm laser is then stabilised such that the sum of the two fields is resonant with the two photon transition. This stabilisation is crucial; being away from resonance by 10's MHz causes the FWM signal to become an order of magnitude smaller.

The pump and coupling beams both pass through Glan-Taylor polarisers before reaching the vapour cell. The polarisers are crossed such that the two beams have orthogonal polarisations, which enables us to filter out scattered laser light. The seed beam is linearly polarised with the same polarisation as the coupling beam. This means that the FWM beam will have orthogonal polarisation, and can be filtered from the coupling beam.

The seed (scanning 780 nm) beam is input at a small angle ($\approx 1.5°$). Ideally this angle would be 0°, however a finite angle must be chosen to allow the signal to be distinguished from laser light. The small angle is achieved by using edge mirrors close to the pump-coupling beam axis, as shown in Fig 7.3. The FWM beam is then produced by the medium at 776 nm in a direction dictated by the phase-matching condition, which is in the reverse direction to the seed beam. The seeded FWM signal is aligned onto and monitored on a photodiode (PD), after being filtered by 776 nm interference filters and a Glan-Taylor polariser. A flipper mirror (FM) is in place so the FWM signal can be switched between the photodiode and a single mode fibre. This fibre is aligned to maximise FWM signal transmission and is connected to a single photon detector (Excelitas SPCM-AQRH Single Photon Counting Module). In this setup the photon detector is connected directly to the oscilloscope.

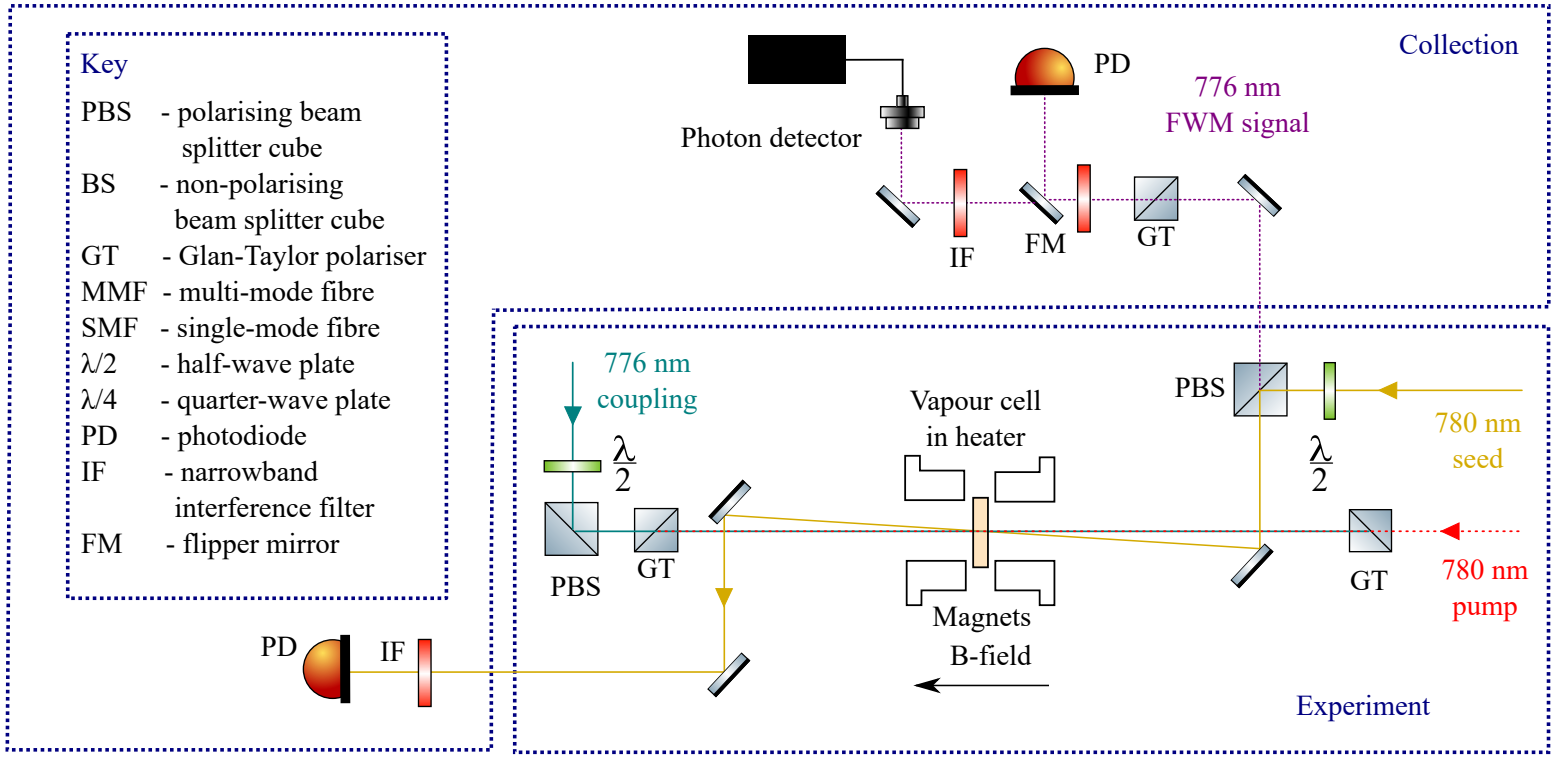

Figure 7.3: Experimental setup for seeded four-wave mixing. A 2 mm isotopically enriched ^{87}Rb vapour cell is mounted in a copper heater and is heated to ≈125 °C. We have the option to place the vapour cell in a 0.6 T magnetic field, which is produced by two cylindrical NdFeB magnets which are placed either side of the cell. The orthogonally linearly polarised pump and coupling beams are counter-propagated through the cell. The seed beam is passed through the cell at a small angle to the pump-coupling axis, using edge mirrors, and its transmission is monitored on a photodiode. The four-wave mixing signal is collected in a direction directly opposite to the seed beam propagation, and is split from the seed beam using a PBS cube. The signal is aligned onto a photodiode and optimised. The signal is also aligned into a single mode fibre onto a photon detector, and a flipper mirror allows the light to be easily switched between the two.

7.3.1 Alignment for FWM signal

Alignment of the seeded FWM signal is relatively straightforward as the signal produced is strong, and can very easily be detected on a photodiode. The general alignment procedure was as follows:

- Pump and coupling beams are aligned on axis through the vapour cell using irises positioned about 30 cm from each side of the cell.
- The pump beam is scanned and its transmission monitored on a photodiode. The coupling beam is on resonance, which produces an EIT feature, similar to those seen in Chapter 4. Small adjustments are made to the alignment to maximise the size of this feature.
- We also monitor blue 420 nm fluorescence collected out of the side of the cell onto a photomultiplier tube. This fluorescence is produced when atoms in the $5D_{5/2}$ decay via the $6P_{3/2}$ state, and is an indicator of population in the $5D_{5/2}$. We adjust the alignment of the coupling beam to maximise the intensity of this fluorescence.
- The seed beam is directed through the cell at a small angle using an edge mirror. We again maximise blue fluorescence intensity while seed and coupling beams are resonant. The pump beam is turned off for this step.
- Pump and coupling beams are both stabilised to resonance, and the seed is scanned. We align the beam path for the FWM signal onto the photodiode by retro-reflecting the seed beam back through the cell, using irises. The retro-reflecting mirror is then removed and small adjustments are made to the mirrors before the photodiode to maximise the signal.
- The FWM signal is coupled into the fibre in a similar way, however as expected, this coupling is more difficult and more trial and error was generally required. Once some signal is found it is important to make sure the mirrors are walked to the maximum. When counts are low, noise combined with the relatively slow visual feedback rate when using the photon detectors with the oscilloscope can make this tricky.

7.3.2 Hyperfine Paschen-Back regime

To move into the Hyperfine Paschen-Back regime the permanent magnets are placed either side of the vapour cell to produce a 0.6 T magnetic field. We have the option

to also include quarter-wave plates before the vapour cell to convert the input polarisations to circular. In the HFPB regime transitions are excited by either left- or right-handed circularly polarised light, while linearly polarised light is an equal sum of both circular handednesses. Thus setting the input light to be circularly polarised means that all of the light, rather than half of the light, will be able to excite the transition. However, introducing circular polarisations makes filtering more difficult. This is partly because two components (quarter-wave plate and GT polariser) on both the input and output now need to need to be optimised together on each channel, rather than just polariser angle when linear polarisations are used. It is also because in general optical components (ie mirrors) are less good at preserving circular polarisations than linear polarisations, so other polarisation components are likely to appear in the light which will not be effectively filtered.

7.4 Results

7.4.1 No magnetic field

7.4.1.1 Changing only coupling detuning

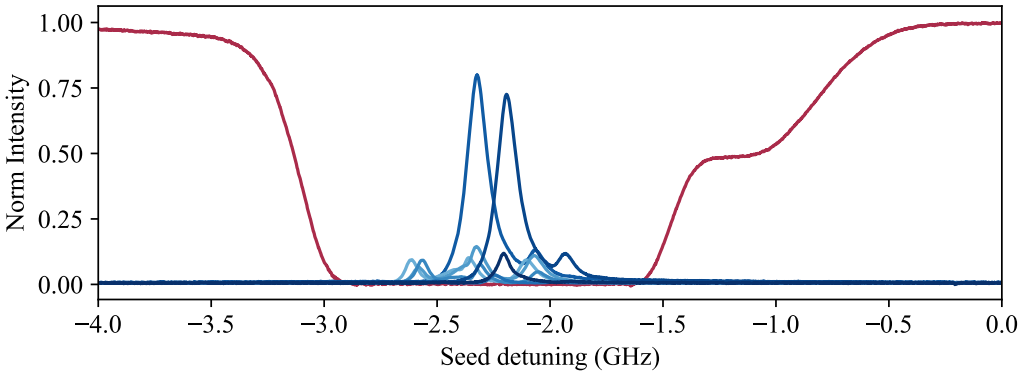

Figure 7.4: Red trace shows the absorption on the D2 $5S_{1/2}(F = 2) \rightarrow 5P_{3/2}$ Doppler broadened feature. The smaller absorption feature to the right is a ^{85}Rb absorption feature from the 2% ^{85}Rb present in our vapour cell. The blue traces are the FWM signals produced when the pump beam is frequency stabilised to the centre of the broad resonance feature, and the coupling detuning is varied around resonance, with the traces getting darker as detuning is increased. Fixed parameters: T =130 °C, pump power = 5 mW, coupling power = 30 mW, seed power = 4 mW (FWM) and 50 µW (transmission).

We begin by carrying out seeded FWM in the absence of a large magnetic field. We investigate the change in FWM signal produced when we frequency stabilise

the pump light to the centre of the $5S_{1/2}(F = 2) \rightarrow 5P_{3/2}$ Doppler broadened envelope, and vary the detuning of the coupling light. Fig 7.4 shows how the seeded FWM produced changes with changing coupling frequency (zero detuning is two photon resonant with the pump beam), when the pump beam is frequency stabilised to resonance. The seed beam is scanned over the same absorption feature ($5S_{1/2}(F = 2) \rightarrow 5P_{3/2}$), and this absorption profile is shown in red. The four-wave mixing signals produced at different coupling detunings are shown in blue, with the traces getting darker as detuning is increased. We see that as coupling detuning decreases the maximum height of the feature decreases, and three approximately equally sized peaks become visible. Altering the detuning by only 100 MHz results in a feature which is barely visible. This suggests that two photon resonance is crucial for this system, meaning a stable two photon lock will be required for the spontaneous case described in the next section.

7.4.1.2 Detuning whilst two photon resonant

We next investigate how the FWM signal changes when we detune both the pump and coupling beams individually, but keep the sum of their detunings zero; that is we remain two-photon resonant. Fig 7.4 shows, in red, the weak 780 nm seed beam transmission profile when scanned over the D2 absorption lines at 130 °C. In blue is the corresponding intensity of 776 nm emitted four-wave mixing signal. In the top panel, the pump and coupling lasers are stabilised to resonance. Moving down the panels, the pump beam is detuned from resonance, and the coupling beam locked to two photon resonance. This detuning can be seen in the small two-photon absorption (780 nm–776 nm) feature on the seed scan.

We see that on resonance the FWM feature is narrow. It is not one single peak but has smaller features from the close lying hyperfine states. As the pump (and correspondingly the coupling) laser is detuned from resonance, we see that the seed frequency at which FWM is produced shifts in the same direction. At the same time the FWM signal broadens, meaning that the range of seed frequencies which produce FWM increases. The FWM traces are all normalised to 0.8 for ease of viewing, but as pump detuning is increased the intensity of FWM light produced decreases. The difference between maximum intensity in the top and bottom figures is a factor of $\sim$500. The change in maximum count rate with coupling detuning is plotted in Fig 7.5, and shows a sharp drop off as the coupling laser is detuned out of the absorption feature, then a slower decrease as the laser is further detuned. We find that both laser frequencies can be detuned by several GHz, as long as they are matched to be two photon resonant, and we still see a strong FWM signal.

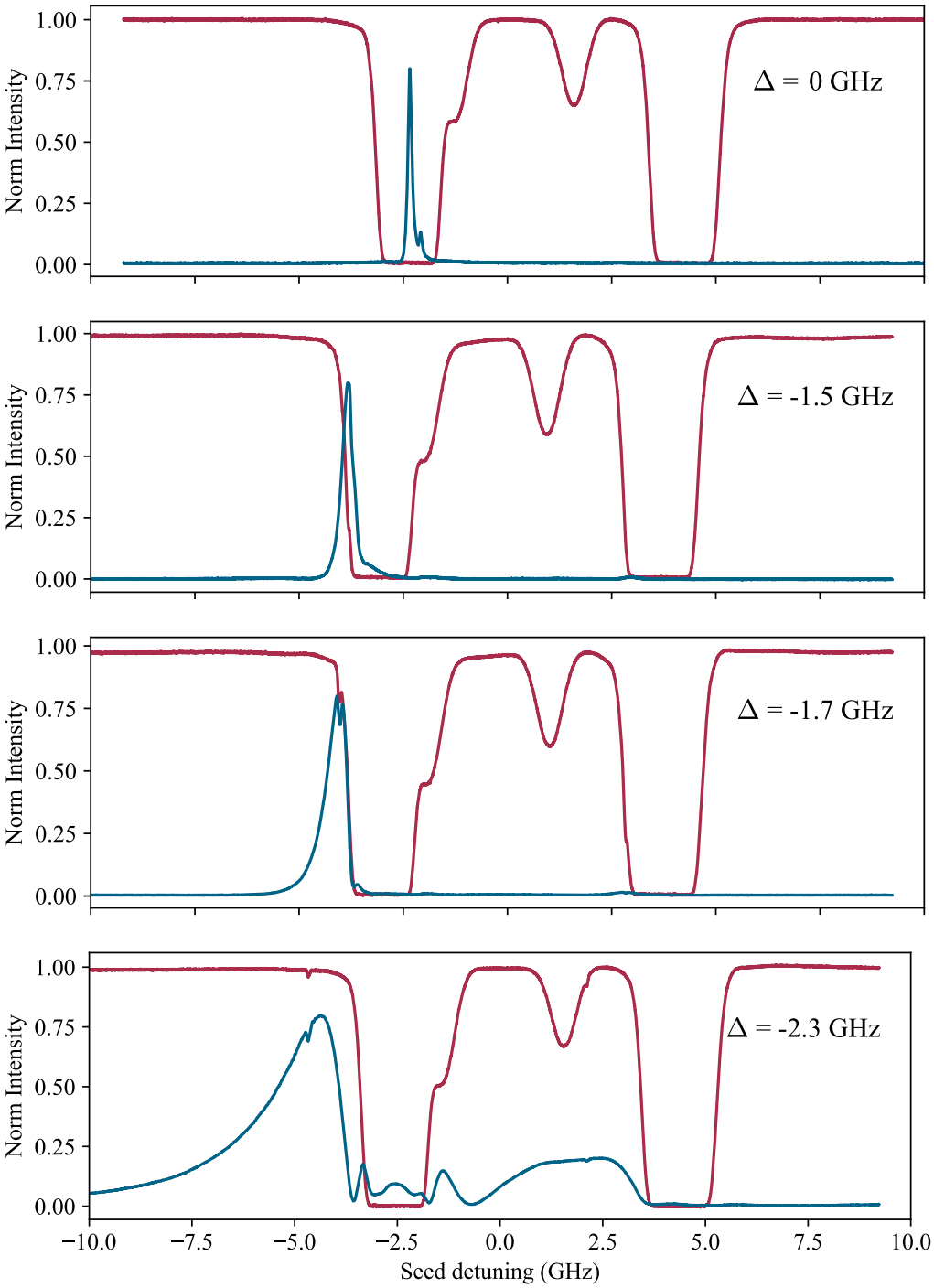
Norm Intensity
1.00
0.75
0.50
0.25
0.00
Δ = 0 GHz
Δ = -1.5 GHz
Δ = -1.7 GHz
Δ = -2.3 GHz
−10.0
−7.5
−5.0
−2.5
0.0
2.5
5.0
7.5
10.0
Seed detuning (GHz)

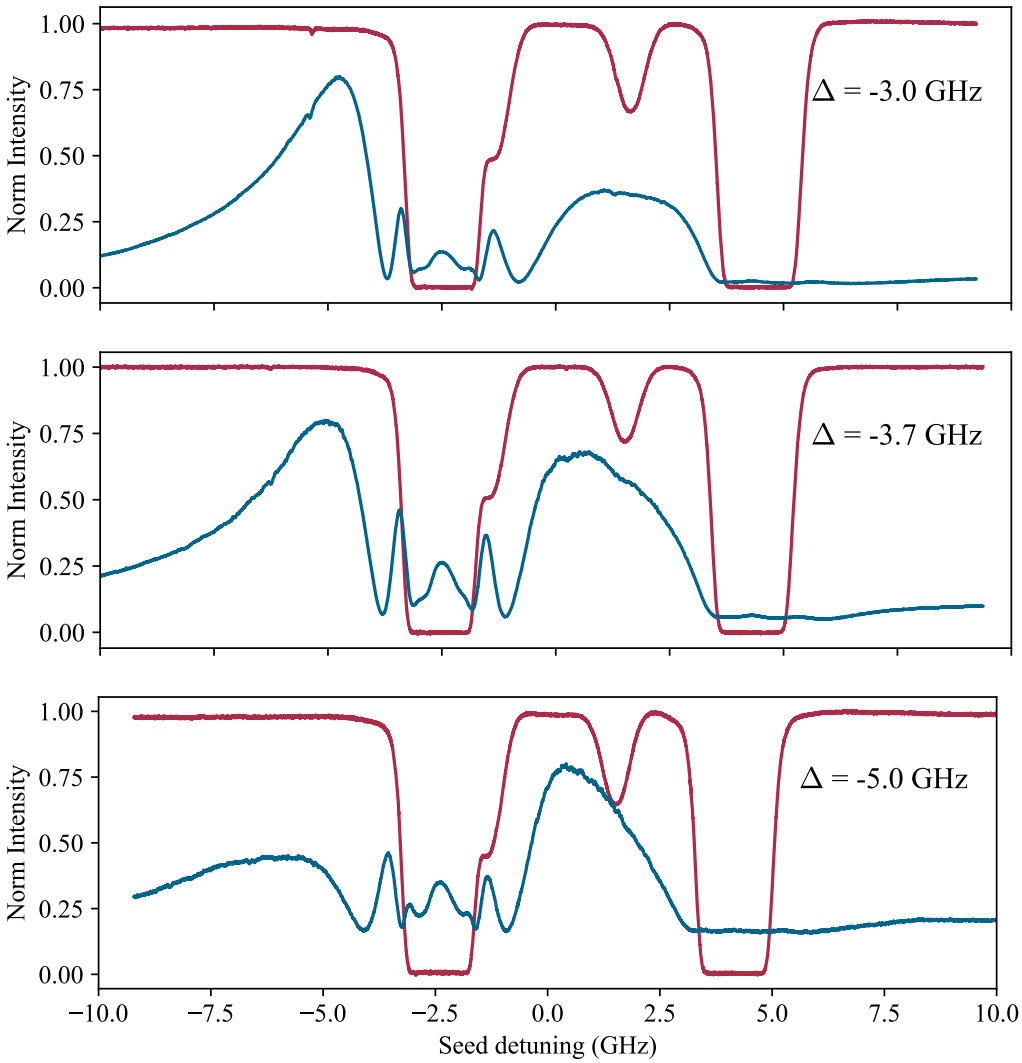

Figure 7.4: The red trace shows the scanning 780 nm seed transmission profile. The blue trace shows the corresponding intensity of 776 nm emitted four wave mixing signal. The top panel is with pump and coupling lasers on resonance. Moving down the page, the pump beam is detuned from resonance, and the coupling beam then locked to two photon resonance. This detuning can be seen in the small two photon absorption feature on the seed scan. The bottom panel has a one-photon detuning of −5 GHz. The FWM traces are normalised to 0.8 for ease of viewing, however as the detuning is increased the FWM intensity decreases. The lowest and highest detuning FWM signals have an amplitude difference of a factor of 500. Fixed parameters: $T = 130\,°\mathrm{C}$, pump power = 5 mW, coupling power = 30 mW, seed power = 4 mW (FWM) and 50 µW (transmission).

This is very different to the case where we detune only one laser, where a 100 MHz detuning causes the signal to disappear completely.

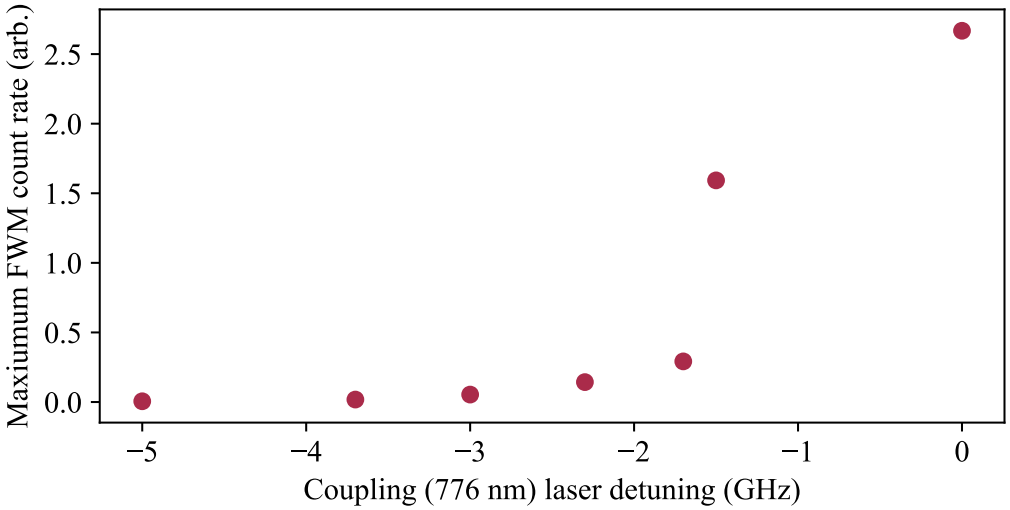

Figure 7.5: Effect of coupling (776 nm) detuning on maximum seeded FWM count. There is a sharp drop off in maximum count rate as the coupling laser is detuned out of the absorption feature. As the laser is further detuned the count rate continues to decrease, but at a much slower rate.

The lower set of panels show the case where a second two-photon resonance feature is appearing, detuned on the other side of the absorption peak. As this moves closer to the peak we see the FWM signal becoming more symmetric around the absorption peak.

This detuning effect is interesting, and not entirely expected. We have not seen it reported in this way elsewhere. [35] and [155] carry out a similar experiment but with only one 780 nm laser, so both seed and pump beams are scanning simultaneously. They report broader and asymmetric features when the one-photon detuning point is within the Doppler envelope, however they see narrower peaks when the detuning is further from resonance. These narrow features agree with our observation that the two-photon pump-coupling resonance condition is important, because this condition is only met for a narrow range of pump frequencies. In [149], in a double lambda scheme, some broad features are reported, but again the scheme is different as two transitions are excited by the same laser, so cannot be independently varied.

One might have assumed that the most FWM would be produced when the seed is on resonance, thinking that the pump and coupling lasers serve only to promote the atoms into the 5D state. As they are two photon resonant and in the counter propagating Doppler free geometry we are not selecting any particular velocity

class. However it seems instead that the route the atoms took to arrive at the 5D state is important, and affects at what seed frequencies FWM takes place.

The cases in the top two panels, where the one transition detuning remains within the absorption feature, show that we are not operating in an optically thick regime for 776 nm photons (where photons produced on resonance are unable to escape), so this is not the reason for the lack of on resonance fluorescence in the lower panels.

In the off-resonance excitation cases, there is a small dip in the FWM spectrum (blue) at the detuning of the pump beam, which looks similar to the two-photon absorption feature seen in the seed transmission spectrum (red). At this seed frequency we see slightly less produced FWM signal. This could be because slightly less of the pump beam now get absorbed, with atoms being promoted by the seed beam instead. This gives an effectively lower pump power, so less FWM signal will be produced. Excitations via the seed will have different phase matching conditions, because of the small input angle difference, and so we will not detect that signal in the same place.

These results show that we have some level of control over the frequency at of the four-wave mixing beam, via the detuning of our incident laser beams. This has implications when we move to the spontaneous FWM case (Section 7.7), in which we are looking to produce single photons; we may have more control over the frequency of the photons produced, however it may be that the input detunings which give the 'purest' single photon source produce photons with frequencies away from the desired frequency. If this were the case, introducing a magnetic field, so we can arbitrarily select the absorption frequencies, may be useful.

7.4.1.3 Effect of changing temperature

We have investigated the effect of changing temperature on the seed spectral dependence of the produced FWM beam intensity. The results are displayed in Fig 7.6, with seed transmission in red and FWM signal in blue. We see that at the highest temperatures (>125 °C, corresponding to number density $N = 2.7 \times 10^{19}\,\mathrm{m}^{-3}$) very nearly all the FWM signal is produced when the seed is negatively detuned from resonance, at a frequency outside of the absorption window. As the temperature is decreased the feature moves closer to, and then inside, the absorption feature, though the peak remains at its edge, until we reach low temperatures (<85 °C, $N = 2.2 \times 10^{18}\,\mathrm{m}^{-3}$) where the feature appears to be more symmetric. The FWM traces are all normalised to 0.8 for ease of viewing, however, the FWM intensity decrease between these two temperatures is a factor of ∼50. The ratio $N_{125^\circ C} : N_{85^\circ C} = 12$. We might expect a $N^2_{125:85}$ factor difference between the

intensities, however this is not quite the case. At the lowest temperatures the signal (measured on a photodiode) is barely distinguishable over the noise. We conclude that the fluorescence we see is not off resonance because the medium is optically thick on resonance. If this were the case, we would also expect to see the fluorescence symmetrically around the absorption line, which we do not.

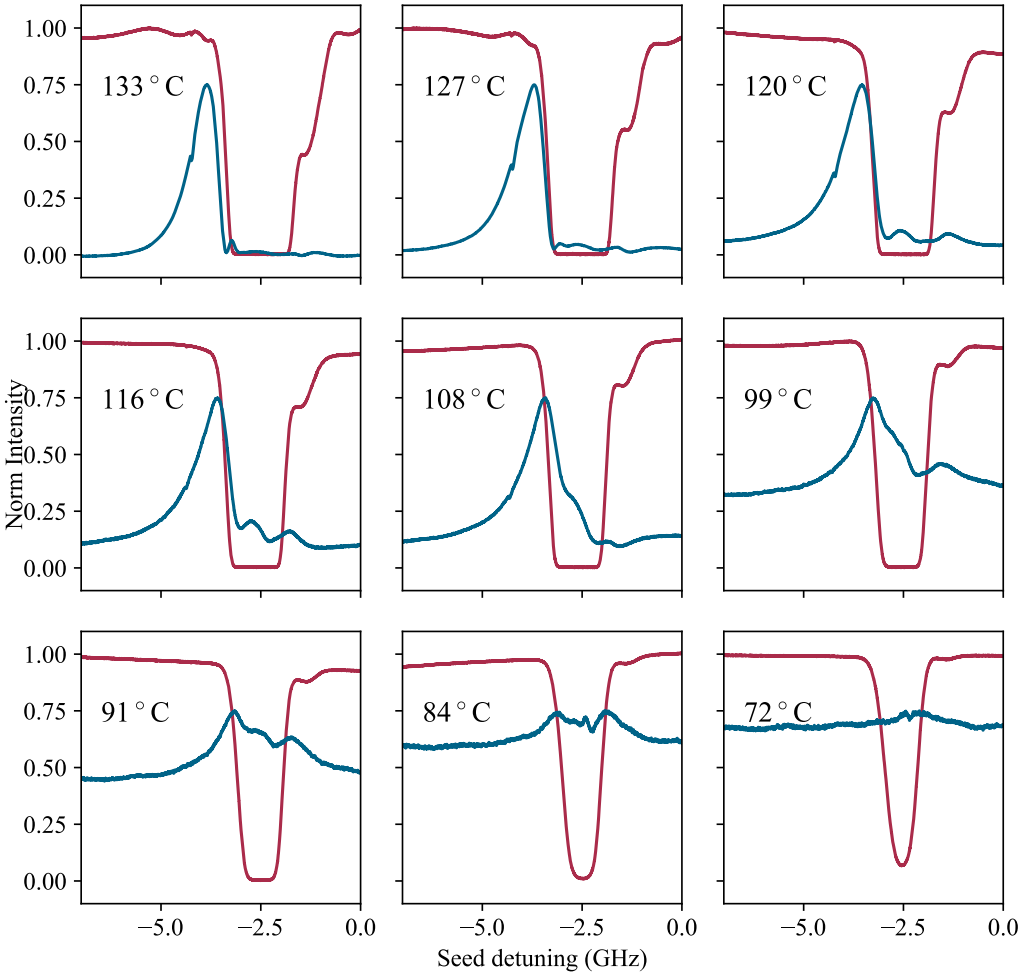

Figure 7.6: The effect of changing temperature on the seeded FWM signal produced. Plots show seed transmission in red and FWM signal in blue. Temperature decreases moving through the panels from 133 °C (top left) to 72 °C (bottom right). The FWM traces are normalised to 0.8 for ease of viewing, however as the detuning is increases the FWM intensity decreases. The lowest and highest detuning FWM signals have an amplitude difference of a factor of ∼180. Fixed parameters: one-photon detuning = −1.8 GHz, pump power = 5 mW, coupling power = 30 mW, seed power = 4 mW (FWM) and 50 µW (transmission).

7.4.2 In the HFPB regime

We now introduce the 0.6 Tesla magnetic field, and repeat the experiment as described in the Section 7.4.1.2. The only differences to the experimental setup are the introduction of the permanent magnet around the experiment and locking cells creating a magnetic field of 0.6 T, and the frequency change of the lasers so they remain resonant with the atomic transitions. Though these transitions are now excited by circularly polarised light, we still use linear for the pump and coupling beams (for the reasons we will outline in Section 7.3.2) which is an equal superposition of both circular handednesses. This has the effect of halving the resonant power of the beams. We place a quarter-wave plate in the path of the seed beam. making this circularly polarised.

Fig 7.7 shows the intensity of FWM signal (blue traces) produced when the seed beam is scanned (transmission is shown in red) over the D2 σ_+ absorption lines. The pump and coupling beams are individually detuned by varying amounts, but are collectively frequency stabilised to two-photon resonance. We see that on resonance (panel a)) the produced FWM signal is narrow in seed detuning ($\sim$0.5 GHz), though broader than in the same case without the magnetic field. When the pump is detuned, the FWM signal retains its double peaked structure, but becomes much broader (FWHM $\sim$ 2GHz) at a detuning of <1GHz (panel d)). At greater detunings the peak separation remains approximately constant, but the intensity of the signal decreases. All FWM signals are normalised to 0.8, but the background is not corrected, so it can be seen that background noise is very significant in the higher detuned cases, particularly in panel f) (detuned by 2.5 GHz). The intensity difference of the FWM signal between panels a) and f) is a factor of $\sim$200.

This is very different behaviour to the zero field case, and has implications for any spectral filtering we will implement when we move to spontaneous FWM.

7.5 Discussion

These results pose an obvious question: Why does increasing the one-photon detuning drastically broaden the lineshape? We see features that are >2 GHz wide, which is much wider than the Doppler width. In the next section we will describe our model for the system in the HFPB regime, which we use to answer this question.

Without the magnetic field we see significant asymmetry in the seeded FWM signal as the one-photon detuning is increased; with the magnetic field we do not. Why do we see such a difference between the magnet and no magnet regimes? We attribute

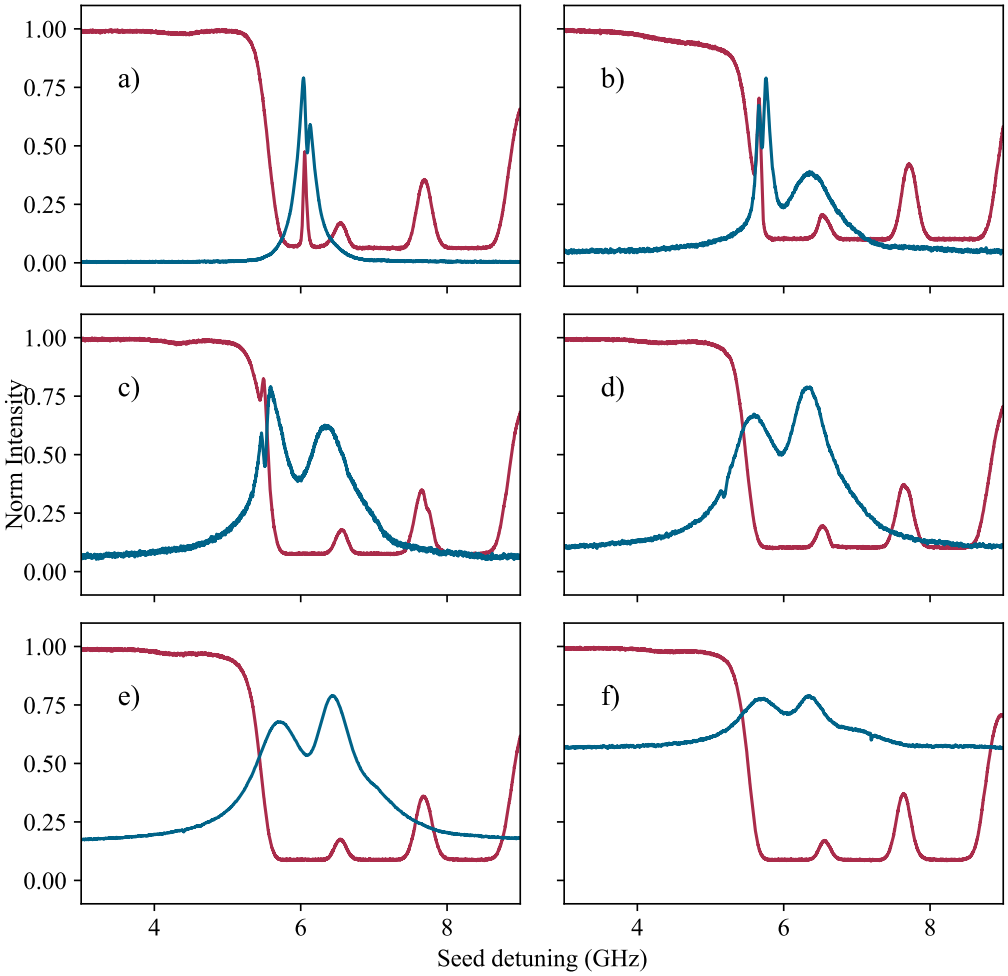

Figure 7.7: The effect of changing one-photon detuning while keeping two-photon resonant on seeded FWM signal in a 0.6 T magnetic field. The red traces show the scanning 780 nm seed beam transmission profile. The blue traces show the corresponding intensity of 776 nm emitted four wave mixing signal. Panel a) is with pump and coupling lasers on resonance. Moving through the panels, the pump beam is detuned from resonance, and the coupling beam locked to two photon resonance. This detuning can be seen in the small two photon absorption feature on the seed scan. The maximum detuning, that in panel f), is 2.5 GHz. Fixed parameters: $T = 120\,°\mathrm{C}$, pump power = 12 mW, coupling power = 30 mW, seed power = 4 mW (FWM) and 50 µW (transmission).

this to unresolved hyperfine transitions in the zero field case, as shown in Fig 7.2, which are asymmetric with respect to the detuned excitation beams, and expect that these features would appear in a complete model, though that is outside the scope of this work.

We also note that the zero-field case is much more tolerant of one-photon detuning point than the HFPB regime. When we detune by approximately $-2.5\,\mathrm{GHz}$ in the zero-field case (panel 4) we still see a strong FWM signal, and the signal remains out to detunings of $-5\,\mathrm{GHz}$ (bottom panel). However in the HFPB regime, this signal is already very weak at $-2.5\,\mathrm{GHz}$ detuning (panel f)).

This information on the frequency at which FWM is produced can be used to inform our filtering strategies when we move the spontaneous FWM setup for single photon pair generation. It is possible that the asymmetry of the zero-field case will make frequency filtering more effective than for the symmetric HFPB case.

7.6 Model

An advantage of the hyperfine Paschen-Back regime is its simplicity; the non-degeneracy of the energy levels allows for easy modelling, so we choose to model our FWM data gathered in this regime. We model the system using the Lindblad master equation (4.1), as introduced in Section 2.1 and developed for a 4-level system in Section 4.5. Here we model the system as four independent states, but set the energy of the two intermediate states to be the same, as shown in Fig 7.8 This approach was taken successfully in [156]. A very similar model was also used and found to fit well to data in the diamond scheme in the HFPB regime [34]. However neither of these cases modelled large intermediate state detunings.

The Hamiltonian for our system is given by

$$\hat{H} = \frac{\hbar}{2}\begin{pmatrix} 0 & \Omega_{01} & 0 & \Omega_{03} \\ \Omega_{01} & -2\Delta_{01} & \Omega_{12} & 0 \\ 0 & \Omega_{12} & -2(\Delta_{01}+\Delta_{12}) & 0 \\ \Omega_{03} & 0 & 0 & -2\Delta_{03} \end{pmatrix}. \tag{7.6}$$

Rabi frequencies Ω_{ab} couple states $|a\rangle$ and $|b\rangle$. The pump and coupling beams are two photon resonant and detuned from the intermediate state by $\Delta_{01} = -\Delta_{12}$, and the seed beam is detuned by Δ_{03}. Spontaneous and collisional decays, Γ_{ab} between states are included via the Lindblad dissipator term, though they are not included in Fig 7.8 for readability.

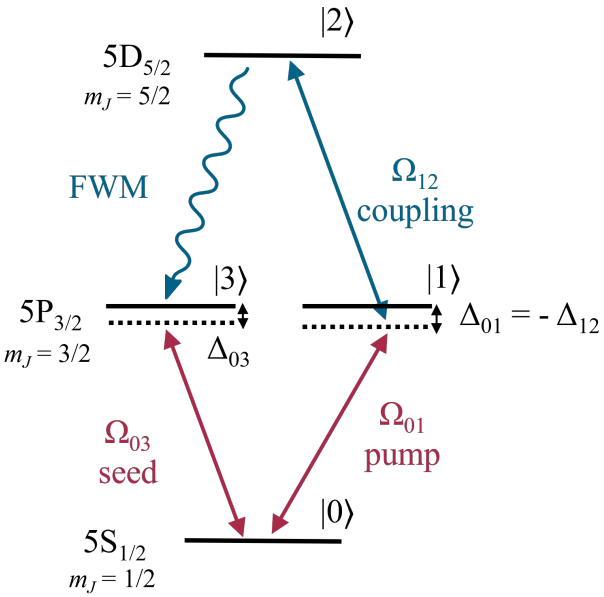

Figure 7.8: Energy level scheme used in FWM double ladder model. We model the system as four independent states, with the two intermediate states, $|1\rangle$ and $|3\rangle$ having the same energy. Rabi frequencies Ω_{ab} couple states $|a\rangle$ and $|b\rangle$. The pump and coupling beams are two photon resonant and detuned from the intermediate state by $\Delta_{01} = -\Delta_{12}$, and the seed beam is detuned by Δ_{03}.

The density matrix for this system is ρ,

$$\hat{\rho} = \begin{pmatrix} \rho_{00} & \rho_{10} & \rho_{20} & \rho_{30} \\ \rho_{01} & \rho_{11} & \rho_{21} & \rho_{31} \\ \rho_{02} & \rho_{12} & \rho_{22} & \rho_{32} \\ \rho_{03} & \rho_{13} & \rho_{23} & \rho_{33} \end{pmatrix}, \tag{7.7}$$

where ρ_{aa} are populations and ρ_{ab} are coherences between states. We solve for the steady state solution of the Lindblad master equation, unlike in Chapter 4, because we are using stretched states, so atoms cannot decay to the other ground state. The FWM signal is given by the coherence between states $|2\rangle$ and $|3\rangle$, $|\rho_{23}|^2$ [52]. Using this model, we obtain results which are qualitatively similar to the experimental results of Fig 7.7.

When we enter into the model Rabi frequencies calculated from the experimental parameters, taking into account the reduced power due to linear polarisation of the seed and coupling beams, we obtain spectra that match the experimental data well off intermediate state resonance, but not so well on resonance. These spectra are shown in Fig 7.9, and have detunings in regimes equivalent to panels a), b) and d)/e) of Fig 7.7. In panel a) the intermediate state detuning $\Delta_{01} = 0$, in b) $\Delta_{01} = 500\,\text{MHz}$ and in c) $\Delta_{01} = 1000\,\text{MHz}$. The broad features of b) and c) agree with

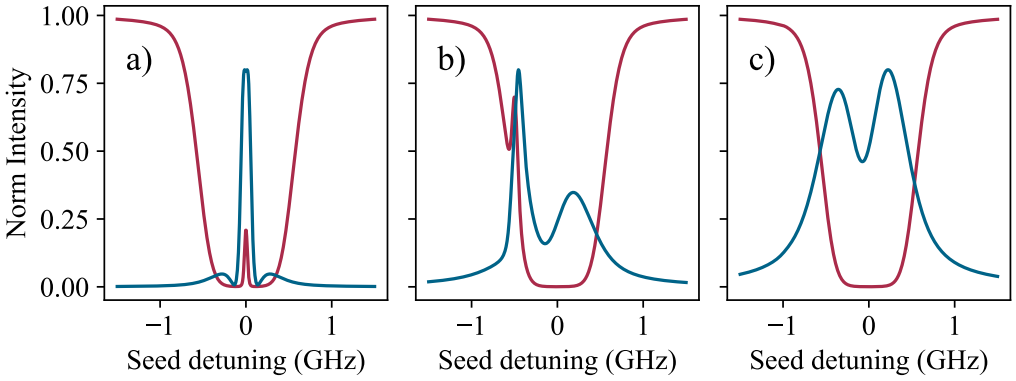

Figure 7.9: Modelled seed transmission (red) and FWM signal (blue) using Rabi frequencies calculated from experimental parameters. In panel a) the intermediate state detuning $\Delta_{01} = 0$, in b) $\Delta_{01} = 500\,\text{MHz}$ and in c) $\Delta_{01} = 1000\,\text{MHz}$. The broad features of b) and c) agree with the data of Fig 7.7, but the expected splitting of the narrow features of a) and b) is not present. Model parameters are: Ω_{pump} =580 MHz, Ω_{coupling} =140 MHz, Ω_{seed} =150 MHz, T =120 °C.

the data of Fig 7.7, but the expected splitting of the narrow features of b) and c) is not present. We have not attempted to fit these spectra to the experimental data. Model parameters are: Ω_{pump} =580 MHz, Ω_{coupling} =140 MHz, Ω_{seed} =150 MHz, T =120 °C.

In order to reproduce our experimental results close to resonance, we find that we need to enter into the model a higher pump Rabi frequency, and a lower seed Rabi frequency. We choose Rabi frequencies of Ω_{pump} =1000 MHz, Ω_{coupling} =140 MHz and Ω_{seed} =10 MHz, with results shown in Fig 7.10. Again, in panel a) the intermediate state detuning $\Delta_{01} = 0$, in b) $\Delta_{01} = 500\,\text{MHz}$ and in c) $\Delta_{01} = 1000\,\text{MHz}$. The narrow split feature in a) now agrees well with with the data of Fig 7.7 panel a), but in panel c) the broad feature has only one peak, rather than the two that we see in the experiment.

It is highly likely that the Rabi frequencies we actually use in the experiment are different to those that we calculate from the beam powers and waists. It is probable that the beams are not completely overlapped inside the cell, which our model does not reflect. The model also does not include the varying power across the beams, which in reality have a Gaussian intensity profile, and could alter the shapes of the signals produced. We also do not include the changing power of the beam as it traverses the cell and is absorbed, which could account for required Rabi frequency differences in the on and off resonance regimes.

We use this model to explain the origin of the broad features we see in the experiment when we detune from the intermediate state, so the probe frequency is

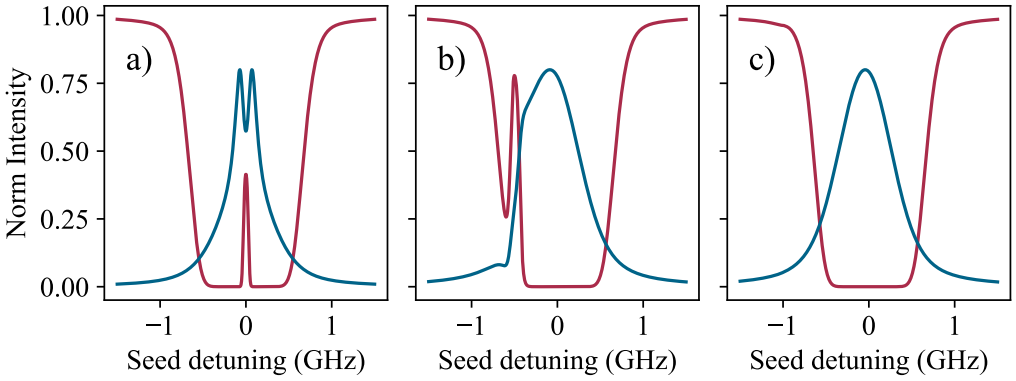

Figure 7.10: Modelled seed transmission (red) and FWM signal (blue) with higher pump Rabi frequency and lower seed Rabi frequency than experimental parameters. In panel a) the intermediate state detuning $\Delta_{01} = 0$, in b) $\Delta_{01} = 500\,\text{MHz}$ and in c) $\Delta_{01} = 1000\,\text{MHz}$. The narrow split feature in a) agrees well with with the data of Fig 7.7 panel a), but in panel c) the broad feature is not split, as we see in the experiment. Model parameters are: Ω_{pump} =1000 MHz, Ω_{coupling} =140 MHz, Ω_{seed} =10 MHz, T =120 °C.

outside of the absorption feature. In Fig 7.11, we plot heatmaps showing how much of the signal is produced by different velocity (v_z) classes of atoms. The top row shows the absorption (red) and FWM (blue) as before. The second row, panels c) and d), show the heatmap of FWM signal produced by atoms of each velocity class. To create this map the strength of the signal produced by each class is weighted by the abundance of atoms at that velocity, which is a Gaussian given by 2.18. The third row, panels e) and f), shows the unweighted signal. As we are using a counter-propagating geometry we see that, as expected, many atomic velocity classes contribute to the FWM signal. This is because, for an atom travelling with velocity v_z, we set $\Delta_{01} \to \Delta_{01} - k_{780}v_z$ and $\Delta_{12} \to \Delta_{12} + k_{776}v_z$. The two photon detuning is therefore $\Delta_{01} + \Delta_{12} + (k_{776} - k_{780})v_z$, and $(k_{776} - k_{780})v_z \approx 0$. The approximation only breaks down for very large v_z. We note that although k is a function of refractive index, n, the refractive index change at typical working temperatures are negligible and has no significant effect on the phase matching condition. Comparing d) and e) we see that when the intermediate state is far detuned from resonance the strongest signal is produced by atoms with a velocity corresponding to that detuning, but as there are very few atoms with this velocity most of the signal we measure is actually produced by atoms with lower velocity. Therefore there is effectively now no velocity selection, which explains the broad features we see.

In panel c), we see two bright spots, with a gap between them in detuning. This gap corresponds to the dip we see in the FWM spectrum in a). We would expect

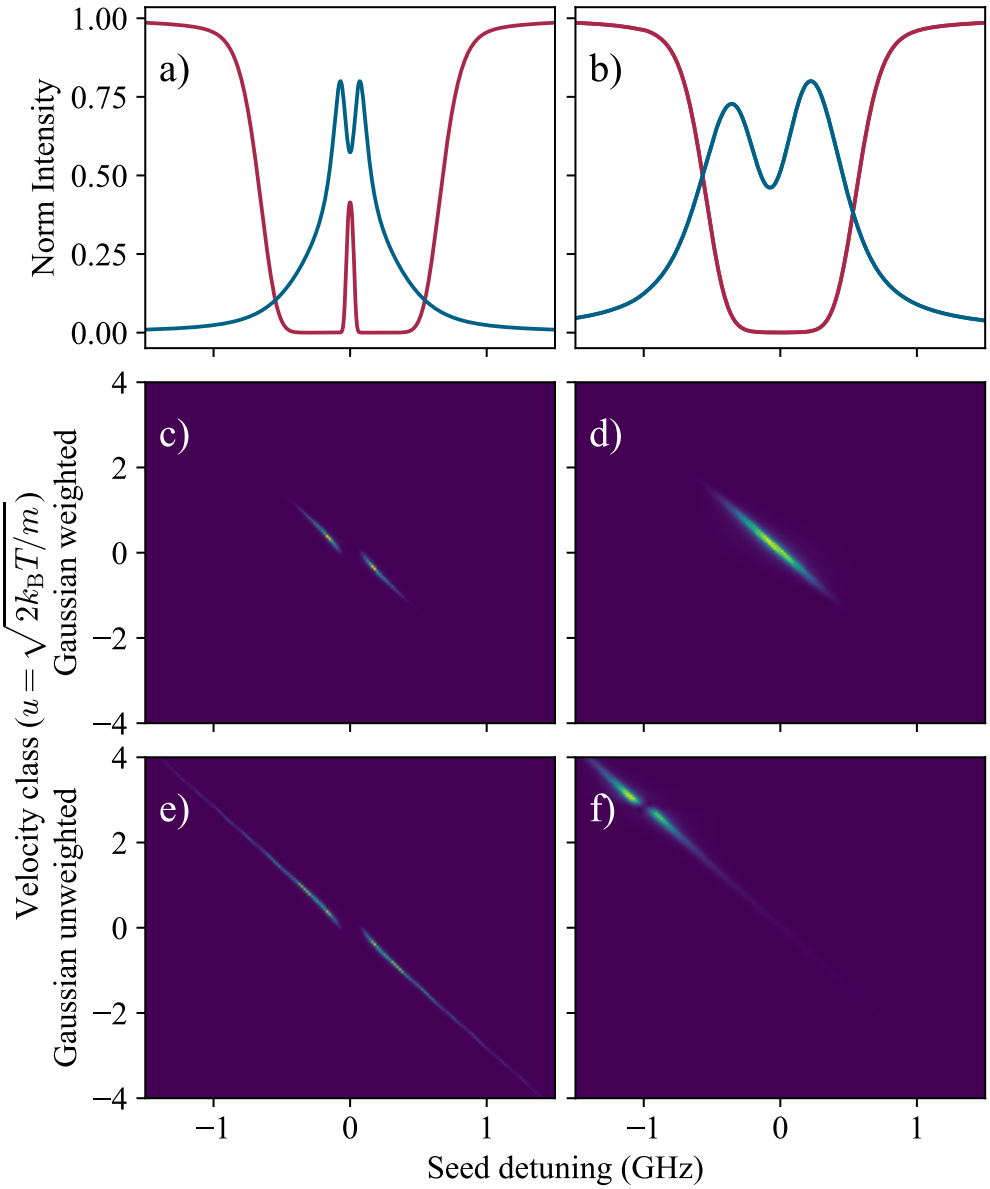

Figure 7.11: Velocity class dependence of FWM. Top panels show seed transmission (red) and FWM signal (blue), for a) $\Delta_{01} = 0$ and b) Δ_{01} =1000 MHz. The middle row shows the corresponding velocity heatmaps for intensity of FWM signal produced. The bottom row again shows velocity heatmaps, but here the signal is not weighted by the atomic velocity distribution, and so shows which velocity classes emit the most FWM signal per atom.

the FWM spectrum to be an integration of the velocity-frequency map over the velocity axis. However we see that this is not the case for the case in panels b) and d); in d) we do not see a dip in the line on the heatmap, and integrating vertically produces a spectrum with only one peak. This difference occurs from the different ways the spectrum and the velocity-resolved heatmap are calculated. For each seed detuning, and each velocity, the Lindblad master equation is solved, to produce a density matrix containing the term ρ_{23}, the coherence between states $|2\rangle$ and $|3\rangle$. This is a complex number. To calculate the FWM signal produced by the whole medium, all the ρ_{23} terms for the different velocity classes are summed, weighted by the atomic velocity distribution, and then the square of the absolute value of the sum is taken, $|\sum_v \rho_{23}|^2$. However, in order to calculate a velocity-resolved heatmap we must take the absolute value of the individual ρ_{23} terms before summing them, as we need a real number to plot. Thus when we sum over velocities after taking the absolute value, we lose information about interferences among the terms. The importance of the order of this calculation and the interference has been noted previously in [52]. Hence we deduce that the dip in panel b) comes from interference between atoms from different velocity groups. This interference means that care must be taken when interpreting the heatmaps, however they can still be useful to see which range of velocity classes are contributing.

We do not attempt to model the zero field system, as that requires including contributions from all the different hyperfine transitions excited simultaneously. A more sophisticated model is described and implemented in [41], however seed scan spectra are not shown.

7.7 Heralded single photon pair generation

7.8 Introduction and Theory

Single photons can be generated using different methods. A very commonly used method is spontaneous parametric down-conversion (SPDC), a process in which a nonlinear crystal converts one high energy photon into a pair of photons with double the wavelength of the original photon, in accordance with the laws of conservation of energy and conservation of momentum. These pairs of photons have correlated polarisations, making them useful for applications in quantum computation and communications [28, 157]. However, SPDC typically has a poor conversion efficiency leading to low photon generation rates [158], and are not naturally matched to atomic frequencies. In this respect a thermal vapour source has a clear advantage. Photon pairs produced in thermal vapour FWM schemes are, by their very

nature, produced at atomic resonance frequencies. For any application also using atomic resonant frequencies, this is a considerable advantage, as a FWM scheme can be chosen to ensure the produced photons are automatically at the required frequency.

It has previously been shown that for several atomic applications, working in the hyperfine Paschen-Back regime produces a clean and easy-to-model system [25, 43, 34]. If further quantum applications, which would require compatible single photons to be input, are to progress in this regime, it would be necessary to have an effective HFPB single photon source. Using the HFPB regime also has the advantage that one can, to an extent limited by the strength of available and practical magnets, arbitrarily tune the transition frequencies around the zero-field resonance by altering the strength of the magnetic field. For example, with our 0.6 T magnetic field we see strong ^{87}Rb D2 excitation peaks in the detuning ranges -17 to -6 GHz and 6 to 17 GHz, as shown in Fig 6.3. This can be seen in the diagrams, and corresponding equations of Section 2.5.1.

7.8.1 What is $g^{(2)}(\tau)$?

The second-order correlation function, $g^{(2)}(\tau)$ is a measure of how correlated photon arrival times are with each other. When looking at correlations between two channels, 1 and 2, the function is expressed mathematically as

$$g^{(2)}_{1,2}(\tau) = \frac{\langle \vec{E}_1^{\dagger}(t+\tau)\vec{E}_1(t+\tau)\vec{E}_2^{\dagger}(t)\vec{E}_2(t)\rangle}{\langle \vec{E}_1^{\dagger}\vec{E}_1\rangle\langle \vec{E}_2^{\dagger}\vec{E}_2\rangle}. \tag{7.8}$$

where $\vec{E}(t)$ is the vector electric field of the relevant channel as a function of time, t. Angle brackets denote an average over statistical fluctuations. This can be described more intuitively in terms of intensities:

$$g^{(2)}_{1,2}(\tau) = \frac{\langle I_1(t+\tau)I_2(t)\rangle}{\langle I_1(t)I_2(t)\rangle}, \tag{7.9}$$

which we can then become number of clicks, n, measured on a photon counter:

$$g^{(2)}_{1,2}(\tau) = \frac{\langle n_1(t+\tau)n_2(t)\rangle}{\langle n_1(t)n_2(t)\rangle}. \tag{7.10}$$

Channels 1 and 2 can be photons from different sources, as will be the case when we look at the correlations between our herald and signal photons, when we will calculate $g^{(2)}_{\mathrm{h,s}}(\tau)$ and expect to see a large peak at $\tau = 0$.

Alternatively channels 1 and 2 can come from the same source, when the light is split on a 50:50 beam-splitter cube. This is called the second-order auto-correlation

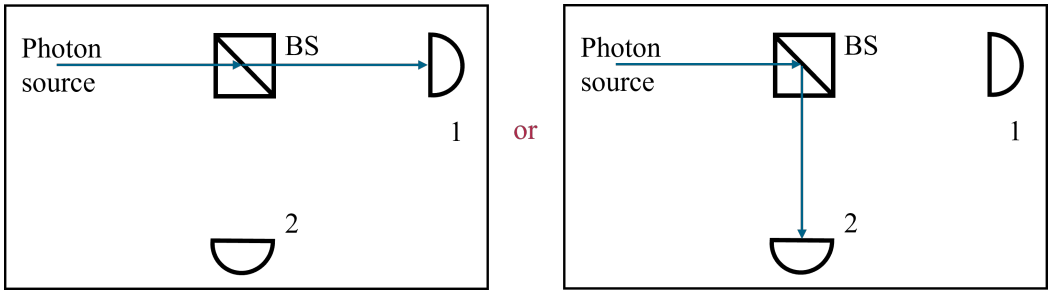

Figure 7.12: Illustration of Hanbury Brown-Twiss experiment. A single photon incident on a beam splitter can either be transmitted or reflected, never both.

function and measures the likelihood of photons arriving (and therefore being produced by the source) with different time gaps between them.

Experimentally this is done by splitting the light from the source in question on a 50:50 beam-splitter cube, and directing the photons from each output port to a single-photon counter, as shown in Fig 7.12. A single photon cannot be split and will travel along either path 1 or path 2, so if the source is producing single photons both detectors will never click at the same time. This is known as a Hanbury Brown-Twiss (HBT) experiment, which was first carried out (with photomultipliers rather than photon-counters) in 1956 [159] and was used to measure the angular size of stars [160]. The difference in arrival times between the photons on counters 1 and 2 are calculated, and these time gaps are histogrammed and normalised to produce a graph like those shown in Fig 7.13. The beam splitter is required because photon-counters have a dead-time, meaning that after one photon has been detected there is a time window in which another cannot be detected. Using only one detector you would see no time gaps shorter than the detector dead-time.

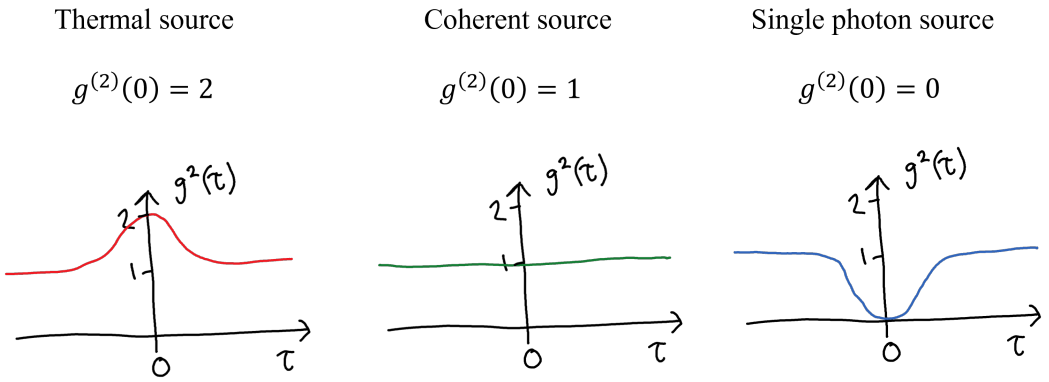

Figure 7.13: Illustration of $g^{(2)}(\tau)$ from different types of source. The left shows and example $g^{(2)}(\tau)$ from a thermal source, such as a light bulb, the middle from a coherent source such as a single mode laser and the left from a single photon source.

The interesting behaviour of the auto-correlation function is around $\tau = 0$, where for a single field mode we can write [161]

$$g^{(2)}(0) = 1 + \frac{\langle(\Delta n)^2\rangle - \langle n\rangle}{\langle n\rangle^2}, \tag{7.11}$$

where $\langle n\rangle$ is the mean photon number and $\langle(\Delta n)^2\rangle$ is the photon number variance. For a perfect single photon source $\langle n\rangle = 1$ and $\langle(\Delta n)^2\rangle = 0$, so $g^{(2)}(0) = 0$.

For a thermal light source, like a light bulb, $g^{(2)}(0) > 1$, meaning that photons are more likely to arrive close together and the light is described as 'bunched'. For a coherent source, like a coherent laser, photons are not more likely to arrive together or apart, so $g^{(2)}(0) = 1$ and the $g^{(2)}(\tau)$ function is flat. From a single photon source, on the other hand, photons are less likely to arrive together, and $g^{(2)}(0) < 1$, with a perfect source having $g^{(2)}(0) = 0$. This is described as 'anti-bunching'. These cases are illustrated in Fig 7.13. This function can be used to determine if the light source is classical, as classical sources have $1 \leq g^{(2)}(0) \leq 2$ [161]. At large values of τ, where $\tau \gg \tau_c$, the coherence time, the function becomes 1.

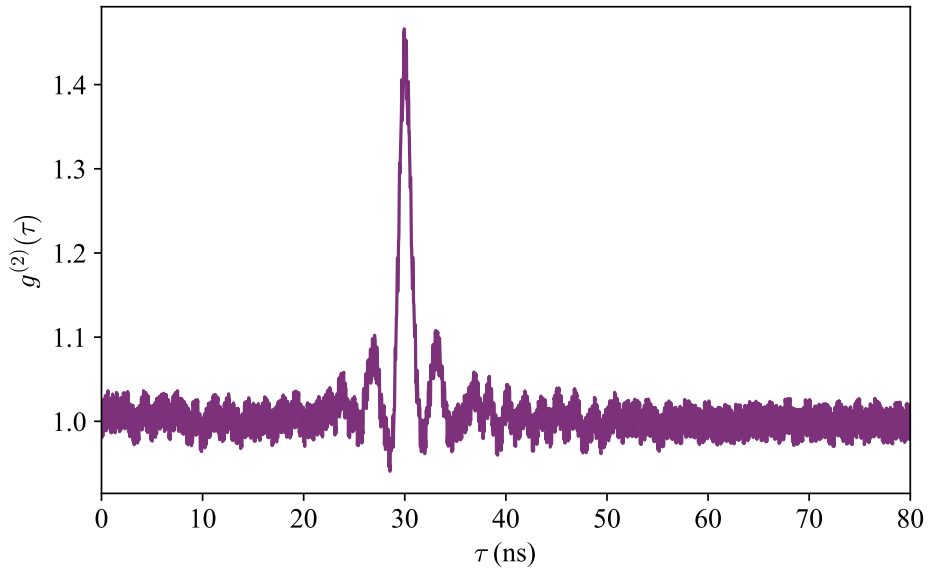

Figure 7.14: $g^2(\tau)$ for 780 nm fluorescence. The trace has a maximum $g^{(2)}(\tau)$ value of 1.5 at a time delay of 31 ns, due a BNC cable delay. Clear ringing is also visible. A moving average of 11 is used for smoothing.

We demonstrate a $g^2(\tau)$ trace from a thermal source by conducting a HBT experiment on D2 line (780 nm) fluorescence from our vapour cell excited with only a resonant 780 nm laser. We see that the trace has a maximum $g^{(2)}(\tau)$ value of 1.5 at a time delay of 31 ns. This value of 1.5 is within the expected range for the

fluorescence a thermal gas of atoms; >1 and <2 [161]. The time delay is due to the BNC cables connecting photon-counter 1, and photon-counter 2 to the counting card having different lengths. We deliberately input this delay to make the data processing easier, because we don't have to calculate for negative values of τ to see the full width of the feature, and to separate out the features when we calculate more than one at once. Time delays can easily be added or removed in later data analysis. Clear ringing is also visible. This is due to beating between the available hyperfine transitions, which are separated by only ∼100 MHz, so multiple transitions are excited in a thermal vapour with Doppler width of ∼600 MHz. The FWHM of the main peak is 1.2 ns. The natural lifetime of the state is well-known to be 27 ns [58], however, as we are working in a thermal vapour we measure a time which is the inverse of the Doppler-broadened linewidth. This measured width suggests a Doppler broadening of $\Gamma_{\text{Dopp}} = \frac{1}{1.2\,\text{ns}} = 800\,\text{MHz}$, which is larger than expected and corresponds to a temperature of 450 °C which is much too high. We also fit a Gaussian to the envelope of the peak including the ringing. This has a FWHM of 4 ns, which corresponds to a frequency linewidth of 250 MHz.

7.9 Using FWM to produce single photons

We make use of the process of spontaneous four-wave mixing to convert our seeded FWM experiment into a single photon source. Fig 7.15 shows energy level diagrams for the two different processes. For simplicity only one state is drawn at each level, however in the zero field case this will not be the case, as shown in Fig 7.2. In spontaneous FWM, pump and coupling beams are used, as in seeded, to excite up to the $5D_{5/2}$ state. However a seed beam is not input, instead the medium spontaneously produces pairs of single photons according to the phase matching condition, which is now

$$\vec{k}_{\text{pump}} + \vec{k}_{\text{coupling}} = \vec{k}_{\text{herald}} + \vec{k}_{\text{signal}}. \tag{7.12}$$

We use the alignment of the seeded setup to collect these correlated pairs. In doing so we select the spatial modes of one particular pair, however this is far from unique and any angular configuration that can produce seeded FWM would produce spontaneous pairs. This fact was used in [38] where two sets of photon pairs were collected, from opposite sides of the optical axis to produce a multiplexed single photon source.

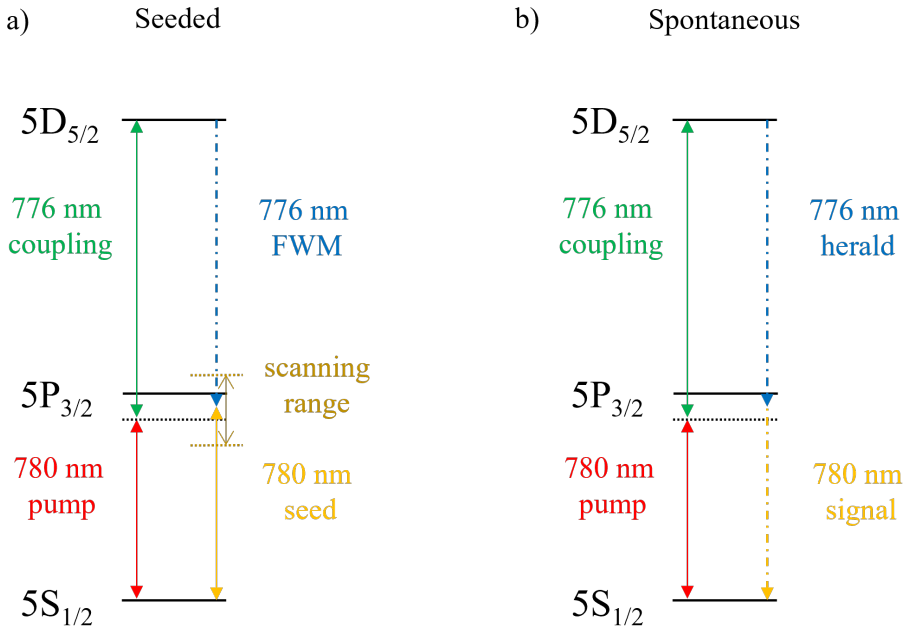

Figure 7.15: Energy level diagram showing the transition between seeded and spontaneous schemes. In a), a seed beam is input and scanned over the intermediate state resonance. To convert to spontaneous the seed beam is removed and a pair of photons are spontaneously emitted at 776 nm and 780 nm in the direction of the seed beam and the produced FWM beam respectively. For simplicity only one state is drawn at each level, however in the zero field case this will not be the case, as shown in Fig 7.2.

7.10 Experimental setup

The experimental setup for single photon production differs in two main ways from that described in Section 7.3. They are:

- We now collect our photon pairs into single mode optical fibres connected to single photon counters. These two fibres are aligned using the seeded FWM setup; one is aligned to maximise coupling of the seed laser beam that has passed through the cell, and the other, in exactly the opposite direction, is aligned to maximally couple the produced seeded FWM beam.
- The seed beam is turned off. Now these fibres collect single photon pairs produced by the medium (as well as other uncorrelated fluorescence, scattered laser light and any other background).

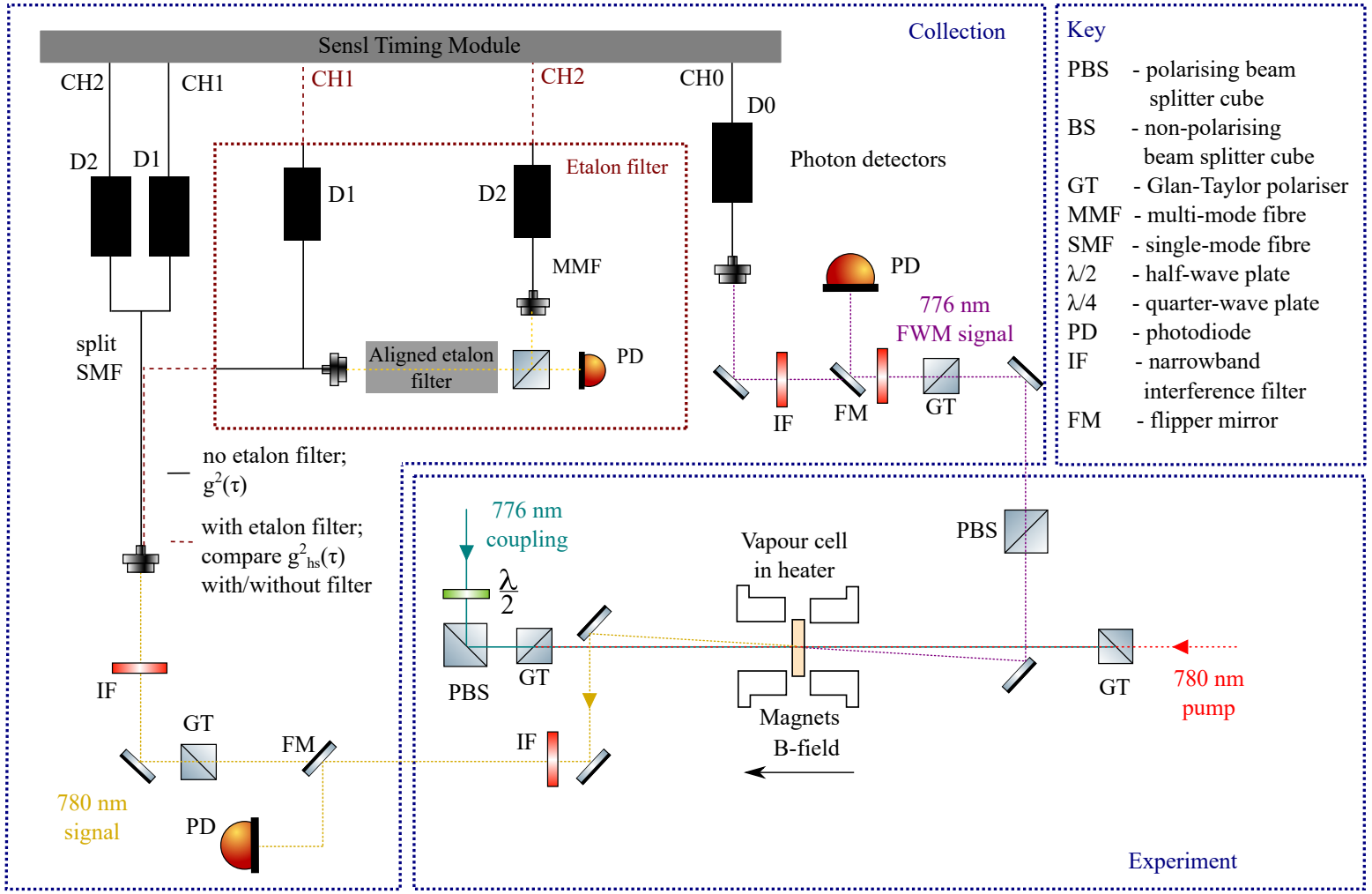

Figure 7.16: Experimental setup for single photon generation. The 'Experiment' section of the setup is the same as in the seeded case in Fig 7.3, with the seed beam removed. The 776 nm spontaneous FWM photons are collected on a photon detector (D1). The correlated 780 nm are collected out of the other end of the vapour cell into a fibre aligned to the seed beam path. In both cases IFs and GT polarisers are used for filtering. Both flipper mirrors are folded down during data taking. During heralded auto-correlation experiments the 780 nm photons are coupled into a split fibre, with each output incident on a photon detector (D1 and D2). All 3 detectors are connected via BNC cables to the photon counting module. When we use the etalon filter and compare $g^{(2)}_{\mathrm{hs}}(\tau)$max with and without it, one arm of the split fibre outputs to the aligned etalon filter module (brown box), before reaching the second detector.

7.11 Counting mechanics

We use single photon avalanche detectors (SPADs) (Excelitas SPCM-AQRH-14-FC) to detect our single photons. They detect a photon arrival, and output voltage pulse through a BNC cable to the counting card. We use a Sensl card (High Resolution Timing Module, HRMTime TDC). It has four channels, and collects data separately on each. We operate the Sensl card in 'continuous running' mode. Each data collection run is started with a signal to the 'start' input of each channel—we connect these together to produce a common time. The output of each photon counter is connected to a stop port of one of the counting card channels. After the 'start', the card records the time of each 'stop' it receives, and stores all these times, along with which channel the photon was detected on. The card then collects data for 1 second, (or less if it receives more counts than it can store), after which the time data is processed in python by the connected computer.

We process the data using python. The raw data is a 2-d array, with one column filled with photon arrival times, and the other column with the index of the channel that photon was detected on. To calculate $g^{(2)}_{\mathrm{hs}}(\tau)$ we use the data from CH0, the herald channel, and either CH1 or CH2, which are both from the split signal channel. Array-wise, we calculate the time gaps between the detection of a photon on CH0 and a photon on CH1. One could calculate all of these time gaps which occur in the one second of data collection, however that would be computationally expensive. Instead we truncate the calculation and look only at the time gaps between photons which arrived with no more than 2 other photons in between. During our experiment we have maximum photon detection rates of $\sim$1 MHz, and therefore a minimum average time gap of $\sim$1 µs, and we only plot correlations to 100 ns. If we were truncating too soon we would expect to see a drop (from 1) in the background level of the cross-correlation, which we do not. In practice increasing the number of time gaps calculated does not alter the results, but does increase the processing time.

We display the $g^{(2)}_{\mathrm{hs}}(\tau)$ results by plotting a histogram of the time gaps. The data processing code displays this histogram live, updating every second to include the previous second's data, so the experiment can be easily monitored. The histogram is normalised using [162]

$$g^{(2)}_{\mathrm{hs}}(\tau) = \frac{G^{(2)}_{\mathrm{hs}}(\tau)}{r_{\mathrm{h}} r_{\mathrm{s}} \Delta\tau T}, \tag{7.13}$$

where $G^{(2)}_{\mathrm{hs}}(\tau)$ is the measured histogram, r_{h} and r_{s} are the count rates on the herald and signal channels respectively, $\Delta\tau$ is the width of each time bin and T is the total integration time. The histogram can also be normalised using the

knowledge that for large values of τ, $g^{(2)}_{\mathrm{hs}}(\tau) = 1$, and normalising to a part of the histogram without a correlation feature. In practise these methods give the same result, which is reassuring.

We can interpret $g^{(2)}_{\mathrm{hs}}(\tau)$ to mean how many times more likely it is that a photon we detect on the signal channel at time τ is part of a heralded pair, rather than just noise. More generally $g^{(2)}_{ij}$ can be expressed in terms of the probabilities of a coincidence between clicks on detectors i and j, P_{ij} and the independent probabilities, P_i and P_j.

$$g^{(2)}_{ij} = \frac{P_{ij}}{P_i P_j} \tag{7.14}$$

Another useful measure of the effectiveness of a paired single photon source, is photon pair rate. This is the rate at which we detect herald-signal pairs. We calculate this parameter alongside the histogram, by calculating the area under the peak (un-normalised), not including the background. This is expressed mathematically as

$$\text{Pair rate} = \frac{1}{T}\left(\sum_{\tau=t_0}^{t_1} G^{(2)}_{\mathrm{hs}}(\tau)\right) - r_{\mathrm{h}} r_{\mathrm{s}}(t_1 - t_0), \tag{7.15}$$

where T is the total integration time and t_0 and t_1 are the start and end of the coincidence window. We can also calculate the heralding rate, that is what fraction of photons on our herald channel are part of a correlated pair using

$$\text{Heralding efficiency} = \frac{\text{Pair rate}}{r_{\mathrm{h}}}. \tag{7.16}$$

This can be calculated for each signal channel separately, or using both combined depending on the context.

7.12 Zero field results

Fig 7.17 shows an example of the $g^{(2)}_{\mathrm{hs}}(\tau)$ signals produced by our system. The red and blue peaks are collected using the 'without etalon' part of the setup shown in Fig 7.16. The red trace shows correlations between CH0 and CH1, and the blue trace shows correlations between CH0 and CH2. CH1 and CH2 are the two output ports of the same signal, split by a split fibre. The time delays–37 µs and 6 µs respectively–are due to different lengths of BNC cable connecting the photon detectors and the counting module, and are not a property of the signals we are measuring. In this case $g^{(2)}_{\mathrm{hs}}\mathrm{max} = (88 \pm 7)$, and the pair rate on each channel was 2.6 Hz. This is comparable to the figures reported in [37]. A $g^{(2)}_{\mathrm{hs}}\mathrm{max}$ of 88 tells us that if we detect a photon on the signal channel at our set time gap

after detecting a photon on the herald channel it is 88 times more likely that that photon is a correlated photon than a noise photon. The peaks have a FWHM of (0.87 ± 0.02) ns.

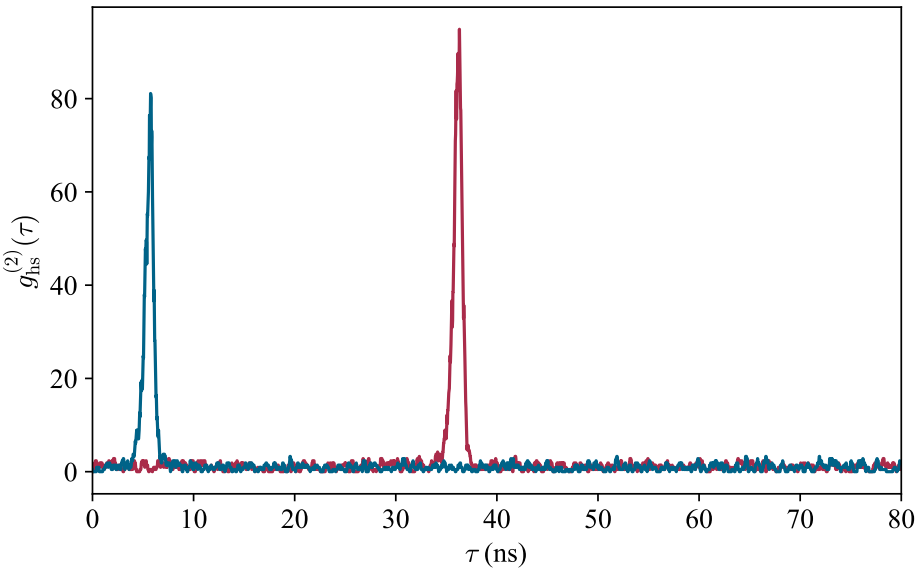

Figure 7.17: Zero field $g^{(2)}_{\mathrm{hs}}$ correlations. The blue and red traces are from each arm of the split fibre, and so are expected to be the same. The data are smoothed by calculating a 5 point moving average. In this case we observe a maximum $g^{(2)}_{\mathrm{hs}}$ of 88 ± 7. Fixed parameters: one-photon detuning $= -3$ GHz, pump power $= 100\,\mu$W, coupling power $= 10$ mW, $T = 125\,^{\circ}$C.

There are many factors which affect the strength of these correlations, some of which are in our control, and some which are not. In the following section we will investigate the dependence of $g^{(2)}_{\mathrm{hs}}(\tau)$ peak height on pump and coupling powers, and temperature.

7.12.1 Dependence on experimental parameters

7.12.1.1 780 nm pump power

Fig 7.18 shows the effect of changing the pump power on $g^{(2)}_{\mathrm{hs}}$max (red) and correlated photon pair rate (blue). Pair rate dependence is quite straightforward; the pair rate increases approximately linearly with increasing pump power. A straight line is fitted and plotted, and has a gradient of $75\,\mathrm{Hz\,mW^{-1}}$. The $g^{(2)}_{\mathrm{hs}}$max dependence is more complicated. At high powers (>5 mW) $g^{(2)}_{\mathrm{hs}}$max is low (in this case <5). As pump power is decreased $g^{(2)}_{\mathrm{hs}}$max increases at an increasing rate. This

increase continues up to around 100 µW, below which $g^{(2)}_{hs}$max falls off sharply. It is expected that $g^{(2)}_{hs}$max increases as pump power decreases. This is because lower pump powers mean there is less population in the intermediate 5P state and consequently fewer uncorrelated 780 nm photons. Correlated photons can only be produced when the atoms have been excited up to the 5D state, so any excitations to the 5P state which are not further excited will become a noise source. It is therefore necessary to make the pump beam significantly weaker than the coupling beam. Below a certain power, which in this parameter space is 100 µW, correlated photon rates become so low that other noise (laser scatter from the coupling laser, and permanent background counts) begin to dominate, and $g^{(2)}_{hs}$max decreases.

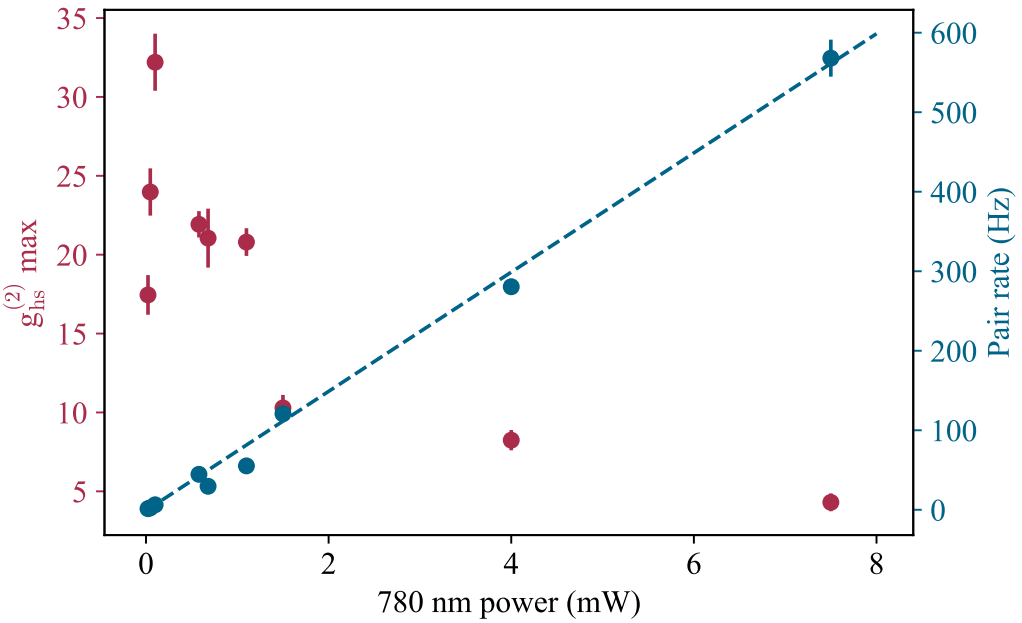

Figure 7.18: The effect of changing 780 nm pump power on $g^{(2)}_{hs}$max and correlated photon pair rate. All other parameters are constant with: coupling power = 20 mW; T = 129 °C; 5P detuning = −2.5 GHz.

7.12.1.2 776 nm coupling power

Fig 7.19 shows the effect of changing coupling (776 nm) power on pair rate and $g^{(2)}_{hs}$max. Again we see a clear linear relationship between power and pair rate, this time with a gradient of 1.5 Hz mW^{-1}. We also see a similar shaped relationship for $g^{(2)}_{hs}$max; there is a sharp increase as power increases from 0, up to a peak, this time at ∼7 mW, and then a slower decay as coupling power is further increased. At higher coupling powers $g^{(2)}_{hs}$max decreases with increasing coupling powers because

although pair rates increase linearly, noise rates increase faster. From the 5D state the atoms may emit correlated photon pairs, however they may also decay in a two-step process, first emitting a 776 nm photon to arrive in the 5P state, and then some time later emitting a 780 nm photon to decay to the ground state. Both of these emitted photons contribute to our experiment as noise, and reduce the 'purity' of our single photons.

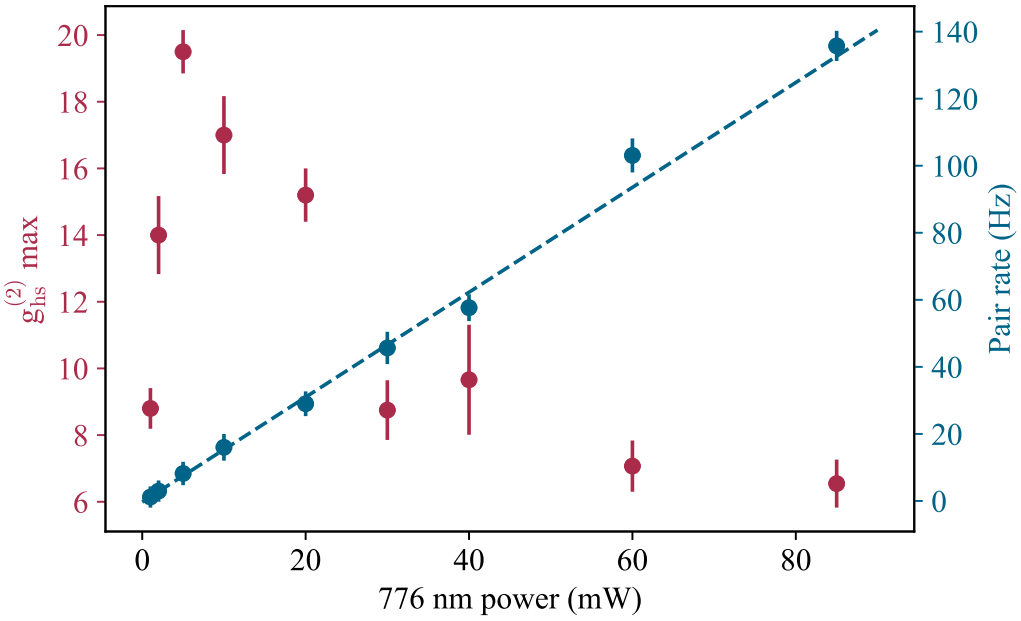

Figure 7.19: The effect of changing 776 nm pump power on $g^{(2)}_{hs}$max and correlated photon pair rate. All other parameters are constant with: pump power = 0.67 mW; T = 129 °C; 5P detuning = −2.5 GHz

7.12.1.3 Dependence on temperature

Cell temperature affects atomic number density in the cell, as discussed in Section 2.4. In Fig 7.20 we plot the effect of changing vapour cell temperature on $g^{(2)}_{hs}$max (red) and pair rate (blue). As the temperature increases, pair rate increases. $g^{(2)}_{hs}$max also increases with pair rate initially, but reaches a maximum at ∼125 °C. Notably, this is a much higher turning point than was observed in the diamond scheme in [44], where the $g^{(2)}_{hs}$max occurred at 85 °C. It is possible that this difference is because we are no longer in a system where many of our noise photons appear as a result of the collisional transfer process discussed in Chapter 6. The rate of this process becomes second order, and therefore increases much more rapidly, at around 85 °C. It is likely instead that we see the turning point at a

temperature where the medium is optically thick. This higher turning point is a significant advantage as it means the source can be operated in a regime where pair rates are faster.

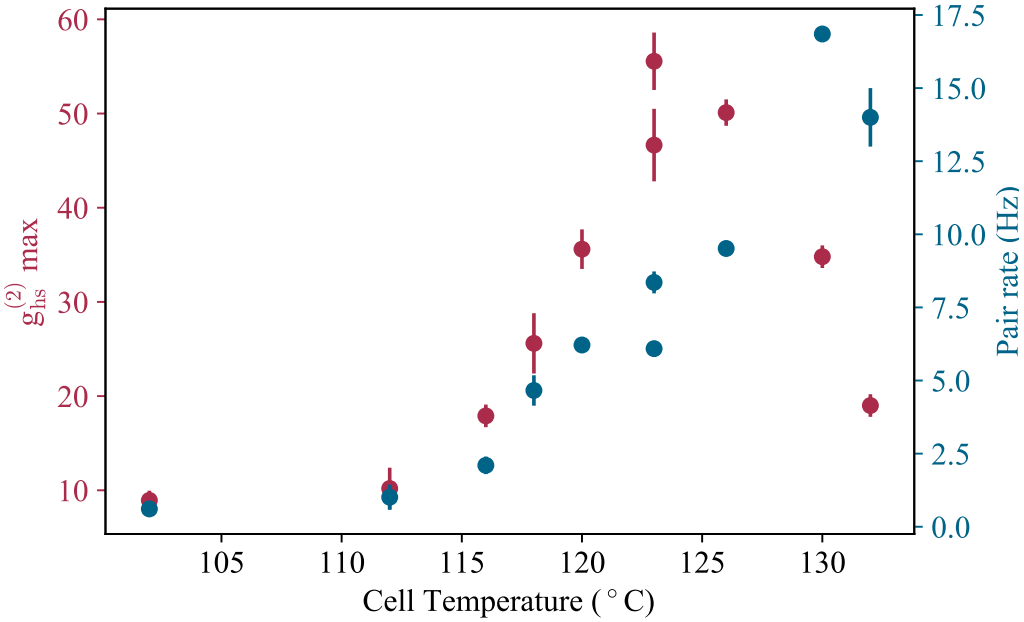

Figure 7.20: The effect of changing cell temperature on $g^{(2)}_{hs}$max and correlated photon pair rate. The temperature was measured with a thermocouple inside the cell heater, and corrected using ElecSus. All other parameters are constant with: pump power = 0.8 mW; coupling power = 37 mW; 5P detuning = −2.5 GHz.

7.12.2 Including etalon filters

We are using a double ladder energy level scheme, so have two pairs of transitions which have the same wavelength. This means that we cannot use interference filters (which have a transmission FWHM of ∼3 nm) to remove the excitation light, or fluorescence from uncorrelated decays, which are at the same frequency as our signal photons.

However, if the signal photons are emitted at a different frequency from our unwanted photons by GHz, or have a different spectral profile (are much broader or narrower in frequency), then we may be able gain an advantage by using a narrower, tunable filter, such as those described in Chapter 5. Our investigations in Section 7.4 suggest that this might be the case. It appears that in the absence of a magnetic field, the FWM signal emitted is broad and off resonance when the excitation lasers are detuned from resonance with the 5P intermediate level. Un-

correlated decays are expected to be emitted on resonance, if their motion has randomised, or at the opposite detuning (the other side of resonance to the excitation frequency) if thier motion has not. This is because we observe each wavelength in the opposite direction from which we excited it.

We therefore include the etalon filter module in our setup, as shown in the brown box in Fig 7.16. The 780 nm signal photons are still coupled into a split single-mode fibre. One arm of this fibre goes straight to a photon detector, as before, while the other is connected to the etalon module. This light passes through the aligned etalon filter, which is temperature stabilised, and the transmission frequency can be tuned by adjusting the temperature. The output of the filter is coupled into a multi-mode fibre which is connected to another photon detector. The $g^{(2)}_{\mathrm{hs}}(\tau)$ peaks plotted in the next sections show direct comparisons between the filtered and unfiltered correlations.

7.12.2.1 130 MHz filters

We first used the widest of our lens etalon filters (130 MHz) on one arm of the herald (776 nm) split fibre. In this experiment we were using the 780 nm photons as the herald, and the 776 nm photons as the signal. This was due to the setup at the time and not for any particular scientific reason. If the pair of photons is actually emitted simultaneously, the order of detection will not make a difference to the measured correlation peak. If there is some delay and the herald is emitted first, with some range of time gaps so the peak is asymmetric (like observed in [36] as quantum beats) the shape of the peak will be reversed in time. This reversal will not apply to shape changes from processes that occur after the photons have been produced, such as passing through the etalon filter.

We found that the etalon could be positioned at a frequency such that a higher $g^{(2)}_{\mathrm{hs}}$max was obtained than without the etalon, however we saw a drop of factor $\sim$100 in correlated photon pair rates. An example of one of these cases is shown in Fig 7.21. Here the noisier blue trace shows the correlation between herald (780 nm) and signal (776 nm) photons, when the signal photon has passed through the etalon. The red trace shows the correlation when the signal photon does not pass through the etalon.

We see that sending photons through the etalon affects the time at which the correlation peak occurs, as well as its shape. The peak becomes broader and asymmetric, with a slower decay on the larger τ edge. The delay occurs because the signal photons on this path travel further, both through the extra optical elements involved in the etalon path, but also through the etalon itself. This path

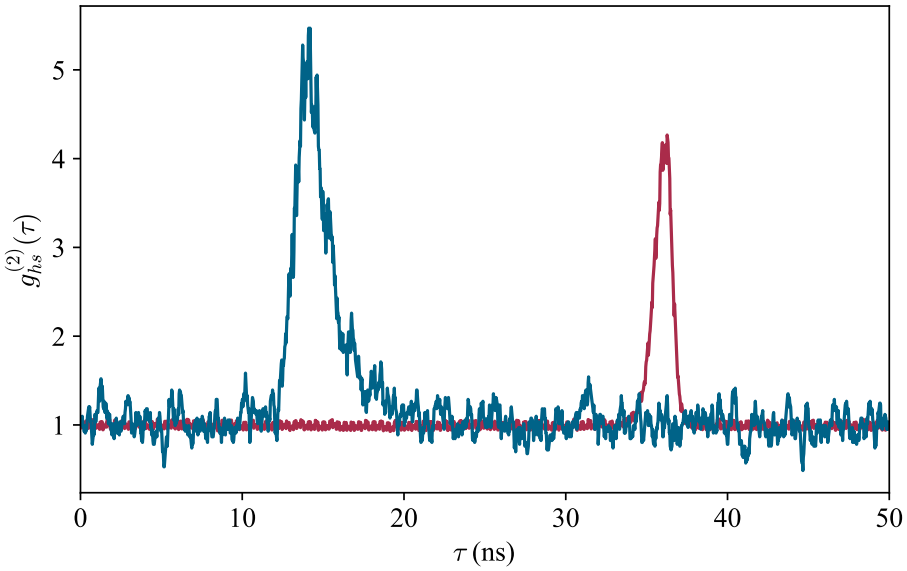

Figure 7.21: Photon pair correlations, comparing 130MHz etalon filter (blue trace) to no filter (red trace). Fixed parameters: one-photon detuning = −3 GHz, pump power = 200 µW, coupling power = 20 mW, T = 125 °C

introduces 1m of extra fibre, with refractive index $n = 1.5$, producing a delay of 5 ns, and 78 cm of free space propagation, which has a delay of 2.6 ns. We observe the peak to be delayed by 8.7 ns (compared to Fig 7.17), implying that the cavity itself introduces a delay of 1.1 ns, and is a small part of the total shift.

We model the effect of the etalon on the correlation feature by convolving the without-etalon feature (close to a Gaussian) with a geometrical decay, which represents the 2% round trip loss from the cavity. The result of this convolution is shown in blue in Fig 7.22, where the red trace is the pre-convolution Gaussian. The model predicts a peak delay of 0.5 ns. The model also explains the broadening, by a factor of 2, and the shape change of the peak observed in Fig 7.21.

We fit the model to the data, allowing the round-trip-loss to vary, and get a best fit which is plotted in black in Fig 7.23. We also plot the gaussian fit, and we see by eye that the decay provides a better fit. The RMS error of the decay fit is 0.23, compared to 0.28 for the gaussian fit. Both these numbers are relatively large due to the high level of noise on the data. The optimal fit occurs when the round trip loss = (0.024 ± 0.001), giving a coating reflectivity of (98.8 ± 0.1) %. This is in agreement with the coating specification, which was quoted as 99%, and the reflectivity we measured in Chapter 5 of (98.9 ± 0.1) %.

Fig 7.4 showed us that when the pump beam is detuned from resonance by more

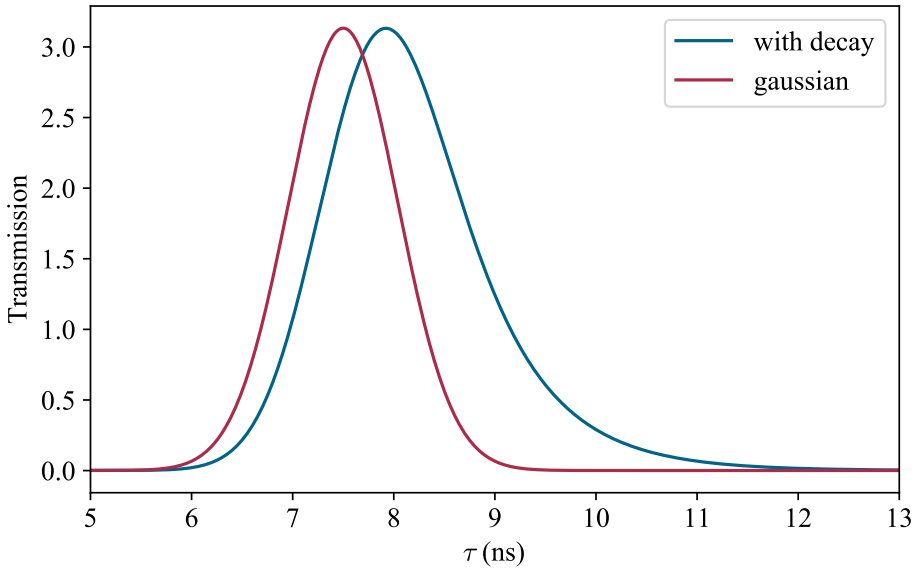

Figure 7.22: The modelled effect of a Gaussian pulse in time (red) passing through the 130 MHz filter cavity. A geometric decay model is used, and the cavity is taken to have length 2.5 mm and reflectivity 98.7%. The model predicts a peak delay of 0.5 ns and shape change introducing an asymmetry and broadening.

than the transition linewidth, a seeded 776 beam is produced for an off resonant range of of 780 seed frequencies several GHz wide. We deduce that this width is mirrored in the 776 light produced, so that the combined energy of the each photon pair equals the two photon transition energy. This is likely to explain why we see such a dramatic fall in pair rate when we use a $\sim$100 MHz filter; we are throwing away the vast majority of our correlated photons. However we are also throwing away an even higher fraction of uncorrelated and scattered photons, so the correlation peak increases in height. We find that the 'through etalon' peak height is more consistent because we no longer rely on the polarisation filtering, so the constant small polarisation fluctuations no longer have such a deleterious effect.

We have found that although we can use these narrow frequency transmission filters to make small improvements to the measured $g^{(2)}_{\mathrm{hs}}$max of our source, the huge drop off in pair rate makes it inviable on a sensible timescale. However, we could potentially reduce the pair rate loss by using a filter with a wider transmission window, comparable to that of the width of the FWM signal. We therefore move to using a similar filter with a 2 GHz linewidth.

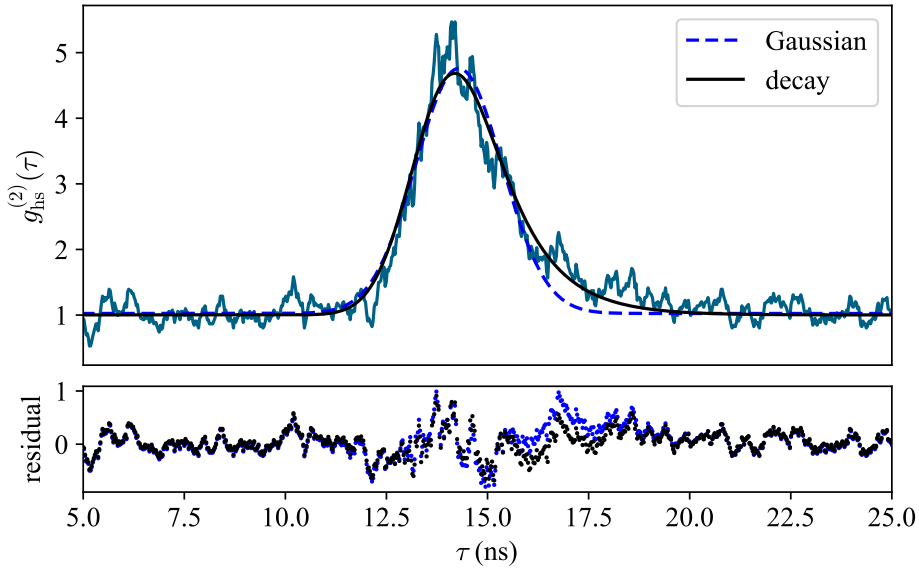

Figure 7.23: Fit of a Gaussian (blue) and a geometrical decay model (black) to 130 MHz filtered $g^{(2)}_{\mathrm{hs}}(\tau)$ correlations. Residuals are plotted. It can be seen that the decay model gives a better fit, with RMS error of 0.23, compared to 0.28 for the Gaussian. Both are relatively high because the data is noisy.

7.12.2.2 2 GHz filters

We introduce the 2 GHz filters described in Section 5.2.2 to the setup on the 780 nm signal channel. To do this we now use the 776 nm photon as the herald and the 780 nm as the signal, with the split fibre coupling the signal photons. We choose to switch the etalon filter to the 780 nm channel because most of the noise is only present when both excitation lasers are on. This means the noise is not laser scatter (which has a similar frequency to desired photons) but fluorescence decays from the 5D state, via $5P_{3/2}$. Therefore its frequency should be clearly distinguishable from most of the desired photons using a 2 GHz narrow-band filter, as we expect it to be detuned the other side of resonance. As our 776 nm coupling beam has a much higher power than the 780 pump beam, the majority of the noise on the 776 nm arm comes from laser scatter, which is in the middle of the frequency spectrum of the desired photons, so we anticipate that adding the filter to this arm will produce less of an improvement.

Another reason to switch filter channels is that it is more difficult to measure the frequency of the transmission window of the etalon filter when the etalon is on the 776 nm collection arm. This is because this is an excited state transition making frequency determination via spectroscopy more complicated. We also only have one 776 nm laser which we wish to keep locked, whereas we have a second 780 nm (seed)

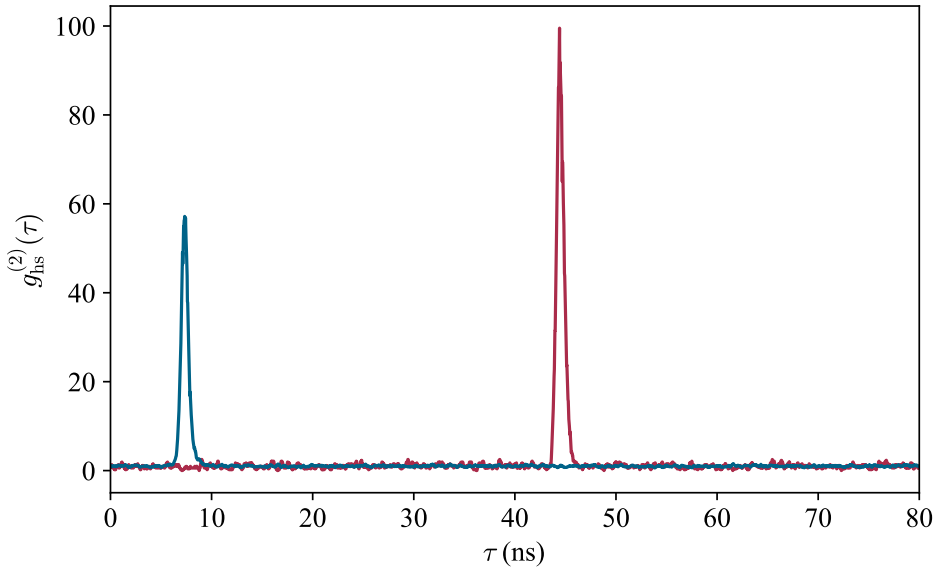

Figure 7.24: $g^{(2)}_{\mathrm{hs}}$ showing the effect of including a 2 GHz etalon filter on the 780 nm signal channel. The blue peak show the correlations without the filter, the red peak shows the correlations with the filter. Without the filter, $g^{(2)}_{\mathrm{hs}}\mathrm{max} = 57$, pair rate = 2.8 Hz, with the filter $g^{(2)}_{\mathrm{hs}}\mathrm{max} = 98$, pair rate = 0.5 Hz. Other parameters: T =127 °C; 780 nm power = 0.7 mW; 776 nm power = 10 mW.

laser which is we can freely scan to determine the etalon transmission frequency, without disrupting our two-photon lock.

We see a consistent improvement in $g^{(2)}_{\mathrm{hs}}\mathrm{max}$ when the 2 GHz filter is in place. One example is shown in Fig 7.24, where the correlations through the etalon are shown in red, while the correlations without the etalon are shown in blue. Without the filter, $g^{(2)}_{\mathrm{hs}}\mathrm{max} = 57$ and pair rate = 2.8 Hz, while with the filter $g^{(2)}_{\mathrm{hs}}\mathrm{max} = 98$ and pair rate = 0.5 Hz. For the data set shown in this figure, other parameters are: T =127 °C; 780 nm power = 0.7 mW; 776 nm power = 10 mW.

We measure the FWHM of the peaks to be (0.80 ± 0.01) ns and (0.86 ± 0.01) ns without and with the etalon respectively. This is a much smaller width increase than we saw with the 130 MHz filter, because, with a reflectivity of 94% the geometric decay is much quicker so the shape of the peak is barely changed.

The time delay introduced by the 2 GHz filter is 6.5 ns. As with the 130 MHz filter, extra fibre length accounts for 5 ns of this and a free-space optical path of 33 cm another 1.1 ns. Our geometric decay model, shown in Fig 7.25, predicts a time delay from the etalon of 0.2 ns, and that the shape is negligibly modified.

The benefit we have seen from the inclusion of one 2 GHz etalon filter suggests that

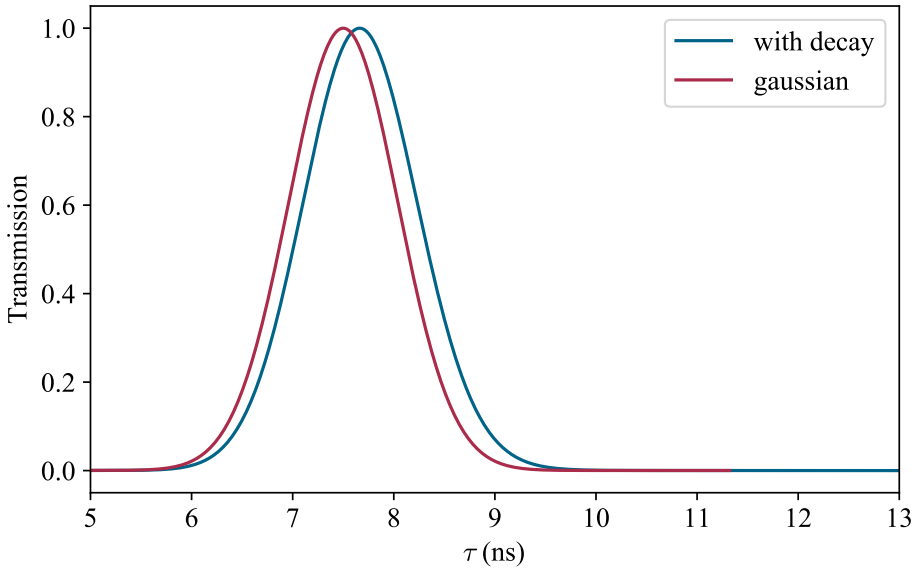

Figure 7.25: Decay model (blue) compared to Gaussian (red) for 2 GHz etalon filter correlations. The decay model introduces a time delay of 0.2 ns and has a negligible impact on the shape of the peak.

adding a second, on the herald arm, could improve the purity of the correlations further. As the pair of filters would be required to select pairs of photons, care would have to be taken to ensure that the filters are 'frequency matched', that is that they are tuned such that the sum of their transition frequencies is the frequency of the two photon transition. This should be achievable using the 2 GHz filters; each filter is stable to $\sim$50 MHz over 24 hours, so even a combined drift of $\sim$100 MHz would only be 10% of the filter linewidth, which should not have too detrimental an effect. It would, however, be near impossible with the 130MHz filters in the current state of temperature control, even if the results with one filter were good enough to warrant trying.

The benefit of including the filter is not constant with changing experimental parameters; as it is filtering 780 nm photons we expect there to be a dependence on 780 nm pump power. If we can effectively filter out a high proportion of the uncorrelated decays, then we should see more benefit at higher pump powers, as we can increase the number of photons we want, whilst not increasing (by so much) the photons we don't want.

Fig 7.26 shows how the ratio of $g^{(2)}_{\mathrm{hs}}$max peak height 'with etalon':'without etalon', varies with input pump power, for the 2 GHz etalon. We see that at high 780 nm powers (>5mW) the ratio reaches 2.75 and plateaus. As the power decreases the ratio decreases, however the individual $g^{(2)}_{\mathrm{hs}}$max values both increase. Below 1 mW

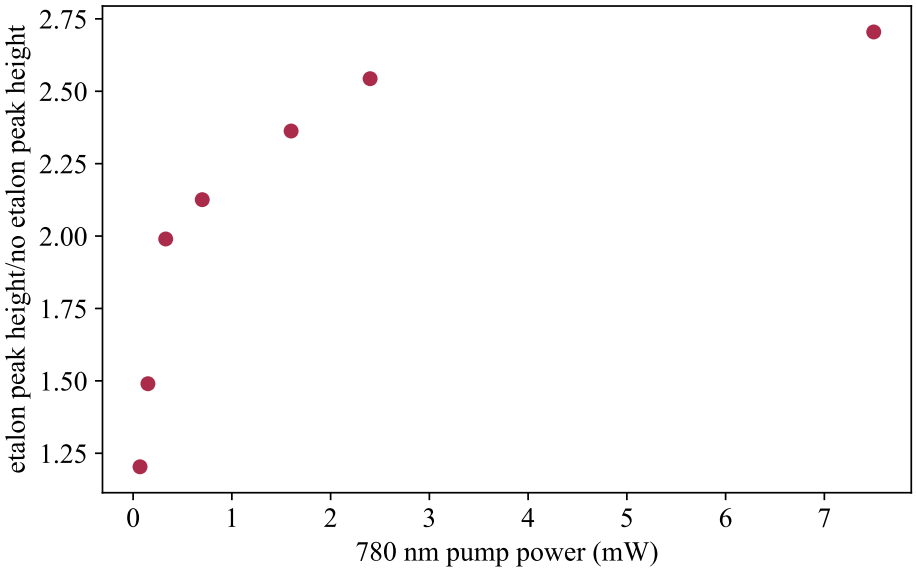

Figure 7.26: Change in ratio of $g^{(2)}_{\mathrm{hs}}$max with-etalon to $g^{(2)}_{\mathrm{hs}}$max without-etalon as 780 nm pump power is varied, for 2 GHz etalon. Fixed parameters are: $T = 132\,°\mathrm{C}$, 776 nm power = 38 mW, one-photon detuning = -2.5 GHz. 780 pump powers range from 70 µW to 7.5 mW

the ratio drops off sharply, and in this regime there is little benefit in using the etalon. At the lowest power plotted, 70 µW, the through etalon pair rate has dropped to 0.35 Hz (without-etalon is 1.6 Hz), with a channel 1 count rate of only 1.1 kHz. The background count of this channel is 0.7 kHz, so more than half of the counts registered are now noise, and this gets more and more significant as the power is decreased, resulting in a lowered $g^{(2)}_{\mathrm{hs}}$max.

We also measure the effect of changing 776 nm on the ratio, and see no significant effect. This indicates that increasing coupling power increases the number of unwanted 776 nm photons more rapidly than the number of unwanted 780 nm photons.

7.13 Hyperfine Paschen-Back regime results

We transfer to the hyperfine Paschen-Back regime setup by placing the magnets around the experiment and locking cells, and tuning the lasers frequencies to those of the 0.6 T field transitions. We must also consider the polarisations required to excited these transitions in the presence of a magnetic field.

Fig 7.27 shows the polarisations of light (left- or right-handed circularly polarised

or linearly polarised) which excite or produced as fluorescence by σ_+, σ_- or π transitions in the presence of a magnetic field, with respect to the orientation of that field. We see that in a magnetic field, when the k-vector of the light is parallel to B, transitions are excited by circularly polarised light. If we set the input laser light to maximally excite the transition (by making it circularly polarised) then the desired correlated signal photons and scattered photons from the laser will have the same polarisation and be indistinguishable through polarisation filtering. There are a few possible methods to get around this, but all have associated losses.

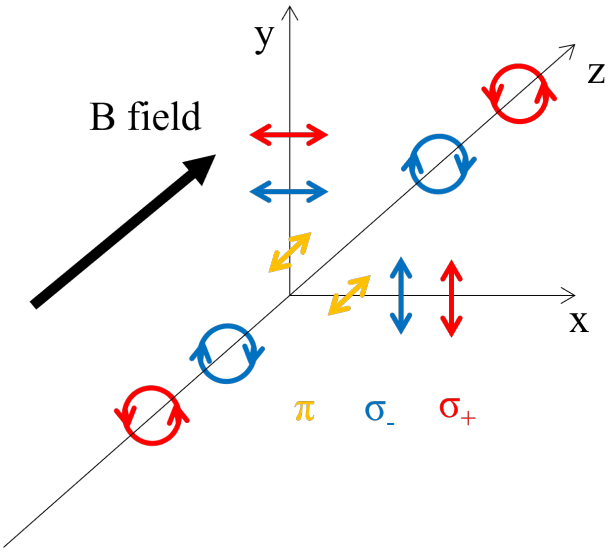

Figure 7.27: Diagram showing the polarisations of light (left- or right-handed circularly polarised or linearly polarised) which can excite or be fluoresced during σ_+, σ_- or π transitions in the presence of a magnetic field, with respect to the orientation of that field.

One option is to input linear light, with the two beams orthogonally polarised, as in the no magnet case. This method allows for effective filtering of the scattered laser light, while still allowing some of the signal light through. However we then lose half the photons on each photon collection channel. We would expect this to reduce $g^{(2)}_{\mathrm{hs}}(\tau)$max by a factor of approximately 4. Our system is not input power limited, as shown in Section 7.12.1, so effectively halving the interaction power of our input beams (only half the linear polarised light excites a σ_+ transition) is not a problem.

This is the method that has given us the best $g^{(2)}_{\mathrm{hs}}(\tau)$ correlations, an example of which are shown in Fig 7.28. However, we only see a $g^{(2)}_{\mathrm{hs}}(\tau)$max of 8, with pair rates of 5 Hz. We believe that herald-signal correlations in the HFPB regime in the double ladder configuration have not previously been reported, so this is still a notable result.

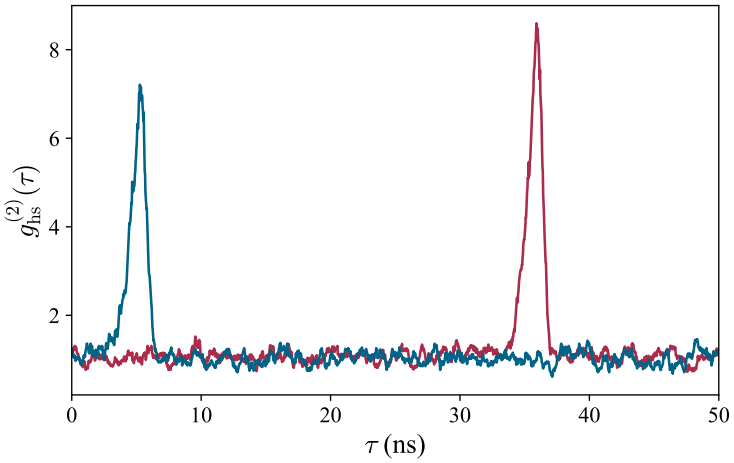

Figure 7.28: A plot of $g_{\mathrm{hs}}^{(2)}(\tau)$ in the HFPB regime with linearly polarised input light. Red and blue traces are from the two arms of the split fibre. The maximum $g_{\mathrm{hs}}^{(2)}(\tau)$ we measured in this regime was 8, much lower than in zero field. Fixed parameters are: T =120 °C; one-photon detuning = −1 GHz; 780 nm power = 0.8 mW; 776 nm power = 25 mW.

We find that for any given correlation height, the pair rate is much lower than we found in corresponding results without the B-field. Some of this decrease will be due to the factor of 4 mentioned earlier, but we may also be seeing the effect of the quicker drop off of FWM with single photon detuning, which we observed in Section 7.5. This means that we are forced to work at a smaller detuning to see a sensible amount of signal (−1 GHz here compared to −1.8 GHz in zero field) which results in more noise.

The heights on this particular figure are slightly asymmetric. This is a reflection of the uncertainty in the maximum and the peaks would converge on the same value with longer integration time.

Another possible option is to use different transitions; currently we are exciting to both stretched states, $5P_{3/2},\ m_J = 3/2$ and $5D_{5/2},\ m_J = 5/2$, as illustrated in Fig 7.29 a) which requires two σ_+ transitions and has no other possible decay channels. This scheme was chosen because these transitions are the strongest (they have the largest dipole matrix elements), and because there is only one possible decay path via the $5P_{3/2}$ state. However it would be possible, as shown in panel b), to excite up from $5P_{3/2},\ m_J = 3/2$ to $5D_{5/2},\ m_J = 1/2$ via a 776 nm σ_- transition. From this state there are two allowed decay paths via 5P back to our ground state, $5S_{1/2},\ m_J = 1/2$: one is our excitation path, and another is via a 776 nm σ_+ transition to $5P_{3/2},\ m_J = -1/2$ and then a 780 nm σ_- transition. Now the excitation beams have a different circular polarisation to the signal photons of

the same wavelength, so polarisation filtering is possible. The laser transitions and the correlated photon transitions now also have different wavelengths, separated by ∼20 GHz, so filtering with an etalon filter to remove laser scatter would be possible. This is technically now a diamond level scheme, as the two intermediate states are different and resolvable.

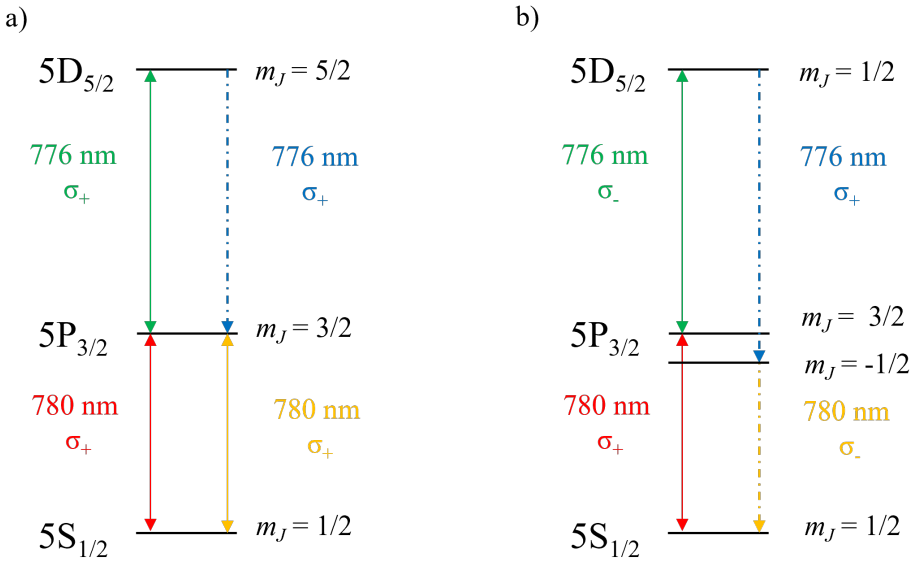

Figure 7.29: Diagram showing a) the original stretched state HFPB regime energy level scheme, and b) the altered energy level scheme using different intermediate states for the excitation and emission photons, giving the transitions different polarisations, as shown, and slightly different wavelengths.

In practice, however, the correlations we could measure using this setup were very weak. We saw a maximum $g^{(2)}_{\mathrm{hs}}(\tau)\mathrm{max}$ of 3, with a pair rate of 2 Hz. There are a few possible factors which contribute to this drop off:

- The changed excitation transition is weaker by a factor 3 than its predecessor, so more power has to be used to achieve the same excitation, meaning more noise.
- The probability of decay via these new transitions is lower, because many more decay pathways are available as the new excited state is not a stretched state.
- Circular polarisations must now be set and filtered. This requires two optical components per set/filter, a quarter-wave plate and a GT polariser, rather than just a polariser as is required for linear polarisations. This means a lot more degrees of freedom, so optimisation is much more difficult.

- circular polarisation is less well maintained by optical elements than linearly polarised light. We have no option but to include edge mirrors on our collection arms before returning the light to a linear polarisation.

It would also be possible to collect correlated herald-signal pairs sideways out of the vapour cell, orthogonal to the excitation axis. In this geometry σ_+ and σ_- fluorescence is linearly polarised, as shown in Fig 7.27. Therefore the excitation lasers could be linearly polarised orthogonal to the fluorescence polarisation, and filtering out laser light should be straightforward. We would also expect to see less light scattered out sideways than forward. A potential disadvantage of this setup is phase matching condition will be less well met. However, as the wavelengths we use are so closely matched, we anticipate this may not be a problem.

We attempted to implement the setup, however, the design of our vapour cell, a 'lollipop' with curved side as described in Section 3.1, made it impractical. The curved sides of the cell act as cylindrical lenses to defocus (but not very uniformly) the light coming out of the cell, and we struggled to align even seeded FWM. We have commissioned cuboidal cells to remove this problem.

7.13.1 Aside - $g^{(2)}_{\mathbf{hs}}(\tau)$ <1

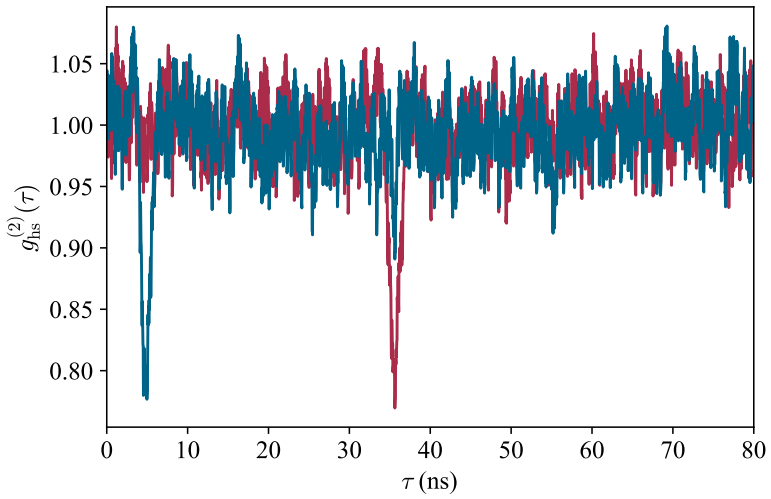

Figure 7.30: Figure showing $g^{(2)}_{\mathrm{hs}}(\tau) < 1$ 'anti-correlations'. In the HFPB regime we excite with linearly polarised light, but use quarter-wave plates to filter the outputs. The output filtering angles can be adjusted such than we see a dip in the $g^{(2)}_{\mathrm{hs}}(\tau)$ spectrum.

Fig 7.30 shows that we can, use a setup in which we excited with linearly polarised light and filter using quarter-wave plates for circular polarisations to see 'anti-correlations', with a $g^{(2)}_{\mathrm{hs}}(\tau) < 1$. This means that if we detect a photon on one channel at time t, we are less likely to detect a photon at a time $t+\tau$ on the other channel. As the pairs of photons we detect are polarisation matched (one is σ_+ and the other σ_-), we can set both filtering arms to select the same polarisation we select one of the pair and reject the other. Rotating the quarter-wave plates lets us switch between correlation dips and correlation peaks. This is included because it is an effect we have not seen reported elsewhere.

7.14 Heralded auto-correlation function

So far we have measured $g^{(2)}_{\mathrm{hs}}(\tau)$ for our system, and have two functions $g^{(2)}_{\mathrm{hs}_1}(\tau)$ and $g^{(2)}_{\mathrm{hs}_2}(\tau)$ when we beam split the photons arriving on the signal channel. This source is a heralded single photon source, meaning that we know to expect a single photon a set time after we detect a herald photon, so in order to calculate the heralded auto-correlation function, we need to measure the histogram for triple coincidence events.

To do this we use the heralding time gap we have measured for correlations between photons arriving on CH0 and CH1: (5.9 ± 0.8) ns. We look for all the counts on CH1 which were detected (5.9 ± 0.8) ns after a count on CH0, and then histogram the time gaps between these CH1 counts, and all CH2 counts. If our source were perfect—all photons detected were from pairs of heralded single photons—we would see zero counts on the histogram at a time gap $\tau = \tau_{hs_2} - \tau_{hs_1}$, where τ_{hs_i} is the time delay of $g^{(2)}_{\mathrm{hs}_i}(\tau)$max. This is because a single heralding photon is paired with only one signal photon, so a signal photon cannot arrive on CH1 and CH2 at times which correspond to the same herald arrival.

In practice, however, we do not see a value of zero, or even a dip: we still see a peak, as shown by the purple trace in Fig 7.31. This is the correlation histogram for detecting an h then s_1 then s_2 photons, as a function of the time gap between s_1 then s_2 with a particular hs_1 time gap, which we write as $G^{(2)}_{\mathrm{hs}_1\mathrm{s}_2}(\tau_{\mathrm{s}_1\mathrm{s}_2})$. We now subscript τ to make it clear which photon channels the time-gap is between, as we will be plotting functions of different time gaps which can be easily confused.

From $G^{(2)}_{\mathrm{hs}_1\mathrm{s}_2}(\tau_{\mathrm{s}_1\mathrm{s}_2})$, we are looking to calculate $g^{(2)}_{\mathrm{s}_1\mathrm{s}_2|\mathrm{h}}(\tau_{\mathrm{s}_1\mathrm{s}_2})$. We follow the method of [163] and [44].

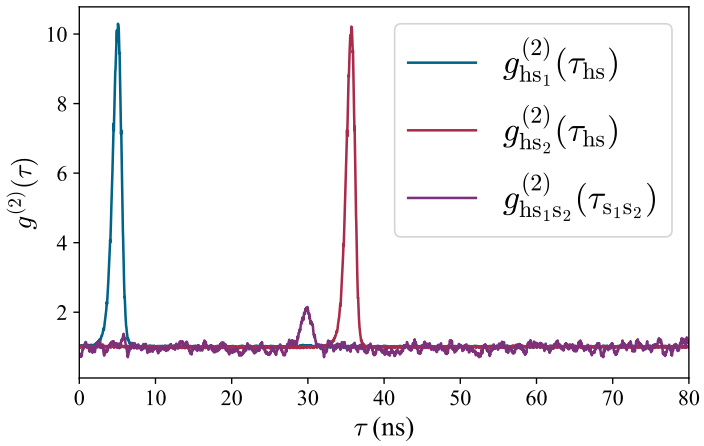

Figure 7.31: The normalised triple coincidence histogram $g^{(2)}_{\mathrm{hs_1s_2}}(\tau_{\mathrm{s_1s_2}})$ (purple), with the double coincidence histograms $g^{(2)}_{\mathrm{hs_1}}(\tau_{\mathrm{hs}})$ (blue) and $g^{(2)}_{\mathrm{hs_2}}(\tau_{\mathrm{hs}})$ (red). Collection time for this data set was 8.5 hours. Fixed parameters are: T =127 °C; 780 nm power = 2 mW; 776 nm power = 20 mW.

Similarly to Eqn 7.14, we can use conditional probabilities write

$$g^{(2)}_{\mathrm{s_1s_2|h}} = \frac{P_{\mathrm{s_1s_2|h}}}{P_{\mathrm{s_1|h}}P_{\mathrm{s_2|h}}}, \tag{7.17}$$

which can be expanded using $P(A|B) = \frac{P(AB)}{P(B)}$ to give

$$\frac{P_{\mathrm{s_1s_2|h}}}{P_{\mathrm{s_1|h}}P_{\mathrm{s_2|h}}} = \frac{P_{\mathrm{hs_1s_2}}P_{\mathrm{h}}}{P_{\mathrm{hs_1}}P_{\mathrm{hs_2}}}. \tag{7.18}$$

If we write this in terms of coincidences we have

$$g^{(2)}_{\mathrm{s_1s_2|h}} = \frac{G^{(2)}_{\mathrm{hs_1s_2}}N_{\mathrm{h}}}{G^{(2)}_{\mathrm{hs_1}}G^{(2)}_{\mathrm{hs_2}}}. \tag{7.19}$$

Here N_{h} is the total number of heralding events, $G^{(2)}_{\mathrm{hs_1s_2}}$ is the number of triple coincidence events between all three channels, and $G^{(2)}_{\mathrm{hs_1}}$ and $G^{(2)}_{\mathrm{hs_2}}$ are the number of pair events between the herald and each of the signal channels.

We now reintroduce the time delay, $\tau_{\mathrm{s_1s_2}}$, into our equations.

$$g^{(2)}_{\mathrm{s_1s_2|h}}(\tau_{\mathrm{s_1s_2}}) = \frac{G^{(2)}_{\mathrm{hs_1s_2}}(\tau_{\mathrm{s_1s_2}})N_{\mathrm{h}}}{G^{(2)}_{\mathrm{hs_1}}(\tau_{\mathrm{s_1s_2}})G^{(2)}_{\mathrm{hs_2}}(\tau_{\mathrm{s_1s_2}})}. \tag{7.20}$$

However, the double coincidence histograms we measure are not functions of $\tau_{\mathrm{s_1s_2}}$, they are functions of τ_{hs} . We instead write this denominator as $N(\tau_{\mathrm{s_1s_2}})$, which is given by

$$N(\tau_{\mathrm{s_1s_2}}) = \int_0^{T_c} G^{(2)}_{\mathrm{hs_1}}(\tau_{\mathrm{hs}})G^{(2)}_{\mathrm{hs_1}}(\tau_{\mathrm{hs}} + \tau_{\mathrm{s_1s_2}})\mathrm{d}\tau_{\mathrm{hs}}. \tag{7.21}$$

Here we are integrating over all possible time delays, τ_{hs} within the our coincidence window of width T_c, which result in a delay of $\tau_{\mathrm{s_1s_2}}$.

We follow this process and calculate the $g^{(2)}_{\mathrm{s_1s_2|h}}(\tau_{\mathrm{s_1s_2}})$, which we will subsequently refer to as $g^{(2)}(\tau)$.

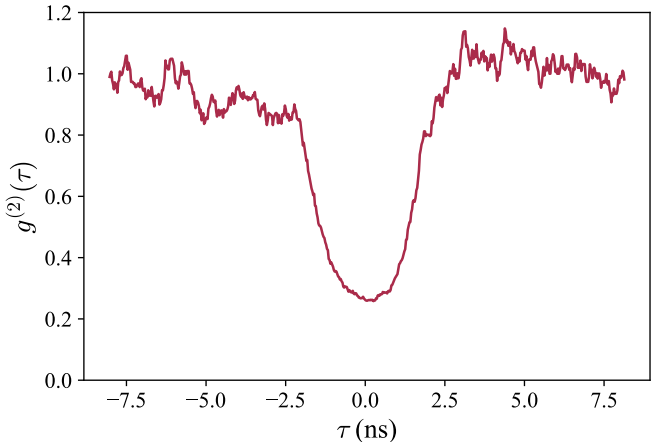

Figure 7.32: Heralded auto-correlation function of our system, calculated from the data in Fig 7.31. It has minimum of $g^{(2)}(0) = 0.25 \pm 0.02$, which is non-classical, and a width of (3.3 ± 0.1) ns.

We return to zero field to calculate the auto-correlation function, as we require a high pair rate and strong correlations. We calculate the heralded auto-correlation function of the photons on our signal channel, the result of which is shown in Fig 7.32. Each histogram involved in the calculation was smoothed before normalisation by calculating a moving average using 20 data points, which equates to 0.5 ns. We obtain a $g^{(2)}(0)$ of 0.25 ± 0.02, which is non classical. We measure the FWHM of this dip to be (3.3 ± 0.1) ns. This is broader then the widths we measured for the $g^{(2)}_{\mathrm{hs}}(\tau)$ peaks in Section 7.12, which is mostly a result of the convolution of the two Gaussian lineshapes in Eqn 7.21. There is also a small broadening effect due to the data smoothing.

It can be clearly seen that the triple coincidence histogram is much noisier that then double coincidence histograms. Because of the pre-selection by the $\mathrm{hs_1}$ time gap, the number of $\mathrm{s_2}$ counts which make it onto the $\mathrm{hs_1s_2}$ histogram is lower than those which make it onto the on $\mathrm{hs_2}$ histogram by a factor of the heralding efficiency on the $\mathrm{s_1}$ channel. The heralding efficiency, given by Eqn 7.16, is the fraction of photons on the herald channel which are followed the appropriate time later by a photon on one of the signal channels.

Table 7.1 shows the rates and integration time of the data shown in Fig 7.31. We are showing these numbers to give a sense of the times required to collect triple

Integration time, T	8.5 h
CH0 count rate	410 kHz
CH1 count rate	37 kHz
CH2 count rate	31 kHz
Pair rate	250 Hz

Table 7.1: Rates for the data in Fig 7.31

coincidence data. In the case of the data set pictured in Fig 7.31, the hs_1 pair rate was 250 Hz, while the herald count rate was 410 kHz, giving a heralding efficiency of 6.1×10^{-4}. This means that our triple coincidence histogram will be populated at a rate approximately 1600x slower than our double coincidence histograms. This number agrees with what we see experimentally: a double coincidence histogram with a similar noise level to this triple coincidence histogram, which was 8.5 hours of data, appears in about 20 seconds.

We could theoretically therefore obtain lower $g^{(2)}(0)$ values than 0.25, by collecting data with the experiment in a more optimal parameter space, where we measure higher values $g^{(2)}_{\mathrm{hs}}(\tau)$max. However, as we saw in Section 7.12.1, we have to make a trade off between high $g^{(2)}_{\mathrm{hs}}(\tau)$max, and pair rate. If we choose to operate with lower pump and/or coupling laser powers, we see lower pair rates, as well as lower uncorrelated photon counts, so it takes longer to build up sensible statistics. We also find that our system is not stable enough to run consistently at high $g^{(2)}_{\mathrm{hs}}(\tau)$max values for the many hours/days required when we move to a parameter space with slower rates.

7.15 Conclusion

We have implemented and investigated a counter-propagating double ladder four-wave-mixing scheme, both in zero magnetic field and in the hyperfine Paschen-Back regime. We report seeded FWM spectra for both regimes, as see a significant broadening of the feature in both cases when the pump and coupling excitation beams are two photon resonant, but the individual beams are detuned to be outside the Doppler broadened resonance feature. We have implemented a model to explain this broadening in the HFPB regime. We also observe a significant asymmetry in the zero field case, due unresolved hyperfine states.

We then move to spontaneous FWM, which, in the zero field case, we demonstrate to be a source of heralded single photon by calculating the heralded auto-correlation function, $g^{(2)}(0) = 0.25 \pm 0.02$. We calculate $g^{(2)}_{\mathrm{hs}}(\tau)$, the correlation function between herald and signal photons for different powers and temperatures

and find that the choice of these parameters is a balance between the purity of the photons produced, and their rate of production. We introduce a narrowband etalon filter on our signal channel, finding this to improve the strength of the two-photon correlations, particularly at higher pump powers. However, again, this improvement comes at the expense of a drop in pair rate.

Finally, we find that when we convert the setup to be in the HFPB regime we are able to see herald-signal correlations, but we find both $g^{(2)}_{\mathrm{hs}}(\tau)\mathrm{max}$ and the pair rate to be significantly lower. We observed that seeded FWM in the HFPB regime is less robust to intermediate state detuning, which may contribute to this. We also attribute this partly to difficulties with polarisation management and filtering, as along axis in the magnetic field the transitions are driven by and emit circularly polarised light, the polarisation of which is less well maintained by optical elements than linearly polarised light.

7.15.1 Outlook

It would be interesting to incorporate the narrow etalon filter (130 MHz) into our seeded setup, and use it as an analyser on the 776 nm FWM signal produced. We expect its frequency to two-photon match the seed photons; it would be interesting to confirm this, and determine the spectral characteristics of the signal for a single seed frequency. Would the results be the same in the spontaneous case? As previously mentioned, calibrating and monitoring the frequency of the etalon for the excited state 776 nm transition is difficult.

We mentioned in the setup section (7.3.1) that we monitor blue light decays from the $6P_{3/2}$ state, as a measure of $5D_{5/2}$ state population to optimise the alignment of our system. However, a more thorough investigation could be done using this method to interrogate the system. For example, a double ladder EIT system, as studied in [25] could be investigated in this way, by monitoring the excited state population. This would allow the 780 nm probe beam power to be increased out of the weak probe limit, as high probe power makes fitting to models difficult when measuring absorption spectra.

There are also many possible configurations of FWM to investigate, accessible with the lasers at our disposal. The co-propagating diamond has been previously studied in our laboratory [44], however we have since made improvements to the two-photon laser stabilisation system, which could improve its performance. We would also like to try this in the counter-propagating geometry, where the signal should be stronger because many velocity classes contribute (7.11), and to compare results in and out of the hyperfine Paschen-Back regime.

Chapter 8

Summary and Outlook

In this chapter we will summarise the four main chapters of this thesis, highlighting the significant results from each. We will also comment on possible future investigations that could follow on from the work presented here.

Chapter 4: Electromagnetically induced transparency in a V-type system. [1] This chapter contained an investigation into V-EIT in ^{87}Rb in the hyperfine Paschen-Back regime. We observed a clean, narrow EIT feature in a V-system and the corresponding enhanced absorption. We showed that the EIT feature has contributions from a coherent process, and an incoherent optical pumping process. The incoherent contribution occurs because of the allowed decay from the excited states to both ground states, and is the cause of the enhanced absorption feature. Our theoretical model captures all of the relevant processes, and gives insight into the role of coherence in explaining the observed narrow spectral features. The theoretical treatment is greatly simplified because the experiment was conducted in the hyperfine Paschen–Back regime, leading to distinct, non-overlapping absorption features.

In the energy level scheme we used the Doppler mismatch between the two wavelengths used is small, but the clean system presented here would easily allow investigation of the effect of large wavelength mismatches, for example the 5S–5P 5S–6P V-system in rubidium [69, 79], which could be the subject of further study.

Chapter 5: Narrowband spectral filtering techniques. [2] We presented an etalon lens cavity filter design, which we built and characterised, and go on to use in subsequent chapters. We compared this to an atomic filter, discussing the advantages of each filter type. We concluded that both designs have merits; the atomic filter is effective when signal light is close to an atomic resonance, while the cavity filter allows greater control over bandwidth and is arbitrarily tunable, but requires temperature stabilisation.

Chapter 6: Collisional Transfer. We investigated the state-changing collisional process in Rb vapour. By investigating the temperature dependence of the process we determined that in the low temperature regime when T<86 °C the process is dominated by Rb-buffer gas collisions and have carried out subsequent experiments in this temperature regime. We used a narrow linewidth (∼100 MHz) etalon filter, from chapter 5 to investigate the collisions further, and concluded that during the collision the m_I quantum number is conserved. We also used the filter to measure the spectral profile of the emitted fluorescence, and implemented a basic model which agrees very well with the experiment in most cases.

We learnt from these investigations that the buffer gas collisional mixing is a significant process, even in vapour cells where no buffer gas has been intentionally included. This effect is detrimental in an experiment which uses a diamond four-wave mixing system as a source of single photons, and could be similarly problematic for other thermal vapour technologies where low noise is important. As the buffer gas is not intentionally introduced during the cell production process, it is likely that the amount of buffer gas in each cell could vary significantly, and that better or worse cells could be found. This collisional transfer measurement could be used to test cells to determine how close to zero buffer gas they actually are.

Rb happens to have a 5S–5P principal resonance fine structure splitting approximately equal to $k_{\mathrm{B}}T$ at 75 °C. Other alkali metals have different splittings; Cs much larger and K much smaller. K vapour is used in solar filters [124] and a more detailed investigation is ongoing. We propose that Cs, with a larger splitting could be used instead of Rb in systems where collisional transfer is a problem.

Chapter 7: Four Wave Mixing. We implemented and investigated a counter-propagating double ladder four-wave-mixing scheme, both in zero magnetic field and in the hyperfine Paschen-Back regime. We report seeded FWM spectra for both regimes, as see a significant broadening of the feature in both cases when the pump and coupling excitation beams are two photon resonant, but the individual beams are detuned to be outside the Doppler broadened resonance feature. We implemented a model to explain this broadening in the HFPB regime. We also observed a significant asymmetry in the zero field case, due unresolved hyperfine states.

We then moved to spontaneous FWM, which, in the zero field case, we demonstrated to be a source of heralded single photon by calculating the heralded autocorrelation function, $g^{(2)}(0) = 0.25 \pm 0.02$. We calculated $g^{(2)}_{\mathrm{hs}}(\tau)$, the correlation function between herald and signal photons for different powers and temperatures and found that the choice of these parameters is a balance between the purity of the photons produced, and their rate of production. We found that when we converted

the setup to be in the HFPB regime we were able to see herald-signal correlations, but found both $g_{\mathrm{hs}}^{(2)}(\tau)$max and the pair rate to be significantly lower. We observed that seeded FWM in the HFPB regime is less robust to intermediate state detuning, which may contribute to this. We also attribute this partly to difficulties with polarisation management and filtering.

In the future it would be interesting to incorporate the narrow etalon filter (130 MHz) into our seeded setup, and use it as an analyser on the 776 nm FWM signal produced. We expect its frequency to two-photon match the seed photons; we would like to confirm this, and determine the spectral characteristics of the signal for a single seed frequency. We could then see if this holds in the spontaneous case.

We monitor blue light decays from the $6P_{3/2}$ state, as a measure of $5D_{5/2}$ state population to optimise the alignment of our system. However, a more thorough investigation could be done using this method to interrogate the system. For example, a double ladder EIT system, as studied in [25] could be investigated in this way, by monitoring the excited state population. This would allow the 780 nm probe beam power to be increased out of the weak probe limit.

There are also many possible configurations of FWM to investigate, accessible with the lasers at our disposal. The co-propagating diamond has been previously studied in our laboratory [44], however we have since made improvements to the two-photon laser stabilisation system, which could improve its performance. We would also like to try the diamond in the counter-propagating geometry, where the signal should be stronger because many velocity classes contribute (7.11), and to compare results in and out of the hyperfine Paschen-Back regime.

Bibliography

[1] C. R. Higgins and I. G. Hughes. Electromagnetically induced transparency in a V-system with ^{8}7Rb vapour in the hyperfine Paschen-Back regime. *Journal of Physics B: Atomic, Molecular and Optical Physics*, 54(16):165403, 2021.

[2] C. R. Higgins, D. Pizzey, R. S. Mathew, and I. G. Hughes. Atomic line versus lens cavity filters: a comparison of their merits. *OSA Continuum*, 3(4):961–970, 2020.

[3] G. K. Woodgate. *Elementary Atomic Structure*. Oxford University Press, 1980.

[4] D. Pizzey, J. D. Briscoe, F. D. Logue, F. S. Ponciano Ojeda, S. A. Wrathmall, and I. G. Hughes. Laser spectroscopy of hot atomic vapours: from 'scope to theoretical fit. *New Journal of Physics*, 24:125001, 2022.

[5] E. Arimondo. V. Coherent population trapping in laser spectroscopy. volume 35 of *Progress in Optics*, pages 257–354. Elsevier, 1996.

[6] M. Fleischhauer, A. Imamoglu, and J. P. Marangos. Electromagnetically induced transparency: Optics in coherent media. *Review of Modern Physics*, 77:633–673, 2005.

[7] R. W. Boyd, L. Hau, H. Wang, G. Eisenstein, S. Noda, and J. Moerk. Slow light and its applications. *Journal of the Optical Society of America B*, 25(12):SL1, 2008.

[8] B. Julsgaard, J. Sherson, J. I. Cirac, J. Fiurášek, and E. S. Polzik. Experimental demonstration of quantum memory for light. *Nature*, 432(7016):482–486, 2004.

[9] K. F. Reim, P. Michelberger, K. C. Lee, J. Nunn, N. K. Langford, and I. A. Walmsley. Single-photon-level quantum memory at room temperature. *Physical Review Letters*, 107(5):053603, 2011.

[10] Q. Fontaine, T. Bienaimé, S. Pigeon, E. Giacobino, A. Bramati, and Q. Glorieux. Observation of the Bogoliubov dispersion in a fluid of light. *Physical Review Letters*, 121(18):183604, 2018.

[11] C. Piekarski, W. Liu, J. Steinhauer, E. Giacobino, A. Bramati, and Q. Glorieux. Measurement of the static structure factor in a paraxial fluid of light using Bragg-like spectroscopy. *Physical Review Letters*, 127(2):023401, 2021.

[12] G. Walker, A. S. Arnold, and S. Franke-Arnold. Trans-Spectral Orbital Angular Momentum Transfer via Four-Wave Mixing in Rb Vapor. *Physical Review Letters*, 108:243601, 2012.

[13] R. F. Offer, A. Daffurn, E. Riis, P. F. Griffin, A. S. Arnold, and S. Franke-Arnold. Gouy phase-matched angular and radial mode conversion in four-wave mixing. *Physical Review A*, 103:L021502, 2021.

[14] A. M. Akulshin, R. J. McLean, A. I. Sidorov, and P. Hannaford. Coherent and collimated blue light generated by four-wave mixing in Rb vapour. *Optics express*, 17(25):22861–22870, 2009.

[15] A. Vernier, S. Franke-Arnold, E. Riis, and A. S. Arnold. Enhanced frequency up-conversion in Rb vapor. *Optics Express*, 18(16):17020–17026, 2010.

[16] M. L. Harris, C. S. Adams, S. L. Cornish, I. C. McLeod, E. Tarleton, and I. G. Hughes. Polarization spectroscopy in rubidium and cesium. *Physical Review A*, 73:062509, 2006.

[17] P. Burdekin, S. Grandi, R. Newbold, R. A. Hoggarth, K. D. Major, and A. S. Clark. Single-Photon-Level Sub-Doppler Pump-Probe Spectroscopy of Rubidium. *Physical Review Applied*, 14:044046, 2020.

[18] L. A. Downes, A. R. MacKellar, D. J. Whiting, C. Bourgenot, C. S. Adams, and K. J. Weatherill. Full-Field Terahertz Imaging at Kilohertz Frame Rates Using Atomic Vapor. *Physical Review X*, 10:011027, 2020.

[19] J. Kitching, S. Knappe, and L. Hollberg. Miniature vapor-cell atomic-frequency references. *Applied Physics Letters*, 81(3):553–555, 2002.

[20] S. Knappe, T. Sander, J. Preusser, R. Mhaskar, J. Kitching, and L. Trahms. Magnetoencephalography with a chip-scale atomic magnetometer. *Biomedical Optics Express*, (3), 2012.

[21] J. U. Sutter, O. Lewis, C. Robinson, A. McMahon, R. Boyce, R. Bragg, A. Macrae, J. Orton, V. Shah, S. J. Ingleby, P. F. Griffin, and E. Riis. Recording the heart beat of cattle using a gradiometer system of optically pumped magnetometers. *Computers and Electronics in Agriculture*, 177:105651, 2020.

[22] J. Sagle, R. K. Namiotka, and J. Huennekens. Measurement and modelling of intensity dependent absorption and transit relaxation on the cesium line. *Journal of Physics B: Atomic, Molecular and Optical Physics*, 29(12):2629–2643, 1996.

[23] Q. Glorieux, T. Aladjidi, P. D. Lett, and R. Kaiser. Hot atomic vapors for nonlinear and quantum optics. *arXiv preprint arXiv:2209.04622*, 2022.

[24] R. W. Boyd. *Non-linear Optics, 2nd edition.* Academic Press, 2003.

[25] D. J. Whiting, J. Keaveney, C. S. Adams, and I. G. Hughes. Direct measurement of excited-state dipole matrix elements using electromagnetically induced transparency in the hyperfine Paschen-Back regime. *Physical Review A*, 93:043854, 2016.

[26] L. Hau, S. Harris, and Cyrus H. Dutton, Z.and Behroozi. Light speed reduction to 17 metres per second in an ultracold atomic gas. *Nature*, 397:594–598, 1999.

[27] R. G. Beausoleil, W. J. Munro, D. A. Rodrigues, and T. P. Spiller. Applications of electromagnetically induced transparency to quantum information processing. *Journal of Modern Optics*, 51(16-18):2441–2448, 2004.

[28] K. Hammerer, A. S. Sørensen, and E. S. Polzik. Quantum interface between light and atomic ensembles. *Review of Modern Physics*, 82:1041–1093, 2010.

[29] A. Das, B. C.a Das, D. Bhattacharyya, S. Chakrabarti, and S. De. Polarization rotation with electromagnetically induced transparency in a V-type configuration of Rb D1 and D2 transitions. *Journal of Physics B: Atomic, Molecular and Optical Physics*, 51(17):175502, 2018.

[30] M. Fleischhauer, A. B. Matsko, and M. O. Scully. Quantum limit of optical magnetometry in the presence of AC Stark shifts. *Physical Review A*, 62:013808, 2000.

[31] D. Budker and M. Romalis. Optical magnetometry. *Nature Physics*, 3(4):227–234, 2007.

[32] R. Santra, E. Arimondo, T. Ido, C. H. Greene, and J. Ye. High-accuracy optical clock via three-level coherence in neutral bosonic ^{88}Sr. *Physical Review Letters*, 94:173002, 2005.

[33] R. T. Willis, F. E. Becerra, L. A. Orozco, and S. L. Rolston. Photon statistics and polarization correlations at telecommunications wavelengths from a warm atomic ensemble. *Optics Express*, 19(15):14632, 2011.

[34] D. J. Whiting, R. S. Mathew, J. Keaveney, C. S. Adams, and I. G. Hughes. Four-wave mixing in a non-degenerate four-level diamond configuration in the hyperfine Paschen–Back regime. *Journal of Modern Optics*, 65(5-6):713–722, 2018.

[35] U. Khadka, H. Zheng, and M. Xiao. Four-wave-mixing between the upper excited states in a ladder-type atomic configuration. *Optics Express*, 20(6):6204–6214, 2012.

[36] D. J. Whiting, N. Šibalić, J. Keaveney, C. S. Adams, and I. G. Hughes. Single-photon interference due to motion in an atomic collective excitation. *Physical Review Letters*, 118:253601, 2017.

[37] Y.-S. Lee, S. M. Lee, H. Kim, and H. S. Moon. Highly bright photon-pair generation in doppler-broadened ladder-type atomic system. *Optics Express*, 24(24):28083–28091, 2016.

[38] O. Davidson, R. Finkelstein, E. Poem, and O. Firstenberg. Bright multiplexed source of indistinguishable single photons with tunable GHz-bandwidth at room temperature. *New Journal of Physics*, 23(7):073050, 2021.

[39] M. Himsworth, P. Nisbet, J. Dilley, G. Langfahl-Klabes, and A. Kuhn. EIT-based quantum memory for single photons from cavity-QED. *Applied Physics B*, 103(3):579–589, 2011.

[40] J. Wolters, G. Buser, A. Horsley, L. Béguin, A. Jöckel, J.-P. Jahn, R. J Warburton, and P. Treutlein. Simple atomic quantum memory suitable for semiconductor quantum dot single photons. *Physical Review Letters*, 119(6):060502, 2017.

[41] H.-R. Noh and H. S. Moon. Four-wave mixing in a ladder configuration of warm ^{8}7Rb atoms: a theoretical study. *Optics Express*, 29(5):6495–6508, 2021.

[42] M. A. Zentile, J. Keaveney, L. Weller, D. J. Whiting, C. S. Adams, and I. G. Hughes. ElecSus: A program to calculate the electric susceptibility of an atomic ensemble. *Computer Physics Communications*, 189:162–174, 2015.

[43] D. J. Whiting, E. Bimbard, J. Keaveney, M. A. Zentile, C. S. Adams, and I. G. Hughes. Electromagnetically induced absorption in a nondegenerate three-level ladder system. *Optics Letters*, 40(18):4289–4292, 2015.

[44] R. S. Mathew. *Single-Photon Generation via Four-Wave Mixing in a Thermal Rubidium Vapour at a High Magnetic Field*. PhD thesis, 2021.

[45] C. J. Foot. *Atomic Physics*. Oxford Master Series in Physics. OUP Oxford, 2005.

[46] C. Cohen-Tannoudji, J. Dupont-Roc, and G. Grynberg. *Atom—Photon Interactions: Basic Process and Appilcations*. Wiley, 2004.

[47] K. Blum. *Density Matrix Theory and Applications*. Springer Series on Atomic, Optical, and Plasma Physics. Springer Berlin Heidelberg, 2012.

[48] B. H. Bransden and C. J. Joachain. *Physics of Atoms and Molecules*. Pearson Education, 2003.

[49] D. Suter. *Two-level atoms*, page 38–73. Cambridge Studies in Modern Optics. Cambridge University Press, 1997.

[50] D. J. Whiting. *Nonlinear Optics in a Thermal Rb Vapour at High Magnetic Fields*. PhD thesis, Durham University, 2017.

[51] U. Volz and H. Schmoranzer. Precision lifetime measurements on alkali atoms and on helium by beam–gas–laser spectroscopy. *Physica Scripta*, 1996(T65):48, 1996.

[52] F. E. Becerra, R. T. Willis, S. L. Rolston, H. J. Carmichael, and L. A. Orozco. Nondegenerate four-wave mixing in rubidium vapor: Transient regime. *Physical Review A*, 82:043833, 2010.

[53] P. Siddons, C. S. Adams, and I. G. Hughes. Off-resonance absorption and dispersion in vapours of hot alkali-metal atoms. *Journal of Physics B: Atomic, Molecular and Optical Physics*, 42(17):175004, 2009.

[54] L. Weller, R. J. Bettles, P. Siddons, C. S. Adams, and I. G. Hughes. Absolute absorption on the rubidium d1 line including resonant dipole–dipole interactions. *Journal of Physics B: Atomic, Molecular and Optical Physics*, 44(19):195006, 2011.

[55] C. B. Alcock, V. P. Itkin, and M. K. Horrigan. Vapour Pressure Equations for the Metallic Elements: 298–2500K. *Canadian Metallurgical Quarterly*, 23(3):309–313, 1984.

[56] R. W. Ohse, J.-F. Babelot, J. Magill, and M. Tetenbaum. An assessment of the melting, boiling, and critical point data of the alkali metals. *Pure and Applied Chemistry*, 57(10):1407–1426, 1985.

[57] L. Weller. *Absolute Absorption and Dispersion in a Thermal Rb Vapour at High Densities and High Magnetic Fields*. PhD thesis, Durham University, 2013.

[58] D. A. Steck. Rubidium 87 D line data. 2021. Available online at `https://steck.us/alkalidata/`.

[59] L. Weller, K. S. Kleinbach, M. A. Zentile, S. Knappe, C. S. Adams, and I. G. Hughes. Absolute absorption and dispersion of a rubidium vapour in the hyperfine Paschen-Back regime. *Journal of Physics B: Atomic, Molecular and Optical Physics*, 45(21):215005, 2012.

[60] J. Keaveney, C. S. Adams, and I. G. Hughes. ElecSus: Extension to arbitrary geometry magneto-optics. *Computer Physics Communications*, 224:311–324, 2017.

[61] C. S. Adams and I. G. Hughes. *Optics f2f - From Fourier to Fresnel*. Oxford University Press, Oxford, UK, 2019.

[62] R. S. Mathew, F. Ponciano-Ojeda, J. Keaveney, D. J. Whiting, and I. G. Hughes. Simultaneous two-photon resonant optical laser locking (STROLLing) in the hyperfine Paschen–Back regime. *Optics Letters*, 43(17):4204–4207, 2018.

[63] L. Weller, T. Dalton, P. Siddons, C. S. Adams, and I. G. Hughes. Measuring the Stokes parameters for light transmitted by a high-density rubidium vapour in large magnetic fields. *Journal of Physics B: Atomic, Molecular and Optical Physics*, 45(5):055001, 2012.

[64] V. I. Yudin, A. V. Taichenachev, Y. O. Dudin, V. L. Velichansky, A. S. Zibrov, and S. A. Zibrov. Vector magnetometry based on electromagnetically induced transparency in linearly polarized light. *Physical Review A*, 82:033807, 2010.

[65] S. Khan, V. Bharti, and V. Natarajan. Role of dressed-state interference in electromagnetically induced transparency. *Physics Letters A*, 380(48):4100–4104, 2016.

[66] S. Dey, S. Mitra, P. N. Ghosh, and B. Ray. EIT line shape in an open and partially closed multilevel V-type system. *Optik*, 126(20):2711–2717, 2015.

[67] R. Hazra and M. M. Hossain. Study of multi-window electromagnetically induced transparency (EIT) and related dispersive signals in V-type systems in the Zeeman sublevels of hyperfine states of 87Rb-D2 line. *Journal of Physics B: Atomic, Molecular and Optical Physics*, 53(23):235401, 2020.

[68] Y. Hoshina, N. Hayashi, K. Tsubota, I. Yoshida, K. Shijo, R. Sugizono, and M. Mitsunaga. Electromagnetically induced transparency in a V-type multilevel system of Na vapor. *Journal of the Optical Society of America B*, 31(8):1808–1813, 2014.

[69] J. R. Boon, E. Zekou, D. J. Fulton, and M. H. Dunn. Experimental observation of a coherently induced transparency on a blue probe in a Doppler-broadened mismatched V-type system. *Physical Review A*, 57:1323–1328, 1998.

[70] A. Lazoudis, T. Kirova, E. H. Ahmed, P. Qi, J. Huennekens, and A. M. Lyyra. Electromagnetically induced transparency in an open V-type molecular system. *Physical Review A*, 83:063419, 2011.

[71] J. R. Boon, E. Zekou, D. McGloin, and M. H. Dunn. Comparison of wavelength dependence in cascade-, Λ-, and Vee-type schemes for electromagnetically induced transparency. *Physical Review A*, 59:4675–4684, 1999.

[72] C. Zhu, C. Tan, and G. Huang. Crossover from electromagnetically induced transparency to Autler-Townes splitting in open V-type molecular systems. *Physical Review A*, 87:043813, 2013.

[73] D. McGloin. Coherent effects in a driven Vee scheme. *Journal of Physics B: Atomic, Molecular and Optical Physics*, 36(13):2861–2871, 2003.

[74] Y. Wu and X. Yang. Electromagnetically induced transparency in V-, Λ-, and cascade-type schemes beyond steady-state analysis. *Physical Review A*, 71:053806, 2005.

[75] J. Zhao, L. Wang, L. Xiao, Y. Zhao, W. Yin, and S. Jia. Experimental measurement of absorption and dispersion in V-type cesium atom. *Optics Communications*, 206(4):341–345, 2002.

[76] S. Scotto, D. Ciampini, C. Rizzo, and E. Arimondo. Four-level N-scheme crossover resonances in Rb saturation spectroscopy in magnetic fields. *Physical Review A*, 92:063810, 2015.

[77] E. H. Cha, T. Jeong, and H.-R. Noh. Two-color polarization spectroscopy in V-type configuration in rubidium. *Optics Communications*, 326:175–179, 2014.

[78] A. Das, B. C. Das, D. Bhattacharyya, and S. De. Effects of probe ellipticity and longitudinal magnetic field on the polarization rotation in a coherently prepared atomic medium. *OSA Continuum*, 4(1):105–120, 2021.

[79] S. Vdović, T. Ban, D. Aumiler, and G. Pichler. EIT at $5^2S_{1/2} \rightarrow 6^2P_{3/2}$ transition in a mismatched V-type rubidium system. *Optics Communications*, 272(2):407–413, 2007.

[80] H.-J. Kang and H.-R. Noh. Coherence effects in electromagnetically induced transparency in V-type systems of 87Rb. *Optics Express*, 25(18):21762–21774, 2017.

[81] D. J. Fulton, S. Shepherd, R. R. Moseley, B. D. Sinclair, and M. H. Dunn. Continuous-wave electromagnetically induced transparency: A comparison of V, Λ, and cascade systems. *Physical Review A*, 52:2302–2311, 1995.

[82] B. A. Olsen, B. Patton, Y.-Y. Jau, and W. Happer. Optical pumping and spectroscopy of Cs vapor at high magnetic field. *Physical Review A*, 84:063410, 2011.

[83] M. A. Zentile, R. Andrews, L. Weller, S. Knappe, C. S. Adams, and I. G. Hughes. The hyperfine Paschen–Back Faraday effect. *Journal of Physics B: Atomic, Molecular and Optical Physics*, 47(7):075005, 2014.

[84] F. S. Ponciano-Ojeda, F. D. Logue, and I. G. Hughes. Absorption spectroscopy and Stokes polarimetry in a 87Rb vapour in the Voigt geometry with a 1.5 T external magnetic field. *Journal of Physics B: Atomic, Molecular and Optical Physics*, 54(1):015401, 2020.

[85] A. Sargsyan, G. Hakhumyan, C. Leroy, Y. Pashayan-Leroy, A. Papoyan, D. Sarkisyan, and M. Auzinsh. Hyperfine Paschen-Back regime in alkali metal atoms: consistency of two theoretical considerations and experiment. *Journal of the Optical Society of America B*, 31(5):1046–1053, 2014.

[86] A. Sargsyan, E. Klinger, G. Hakhumyan, A. Tonoyan, A. Papoyan, C. Leroy, and D. Sarkisyan. Decoupling of hyperfine structure of Cs D1 line in strong magnetic field studied by selective reflection from a nanocell. *Journal of the Optical Society of America B*, 34(4):776–784, 2017.

[87] L. Ma, D. A. Anderson, and G. Raithel. Paschen-Back effects and Rydberg-state diamagnetism in vapor-cell electromagnetically induced transparency. *Physical Review A*, 95:061804, 2017.

[88] S. George, N. Bruyant, J. Béard, S. Scotto, E. Arimondo, R. Battesti, D. Ciampini, and C. Rizzo. Pulsed high magnetic field measurement with a rubidium vapor sensor. *Review of Scientific Instruments*, 88(7):073102, 2017.

[89] I. G. Hughes. Velocity selection in a Doppler-broadened ensemble of atoms interacting with a monochromatic laser beam. *Journal of Modern Optics*, 65(5-6):640–647, 2018.

[90] A. M. Fox and D. Fox. *Optical Properties of Solids*. Oxford Universtiy Press, 2001.

[91] A. MacRae, T. Brannan, R. Achal, and A. I. Lvovsky. Tomography of a high-purity narrowband photon from a transient atomic collective excitation. *Physical Review Letters*, 109:033601, 2012.

[92] N. Sinclair, E. Saglamyurek, H. Mallahzadeh, J. A. Slater, M. George, R. Ricken, M. P. Hedges, D. Oblak, C. Simon, W. Sohler, and W. Tittel. Spectral multiplexing for scalable quantum photonics using an atomic frequency comb quantum memory and feed-forward control. *Physical Review Letters*, 113:053603, 2014.

[93] J. A. Zielińska, F. A. Beduini, V. G. Lucivero, and M. W. Mitchell. Atomic filtering for hybrid continuous-variable/discrete-variable quantum optics. *Optics Express*, 22(21):25307–25317, 2014.

[94] P. K. Tan, G. H. Yeo, H. S. Poh, A. H. Chan, and C. Kurtsiefer. Measuring temporal photon bunching in blackbody radiation. *The Astrophysical Journal*, 789(1):L10, 2014.

[95] D. Bouwmeester, J. Pan, K. Mattle, M. Eibl, H. Weinfurter, and A. Zeilinger. Experimental quantum teleportation. *Nature*, 390:575–579, 1997.

[96] M. Hosseini, G. Campbell, B. M. Sparkes, P. K. Lam, and B. C. Buchler. Unconditional room-temperature quantum memory. *Nature Physics*, 7(10):794–798, 2011.

[97] D. G. England, K. A. G. Fisher, J.-P. W. MacLean, P. J. Bustard, R. Lausten, K. J. Resch, and B. J. Sussman. Storage and retrieval of THz-bandwidth single photons using a room-temperature diamond quantum memory. *Physical Review Letters*, 114:053602, 2015.

[98] M. Yukawa, K. Miyata, T. Mizuta, H. Yonezawa, P. Marek, R. Filip, and A. Furusawa. Generating superposition of up-to three photons for continuous variable quantum information processing. *Optics Express*, 21(5):5529–5535, 2013.

[99] N. Schlosser, G. Reymond, and P. Grangier. Collisional blockade in microscopic optical dipole traps. *Physical Review Letters*, 89:023005, 2002.

[100] C. Fricke-Begemann, M. Alpers, and J. Höffner. Daylight rejection with a new receiver for potassium resonance temperature LIDARs. *Optics Letters*, 27(21):1932–1934, 2002.

[101] A. Popescu, K. Schorstein, and T. Walther. A novel approach to a LIDAR for remote sensing of the ocean temperature. *Applied Physics B*, 79(8):955–961, 2004.

[102] S.H. Gong, G.T. Yang, X.W. Cheng, S.S. Gong, J.Y. Xu, F.Q. Li, W. Gong, and J.H. Wang. LIDAR observation campaigns on diurnal variations of the sodium layer in Beijing and Wuhan, China. *Science China Earth Sciences*, 58(8):1377–1386, 2015.

[103] S. H. Bloom, P. A. Searcy, K. Choi, R. Kremer, and Eric Korevaar. Helicopter plume detection by using an ultranarrow-band noncoherent laser doppler velocimeter. *Optics Letters*, 18(3):244–246, 1993.

[104] J. Keaveney, W. J. Hamlyn, C. S. Adams, and I. G. Hughes. A single-mode external cavity diode laser using an intra-cavity atomic Faraday filter with short-term linewidth <400 kHz and long-term stability of <1 MHz. *Review of Scientific Instruments*, 87(9):095111, 2016.

[105] X. Miao, L. Yin, W. Zhuang, B. Luo, A. Dang, J. Chen, and H. Guo. Note: Demonstration of an external-cavity diode laser system immune to current and temperature fluctuations. *Review of Scientific Instruments*, 82(8):086106, 2011.

[106] M. Faraday. I. Experimental researches in electricity. Nineteenth series. *Philosophical Transactions of the Royal Society of London*, 136:1–20, 1846.

[107] J. Keaveney, S. A. Wrathmall, C. S. Adams, and I. G. Hughes. Optimized ultra-narrow atomic bandpass filters via magneto-optic rotation in an unconstrained geometry. *Optics Letters*, 43(17):4272–4275, 2018.

[108] R. P. Abel, U. Krohn, P. Siddons, I. G. Hughes, and Charles S. Adams. Faraday dichroic beam splitter for raman light using an isotopically pure alkali-metal-vapor cell. *Optics Letters*, 34(20):3071–3073, 2009.

[109] J. Menders, K. Benson, S. H. Bloom, C. S. Liu, and Eric Korevaar. Ultranarrow line filtering using a Cs Faraday filter at 852 nm. *Optics Letters*, 16(11):846–848, 1991.

[110] M. D. Rotondaro, B. V. Zhdanov, and R. J. Knize. Generalized treatment of magneto-optical transmission filters. *Journal of the Optical Society of America B*, 32(12):2507–2513, 2015.

[111] M. A. Zentile, D. J. Whiting, J. Keaveney, C. S. Adams, and I. G. Hughes. Atomic Faraday filter with equivalent noise bandwidth less than 1 GHz. *Optics Letters*, 40(189):2000–2003, 2015.

[112] D. J. Dick and T. M. Shay. Ultrahigh-noise rejection optical filter. *Optics Letters*, 16(11):867–869, 1991.

[113] H. Chen, C. Y. She, Paul Searcy, and Eric Korevaar. Sodium-vapor dispersive Faraday filter. *Optics Letters*, 18(12):1019–1021, 1993.

[114] W. Kiefer, R. Löw, J. Wrachtrup, and I. Gerhardt. Na-Faraday rotation filtering: The optimal point. *Scientific Reports*, 4(1):6552, 2014.

[115] L. N. Hadley and D. M. Dennison. Reflection and Transmission Interference Filters Part I. Theory. *Journal of the Optical Society of America*, 37(6):451–465, 1947.

[116] P. Palittapongarnpim, A. MacRae, and A. I. Lvovsky. Note: A monolithic filter cavity for experiments in quantum optics. *Review of Scientific Instruments.*, 83(6):066101, 2012.

[117] P. Maunz, T. Puppe, I. Schuster, N. Syassen, P. W. H. Pinkse, and G. Rempe. Cavity cooling of a single atom. *Nature*, 428(6978):50–52, 2004.

[118] SCHOTT. *Temperature Coefficient of the Refractive Index.*

[119] A. MacRae. *An atomic source of quantum light.* PhD thesis, University of Calgary, University of Calgary, 2012.

[120] Lightmachinery op-7423-x etalon specification sheet. `https://lightmachinery.com/media/1657/op-7423-x-a-1-inch-etalon-various-thickness.pdf`. Accessed: 2022-20-24.

[121] Lightmachinery fused silica etalons. `https://lightmachinery.com/optics-catalog/etalons-fused-silica/#solidfusedsilicaetalonsfinesse30,700nmto850nm`. Accessed: 2022-20-24.

[122] M. A. Zentile, J. Keaveney, R. S. Mathew, D. J. Whiting, C. S. Adams, and I. G. Hughes. Optimization of atomic Faraday filters in the presence of homogeneous line broadening. *Journal of Physics B: Atomic, Molecular and Optical Physics*, 48(18):185001, 2015.

[123] A. Ahlrichs, C. Berkemeier, B. Sprenger, and O. Benson. A monolithic polarization-independent frequency-filter system for filtering of photon pairs. *Applied Physics Letters*, 103(24):241110, 2013.

[124] R. Erdélyi, M. B. Korsós, X. Huang, Y. Yang, D. Pizzey, S. A. Wrathmall, I. G. Hughes, M. J. Dyer, V. S. Dhillon, B. Belucz, R. Brajsa, P. Chatterjee, X. Cheng, Y. Deng, S. V. Domínguez, R. Joya, P. Gömöry, N. G. Gyenge, A. Hanslmeier, A. Kucera, D. Kuridze, F. Li, Z. Liu, L. Xu, M. Mathioudakis, S. Matthews, J. R.T. McAteer, A. A. Pevtsov, W. Pötzi, P. Romano, J. Shen, J. Temesváry, A. G. Tlatov, C. Triana, D. Utz, A. M. Veronig, Y. Wang, Y. Yan, T. Zaqarashvili, and F. Zuccarello. The Solar Activity Monitor Network - SAMNet. *Journal of Space Weather and Space Climate*, 12:2, 2022.

[125] A. Sieradzan and F. A. Franz. Quenching, depolarization, and transfer of spin polarization in Rb-N_2 collisions. *Physical Review A*, 25:2985–2995, 1982.

[126] F. A. Franz and C. Volk. Spin relaxation of rubidium atoms in sudden and quasimolecular collisions with light-noble-gas atoms. *Physical Review A*, 14:1711–1728, 1976.

[127] G. A. Pitz, D. M. Stalnaker, E. M. Guild, B. Q. Oliker, P. J. Moran, S. W. Townsend, and D. A. Hostutler. Advancements in flowing diode pumped alkali lasers. In Steven J. Davis, Michael C. Heaven, and J. Thomas Schriempf, editors, *High Energy/Average Power Lasers and Intense Beam Applications IX*, volume 9729, page 972902. International Society for Optics and Photonics, SPIE, 2016.

[128] M. D. Rotondaro and G. P. Perram. Collisional broadening and shift of the rubidium D1 and D2 lines ($5^2S_{1/2} \rightarrow 5^2P_{1/2}$, $5^2P_{3/2}$) by rare gases, H_2, D_2, N_2, CH_4 and CF_4. *Journal of Quantitative Spectroscopy and Radiative Transfer*, 57(4):497–507, 1997.

[129] M. D. Rotondaro and G. P. Perram. Role of rotational-energy defect in collisional transfer between the $5^2P_{1/2,3/2}$ levels in rubidium. *Physical Review A*, 57:4045–4048, 1998.

[130] M. D. Rotondaro and G. P. Perram. Collision-induced transitions between the Zeeman-split (J, m) levels of Rb$(5^2P_{1/2}, 5^2P_{3/2})$. *Physical Review A*, 58:2023–2029, 1998.

[131] M. Zentile. *Applications of the Faraday Effect in Hot Atomic Vapours*. PhD thesis, Durham University, 2015.

[132] Laser2000. 780 nm maxline® laser clean-up filter. `https://photonics.laser2000.co.uk/products/light-delivery-and-control/microscopy-filters/individual-filters/bandpass-filters/780-nm-maxline-laser-clean-up-filter/`.

[133] P. Siddons, C. S. Adams, C. Ge, and I. G. Hughes. Absolute absorption on rubidium D lines: comparison between theory and experiment. *Journal of Physics B: Atomic, Molecular and Optical Physics*, 41(15):155004, 2008.

[134] S. Appelt, A. Ben-Amar Baranga, C. J. Erickson, M. V. Romalis, A. R. Young, and W. Happer. Theory of spin-exchange optical pumping of ^{3}He and ^{129}Xe. *Physical Review A*, 58:1412–1439, 1998.

[135] Combination of Profiles, 2022. `https://phys.libretexts.org/Bookshelves/Astronomy__Cosmology/Stellar_Atmospheres_(Tatum)/10%3A_Line_Profiles/10.04%3A_Combination_of_Profiles`,[Online; accessed 2022-09-22].

[136] 3D Collisions, 2004. `https://atmos.illinois.edu/courses/atmos100/userdocs/3Dcollisions.html`, [Online; accessed 2022-09-23].

[137] K. E. Gibble and A. Gallagher. Measurements of velocity-changing collision kernels. *Physical Review A*, 43:1366–1380, 1991.

[138] S. Kasai, R. Mizutani, R. Kondo, M. Hasuo, and T. Fujimoto. Dynamics of metastable argon atoms in a thin discharge cell: Single beam absorption spectroscopy and a monte carlo study of the velocity distribution. *Journal of the Physical Society of Japan*, 72(8):1936–1942, 2003.

[139] B. H. McGuyer, R. Marsland, B. A. Olsen, and W. Happer. Cusp kernels for velocity-changing collisions. *Physical Review Letters*, 108:183202, 2012.

[140] A. L. Stancik and E. B. Brauns. A simple asymmetric lineshape for fitting infrared absorption spectra. *Vibrational Spectroscopy*, 47(1):66–69, 2008.

[141] F. S. Ponciano-Ojeda. *Stokes polarimetry and magnetometry using a thermal Rb vapour in the Voigt geometry with large magnetic field*. PhD thesis, Durham University, 2021.

[142] B. L. Schmittberger Marlow. Degenerate four-wave-mixing as a low-power source of squeezed light. *Optics Express*, 28(25):38169–38183, 2020.

[143] K. R. MacDonald, W. R. Tompkin, and R. W. Boyd. Passive one-way aberration correction using four-wave mixing. *Optics Letters*, 13(6):485–487, 1988.

[144] T. G. Alley, M. A. Kramer, D. R. Martinez, and L. P. Schelonka. Single-pass imaging through a thick dynamic distorter using four-wave mixing. *Optics Letters*, 15(1):81–83, 1990.

[145] P. S. Hsu, A. K. Patnaik, and G. R. Welch. Controlled parametric generation in a double-ladder system via all-resonant four-wave mixing. *Optics Letters*, 33(4):381–383, 2008.

[146] V. Boyer, C. F. McCormick, E. Arimondo, and P. D. Lett. Ultraslow propagation of matched pulses by four-wave mixing in an atomic vapor. *Physical Review Letters*, 99:143601, 2007.

[147] V. Boyer, A. M. Marino, R. C. Pooser, and P. D. Lett. Entangled images from four-wave mixing. *Science*, 321(5888):544–547, 2008.

[148] R. M. Camacho, P. K. Vudyasetu, and J. C. Howell. Four-wave-mixing stopped light in hot atomic rubidium vapour. *Nature Photonics*, 3(2):103–106, 2009.

[149] S. Kim and A. M. Marino. Generation of 87rb resonant bright two-mode squeezed light with four-wave mixing. *Optics Express*, 26(25):33366–33375, 2018.

[150] R. T. Willis, F. E. Becerra, L. A. Orozco, and S. L. Rolston. Four-wave mixing in the diamond configuration in an atomic vapor. *Physical Review A*, 79:033814, 2009.

[151] G. Walker, A. S. Arnold, and S. Franke-Arnold. Trans-spectral orbital angular momentum transfer via four-wave mixing in Rb vapor. *Physical Review Letters*, 108:243601, 2012.

[152] F. Wen, H. Zheng, X. Xue, H. Chen, J. Song, and Y. Zhang. Electromagnetically induced transparency-assisted four-wave mixing process in the diamond-type four-level atomic system. *Optical Materials*, 37:724–726, 2014.

[153] R. C. Pooser and B. Lawrie. Ultrasensitive measurement of microcantilever displacement below the shot-noise limit. *Optica*, 2(5):393–399, 2015.

[154] F. Ripka, Y.-H. Chen, R. Löw, and T. Pfau. Rydberg polaritons in a thermal vapor. *Physical Review A*, 93:053429, 2016.

[155] U. Khadka, H. Zheng, and M. Xiao. Interferometric control of parametrically amplified waveforms. *Physical Review A*, 84:043814, 2011.

[156] Y.-S. Lee and H. S. Moon. Atomic coherence effects in four-wave mixing process of a ladder-type atomic system. *Optics Express*, 24(10):10723–10732, 2016.

[157] K. A. Forbes, J. S. Ford, and D. L. Andrews. Nonlocalized generation of correlated photon pairs in degenerate down-conversion. *Physical Review Letters*, 118:133602, 2017.

[158] B. Jin, D. Mishra, and C. Argyropoulos. Efficient single-photon pair generation by spontaneous parametric down-conversion in nonlinear plasmonic metasurfaces. *Nanoscale*, 13:19903–19914, 2021.

[159] R. Hanbury Brown and R. Q. Twiss. Correlation between photons in two coherent beams of light. *Nature*, 177(4497):27–29, 1956.

[160] R. Hanbury Brown and R. Q. Twiss. A test of a new type of stellar interferometer on sirius. *Nature*, 178(4541):1046–1048, 1956.

[161] C. Gerry and P. Knight. *Introductory Quantum Optics*. Cambridge University Press, 2004.

[162] B. Srivathsan, G. K. Gulati, B. Chng, G. Maslennikov, D. Matsukevich, and C. Kurtsiefer. Narrow band source of transform-limited photon pairs via four-wave mixing in a cold atomic ensemble. *Physical Review Letters*, 111:123602, 2013.

[163] B. Srivathsan. *Heralded Single Photons For Efficient Interaction with Single Atoms*. PhD thesis, 2014.

Colophon

This thesis is based on a template developed by Matthew Townson and Andrew Reeves. It was typeset with LaTeX 2_ε. It was created using the *memoir* package, maintained by Lars Madsen, with the *madsen* chapter style. The font used is Latin Modern, derived from fonts designed by Donald E. Kunith.